Study of nuclear structure near the Z = 82 and N = 82 shell closures

By

HARIDAS PAI

Enrolment No: PHYS04200704004

Variable Energy Cyclotron Centre, Kolkata

A thesis submitted to
The Board of Studies in Physical Sciences

In partial fulfillment of requirements

For the Degree of

DOCTOR OF PHILOSOPHY

of

HOMI BHABHA NATIONAL INSTITUTE

June, 2012

Homi Bhabha National Institute

Recommendation of the Viva Voce Board

As members of the Viva Voce Board, we certify that we have read the dissertation prepared by **Haridas Pai** entitled **Study of nuclear structure near the Z = 82 and N = 82 shell closures** and recommend that it may be accepted as fulfilling the dissertation requirement for the degree of Doctor of Philosophy.

....**Date:**
Chairman- Dr. S.R. Banerjee

....**Date:**
Supervisor- Dr. C. Bhattacharya

....**Date:**
Co-supervisor- Dr. G. Mukherjee

....**Date:**
Member 1- Dr. A. Goswami

....**Date:**
Member 2- Dr. V.S. Pandit

....**Date:**
Member 3- Shri A. Roy

....**Date:**
External examiner- Dr. S.K. Mandal

Finally approval and acceptance of this dissertation is contingent upon the candidate's submission of the final copies of the dissertation to HBNI.
I hereby certify that I have read this dissertation prepared under my direction and recommend that it may be accepted as fulfilling the dissertation requirement.

date:

Place:

STATEMENT BY AUTHOR

This dissertation has been submitted in partial fulfillment of requirements for an advanced degree at Homi Bhabha National Institute (HBNI) and is deposited in the Library to be made available to borrowers under rules of the HBNI.

Brief quotation from this dissertation are allowable without special permission, provided that accurate acknowledgement of source is made. Requests for permission for extended quotation from or reproduction of this manuscript in whole or in part may be granted by the Competent Authority of HBNI when in his or her judgement the proposed use of the material is in the interests of scholarship. In all other instances, however, permission must be obtained from the author.

Haridas Pai

DECLARATION

I, hereby declare that the investigation presented in the thesis has been carried out by me. The work is original and has not been submitted earlier as a whole or in part for a degree/diploma at this or any other Institution/University.

Haridas Pai

Dedicated to my 'Nation'

ACKNOWLEDGMENTS

I gratefully acknowledge the constant and invaluable academic and personal support received from my supervisors Dr. Chandana Bhattacharya and Dr. Gopal Mukherjee throughout my thesis work. I am really thankful and indebted to them for having been the advisors everyone would like to have, for their clear and enthusiastic discussion, for helping me to find my firm grounding in the research problem and without their dedicated supervision it would have been never possible to complete this thesis.

I am very much indebted to Prof. Bikash Sinha, former Director and Homi Bhabha Chair, Variable Energy Cyclotron Centre (VECC), Prof. Dinesh Kumar Srivastava, Head, Physics Group, VECC, Prof. Sailajananda Bhattacharya, Head, experimental nuclear physics division, VECC, for giving me the encouragement and kind support. I am grateful to our Director, Prof. Rakesh Kumar Bhandari as well to our Group Head for providing a vibrant working atmosphere and full edged facility which helped me immensely during my research work.

I am very much indebted to Dr. Sarmishtha Bhattacharyya, Dr. Tumpa Bhattacharjee and Dr. Somen Chanda for their suggestions and help through out my Ph. D. work.

I am extremely grateful to Dr. Santanu Pal, Head, Theoretical Physics Division, VECC, Dr. S. R. Banerjee, Head, Experimental Nuclear Physics Section, VECC, Dr. S. K. Basu, Dr. R.K. Bhowmik, Professor Asimananda Goswami and Professor Maitreyee Saha Sarkar from Saha Institute of Nuclear Physics for their encouragement and kind support. I have really enjoyed the discussion with them on various physics issues.

I would like to give my sincere thanks to Dr. Rudrajyoti Palit from TIFR for his helps and suggestions at various stages.

It is my great pleasure to thank Jhilam da for his constant teaching and kind support throughout my thesis work.

I am really grateful to Dr. Somenath Chakraborty, Dr. Sudipta Narayan Roy, Dr. Bikash Chandra Gupta, Dr. Buddhadev Mukherjee and Dr. Ashis Bhattacharyya from Visva-Bharati University for their encouragement and inspiration.

I would like to mention a special thank to my friend and mentor Ashish Pal, without whom it would never been possible to start the journey of physics for me.

Due to limited space I could not mention some of my teachers, friends, juniors, whose constants constructive discussions encourage me enormously from my schooling days, are always been very close to me and I always thank them from the core of my heart.

I would like to thank Dr. Jan-e Alam, Dr. P. Barat, Dr. V. S. Pandit, Dr. Bedangadas Mohanty, Dr. A. K. Dubey, Dr. S. Sarkar, Dr. D. N. Basu, Dr. S. Chattopadhya, Dr. T. Mukhopadhyay, Dr. T. K. Nayak, Dr. P. Das, Dr. M. Bhattacharya, Dr. T. K. Ghosh, Dr. A. Dey, Dr. S. Dasgupta, K. Banerjee, S. Kundu, T. K. Rana, J. K. Meena, R. Pandey, S. Mukhopadhyay, D. Pandit, Dr. S. Pal, D. Banerjee, Dr. R. Guin, and Dr. S. K. Das for their suggestions, advice and constant encouragement.

The excellent support and encouragement received from Ms. Anindita Chowdhury, Mr. Pulak Mukhopadhyay and Mr. Subrata Mukherjee of Physics Laboratory, VECC, is acknowledged with thanks.

The help of all the collaborators in the present work, from different institutions (VECC, TIFR, IUAC, SINP) and Universities (Delhi University, Guru Nanak Dev University, Panjab University, Fakir Chand College-Calcutta University), in India are gratefully acknowledged. The effort of the operators of the accelerators at VECC, TIFR and IUAC, and all the participating group in the CLOVER Array Collaboration are acknowledged.

I was extremely fortunate to have Victor Roy, Santosh Kumar Das, Payal Mohanty, Sabyasachi Ghosh, Pratap Roy and Amlan Dutta, as my companions, whose constructive criticism and friendly advice will remain in my memory.

I would like to express my sincere thanks to Prasun da, Jajati da, Jamil di, Rupa di, Pravash da, Partha da, Arnomitra di, Tapasi di, Sidharth da, Mriganka da, Saikat da, Prithis da, Sanjib da, swagata, santosh da, Sudatta di, Negi da and Tarkeshwar da for their encouragement and support.

It is a pleasure to thank Nihar, Sudipan, Subhash, Trambak, Surasree, Somnath, Younus, Manish, Vishal, Arnab, Abhisek, Nasim, Somnath, Debojit, Amal, Rihan, Sumit, Subikash, Arindam, Balaram, Maitreyee, Sukanya and Abijit Bisoi for their support.

I would like to express my sincere thanks to all the well wishers of VECC and elsewhere.

I am deeply indebted and grateful to my parents, uncle, brother, sister and rest of my family members. I do appreciate the unlimited support, love and encouragement that you have given to me during my study. Without them I would be nothing. Thank you very much. At this moment, I very much remember with gratitude that my father and sister always encouraged my likings and gave confidence to produce my best.

I sincerely apologize inadvertent omission of any name from the above list of acknowledgment.

Haridas Pai

SYNOPSIS

This thesis work is devoted to the experimental investigation of the high spin structure of the nuclei near Z = 82 and N = 82 shell closures. In the present work, the high spin states in ^{194,197}Tl (Z = 81) and ^{195,198}Bi (Z = 83) with proton numbers close to and on either side of the Z = 82 spherical shell closure and in ^{134}Cs (Z = 55) with neutron number close to the N = 82 spherical shell closure have been studied by high resolution gamma ray spectroscopic method. Fusion-evaporation reactions, using both heavy and light ion beams, were used to populate the high spin states in these nuclei. Several experiments were performed at three major accelerator centres in India i.e at VECC (Kolkata), TIFR (Mumbai) and IUAC (New Delhi) and different configurations of the Indian National Gamma Array (INGA), consisted of Clover HPGe detectors, were used in these investigations. A small in-house setup at VECC, consisted of a clover, a single crystal HPGe and a LEPS (Low Energy Photon Spectrometer) detector, was also used for one of the experiments using α beam. New and improved level schemes of these nuclei have been proposed in this work which were obtained from the analysis of γ-γ matrices and γ-γ-γ cubes. The coincidence relations among the detected γ-rays and their intensity relations were used to build up the level schemes. Definite spin and parity of the excited states in these nuclei were assigned from the knowledge of the multipolarity and type (electric or magnetic) of the emitted γ-rays which were determined from the Directional Correlation of Oriented (DCO) states ratio and the Integrated Polarization (IPDCO) measurements, respectively. The Total Routhian Surface (TRS) calculations were performed using cranked shell model with Woods-Saxon potential to understand the results obtained in this work. For the Magnetic Rotational (MR) bands, observed in this work, the particle-hole interaction strengths were determined using semiclassical calculations.

The nuclei near the Z = 82 and the N = 82 shell closures in A $\sim$ 190 and A $\sim$ 130 mass regions, respectively, are crucial laboratories to observe interesting nuclear structure phenomena and to test a variety of nuclear models. The proximity of the spherical shell closures and competing shape (prolate and oblate) driving effects of the high-j orbitals ($\pi h_{9/2}$, $\pi i_{13/2}$ & $\nu i_{13/2}$ for Thallium and Bismuth nuclei and $\pi h_{11/2}$ & $\nu h_{11/2}$ for the Cesium nucleus), near the proton and neutron Fermi levels, induce shape co-existence and triaxiality in the nuclei in these regions.

Therefore, apart from normal deformed band structures, the MR band and chiral doublet bands are expected in these nuclei.

Because of the reinforcing effect of proton and neutron spherical magic gaps at Z = 82 and N = 126, the heavy Bismuth nuclei ($A > 200$) are mostly spherical, the excited states of which can be understood from the spherical shell model as the odd proton occupies different shell model states above Z = 82. In the present thesis work, MR bands have been observed in ^{198}Bi with multi particle-hole configuration at higher excitation energy. This indicates that the shears mechanism plays important role for the generation of angular momenta in the near spherical lighter Bismuth nuclei with $A < 200$. As the neutron number deviates further from the $N = 126$ spherical shell closure towards midshell, the deformation is expected to set in for the neutron deficient isotopes. Rotational bands, characteristic of a deformed nucleus, have indeed been observed for the very neutron deficient isotopes ^{191,193}Bi. However, as the high spin states in ^{195}Bi were not well studied and no rotational band has been reported so far in ^{197}Bi, the neutron number corresponding to the onset of deformation in Bi nuclei was not known. In the present thesis work, a rotational band in ^{195}Bi has been observed at low excitation which clearly suggests $N = 112$ as the border of sphericity in Bi isotopes. In other words, the present thesis work indicates that the effect of $N = 126$ shell closure to reinforce the spherical shape in nuclei lessens for neutron number $N \leq 112$.

The $\pi[505]9/2^-$ and $\pi[606]13/2^+$ Nilsson orbitals are the intruder proton orbitals for the Thallium (Z = 81) nuclei. These orbitals, play significant role in breaking the spherical symmetry in a nucleus close to the spherical magic number. Deformed rotational band structure may develop based on these proton intruder levels particularly for the isotopes with near-midshell neutron number favoring deformation. It is important to know the excitation energies of these intruder levels in an odd-A isotope and a possible low-lying deformed band structure in an odd-odd isotope of Thallium. In the present thesis work, the hitherto, unknown $\pi i_{13/2}$ level has been discovered in ^{197}Tl. In odd-odd nucleus ^{194}Tl, rotational band, based on $\pi h_{9/2} \otimes \nu i_{13/2}$ configuration, has been extended beyond the band crossing frequency. The properties of this band have been compared with those in ^{190}Tl and ^{198}Tl, which are reported to have contrasting structures. In ^{198}Tl, this band was interpreted as due to chiral symmetry breaking and a triaxial shape has been proposed while the similar band in ^{190}Tl was interpreted assuming oblate deformation. Therefore, it was important to know the band structure in the intermediate isotopes. In the present work, the band based on the above configuration in ^{194}Tl show similar behaviour as those in ^{190,198}Tl. It has been shown that the signature splitting and the moment of inertia for this band is very similar in all these three isotopes. The TRS calculations also suggest oblate deformation for all the three isotopes with similar deformation. Moreover, a MR band has also been observed in ^{194}Tl in this work, based on a six quasiparticle configuration. It may be pointed out that it is for the first time that a MR band has been observed for an odd-proton nucleus below $Z = 82$ in the Pb-Hg region.

In order to extend the present work for the nuclei near $N = 82$ shell closure, detailed investigation of the high spin states in ^{134}Cs has been carried out. The knowledge about the excited states in this odd-odd nucleus with neutron number $N = 79$ was limited to 8^- only, prior to the present work. In the present work, the high spin states have been extended up to an excitation energy of 3.8 MeV and spin of 16^+ with the observation of several band structures including a band based on $\pi h_{11/2} \otimes \nu h_{11/2}$ configuration for the first time in this neutron rich nucleus. The lighter, neutron deficient Cesium isotopes are known to be deformed and the band structure based on the above configuration in the odd-odd isotopes, are reported as, arises due to chiral symmetry breaking with a stable triaxial deformation. A very different structure compared to its lighter isotopes has, however, been observed for the $\pi h_{11/2} \otimes \nu h_{11/2}$ band in ^{134}Cs. This band in ^{134}Cs has been found to be composed of only M1 transitions with no E2 crossover transitions which indicate its MR nature. Therefore, the chirality seems to breakdown for neutron number $N = 79$ in Cesium isotopes. The tilted axis cranking (TAC) calculations also suggest a change in structure for ^{134}Cs compared to its immediate odd-odd neighbor ^{132}Cs. A close investigation of the calculated TRS shows that a stable triaxial minimum appeared for the lighter isotopes of Cesium up to N = 77 and the surface becomes very gamma soft for the isotopes with $N \geq 79$ i.e as the neutron number is getting closer to the $N = 82$ shell closure. The gamma softness destroys the chiral behaviour and the near spherical shape favors MR band in ^{134}Cs for the above configuration. The results obtained for ^{134}Cs in this thesis work suggest that $N = 77$ defines the border of triaxial deformation and chirality in odd-odd Cs isotopes.

LIST OF PUBLICATIONS

(A) Relevant to the present Thesis

In referred journals :

1. **Structural change of the unique-parity $\pi h_{11/2} \otimes \nu h_{11/2}$ configuration in ^{134}Cs.**
   H. Pai, G. Mukherjee, A. Raghav, R. Palit, C. Bhattacharya, S. Chanda, T. Bhattacharjee, S. Bhattacharyya, S.K. Basu, A. Goswami, P.K. Joshi, B.S. Naidu, Sushil K. Sharma, A.Y. Deo, Z. Naik, R.K. Bhowmik, S. Muralithar, R.P. Singh, S. Kumar, S. Sihotra, and D. Mehta.
   Phys. Rev. C **84**, 041301(R) (2011).

2. **High spin band structures in doubly-odd ^{194}Tl.**
   H. Pai, G. Mukherjee, S. Bhattacharyya, M.R. Gohil, T. Bhattacharjee, C. Bhattacharya, R. Palit, S. Saha, J. Sethi, T. Trivedi, Shital Thakur, B.S. Naidu, S.K. Jadav, R. Donthi, A. Goswami and S. Chanda.
   Phys. Rev. C **85**, 064313 (2012).

3. **Onset of deformation at N = 112 in Bi nuclei.**
   H. Pai, G. Mukherjee, R. Raut, S.K. Basu, A. Goswami, S. Chanda, T. Bhattacharjee, S. Bhattacharyya, C. Bhattacharya, S. Bhattacharya, S.R. Banerjee, S. Kundu, K. Banerjee, A. Dey, T.K. Rana, J.K. Meena, D. Gupta, S. Mukhopadhyay, Srijit Bhattacharya, Sudeb Bhattacharya, S. Ganguly, R. Kshetri, and M.K. Pradhan.
   Phys. Rev. C **85**, 064317 (2012).

Results Reported in Conferences/Symposia :

1. **High spin spectroscopy of ^{134}Cs.**
   H. Pai, G. Mukherjee, S. Bhattacharyya, T. Bhattacharjee, R. palit A. Y. Deo, P.K.

Joshi, B. S .Naidu, S. Sharma, A. Raghav, Z. Naik, A. Goswami, S. kumar, S.Sihotra and D. Mehta.

Proceedings of the International Symposium on nuclear physics, DAE, Vol **54** 88 (2009).

2. **Deformed shapes in odd-odd nuclei near Z = 82.**

   G. Mukherjee, **H. Pai**, S. Bhattacharya, C. Bhattacharya, S. Bhattacharyya, S. Chanda, T. Bhattacharjee, S. K. Basu, S. Kundu, T. K. Ghosh, K. Banerjee, T. K. Rana, J. K. Meena, R. K. Bhowmik, R. P. Sing, S. Muralithar and R. Garg.

   Proceedings of the International Symposium on nuclear physics, DAE, Vol **54** 98 (2009).

3. **Structure of Odd-Odd Nucleus ^{134}Cs at High Spin.**

   H. Pai, G. Mukherjee, R.K. Bhowmik, S. Bhattacharyya, T. Bhattacharjee, C. Bhattacharya, S.K. Basu, R. Palit, S. Chanda, A.Y. Deo, P.K. Joshi, B. S. Naidu, Z. Naik, Sushil K. Sharma, A. Raghav, A. Goswami, S. Kumar, S. Sihotra, D. Mehta, S. Muralithar, R.P. Singh, N.S. Pattabiraman and S.S. Ghugre.

   Nuclear Structure 2010 Clark-Kerr Campus, U. C. Berkeley, CA August 8th - August 13th, 2010.

4. **Study of magnetic rotation in ^{198}Bi.**

   H. Pai, G. Mukherjee, S. Bhattacharya,C. Bhattacharya, S. Bhattacharyya, S. Chanda, T. Bhattacharjee, S.K. Basu, S. Kundu, T.K. Ghosh, K. Banerjee, T.K. Rana, J.K. Meena, R.K. Bhowmik, R.P. Singh, S. Muralithar and R. Garg.

   Proceedings of the DAE Symposium on nuclear physics, Vol **55** 80 (2010).

5. **Change over from Chiral to Shears geometry in Cs isotopes.**

   G. Mukherjee and **H. Pai**.

   Proceedings of the DAE Symposium on nuclear physics, Vol **55** 82 (2010).

6. **Coexistence of different band structures in odd-odd ^{194}Tl.**

   H. Pai, G. Mukherjee, S. Bhattacharyya, M.R. Gohil, C. Bhattacharya, R. Palit, A. Goswami, T. Bhattacharjee, S. Saha, J. Sethi, T. Trivedi, S. Thakur, B.S. Naidu, S.K. Jadav and R Donthi.

   Proceedings of the DAE Symposium on nuclear physics Vol **56** 198 (2011).

7. **Gamma ray spectroscopy of ^{197}Tl using α beam.**

   H. Pai, G Mukherjee, S. Bhattacharyya, M.R. Gohil, C. Bhattacharya, S. Bhattacharya, A. Goswami, T. Bhattacharjee, S. Chanda, K. Banerjee, S.R. Banerjee, A. Chowdhury, P. Chowdhury,T.K. Ghosh, S. Kundu, J.K. Meena, P. Mukhopadhyay, S. Mukhopadhyay, S. Pal, R. Pandey, D. Pandit, G. Prajapati, S. Rajbangshi and T.K. Rana.

   Proceedings of the DAE Symposium on nuclear physics Vol **56** 286 (2011).

(B) Other publications (in refereed journals)

1. **Cluster emission in ^{13}C + ^{12}C and ^{12}C + ^{12}C reactions at $\sim$ 6 MeV/Nucleon.**

   T. K. Rana, C. Bhattacharya, S. Kundu, K. Banerjee, S. Bhattacharya, G. Mukherjee, T. K. Ghosh, J. K. Meena, P. Dhara, M. Biswas, **H. Pai**, K. Mahata, Suresh Kumar, K. Ramachandran, P. C. Rout, S. K. Pandit, V. Nanal and R. G. Pillay.

   International Journal of Modern Physics E **20**, 789 (2011).

2. **Measurement and simulation of neutron response function of organic liquid scintillator detector.**

   M. Gohil, K. Banerjee, S. Bhattacharya, C. Bhattacharya, S. Kundu, T.K. Rana, G. Mukherjee, J.K. Meena, R. Pandey, **H. Pai**, T.K. Ghosh, A. Dey, S. Mukhopadhyay, D. Pandit, S. Pal, S.R. Banerjee and T. Bandhopadhyay.

   Nucl. Instrum. Meth. Phys. Res. A **664**, 304 (2012).

3. **Measurement of giant dipole resonance width at low temperature: A new experimental perspective.**

   S. Mukhopadhyay, Deepak Pandit, Surajit Pal, Srijit Bhattacharya, A. De, S. Bhattacharya, C. Bhattacharya, K. Banerjee, S. Kundu, T.K. Rana, G. Mukherjee, R. Pandey, M. Gohil, **H. Pai**, J.K. Meena and S.R. Banerjee.

   Physics Letters B **709**, 9 (2012).

4. **Complex-fragment emission in low-energy light-ion reactions.**

   S. Kundu, C. Bhattacharya, K. Banerjee, T. K. Rana, S. Bhattacharya, A. Dey, T. K.

Ghosh, G. Mukherjee, J. K. Meena, P. Mali, S. Mukhopadhyay, D. Pandit, **H. Pai**, S. R. Banerjee, and D. Gupta P. Banerjee, Suresh Kumar, A. Shrivastava, A. Chatterjee, K. Ramachandran, K. Mahata, S. Pandit and S. Santra.
Phys. Rev. C **85**, 064607 (2012).

5. **Variation of nuclear level density with angular momentum.**
K. Banerjee, S. Bhattacharya, C. Bhattacharya, M. Gohil, S. Kundu, T. K. Rana, G. Mukherjee, R. Pandey, P. Roy, **H. Pai**, A. Dey, T. K. Ghosh, J. K. Meena, S. Mukhopadhyay, D. Pandit, S. Pal and S. R. Banerjee.
Phys. Rev. C **85**, 064310 (2012).

Results Reported in Conferences/Symposia :

1. **Lifetime measurements in ^{139}Pr.**
S. Chanda, T. Bhattacharjee, S. Bhattacharyya, **H. Pai**, G. Mukherjee, S. K. Basu, R. Garg, J. Kaur, G. Mohanty, P. Sugathan, R. P. Sing, S. Muralithar, N. Madhavan, A. Jhingan, A. Dhal, R. K. Bhowmik, C. M. Petrache, I. Ragnarsson, S. Bhowal and G. Gangopadhyay.
Proceedings of the International Symposium on nuclear physics, DAE, Vol **54** 94 (2009).

2. **Spectroscopy of ^{207}Rn across isomeric state.**
S. Bhattacharyya, T. Bhattacharjee, S. Chanda, **H. Pai**, G. Mukherjee, S. K. Basu, R. K. Bhowmik, A. Dhal, R. Garg, A. Jhingan, J. Kaur, N. Madhavan, G. Mohanty, S. Muralithar, R. P. Sing and P. Sugathan.
Proceedings of the International Symposium on nuclear physics, DAE, Vol **54** 100 (2009).

3. **Isoscaling in ^{13}C + ^{12}C and ^{12}C + ^{12}C reactions at $\sim$ 6 MeV/u.**
T. K. Rana, C. Bhattacharya, S. Kundu, K. Banerjee, S. Bhattacharya, G. Mukherjee, T. K. Ghosh, J. K. Meena, P. Dhara, M. Biswas, **H. Pai**, K. Mahata, Suresh Kumar, K. Ramachandran, P. C. Rout, S. K. Pandit, V. Nanal and R. G. Pillay.
Proceedings of the International Symposium on nuclear physics, DAE, Vol **54** 388 (2009).

4. **Measurement of lifetime and transition moments near doubly closed ^{146}Gd.**

   T. Bhattacharjee, D. Banerjee, A. Chowdhury, S. Bhattacharyya, R. Guin, S. K. Das, S. K. Basu, P. Das, C. C. Dey, **H. Pai** and P. Mukhopadhyay.

   Proceedings of the DAE Symposium on nuclear physics, Vol **55** 12 (2010).

5. **Rotational particle coupling in ^{134}Cs.**

   T. Bhattacharjee, **H. Pai** and S. Bhattacharya.

   Proceedings of the DAE Symposium on nuclear physics, Vol **55** 62 (2010).

6. **High Spin Spectroscopy of odd-odd ^{140}Pr.**

   T. Bhattacharjee, S. Chanda, S. Bhattacharyya, **H. Pai**, G. Mukherjee, S. K. Basu, R. K. Bhowmik, A. Dhal, R. Garg, A. Jhingan, J. Kaur, N. Madhavan, G. Mohanty, S. Muralithar, R. P. Singh and P. Sugathan.

   Proceedings of the DAE Symposium on nuclear physics, Vol **55** 70 (2010).

7. **Study of odd Osmium isotopes from EC decay.**

   S. Bhattacharyya, T. Bhattacharjee, D. Banerjee, R. Guin, S. K. Das, **H. Pai**, A. Chowdhury, G. Mukherjee and P. Das.

   Proceedings of the DAE Symposium on nuclear physics, Vol **55** 78 (2010).

8. **Three α-decays of Hoyle state of ^{12}C in ^{12}C + ^{12}C reaction.**

   T. K. Rana, C. Bhattacharya, S. Kundu, K. Banerjee, S. Bhattacharya, G. Mukherjee, T. K. Ghosh, J. K. Meena, P. Dhara, M. Biswas, **H. Pai**, K. Mahata, Suresh Kumar, K. Ramachandran, P. C. Rout, S. K. Pandit, V. Nanal and R. G. Pillay.

   Proceedings of the DAE Symposium on nuclear physics, Vol **55** 230 (2010).

9. **Angular momentum gated neutron evaporation studies.**

   K. Banerjee, S. Kundu, T. K. Rana, C. Bhattacharya, G. Mukherjee, M. Gohil, J. K. Meena, R. Pandey, **H. Pai**, A. Dey, M. Biswas, S. Mukhopadhyay, D. Pandit, S. Pal, S. R. Banerjee, T. Bandhopadhyay and S. Bhattacharya.

   Proceedings of the DAE Symposium on nuclear physics, Vol **55** 324 (2010).

10. **Geant4 simulation of pulse-height response function of liquid scintillator based neutron detector.**
M. Gohil, K. Banerjee, C. Bhattacharya, S. Kundu, T. K. Rana, G. Mukherjee, J. K. Meena, R. Pandey, **H. Pai**, M. Biswas, A. Dey, T. Bandhopadhyay and S. Bhattacharya.
Proceedings of the DAE Symposium on nuclear physics, Vol **55** 720 (2010).

11. **Spectroscopy of heavy isotopes of Hg and Au from incomplete fusion reaction.**
S. Bhattacharyya, S. Dasgupta, **H. Pai**, A. Shrivastava, G. Mukherjee, R. Palit, T. Bhattacharjee, S. Chanda, A. Chatterjee, V. Nanal, S.K. Pandit, S. Saha and S. Thakur.
Proceedings of the DAE Symposium on nuclear physics Vol **56** 354 (2011).

12. **High spin structure of ^{200,201}Tl isotopes.**
S. Dasgupta, S. Bhattacharyya, **H. Pai**, A. Shrivastava, G. Mukherjee, R. Palit, T. Bhattacharjee, S. Chanda, A. Chatterjee, V. Nanal, S.K. Pandit, S. Saha and S. Thakur.
Proceedings of the DAE Symposium on nuclear physics Vol **56** 356 (2011).

13. **Excited states of neutron rich ^{150}Pm using (p, nγ) reaction.**
T. Bhattacharjee, D. Banerjee, K. Banerjee, S. R. Banerjee, S. K. Basu, C. Bhattacharya, S. Bhattacharya, S. Bhattacharyya, S. Chanda, A. Chowdhury, S. K. Das, T. K. Ghosh, A. Goswami, M. R. Gohil, R. Guin, S Kundu, J. K. Meena, G. Mukherjee, P. Mukhopadhyay, S. Mukhopadhyay, **H. Pai**, S. Pal, R. Pandey, D. Pandit, G. Prajapati, S. Rajbanshi and T. Rana.
Proceedings of the DAE Symposium on nuclear physics Vol **56** 358 (2011).

14. **Complete spectroscopy of ^{146}Eu using alpha beam from VEC.**
T. Bhattacharjee, D. Banerjee, P. Das, S. Das, A. Chowdhury, S. Bhattacharyya, R. Guin, **H. Pai** and P. Mukhopadhyay.
Proceedings of the DAE Symposium on nuclear physics Vol **56** 372 (2011).

15. **Polarization Asymmetry Measurements for the Yrast Band of ^{85}Rb.**
S. Kumar ,V. Kumar, Ritika. Garg, Naveen. Kumar, S. Verma, S. Mandal,T . Trivedi, S. Saha, J. Sethi, Gayatri, Arindam. Nandi, B.S. Naidu, S.K. Jadav, Rajneesh, R. Palit,

D. Choudhary, A.k. Jain, **Haridas Pai** and G. Mukherjee.

Proceedings of the DAE Symposium on nuclear physics Vol **56** 322 (2011).

16. **Negative Parity States in ^{86}Sr.**

    S. Kumar ,V. Kumar, Ritika. Garg, Naveen. Kumar, S. Verma, S. Mandal,T . Trivedi, S. Saha, J. Sethi, Gayatri, Arindam. Nandi, B.S. Naidu, S.K. Jadav, Rajneesh, R. Palit, D. Choudhary, A.k. Jain, **Haridas Pai** and G. Mukherjee.

    Proceedings of the DAE Symposium on nuclear physics Vol **56** 400 (2011).

17. **Measurement of relative production cross-section of 3n and 4n evaporation channels of an α-induced fusion reaction.**

    Mahua Chakraborty, **H. Pai** and G. Mukherjee.

    Proceedings of the DAE Symposium on nuclear physics Vol **56** 666 (2011).

18. **Extraction of angular momentum gated nuclear level density parameter.**

    K. Banerjee, C. Bhattacharya, M. Gohil, S. Kundu, T. K. Rana, G. Mukherjee, R. Pandey, **H. Pai**, Pratap Roy, T. K. Ghosh, J. K. Meena, S. Mukhopadhyay, D. Pandit, S. Pal, S. R. Banerjee and S. Bhattacharya.

    Proceedings of the DAE Symposium on nuclear physics Vol **56** 594 (2011).

19. **Study of light-particle evaporation spectra (n, p, α) in ^{4}He + ^{93}Nb reaction.**

    Pratap. Roy, K. Banerjee, S. Kundu, T.K. Rana, C. Bhattacharya, M. Gohil, G. Mukherjee, J.K. Meena, R. Pandey, **H. Pai**, A. Dey, T.K. Ghosh, S. Mukhopadhyay, D. Pandit, S. Pal, S.R. Banerjee and S. Bhattacharya.

    Proceedings of the DAE Symposium on nuclear physics Vol **56** 540 (2011).

20. **Structure and decay mechanism of Hoyle state.**

    T. K. Rana, S. Bhattacharya, C. Bhattacharya, S. Kundu, K. Banerjee, G. Mukherjee, J. K. Meena, R. Pandey, M. Gohil, **H. Pai**, A. Dey, T. K. Ghosh, M. Biswas and G. Prajapati.

    Proceedings of the DAE Symposium on nuclear physics Vol **56** 492 (2011).

21. **Study of Single nucleon transfer in $\alpha + {}^{12}$C reaction.**

    R. Pandey, T.K Rana, M. Biswas, A. Dey, C. Bhattacharya, S. Kundu, K. Banerjee, G. Mukherjee, T.K. Ghosh, J.K Meena, **H Pai**, M Gohil and S Bhattacharya. Proceedings of the DAE Symposium on nuclear physics Vol **56** 634 (2011).

22. **Low energy neutron response function of BC501A detector.**

    M. Gohil, K. Banerjee, C. Bhattacharya, S. Kundu, T. K. Rana, G. Mukherjee, R. Pandey, **H. Pai**, P. Roy, T. K. Ghosh, J. K. Meena and S. Bhattacharya.

    Proceedings of the DAE Symposium on nuclear physics Vol **56** 1046 (2011).

Contents

List of Figures

List of Tables

Chapter 1

Introduction

One can say that the journey of nuclear physics began with the discovery of nucleus by Ernest Rutherford in 1911. Even after 100 years of the discovery of the nucleus, many of the informations about the structure and the dynamical properties of the nucleus are still unknown. Till date nuclear physics remains an interesting subject and by no means a finished edifice. In the last 100 years, enormous development have been observed both experimentally and theoretically in this field. The progress in nuclear physics has been possible due to new innovations in detectors and accelerator technologies. On the other hand, various theoretical models have been developed and modified based on the experimental observations during this period.

The validity and acceptability of a nuclear structure model depends largely on how successfully it can explain the excited states of a nucleus. The liquid drop model was the first model proposed by Niels Bohr in 1939 [1] to describe the nuclear properties. This model describes successfully the bulk properties (binding energies) of a nucleus. However, the liquid drop model could not explain the certain discontinuities of some nuclear properties, such as two neutron or two proton separation energies, the magnetic moments etc. at nucleon numbers 2, 8, 20, 28, 50, 82 and 126 which are the so-called "*magic numbers*". The magic nuclei, corresponding to these magic numbers, show extra stability. This gave rise to the concept of closed shell nuclei and gave birth to the most successful nuclear model, the "*shell model*" [2], which was first proposed in the year 1949. This model could successfully describe the magic numbers and the

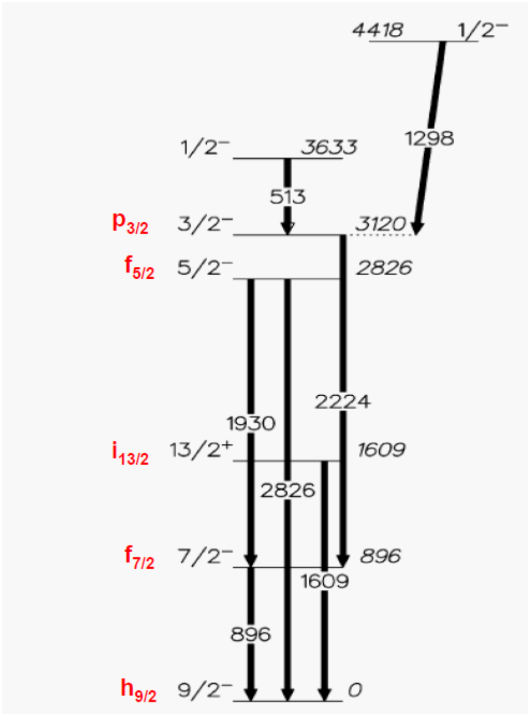

Figure 1.1: Level scheme of ^{209}Bi [3].

excited states in nuclei, in particular, for the single particle excitation in magic nuclei or near shell closure nuclei. There exist many other nuclear models in the literature, to describe the different aspects of nuclear structure and nuclear excitations. Mainly two types of excitations are involved in atomic nuclei, namely single particle and collective excitation.

• **Single particle excitation:** One of the most common method of generation of angular momenta in nuclei is via single particle excitation. According to the shell model, the spin and parity (J^π) of an odd-A nucleus are determined by the last unpaired particle. For example, the ground state spin and parity of ^{209}Bi (Z = 83, N = 126) is $J^\pi = 9/2^-$ corresponding to the occupation of the odd proton (unpaired valence particle) in the $h_{9/2}$ orbital which is situated just above the spherical magic number Z = 82. The level scheme of ^{209}Bi, as obtained by M. Lipoglavsek et al. from proton capture reaction on ^{208}Pb [3], has been shown in Fig 1.1. The excited states in this nucleus with $J^\pi = 7/2^-$, $13/2^+$, $5/2^-$ and $3/2^-$ have the highest single proton strengths and hence, they correspond, almost entirely, to the occupation of the odd-proton in the single particle spherical orbitals $f_{7/2}$, $i_{13/2}$, $f_{5/2}$ and $p_{3/2}$, respectively, situated above the $h_{9/2}$ orbital.

• **Collective excitation:** Collective excitations in nuclei are realized mainly through rotation and vibration resulted due to the collective motions of the nucleons.

In deformed nuclei, rotational bands [4, 5, 6] are observed and their excitation energies follow the $I.(I+1)$ rotational pattern, where 'I' is the total angular momentum.

On the other hand, energy levels in vibrational nuclei [7] are equidistant and follow the relation n$\hbar\omega$, where n = 0, 1, 2, ... are the number of phonons.

In addition to the above two excitations, angular momentum in nuclei can also be generated by other exotic modes, like magnetic rotation [8, 9], chiral rotation [10], etc.

• **Magnetic rotation:** Magnetic rotation (MR) is a well established mode of nuclear excitation. MR bands, consisting of long regular sequences of strong ΔI = 1 M1 transitions with very weak ΔI = 2 E2 crossovers, were discovered in many near spherical nuclei [8, 9]. These bands are formed by the coupling of particles and holes in high-j orbitals. Angular momenta are generated, in an MR band, by shears mechanism with step-by-step alignment of the particle and hole spins into the direction of the total angular momentum which resembles the closing of the blades of a pair of shears. A MR band can be identified from its different signatures as described in Ref.[8]. However, the most convincing experimental signature for the shears mechanism is the decreasing of the intraband B(M1) values with increasing spin. A MR band terminate when the shears are fully closed.

• **Chiral rotation:** A stable triaxial shape is needed for the occurrence of the chiral rotation in nuclei. A spontaneous breaking of the chiral symmetry can take place for configurations where the angular momentum vectors of the valence protons, valence neutrons, and the core are mutually perpendicular [10]. In this rotation high-j particles and holes are involved. The common experimental characteristics of chirality is the existence of two nearly degenerate ΔI = 1 bands of the same parity, which are called chiral doublet bands. For ideal chiral doublet bands, the corresponding properties such as energies, spin alignments, shapes, electromagnetic transition probabilities (B(E2) and B(M1) values for intraband transitions of the two bands must be same or very similar in practice) should be identical. The best examples of nuclear chirality have been found, till date, in ^{126}Cs [11], ^{128}Cs [12] and ^{135}Nd [13].

These interesting phenomena provide an opportunity to test the validity of different models and to study several aspects of nuclear excitation. These structural phenomena and their evolution in nuclei can be investigated through γ-ray spectroscopic methods.

In this thesis work, different excitation modes of nuclei in A = 190 and 130 regions have been studied with proton and neutron numbers close to 82, respectively, which is the common heaviest magic number for protons and neutrons. All the above modes of excitation may be realized in these nuclei and hence experimental study of the nuclei in these regions are important to test the validity of different models.

Nuclei around Z = 82 (in A $\sim$ 190 region) show a variety of shapes as one goes down in neutron number from N = 126 shell closure to midshell. In this region, the spherical shell model states $\pi s_{1/2}$, $\pi h_{9/2}$, $\pi i_{13/2}$, and $\pi f_{7/2}$ are available. The Nilsson diagram corresponding to this region shows that both the [505]$9/2^-$ and the [606]$13/2^+$ proton orbitals, originated from the $h_{9/2}$ and the $i_{13/2}$ spherical states, have strong shape driving effect towards oblate shape. On the other hand, the [541]$1/2^-$ and [660]$1/2^+$ proton orbitals, originated from the same spherical states, have strong shape driving effect towards prolate shape. Moreover, unique parity $\nu i_{13/2}$ orbital is also accessible for neutrons in this region. To probe the different spherical single particle (like ^{209}Bi) and Nilsson levels, study of odd-Z nuclei are necessary. The competing nature of different Nilsson orbitals are reflected in the calculated shapes of different nuclei in this region which show the occurrence of various shapes including shape coexistence [14, 15]. Two proton excitations across the shell gap are generally responsible for oblate deformed structure in this region where as, multiparticle excitations having four or more protons induce prolate deformations [16].

Qualitative information on the evolution of nuclear shapes in a isotopic chain can be obtained from the the ratio of excitation energies of $E(I)/E(I-2)$ (I = 4, 6 or 8). This also gives information about the method of generation of angular momentum 'I' in a nucleus.

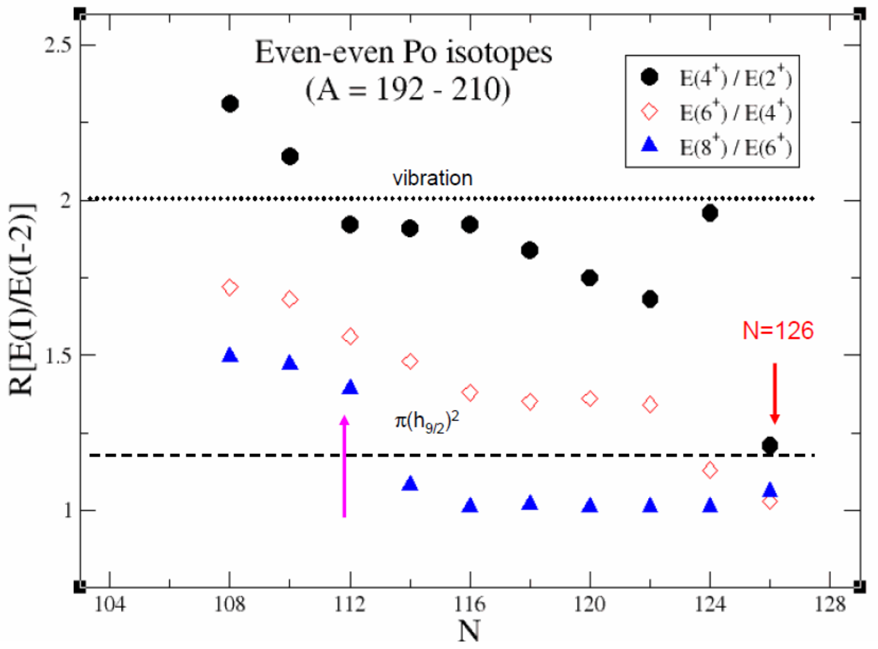

Figure 1.2: Systematic of ratio of excitation energies E(I)/E(I-2), for angular momentum I = 4,6 and 8 for Po (Z = 84) isotopes as a function of neutron number N.

The values of these ratios are shown in Fig 1.2 for polonium (Z = 84) isotopes as a function of neutron number N. The ratio of the energies of 4^+ level to 2^+ level is equal to 3.33 in the rotational limit, while in the vibrational limit it is equal to 2.0. The dotted line in Fig. 1.2 corresponds to the vibration limit of the ratios whereas the dashed line is the calculated single particle energies for two quasi-particle excitation in $h_{9/2}$ orbital for spherical shape. It can be seen that in even-even Po (Z = 84) isotopes the ratio of the excitation energies of 4^+ and 2^+ remains close to the vibrational limit ($E_{4^+}/E_{2^+} \sim 2$) until $N = 112$, below which it starts to increase towards the rotational limit [17]. Similarly, the E_{8^+}/E_{6^+} ratio deviates from the $\pi(h_{9/2})^2$ limit for the lighter isotopes with neutron number below $N = 114$. These indicate a clear evidence of structural change for neutron number $N \leq 114$.

In the Bismuth nuclei (Z = 83) a variety of structures are identified from spherical to superdeformed shapes as one goes down in neutron number from N = 126 shell closure to midshell (around N = 110). As mentioned earlier, a spehrical shape is evident from the excited states in ^{209}Bi (N = 126) [3] whereas, collective rotational bands have been observed in ^{191,193}Bi [18] which indicate deformed shape in bismuth nuclei for neutron number N = 109, 110. Superdeformed bands have also been identified in this region in Bi isotopes in a Gammasphere experiment [19]. On the other hand, low lying states in $^{197-201}$Bi could be interpreted in terms of shell model and weak coupling of the odd proton to the neutron-hole states in the neighboring Pb core [20, 21]. Recently, a magnetic rotational band has been reported at high excitation (> 4 MeV) energy, indicating a small deformation at high excitation in ^{197}Bi [22]. Therefore, in other words, the neutron magic gap at N = 126 seems to reinforce the Z = 82 magic gap until at least N = 114 to induce spherical shapes in the heavy mass Bismuth nuclei. It is, however, an open question whether the effect of this reinforcement continues up to even lower values of the neutron number or breaks down due to the *onset of deformation* in the Bi isotopes at N = 112, where deformed shell gap exists in the Nilsson diagram. High spin states of the odd-Z ^{195}Bi have been studied, in the present thesis work, using γ-ray spectroscopic techniques with this aim.

In A = 190 region, valence protons occupy high-j and high-Ω orbital ($\pi h_{9/2}$) and valence neutrons occupy high-j, low-Ω orbital ($\nu i_{13/2}$) for oblate deformation. This is an ideal situation for magnetic rotation [8, 9] to occur. Such bands were found in several Pb and Bi isotopes [8, 9, 22, 23]. In many cases, particularly in Bi isotopes, the excitation energies and definite spin-parities (J^{π}) could not be assigned for such bands. So, the configurations could not be established. Therefore, in this thesis work, a detailed study of the high-spin spectroscopy of odd-odd nucleus ^{198}Bi has been done with an aim to investigate the magnetic rotational bands in this nucleus.

The Nilsson orbitals $\pi[505]9/2^{-}$ and $\pi[606]13/2^{+}$ are the intruder proton orbitals for the Thallium (Z = 81) nuclei. They are originated from the $\pi h_{9/2}$ and $\pi i_{13/2}$ levels, respectively, situated below the Z = 82 shell closure. These Nilsson orbitals, intrudes from the major shell above Z = 82 into the shell below it for oblate deformation. Therefore, these orbitals, play significant role in breaking the spherical symmetry in a nucleus close to the spherical magic number. Moreover, the $\pi i_{13/2}$ level lies above the Z = 92 spherical sub-shell closure. Hence, the ‘intruder’ $i_{13/2}$ level in lighter Tl nuclei provides an opportunity to study the properties of the levels for the heavy nuclei above Z = 92 which are, otherwise, difficult to study. In odd-A Tl isotopes, rotational bands based on the intruder $\pi[505]9/2^-$ Nilsson state originating from the $h_{9/2}$ proton orbital with oblate deformation have been observed [24, 25, 26, 27]. On the other hand, the $\pi[606]13/2^+$ Nilsson state, originated from the proton $i_{13/2}$ orbital with oblate deformation have been observed in lighter odd-mass Tl nuclei but it is still unknown in ^{197}Tl. The intruder levels are, often, non-yrast and can be better accessed by α-induced fusion evaporation reactions. In the present thesis work, the γ-ray spectroscopy of ^{197}Tl has been studied using α beam in order to investigate the proton $i_{13/2}$ intruder state along with the multi-quasiparticle states in this nucleus.

The study of band structure based on $\pi h_{9/2} \otimes \nu i_{13/2}$ configuration in odd-odd Tl isotopes is another point of interest. Indication of collective rotational bands based on this configuration have been reported in a few doubly-odd Tl isotopes in this mass region [28, 29, 30, 31, 32, 33]. But in most cases there are ambiguities on level energies, spins and parities except in ^{190}Tl [28] and ^{198}Tl [34]. However, the band based on the above configuration in these two nuclei have been interpreted differently in these two nuclei. A rotational structure with oblate deformation has been used to describe the above band in ^{190}Tl but in ^{198}Tl, the same band along with a weak side band, was interpreted as chiral doublet structure with triaxial deformation. So, detailed experimental as well as theoretical investigations are required for the understanding of the structure of the bands based on $\pi h_{9/2} \otimes \nu i_{13/2}$ configuration in the odd-odd Tl nuclei. Therefore, with the above motivation in mind, the high spin states of ^{194}Tl have been studied using γ-ray spectroscopic techniques in the present thesis work.

On the other hand, nuclei near N = 82 in A $\sim$ 130 region, both protons and neutrons lie in the 50 - 82 subshell space. The spherical shell model states $s_{1/2}$, $d_{3/2}$, $d_{5/2}$, $g_{7/2}$ and $h_{11/2}$ are available both for valence neutrons and protons for the nuclei in this region. Collective rotational bands [35, 36] and single particle excitations [37] have been reported in many of the nuclei in this region. The valence protons occupy lower half of the unique parity $\pi h_{11/2}$ orbital, which drives a nucleus to a prolate shape, while valence neutrons occupy the upper half of the unique parity $\nu h_{11/2}$ orbital, which favors an oblate shape. These competing shape driving orbitals may induce drastic change in shape with rotational frequency and particle number. This also leads to γ-softness and triaxiality in the nuclei. As a result exotic phenomena like chiral doublet bands, arise due to chiral symmetry breaking and MR bands, arise due to shears mechanism, have been observed in many nuclei (^{138}Ce, ^{132}Cs, ^{134}Pr etc.) in this region [38, 39, 40, 41, 42]. In particular, the chiral doublet bands have been reported for the Cs isotopes with neutron number $N = 71 - 77$ for the $\pi h_{11/2} \otimes \nu h_{11/2}$ configuration [42, 43, 44].

As the neutron number increases towards N = 82 shell closure, it is an open question whether the shape driving effects of the neutrons are strong enough to stabilize the triaxial shape, so that the similar band structure (chiral doublet bands) persists for the heavier odd-odd Cs isotopes. While approaching the N = 82 shell closure, the potential energy surfaces tend to be γ-soft with small deformation. For Cs nuclei, the valence protons occupy the lower-Ω part of the $h_{11/2}$ orbital and as the neutron number increases, the valence neutron holes occupy the high-Ω components of the $h_{11/2}$ orbital. These conditions are ideal for destroying the chiral arrangement and emergence of the MR bands. ^{132}Cs (N = 77) is the heaviest isotope of Cs for which the $\pi h_{11/2} \otimes \nu h_{11/2}$ configuration has been identified with chiral doublet bands built on it [42, 45]. Rainovski, et al, [42] conjectured that N = 77 forms the border of the island of chirality when the neutron number approaches N = 82. In addition to the chiral doublet bands, different multi-quasiparticle bands including a magnetic rotational band have been observed in ^{132}Cs [45]. However, the information on the high spin states in the next heavier odd-odd Cs isotope, i.e ^{134}Cs (N = 79) is very scarce. The $\pi h_{11/2} \otimes \nu h_{11/2}$ configuration has not yet been identified in ^{134}Cs.

Therefore, to address the above issue of persistence of chirality for the $\pi h_{11/2} \otimes \nu h_{11/2}$ configuration in the heavier isotopes of Cs, the high spin states in ^{134}Cs near N = 82 magic gap have been studied and the nature of the band built on this configuration has been investigated in detail in the present thesis work.

Table 1.1 summarizes the nuclei studied and measurements performed in this thesis work.

To study the above interesting structural phenomena, one has to populate the excited states in nuclei at high spin. High spin states can be achieved in a nucleus through heavy-ion induced fusion-evaporation reaction (most efficient way). When an accelerated projectile nucleus (with energy greater than the Coulomb energy between the target and the projectile nuclei)

Table 1.1: Details of experimental studies and measurements performed using different accelerator facilities and detector arrays.

Nucleus studied	Accelerator & Laboratory	Reaction used	Projectile Energy	Measurements done	Array used
^{134}Cs (Experiment-1)	14 UD Pelletron Facility at Mumbai	^{130}Te(^{11}B, α3n)	52 MeV	singles, $\gamma\gamma$ and $\gamma\gamma\gamma$ coincidence, DCO and Polarization	INGA-Phase I with 8 Clovers
^{134}Cs (Experiment-2)		^{130}Te(^{7}Li, 3n)	30 MeV	$\gamma\gamma$ coincidence, DCO and Polarization	Partial-INGA with 7 Clovers
^{194}Tl (Experiment-3)		^{185,187}Re(^{13}C, xn)	75 MeV	$\gamma\gamma$ coincidence, DCO and Polarization	INGA-Phase V with 15 Clovers
^{198}Bi (Experiment-4)	15 UD Pelletron Facility at IUAC, New Delhi	^{185,187}Re(^{16}O, xn)	112.5 MeV	singles, $\gamma\gamma\gamma$ coincidence, DCO and Polarization	INGA-Phase IV with 15 Clovers
^{195}Bi (Experiment-5)	K = 130 Cyclotron at VECC, Kolkata	^{181}Ta(^{20}Ne,6n)	145 MeV	singles, $\gamma\gamma$ coincidence, DCO and Polarization	INGA-Phase III with 8 Clovers
^{197}Tl (Experiment-6)		^{197}Au(^{4}He, 4n)	48 MeV	-do-	Modest inhouse facility with 2 HPGe, one Clover, one LEPS

collides and fuses with a target nucleus, a compound nucleus is formed. The compound nucleus cools down by particle evaporation and decay to the ground state by emitting γ rays (discrete in nature) along the yrast line. In γ-ray spectroscopy experiment, these discrete γ-rays are detected by the high-purity germanium detector (HPGe) to understand the nuclear structure information. After collecting data one has to built the level scheme using coincidence and intensity relations. The level scheme is a fingerprint of nuclear structure and gives the information about different kinds of structural phenomena in nuclei. Finally, the experimental results are interpreted with the help of theoretical model calculations.

The present thesis has been arranged in the following way: A brief introduction of the nuclear models relevant to the present thesis work is described in chapter 2. Experimental techniques and data analysis have been discussed in chapter 3. The experimental results for ^{194}Tl, ^{195}Bi, ^{197}Tl, ^{198}Bi and ^{134}Cs nuclei and the interpretation of the results have been discussed in chapters 4, 5, 6, 7 and 8, respectively. Finally, the summary and outlook of this thesis work are presented in Chapter 9.

Bibliography

[1] A. Bohr and B. R. Mottelson, "Nuclear structure, vol. II", Benjamin Reading, Massachusetts 1975. Ch 4.

[2] M. G. Mayer, Phys. Rev. **75**, 1969 (1949).

[3] M. Lipoglavsek, et al., Phys. Lett. **B 593**, 61 (2004).

[4] D. Ward et al., Nucl. Phys. **A 332**, 433 (1979).

[5] H. Beuscher et al., Z.Phys. **263**, 201 (1973).

[6] D. Ward et al., Nucl. Phys. **A 600**, 88 (1996).

[7] A. Sharma et al.,Z.Phys. **354**, 347 (1996).

[8] R.M. Clark and A.O. Macchiavelli, Ann. Rev. Nucl. Part. Sci. **50** , 1 (2000).

[9] H. Hübel, Prog. Part. Nucl. Phys. **54**, 1 (2005).

[10] S. Frauendorf, Rev. Mod. Phys. **73**, 463 (2001).

[11] E. Grodner et al., Phys. Lett. **B 703**, 46 (2011).

[12] E. Grodner et al., Phys. Rev. Lett. **97**, 172501 (2006).

[13] S. Mukhopadhyay et al., Phys. Rev. Lett. **99**, 172501 (2007).

[14] K. heyde, P. Van Isacker, M. Waroquier, J. L. Wood and R.A. Meyer, Phys. Rep. **102**, 291 (1983).

[15] A.N. Andreyev et al., Nature **405**, 430 (2000).

[16] J. L. Wood, K. Heyde, W. Nazarewicz, M. Huyse, and P. Van Duppen, Phys. Rep. **215**, 101 (1992).

[17] L.A. Bernstein et al. Phys. Rev. **C 52**, 621 (1995).

[18] P. Nieminen et al., Phys. Rev. **C 69**, 064326 (2004).

[19] R.M. Clark et al., Phys. Rev. **C 53**, 117 (1996).

[20] T. Chapuran et al., Phys. Rev. **C 33**, 130 (1986).

[21] W.F. Piel et al., Phys. Rev. **C 31**, 2087 (1985).

[22] G.K. Mabala et al., Euro. Phys. J. **A 25**, 49 (2005)

[23] P.J. Dagnall et al., J. Phys. G: Nucl. Part. Phys. **20** 1591 (1994).

[24] R.M. Lieder et al., Nucl. Phys. **A 299**, 255 (1978).

[25] A.J. Kreiner et al., Phys. Rev. **C 38**, 2674 (1988).

[26] M.G. Porquet et al., Phys. Rev. **C 44**, 2445 (1991).

[27] W.Reviol et al., Phys. Scr. **T 56**, 167 (1995).

[28] C.Y. Xie et al., Phys. Rev. **C 72**, 044302 (2005).

[29] A.J. Kreiner et al., Phys. Rev. **C 21**, 933 (1980).

[30] A.J. Kreiner et al., Phys. Rev. **C 20**, 2205 (1979).

[31] A.J. Kreiner et al., Nucl. Phys. **A 308**, 147 (1978).

[32] A.J. Kreiner et al., Nucl. Phys. **A 282**, 243 (1977).

[33] A.J. Kreiner et al., Phys. Rev. **C 23**, 748 (1981).

[34] E.A. Lawrie et al., Phys. Rev. **C 78**, 021305(R) (2008).

[35] R. Kühn et al., Nucl.Phys. **A 594**, 87 (1995).

[36] R. Ma et al., Phys. Rev. **C 41**, 717 (1990).

[37] K. Li et al., Phys. Rev. **C 75**, 044314 (2007).

[38] K. Starosta et al., Nucl. Phys. **A 682**, 375c (2001).

[39] C.M. Petrache et al., Z. Phys. **A 344**, 227 (1992); C.M. Petrache et al., Nucl. Phys. **A 597**, 106 (1996).

[40] C.W. Beausang et al., Nucl. Phys. **A 682**, 394c (2001).

[41] T. Bhattacharjee et al., Nucl.Phys. **A 825**, 16 (2009).

[42] G. Rainovski et al., Phys. Rev. **C 68**, 024318 (2003).

[43] T. Koike et al., Phys. Rev. **C 67**, 044319 (2003).

[44] S. Wang et al., Phys. Rev. **C 74**, 017302 (2006).

[45] G. Rainovski et al., J. Phys. G: Nucl. Part. Phys. **29** 2763 (2003).

Chapter 2

Nuclear Models

Atomic nucleus is a complex many-body quantum system consists of neutrons and protons. The short-range strong nuclear force binds the nucleons into the nucleus. Unfortunately, the nuclear force is not well understood and the exact form of the nucleon-nucleon strong interaction is not known. In order to understand the basic properties of the nuclei, different models are thus necessary. Over the decades, different nuclear models have been proposed. In this chapter, a few of the models will be briefly described.

2.1 Liquid drop model

Historically, the liquid drop model was the first model developed to describe the nuclear properties. It describes the bulk properties (binding energies) and collective phenomena, such as vibrations and rotations of the nucleus. The idea came mainly from the consideration that nuclear forces exhibit a saturation properties and from the fact that the nucleus has a low compressibility and a well defined nuclear surface. The binding energy per nucleon as a function of mass number A is found to be fairly constant ($\simeq$ -8.5 MeV), which indicates the saturation properties of nuclear force. The picture of a nucleus as a drop of a liquid accounts for the observed variation in the 'binding energy per nucleon' with mass number A through the

Bethe-Weizs*ä*cker semi-empirical mass formula [1, 2]:

$$B(N, Z) = a_V A + a_S A^{\frac{2}{3}} + a_C \frac{Z^2}{A^{\frac{1}{3}}} + a_I \frac{(N - Z)^2}{A} + \delta(A) \tag{2.1}$$

where one obtains by a fit [3]: a_V = -15.68 MeV; a_S = 18.56 MeV; a_C = 0.717 MeV; a_I = 28.1 MeV. $\delta(A)$ is the pairing energy which is given by,

$$\begin{aligned}
\delta(A) &= 34.\, A^{-\frac{3}{4}} MeV \quad for\ even - even\ nuclei \\
&= 0 \quad MeV \quad for\ even - odd\ nuclei \\
&= -34.\, A^{-\frac{3}{4}} MeV \quad for\ odd - odd\ nuclei
\end{aligned}$$

In the equation 2.1 first term is the volume term, second term is the surface term, third term is due to the Coulomb repulsion and the fourth term is symmetry energy term. The overall systematics in the experimental binding energy per nucleon was reproduced quite well with this mass formula. This model is able to explain certain features of nuclear fission, but is not very successful in describing the actual excited states as it gives too large level distances. Few more experimental observations which could not be explained with this mass formula. These observations are certain discontinuities of some nuclear properties, such as, two neutron or two proton separation energy, the magnetic moments etc., at nucleon numbers 2, 8, 20, 28, 50, 82 and 126 which are the so-called "*magic numbers*". Nuclei in which either N or Z is equal to one of these magic numbers show extra stability. This gave rise to the concept of closed shell nuclei and most successful nuclear model, the "*shell model*," appeared in 1949.

2.2 Shell model

Shell model of the nucleus originated from the theoretical attempts to explain the extra stability of certain nuclei having nucleon numbers equal to the magic numbers (2, 8, 20, 28,50, 82 and 126), which are analogous to the inert gases in atomic physics. This model is based on the mean field approximation, where each nucleon is assumed to move independently in a potential that represents an average interaction with the other nucleons in the nucleus. Unlike the atomic case where the central mean field is provided by the Coulomb field of the heavy nucleus at the center of mass, in the nuclear case the mean field is produced by the nucleons themselves. The nuclear "shell model", independently proposed by Mayer [4] and Haxel, Jensen and Suess [5], in 1949. This model was capable of explaining not only the magic numbers but also many other nuclear properties such as spin, magnetic moment and energy levels [6, 7]. The Hamiltonian $\mathcal{H}$ of A nucleon system is assumed to be a sum of one body kinetic energy part and a two body potential energy term :

$$\mathcal{H} = \sum_{i=1}^{A} -\frac{\hbar^2}{2m_i}\nabla_i^2 + \frac{1}{2}\sum_{i,j=1}^{A} V_{i,j} \tag{2.2}$$

The Hamiltonian can be rewritten by adding and subtracting an average one body term U(r_i) as,

$$\mathcal{H} = \sum_{i=1}^{A} [T_i + U(r_i)] + \left(\frac{1}{2}\sum_{i,j=1}^{A} V_{i,j} - \sum_{i=1}^{A} U(r_i)\right) = \mathcal{H}_0 + \mathcal{H}_{res} = \sum_{i=1}^{A} h_0(i) + \mathcal{H}_{res} \tag{2.3}$$

where $\mathcal{H}_0$ is the one body part of the Hamiltonian which describes the motion of A nucleons in the mean field U(r_i) and $\mathcal{H}_{res}$ is the "residual interaction" which is two body part of the Hamiltonian. The one body part U(r_i) appearing in $\mathcal{H}_0$ is chosen in such a way that the residual interaction part $\mathcal{H}_{res}$ becomes small enough to be treated as a non-relativistic perturbation. In microscopic theories, this mean field can either be calculated from Brueckner theory [8] starting from the free nucleon-nucleon interaction or using the self-consistent Hartree-Fock procedure [9, 3]. However, an analytic phenomenological 'Woods-Saxon' potential used extensively as a mean field (U(r_i)), which is given by:

$$V_{WS}(r) = -\frac{V_0}{1 + exp[(r - R)/a]} \tag{2.4}$$

where V_0 is the depth of the potential ($\sim$ 50 MeV), radius $R \approx 1.2A^{1/3}$ fm and the surface thickness a $\approx$ 0.5 fm. In the above expression $V(r)$ has been shown to depend on r only. Such a potential is spherically symmetric and hence the model is called the "spherical shell model."

If a spherically symmetric harmonic oscillator potential $V_{HO}(r) = \frac{1}{2}m\omega_0^2(r^2 - R_0^2)$ is used as a mean field, where R_0 is the mean radius of nucleus, then the shell energies (energy eigen-values) are given by

$$\epsilon_N = \left(N + \frac{3}{2}\right)\hbar\omega_0 \tag{2.5}$$

where, N = 2(n - 1) + ℓ is the *principal quantum number*, n is the *radial quantum number*. However, above shell energies still do not reproduce the experimentally observed magic numbers above 20.

Several attempts have been made to modify the potential to get the experimentally observed magic numbers. Mayer [4] and Haxel, Jensen and Suess [5] in 1949, added a spin-orbit interaction term *f(r)***l.s** to the mean field. This interaction splits up the degeneracy in $j = l \pm \frac{1}{2}$ levels. The expectation value of the spin-orbit interaction can be written as

$$\langle snljm \mid f(r)\mathbf{l.s} \mid snljm\rangle \propto j(j+1) - l(l+1) - \frac{3}{4} \tag{2.6}$$

which for $j = l \pm \frac{1}{2}$ gives the splitting of energy ΔE $\sim 2l + 1$. The $j = l + \frac{1}{2}$ levels are lying energetically always below the $j = l$ - $\frac{1}{2}$ levels and splitting increases with l. In the extreme single particle shell model, the properties of the nucleus is determined by the outermost valance nucleon only. Ground state properties of many nuclei close to magic numbers are explained successfully by this model. However, for most of the nuclei it necessary to take into account more than one nucleon.

2.3 Collective model

The shell model, as described above, has been quite successful in explaining nuclei close to the magic numbers. However, while moving away from the closed shells, some simple and systematic features start to show up, which could not be understood in terms of shell model. For example, large ground state quadrupole moment, enhanced E2 transition probabilities,'rotor like' energy spectrum etc. These observations suggest that in these nuclei, such large effects can arise through a coherent participation of all the nucleons. To understand the collective features away from the closed shells, A. Bohr and B. Motelsson [10] had developed *Collective model*. The Collective Model, extends the liquid drop model by including motions of the whole nucleus such as rotations and vibrations. The Collective Model emphasizes the coherent behavior of all of the nucleons. This model is based on the concept of a nuclear surface defined by the surface coordinate R in the (θ, ϕ) as

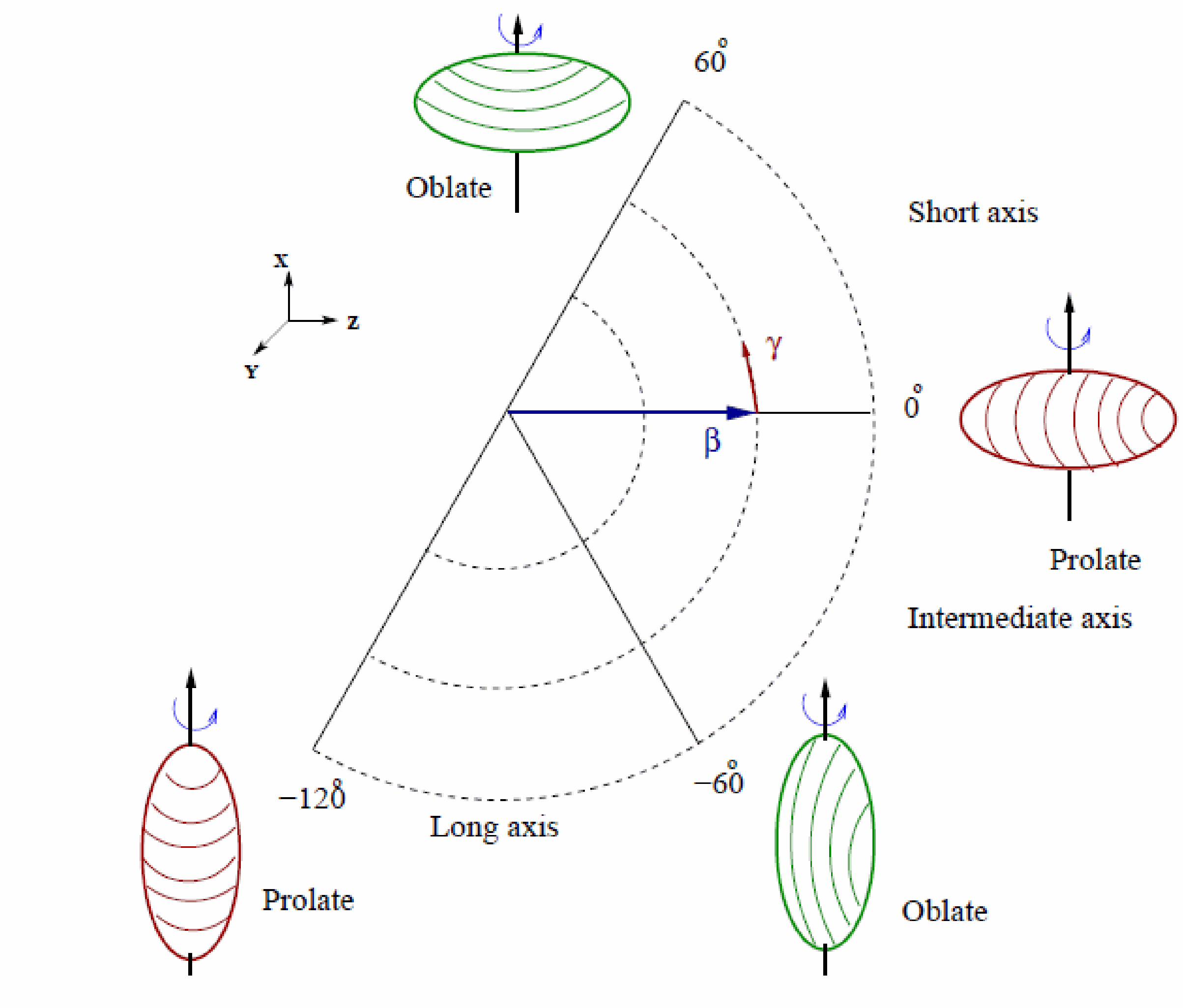

Figure 2.1: Various nuclear shapes in $(\beta - \gamma)$ plane. On the top left is shown the principal axes of intrinsic frame. Figure taken from ref. [11]. Lund conventions [13] have been used.

$$R(\theta, \phi) = R_0 \left[1 + \sum_{\lambda=0}^{\infty} \sum_{\mu=-\lambda}^{\lambda} \alpha^*_{\lambda\mu} Y_{\lambda\mu}(\theta, \phi) \right] \tag{2.7}$$

where R_0 is the radius of the spherical nucleus. The $\alpha^*_{\lambda\mu}$ represent the expansion of any general function of the angels (θ, ϕ) interms of the complete set of spherical harmonics $Y_{\lambda\mu}(\theta, \phi)$. λ is multipolarity of the shape oscillations, μ is the projection of λ. The $\lambda = 0$, 1 terms are called as monopole mode and dipole mode, respectively. These monopole and dipole terms can be discarded based on the arguments of incompressibility and translational symmetry, respectively.

Considering $\lambda = 2$ term in the expansion and making suitable transformation to intrinsic frame with axis 1, 2 and 3, the five coefficients of $\alpha_{2\mu}$ reduces to two real independent deformation parameters a_{20} and $a_{22} = a_{2-2}$ (for axially symmetric quadrupole deformation). These two parameters can be expressed, interms of the Hill-Wheeler [12] coordinates β and γ as:

$$a_{2,0} = \beta cos\gamma, \quad a_{2,2} = \frac{1}{\sqrt{2}}\beta sin\gamma \tag{2.8}$$

such that,

$$\sum_{\mu} \mid \alpha_{2,\mu} \mid^2 = a_{2,0}^2 + 2a_{2,2}^2 = \beta^2 \tag{2.9}$$

β represents the degree of deformation, while the parameter γ gives the degree of axial asymmetry. The expression for the radius 2.7 using the spherical harmonics $Y_{2,0}$ and $Y_{2,\pm2}$ in the intrinsic frame can be written as:

$$R(\theta,\phi) = R_0\left[1 + a_{20}Y_{2,0}(\theta,\phi) + a_{22}Y_{2,2}(\theta,\phi) + a_{2-2}Y_{2,-2}(\theta,\phi)\right] \tag{2.10}$$

$$R(\theta,\phi) = R_0\left[1 + \beta\sqrt{\frac{5}{16\pi}}\left(cos\gamma\left(3cos^2\theta - 1\right) + \sqrt{3}sin\gamma sin^2\theta cos2\phi\right)\right] \tag{2.11}$$

Increment in length δR = R(θ, ϕ) - R_0 along the three body fixed axes can be written as (From equation 2.11),

$$\delta R_k = R_0\sqrt{\frac{5}{4\pi}}\beta cos\left(\gamma - \frac{2\pi}{3}k\right) \tag{2.12}$$

where, k = 1, 2, 3. Two distinct axially symmetric shapes are possible for different orientations in space, viz.,

1. **Prolate** shapes : for $\gamma = 0°$, 120° and 240°
2. **Oblate** shapes : for $\gamma = 60°$, 180° and 300°

In Fig. 2.1 we have shown nuclear shapes in the $\beta - \gamma$ plane for $\lambda = 2$. In this figure, Lund conventions [13] have been used. $\gamma = 0°$ (-60°) correspond to collective prolate (collective oblate), whereas the $\gamma = 60°$ (-120°) describes the non-collective oblate (non-collective prolate). If the value of γ is not a multiple of 60°, then triaxial shapes occur. Due to discrete symmetries, the interval $0 \leq \gamma \leq 60°$ is sufficient to describe all the quadrupole shapes.

2.4 Nilsson Model

The Nilsson model is a shell model for a deformed nucleus. It provides a description of single particle motion in a nonspherical potential. In this model modified axial symmetric Harmonic-Oscillator potential [14] was used to investigate the effect of deformation on the single particle orbitals. The anisotropic harmonic oscillator potential can be written as

$$V(r) = \frac{1}{2}m\left(\omega_x^2 x^2 + \omega_y^2 y^2 + \omega_z^2 z^2\right) \tag{2.13}$$

where ω_x, ω_y and ω_z are the three frequencies of the oscillator along three axes. The condition of volume conservation is

$$\omega_x \omega_y \omega_z = \text{constant} = \tilde{\omega}_0^3. \tag{2.14}$$

For nuclear shapes which are axially symmetric about z-axis, $\omega_x = \omega_y = \omega_\perp$ and these can be expressed in terms of a deformation parameter δ, using the following prescription:

$$\begin{aligned} \omega_\perp &= \omega_0(\delta)\sqrt{1 + \tfrac{2}{3}\delta} \\ \omega_z &= \omega_0(\delta)\sqrt{1 - \tfrac{4}{3}\delta}, \end{aligned} \tag{2.15}$$

which ensures conservation of volume only up to second order in δ and gives the expression for $\omega_0(\delta)$ as

$$\omega_0(\delta) = \tilde{\omega}_0\left(1 + \frac{2}{3}\delta^2\right). \tag{2.16}$$

The parameter δ is related to the deformation parameter, β, by the following relation:

$$\delta \approx \frac{3}{2}\sqrt{\frac{5}{4\pi}}\beta \approx 0.95\beta. \tag{2.17}$$

The Nilsson Hamiltonian can be more commonly written as

$$H = -\frac{\hbar^2}{2m}\nabla^2 + \frac{1}{2}m\omega_0^2 r^2 - \beta_0 m\omega_0^2 r^2 Y_{20}(\theta,\phi) - \kappa\hbar\tilde{\omega}_0 2\hat{\ell}\cdot\hat{s} + \mu\left(\hat{\ell}^2 - \langle\hat{\ell}^2\rangle_N\right) \tag{2.18}$$

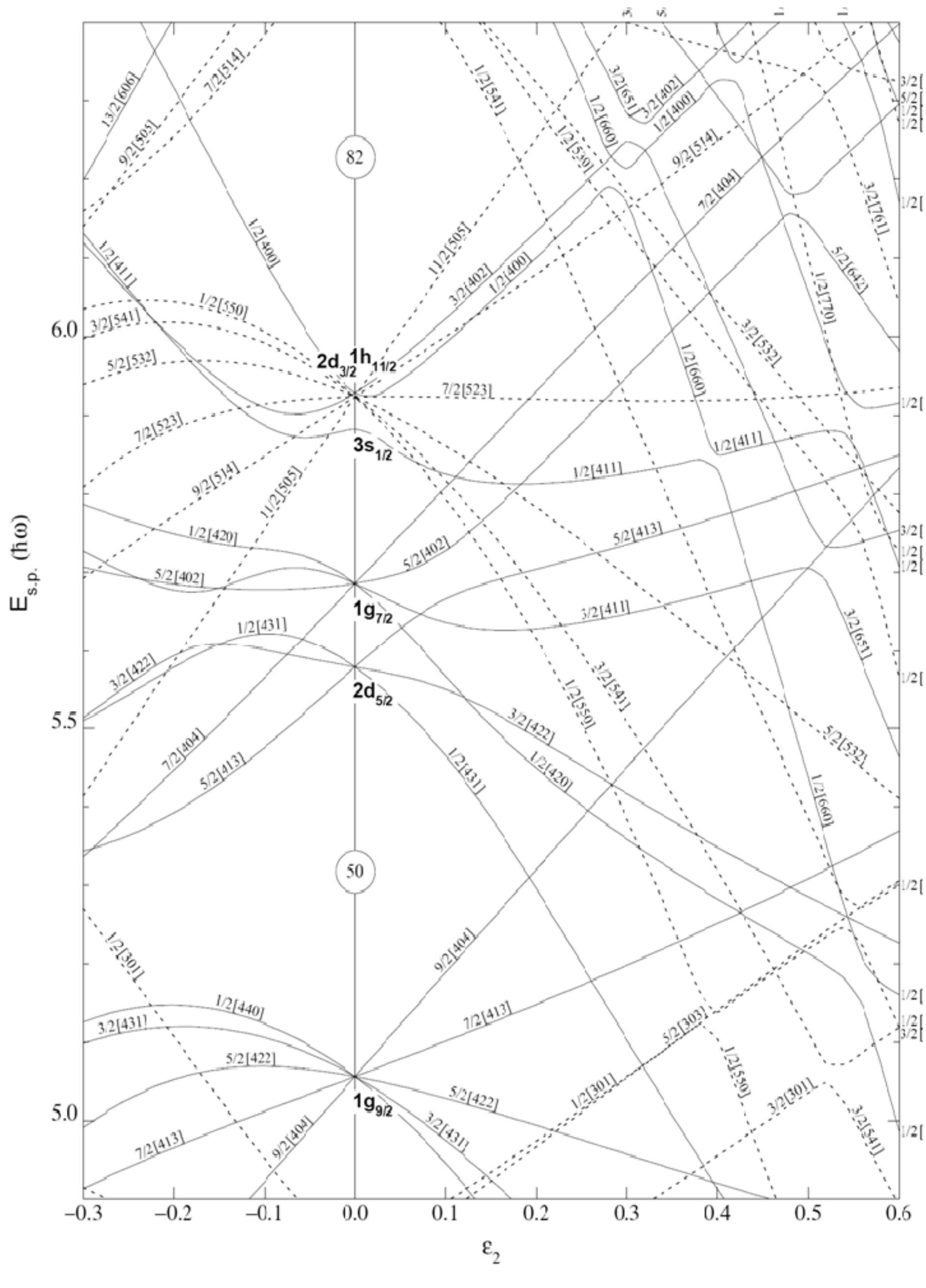

Figure 2.2: Nilsson diagram of single-particle levels for neutrons (50≤N≤82) as a function of deformation ε_2 ($\varepsilon_2 = \delta$). The solid lines correspond to positive parity orbitals and the dashed lines correspond to negative parity orbitals. Figure taken from ref. [16].

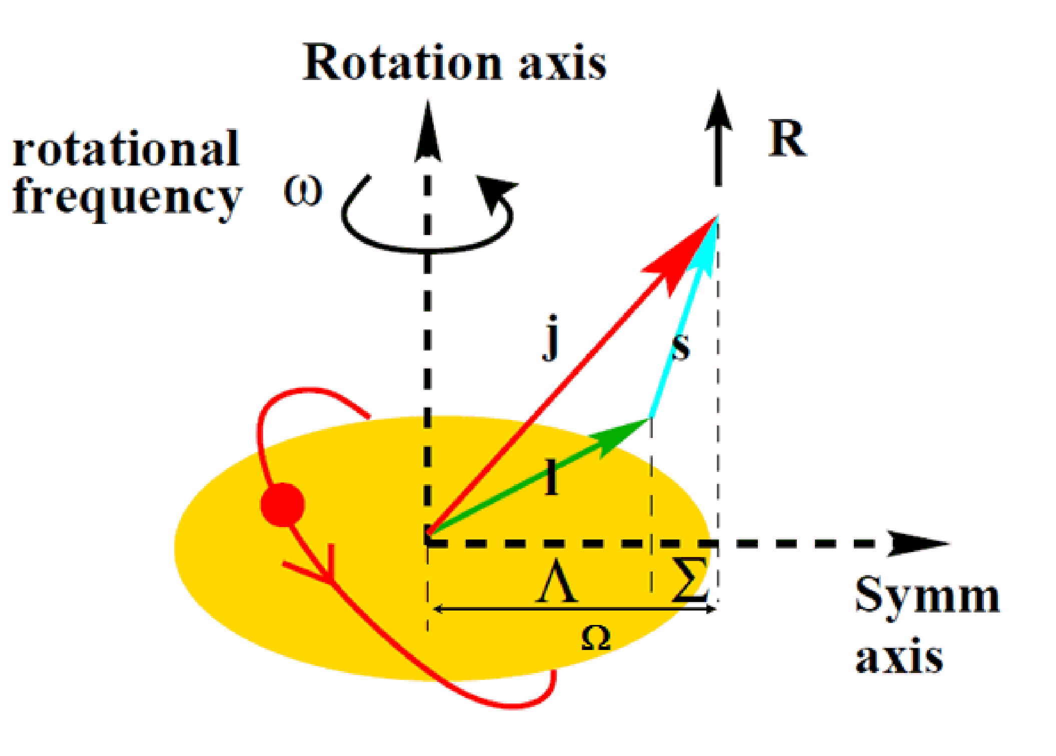

Figure 2.3: Asymptotic quantum numbers Λ, Σ and Ω for the Nilsson model are shown.

The factors κ and μ determine the strength of the spin-orbit and ℓ^2 terms, respectively. The value of κ and μ are different for different shell [15]. A sample of Nilsson levels is given in Fig. 2.2 wherein the levels are labeled with the asymptotic quantum numbers $\Omega^{\pi}[Nn_z\Lambda]$ where $\Omega = \Lambda + \Sigma$. N is the principle quantum number and n_z its projection on the symmetry axis, n_z = 0, 1, 2, 3, . . . , N. Λ, Σ and Ω are the projections of the orbital angular momentum **l**, the spin **s** and the total angular momentum j of the odd nucleon on the symmetry axis, respectively, see Fig. 2.3.

The asymptotic quantum numbers arise from $[Nn_z\Lambda]$ in the large deformation limit where $l.s$ term becomes relatively weak, and the solutions resemble those of the anisotropic oscillator with cylindrical symmetry. Only Ω and the parity $\pi = (-1)^N$ are the good quantum numbers. Each spherical (N,l, j) level is now split up into $j + \frac{1}{2}$ doubly-degenerate states, according to the ±Ω degeneracy.

The Nilsson model has been successfully used to describe a large amount of data for nuclei with moderate to large ground state deformation.

2.5 Cranking Model

The application of single-particle models for rapidly rotating nuclei are mainly described within the framework of the cranking model. The model gives a microscopic description of the influence of rotation on single-particle motion. The first mathematical formulation of the cranking model was introduced by Inglis [17, 18] and has been further developed by Bengtsson and Frauendorf [19]. The rotation is treated classically and the nucleons are considered as independent particles moving in an average rotating potential. Here, the intrinsic (body-fixed) coordinate system (x_1, x_2, x_3) is used which has a fixed orientation at all times with respect to the nuclear potential. It rotates with rotational frequency, ω, relative to the laboratory coordinate system (xyz), which has been shown in Fig. 2.4. If intrinsic coordinates rotate around an axis perpendicular to the symmetry axis and the symmetry axis coincides with the intrinsic axis, x_3, and the intrinsic axis, x_1, coincides with the laboratory axis x, than the total cranking Hamiltonian for N particle system is given by:

$$H_\omega = H^0 - \omega J_x = \sum_{\mu=1}^{N} h_\mu^0 - \omega j_{x\mu} \tag{2.19}$$

where H_ω is the the total Hamiltonian in the rotating frame, H^0 is total Hamiltonian in the laboratory system and J_x is the total angular momentum projection onto the rotation axis. On the other hand, $h_\mu^\omega = h_\mu^0 - \omega j_{x\mu}$ is the single particle Hamiltonian in the rotating frame, h_μ^0 is the single particle Hamiltonian in the laboratory system and $j_{x\mu}$ is the single particle angular momentum projection onto the rotation axis. The $-\omega j_{x\mu}$ term contains the Coriolis and centrifugal forces in the rotating co-ordinate system. The Coriolis force responsible to align the angular momentum of the nucleons with the rotation axis [20]. The eigenvalues of this Hamiltonian (H_ω), are known as *Routhians.* The total energy in the laboratory frame,

$$E = \sum_{\mu=1}^{N} e_\mu^\omega + \omega \sum_{\mu=1}^{N} \langle \mu^\omega \mid j_x \mid \mu^\omega \rangle \tag{2.20}$$

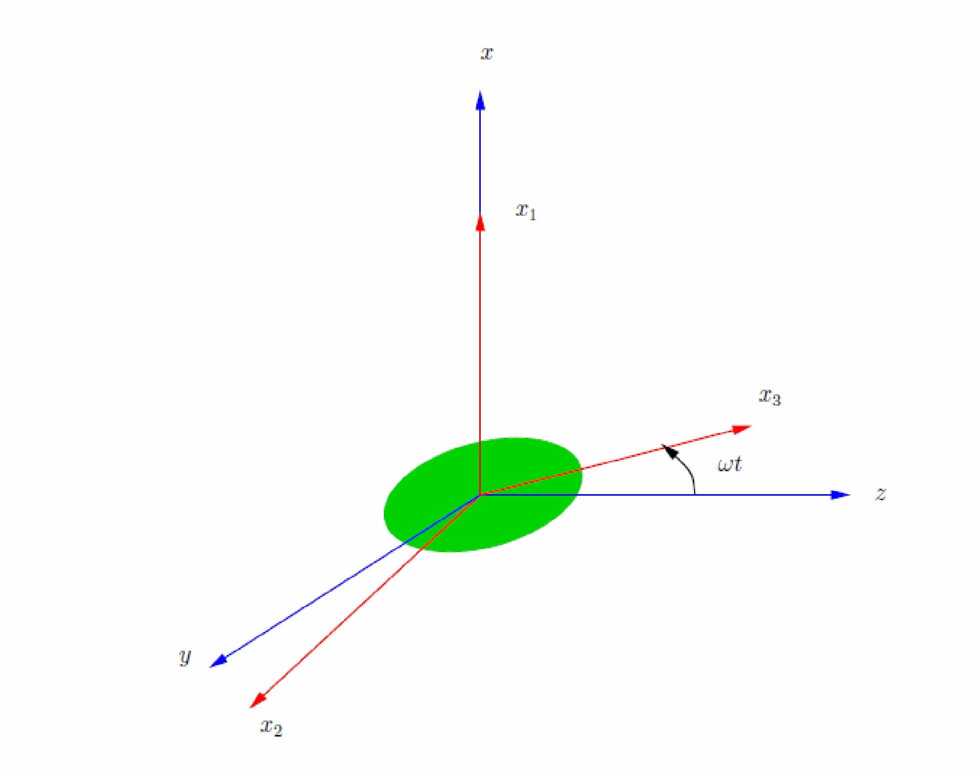

Figure 2.4: The body-fixed coordinates (x_1, x_2, x_3) and the laboratory coordinates (xyz).

where e_μ^ω denote the eigenvalues (single particle Routhian) and $\mid \mu^\omega\rangle$ are the single particle eigenfunctions in the rotating frame. The projection of the total angular momentum onto the rotation axis can be written as,

$$I_x = \sum_{\mu=1}^{N} \langle \mu^\omega \mid j_x \mid \mu^\omega \rangle \tag{2.21}$$

The slope of the Routhian is related to the alignment, i_x can be defined as

$$i_x = -\frac{de_\mu^\omega}{d\omega} \tag{2.22}$$

Ω (Nilsson quantum number) is no longer a conserved quantity in the cranking model. Because the $-\omega j_x$ term in the cranking Hamiltonian breaks the time-reversal symmetry. Only parity, π: which describes the symmetry under space reflection and *signature,* α are good quantum number. *Signature* describes the symmetry under a rotation of 180° about the rotation axis. The rotation operator is defined by

$$\mathcal{R}_x = exp(-i\pi j_x) \tag{2.23}$$

with the eigenvalues

$$r = exp(-i\pi\alpha) \tag{2.24}$$

Signature quantum number α [21] is related to the total angular momentum by

$$I = \alpha \ mod \ 2 \tag{2.25}$$

Systems with an even number of nucleons $\alpha = 0$ or 1, while for odd number of nucleons $\alpha = \pm\frac{1}{2}$.

2.6 Total Routhian Surface (TRS) calculations

The total Routhian surface (TRS) calculations have been performed in this thesis work, as prescribed by Nazarewicz *et al.* [22, 23]. The total routhian E^ω(Z, N; $\hat{\beta}$) of a nucleus (Z, N) as a function of deformation can be obtained from the sum of the liquid-drop energy,

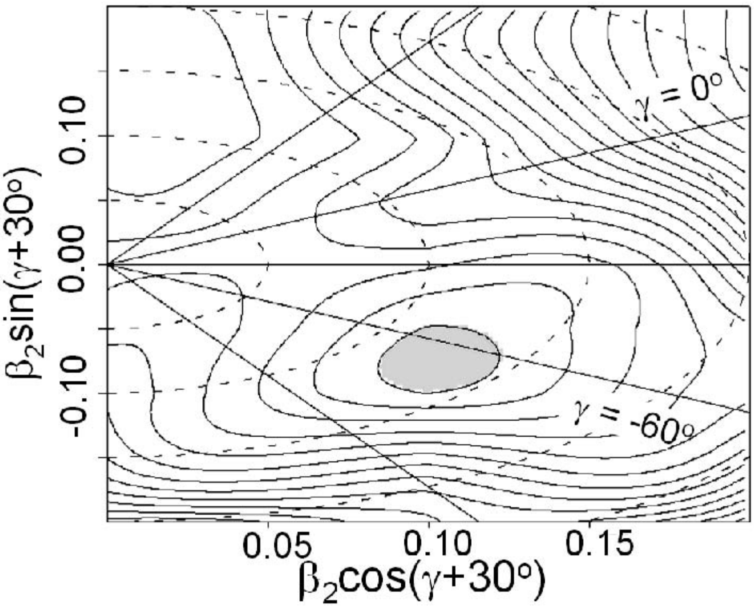

Figure 2.5: Total Routhian surfaces calculated for the $13/2^+$ configurations in ^{195}Bi.

shell correction energy and the pairing correction energy within the cranked Woods-Saxon, Bogolyubov, Strutinsky approach as:

$$E^{\omega}(Z, N; \hat{\beta}) = E^{\omega}_{LD}(Z, N; \hat{\beta}) + E^{\omega}_{shell}(Z, N; \hat{\beta}) + E^{\omega}_{pair}(Z, N; \hat{\beta}), \tag{2.26}$$

where $\hat{\beta}$ denotes the complete set of deformation parameters. The shell correction energy is calculated using the Strutinsky shell corrections method with a deformed Woods-Saxon potential. The Hartee-Fock-Bogoliubov code of Nazarewicz *et al.* [22, 23] has been employed for the TRS calculations in this work. The TRSs have been calculated in $(\beta_2, \gamma, \beta_4)$ deformation mesh points with minimization on β_4. The procedure of such calculations have been outlined in Ref. [24, 25]. The contour plots of the TRSs, calculated for ^{195}Bi have been shown in Fig. 2.5. This calculations have been performed for the 1-quasiparticle $\pi i_{13/2}$ configuration. The minimum of this contours gives the ground state deformation of the nucleus in terms of β and γ. In these plots, $\gamma = 0^o$ corresponds to a prolate shape and $\gamma = -60^o$ to an oblate shape. The value of γ lies in between these two limits for a triaxial shape and $\gamma = \pm 30^o$ corresponds to the maximum of triaxiality. This Figure clearly shows a minimum in the TRS at a deformation of $\beta_2 \sim 0.13$ and $\gamma \sim -60^o$, indicating an oblate shape for ^{195}Bi in this configuration.

2.7 Phenomenon of Magnetic rotation

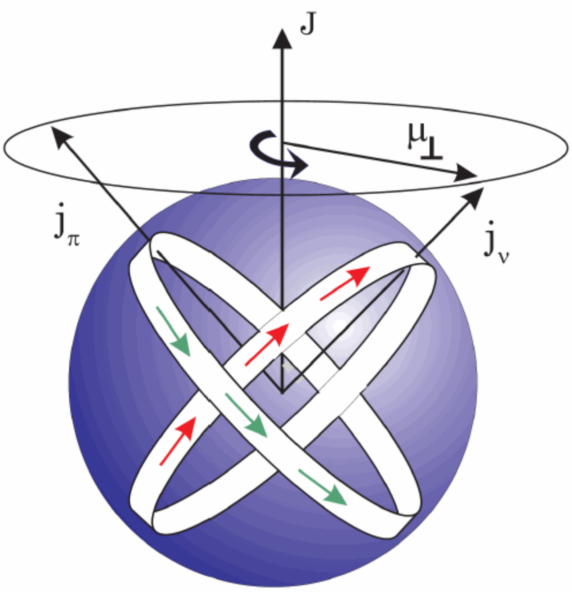

Figure 2.6: A schematic diagram illustrating the spin-coupling concept for magnetic rotation.

Magnetic rotation (MR) was first discovered in Pb region and is now a well established phenomenon. One of the first examples of such band was found in ^{199}Pb [26]. This band arises from the anisotropy of the net magnetic dipole moment instead of net quadrupole moment giving rise to strong streached M1 transitions with weak or missing stretched E2 transitions. Since the perpendicular component of the magnetic moment vector $\mu_{\perp}$ rotates around the total angular momentum, this type of rotation is called magnetic rotation (see Fig. 2.6). MR bands are formed by the coupling of particles and holes in high-j orbitals. Angular momentum generated along the MR bands is by a step-by-step alignment of the particle and hole spins into the direction of the total angular momentum without any contribution from the rotation of the core. Since this resembles the closing of the blades of a pair of shears, they have also been called "shears bands" [27]. Experimental proof for the shears mechanism are the decreasing B(M1) values with increasing spin and the bands terminate when the shears are closed. The general features of these bands are :

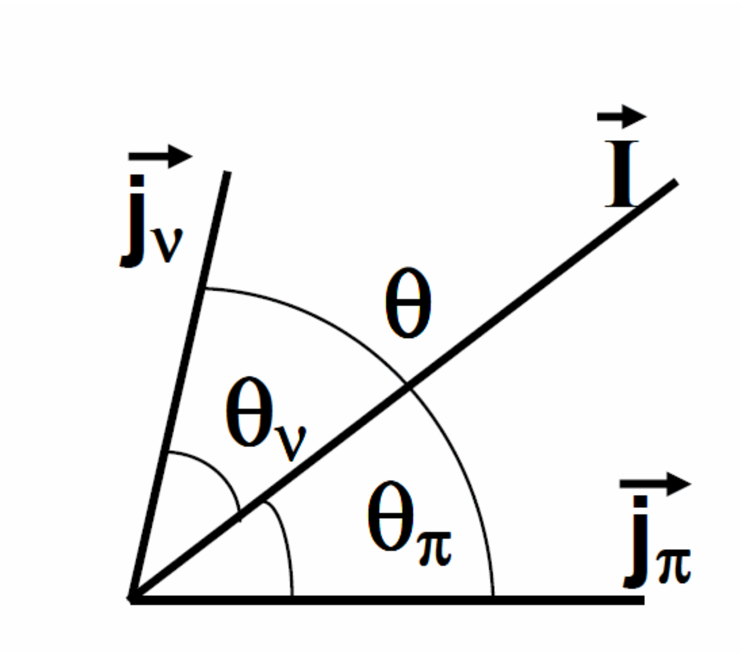

Figure 2.7: Schematic picture of the angular momentum coupling between protons and neutrons in a shear band.

• The level energies (E) and the spin (I) in the band follow the pattern $E(I)-E(I_o) \sim A*(I-I_o)^2$ where, E_o and I_o are the energy and spin of the band head, respectively.

• The bands consist of strong M1 transitions with only weak E2 crossovers resulting in large B(M1)/B(E2) ratios, $\geq$20 $\mu_N^2/(eb)^2$.

• The value of reduced transition probability B(M1) is typically $\sim$ 2 - 10 μ_N^2.

• The structures have small deformation ($|\epsilon| \leq 0.1$).

• The ratio of dynamic moment of inertia ($\mathcal{J}^{(2)}$) and reduced E2 strengths $\mathcal{J}^{(2)}$/B(E2) is $\geq$ 100 $MeV^{-1}(eb)^{-2}$, which exceeds the ratios obtained for the normal deformed [$\sim$ 10 $MeV^{-1}(eb)^{-2}$] and superdeformed bands [$\sim$ 5 $MeV^{-1}(eb)^{-2}$].

Magnetic rotational bands was understood on the basis of a **semi-classical** approach developed by R. M. Clark and A. O. Macchiavelli [28], that describes the coupling of two long angular momentum vectors $\vec{j}_\pi$ and $\vec{j}_\nu$, which are the angular momentum of the proton and neutron, respectively. The shears angle θ (angle between the vectors $\vec{j}_\pi$ and $\vec{j}_\nu$) is one of the important degrees of freedom in describing the properties of shears band and is shown in figure 2.7. The shears angle θ, can be derived using the semi-classical expression

$$\begin{aligned} cos\theta &= \frac{\vec{j}_\nu \cdot \vec{j}_\pi}{\mid \vec{j}_\nu \mid\mid \vec{j}_\pi \mid} \\ &= \frac{I_{shears}(I_{shears}+1) - j_\nu(j_\nu+1) - j_\pi(j_\pi+1)}{2\sqrt{j_\nu(j_\nu+1)j_\pi(j_\pi+1)}} \end{aligned} \tag{2.27}$$

where I_{shears} is the angular momentum generated only due to shears mechanism and can be written by subtracting the contribution of core rotation (R_{core}) from the experimentally observed angular momentum I (total angular momentum) as:

$$\begin{aligned} \vec{I}_{shears} &= \vec{I} - \vec{R}_{core}, where \\ R_{core} &= \frac{\Delta R}{\Delta I}(I - I_{bandhead}), and \\ \frac{\Delta R}{\Delta I} &\approx \frac{[I_{max} - (j_\pi + j_\nu)]}{(I_{max} - \sqrt{j_\pi^2 + j_\nu^2})}. \end{aligned} \tag{2.28}$$

The core contribution ranges from about 5% to 15% of the total angular momentum for most bands in the Pb region [29]

According to the prescription of Macchiavelli *et al.* [30], the excitation energies of the states in shears bands correspond to the change in the potential energy because of the recoupling of the angular momenta of the shears. The excitation energies of the states in the band with respect to the band head energy can be written as:

$$V(I(\theta)) = E_I - E_b = (3/2)V_2\ cos^2\theta \tag{2.29}$$

where, E_I is the energy of the level with angular momentum I, θ is the corresponding shears angle, E_b is the band head energy and V_2 is the strength of the interaction between the blades of the shears. Therefore, V_2 can be calculated by using the experimentally observed energy levels of the shears band. Typical value of V_2 (effective interaction), for per particle-hole pair found to be $\sim$ 300 keV in the Pb nuclei.

In this model, the reduced M1 strength is given by the expressions [30]

$$B(M1, I \rightarrow I-1) = \frac{3}{8\pi}\vec{\mu}_\perp^2 = \frac{3}{8\pi}g_{eff}^2 j_\pi^2 sin^2\theta_\pi[\mu_N^2] \tag{2.30}$$

where $g_{eff} = g_\pi - g_\nu$ and θ_π is the proton angle which can be derived as

$$tan\theta_\pi = \frac{j_\nu sin\theta}{j_\pi + j_\nu cos\theta} \tag{2.31}$$

From the experimental B(M1) values and the calculated shears angle, it would be possible to extract the g_{eff} for a particular band configuration. Further details of the 'magnetic rotation' can be found in the articles [28, 31].

Bibliography

[1] C.F.Von Weizs*ä*cker, Z. Phys. **96**, 431 (1936).

[2] H.A. Bethe, Rev. Mod. Phys. **8**, 82 (1936).

[3] P. Ring and P. Schuck, The Nuclear Many-Body Problem, Springer-Verlag Berlin Heidelberg (1980).

[4] M. G. Mayer, Phys. Rev. **75**, 1969 (1949).

[5] O. Haxel, J.H.D. Jensen and H.E. Suess, Phys. Rev. **75**, 1766 (1949).

[6] M.G. Mayer and J.H.D. Jensen, Elementary Theory of Nuclear Shell Structure (John Wiley, 1955).

[7] E. Feenberg, Shell Theory of the Nucleus (Princeton University Press, 1955).

[8] B. D. Day, Rev. Mod. Phys., **39**, 719 (1967).

[9] N. E. Reid, M. K. Banerjee, G. J. Stephense Jr., Phys. Rev. **C5**, 41 (1972).

[10] A. Bohr, Mat. Fys. Medd. Dan. Vid. Selsk. **26** No. 14 (1952).

[11] Ali Al-Khatib's Thesis (High-Spin γ-Ray Spectroscopy of ^{124}Ba, ^{124}Xe and ^{125}Xe).

[12] D. L. Hill and J. A. Wheeler, Phys. Rev. **89**, 1102 (1953).

[13] G. Andersson et al., Nucl. Phys. **A 268**, 205 (1976).

[14] S. G. Nilsson, Kgl. Danske Videnskab Mat. Fys. Medd. **29**, No. 16 (1955).

[15] T. Bengtsson and I. Ragnarsson, Nucl. Phys. **A 436**, 14 (1985).

[16] R. B. Firestone, et al., Table of Isotopes (John Wiley and Sons, Inc., New York (1999)).

[17] D.R.Inglis, Phys. Rev. **96**, 1059 (1954).

[18] D.R.Inglis, Phys. Rev. **97**, 701 (1955).

[19] R. Bengtsson and S. Fraunendorf, Nucl. Phys. **A 327**, 139 (1979).

[20] F. Stephens, Rev. Mod. Phys. **47**, 43 (1975).

[21] A. Bohr and B. R. Mottelson: Nuclear Structure, vol. II (W. A. Benjamin, Inc., New York, 1975)

[22] W. Nazarewicz et al., Nucl. Phys. **A 512**, 61 (1990).

[23] W. Nazarewicz et al., Nucl. Phys. **A 435**, 397 (1985).

[24] G. Mukherjee et al., Phys. Rev. **C 64** (2001) 034316.

[25] G. Mukherjee et al., Nucl. Phys. **A 829**, 137 (2009).

[26] H. Hübel, Contribution to Weatherill Symposium, Philadelphia, 1991 (unpublished).

[27] G. Baldsiefen et al., Nucl. Phys. **A 574**, 521 (1994).

[28] R.M. Clark and A.O. Macchiavelli, Ann. Rev. Nucl. Part. Sci. **50** , 1 (2000).

[29] A.O. Macchiavelli et al., Phys. Rev. **C 58** R621 (1998).

[30] A.O. Macchiavelli *et al.*, Phys. Rev. C **57**, R1073 (1998).

[31] H. Hübel, Prog. Part. Nucl. Phys. **54**, 1 (2005).

Chapter 3

Experimental Techniques and Data Analysis

Special techniques are needed to investigate the nuclear structure at high spin. In this chapter, I will describe about the population of high spin states in atomic nuclei and the detailes of the experiments and the setup used for this thesis work.

3.1 Population of High Angular Momentum States in Nuclei

There have been several methods of production of nuclei at high angular momentum. Among them, the heavy ion induced fusion-evaporation reaction is the most efficient method. Formation and the de-excitation mechanisms of the compound nucleus have been shown in figures 3.1 and 3.2. When an accelerated projectile nucleus having an energy greater than the Coulomb energy between target and projectile nuclei, collides and fuses with a target nucleus, a compound nucleus is formed. Fusion occurs between the projectile nucleus and target nucleus within 10^{-22} to 10^{-20} sec. The compound system is a very "hot" and it rotates very rapidly. It first cools down by particle evaporation within $\sim 10^{-16}$ sec. Evaporating particles are neutrons,

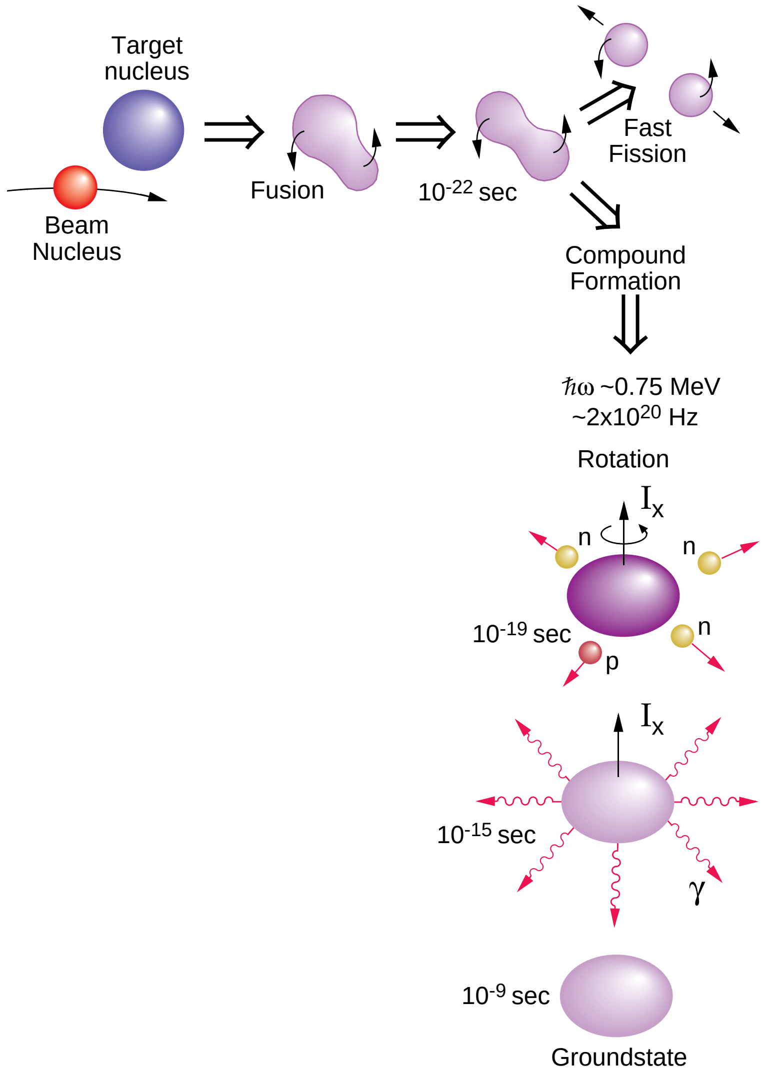

Figure 3.1: Formation and decay of the compound nucleus in a heavy-ion induced fusion-evaporation reaction. Figure taken from ref. [1].

protons, or alphas. Probability of evaporation of neutrons are more than protons, or alphas because neutrons do not face a Coulomb barrier. On the other hand protons and alphas being charge particles, their evaporation are hindered by the Coulomb barrier. Compound nucleus loses considerable amount of the excitation energy of about 8 MeV (one neutron separation energy) and only a few units of angular momentum (about $1\hbar$) per neutron evaporation. Particle evaporation is no longer possible when the excitation energy becomes less than the particle emission threshold and the residual nucleus enters the 'entry-line' which is roughly one neutron

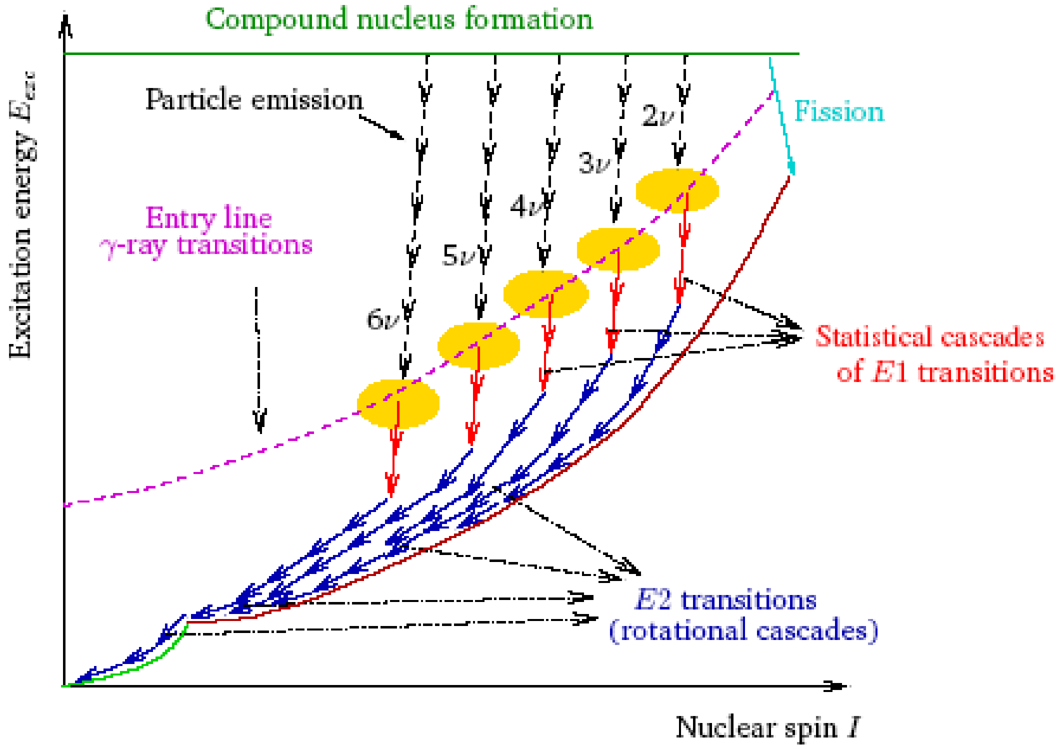

Figure 3.2: Excitation energy as a function of the nuclear spin (angular momentum) I for the heavy-ion induced fusion-evaporation reaction. Figure taken from ref. [2].

binding energy above the 'Yrast line' (see Fig-3.2). From the entry-line residual nucleus decay by subsequently emitting statistical γ rays which are mainly E1-transitions. They take away only a few units of angular momentum, but much of energy. Since the nuclear level density is very high around the entry-line, statistical γ-ray transitions are called quasi-continuum transitions. The yrast line corresponds to the minimum excitation energy for a given spin. Yrast is a Swedish word and its meaning is 'fastest rotating'. After that, the residual nucleus comes to the ground state by emitting a cascade of γ transitions along the yrast line. These γ rays are discrete in nature. These are collective E2 rotational cascades in case of deformed nuclei. In γ-ray spectroscopy experiment these discrete γ-rays are detected to understand the nuclear structure information. With-in about 10^{-9} seconds the total decay process is completed.

3.2 Detection of γ-radiation

The detection of the emitted γ-rays from the excited nuclei of interest provides information on the nuclear levels. For the detection of γ-rays in a detector and to measure their energy, the γ-rays must lose its energy in the detector medium. The interaction of γ rays in matter is distinctly different from that of charged particles. Mainly three process are involved for the interaction of γ rays with matter. These are Photoelectric effect, Compton Scattering and Pair Production.

3.2.1 Photoelectric effect

In this process, γ-ray photons interact with a bound atomic electron and transferred its full energy to an atomic electron. A small part of the incident γ energy is used to overcome the electron binding energy, where as the rest is transferred to the freed electron as kinetic energy. The kinetic energy E_e of the emitted photoelectron is given by the expression:

$$E_e = E_\gamma - E_b \tag{3.1}$$

where E_γ is the incident γ-ray energy and E_b is the electron binding energy. The probability of Photoelectric effect depends on the energy of the γ-ray as well as the atomic number Z of the detector material. The cross-section of photo-electric effect is given by the expression:

$$\sigma_{photo} \propto \frac{Z^N}{E_\gamma^{3.5}} \tag{3.2}$$

where N varies between 4 to 5. Equation 3.2 shows that photo-electric effect cross-section decreases with increase in energy and increases rapidly with the atomic number Z of the medium.

3.2.2 Compton scattering

In the Compton scattering process, the incident γ-ray photon is scattered by a free or weakly bound electron and transfers a portion of its energy to the electron. From the energy and momentum conservation relations, the energy of the scattered photon is given by,

$$E_{\gamma}^{'} = \frac{E_{\gamma}}{1 + (1 - cos\theta)(\frac{E_{\gamma}}{m_0c^2})} \tag{3.3}$$

where θ is the scattering angle, E_{γ} is the incident photon energy, and m_0c^2 is the rest mass energy of the electron. The kinetic energy of the electron is given by,

$$E_e = E_{\gamma} - E_{\gamma}^{'} = \frac{E_{\gamma}^2(1 - cos\theta)}{m_0c^2 + E_{\gamma}(1 - cos\theta)} \tag{3.4}$$

The maximum energy transfer to the electron happens when the γ-ray photon is scattered at an angle $\theta = 180°$. It can be seen that, a continuum of energies can be transferred to the electron, ranging from $\theta = 0°$ to $\theta = 180°$. In this process, γ-ray photon never loses its full energy within the detector medium. As a result, a continuous 'Compton background' occures at lower energies, in the energy spectrum.

3.2.3 Pair production

In this process, electromagnetic energy is converted into matter. Pair production takes place when the incident γ ray with an energy greater or equal to twice the rest mass energy of the electron ($E_{\gamma} \geq 2m_0c^2 = 1.022$ MeV), passes near the strong electromagnetic field of an atomic nucleus. In this interaction the γ ray disappears and a pair of electron and positron is created. The nucleus receives a very small amount of recoil energy to conserve the linear momentum. The electron and the positron are slowed down rapidly as a result of collisions with atoms in the detector medium. Once the kinetic energy of the positron becomes very low, the positron annihilate with an electron in the detector medium and two annihilation γ-rays with energies of 0.511 MeV are produced. When one of the annihilation γ rays escapes from the detector then it results in a single escape peak, located 0.511 MeV (m_0c^2) below the photopeak in the spectrum. If both of the annihilation γ rays escape from the detector, it results in a double escape peak in the spectrum which is located 1.022 MeV ($2m_0c^2$) below the full-energy peak. The probability of pair production approximately varies with square of the Z (atomic number).

Thus partial or complete transfer of the γ-ray energy to the electrons within the detector material takes place by the above three processes. Among the three processes photoelectric effect is the important one for γ-ray spectroscopy experiment because γ-ray deposits its full energy in this process. In γ-ray spectroscopy, the detector used to detect γ rays should therefore be constructed with high Z material so that the photoelectric cross-section is maximized. Moreover for high resolution γ-ray spectroscopy the detectors should have the good energy resolution and reasonable efficiency. Semiconductor detectors made of High-Purity Germanium (HPGe) crystals are preferably used for the detection of γ-rays photons in γ spectroscopy experiment.

3.3 High-Purity Germanium (HPGe) detectors

High-purity germanium detector is a main tool for high resolution γ-ray spectroscopy. These detectors are semiconductor type detectors. The important parameter which is of consideration is the active volume of the detector determined by the thickness d of the depletion region. Detectors with much larger depletion depth are required for γ-ray spectroscopy. For a semiconductor detector, the depletion depth is given by [3]

$$d = \left(\frac{2\epsilon V}{eN}\right)^{1/2} \tag{3.5}$$

where, V is the reverse bias voltage, N represents the net impurity concentration in the initial semiconductor material, ϵ is the dielectric constant and e is the electronic charge. If germanium of normal semiconductor purity is employed, the maximum achievable depletion depth is only a few mm even at bias voltages close to the breakdown level. Thus, the impurity concentration should be much reduced down to 10^{10} atoms/cm^3 in order to realize intended depletion depths of the order of a few cm. At this impurity concentration, a reverse bias voltage of 1 kV can produce a depletion depth of 1 cm. The required impurity concentration corresponds to levels less than 1 part in 10^{12}, which is quite challenging. Since, impurity concentration is much lower (10^{10} atoms/cm^3), HPGe detector is called a High-purity germanium detector. HPGe detector has an excellent energy resolution ($\sim$ 2 keV at 1 MeV) compared with gas detectors or scintillators. To create one ion pair $\sim$ 35 eV energy is required for a gas detectors, on the other hand $\sim$ 100 eV or more energy is required to create photoelectrons in scintillator detector. Energy resolution is better in germanium detector because only $\sim$ 3 eV energy is required to

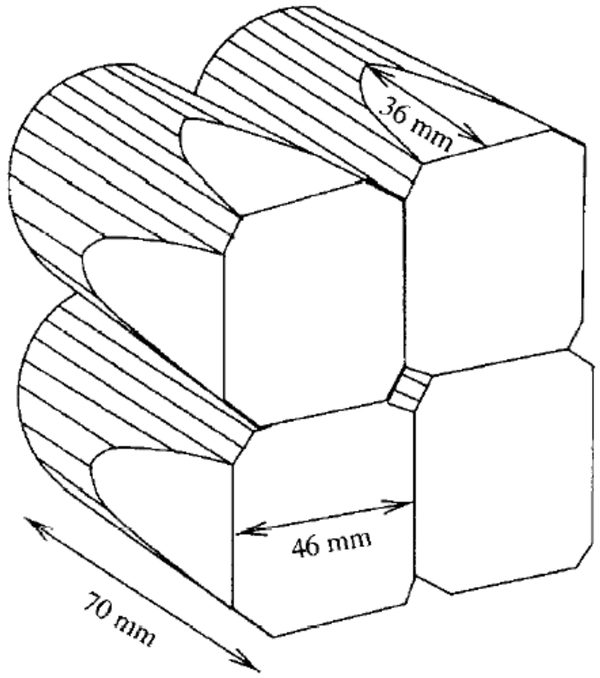

Figure 3.3: A schematic geometry of Clover detector [4].

create one electron-hole pair (information carrier). HPGe detector must be operated at liquid nitrogen temperature (77 K) to reduce the leakage current due to its smaller band gap ($\sim$ 0.7 eV). Unlike Ge(Li) or Si(Li) detectors these detectors need not always be kept at liquid nitrogen temperature, when not in use. However, time resolution of HPGe detector ($\sim$ 10 ns) is poor comparison with scintillator detectors.

3.4 Clover detectors

Clover detector is a composite detector, shown in Fig. 3.3, consists of four n-type coaxial HPGe crystals placed in a four-leaf clover arrangement using a common cryostat [4]. The diameter and length of each crystal, used in the present work are 50 mm and 70 mm, respectively. The spacing between two adjacent crystals is 0.2 mm. These detectors were used first time in EUROBALL setup. The Clover detectors have the following features,

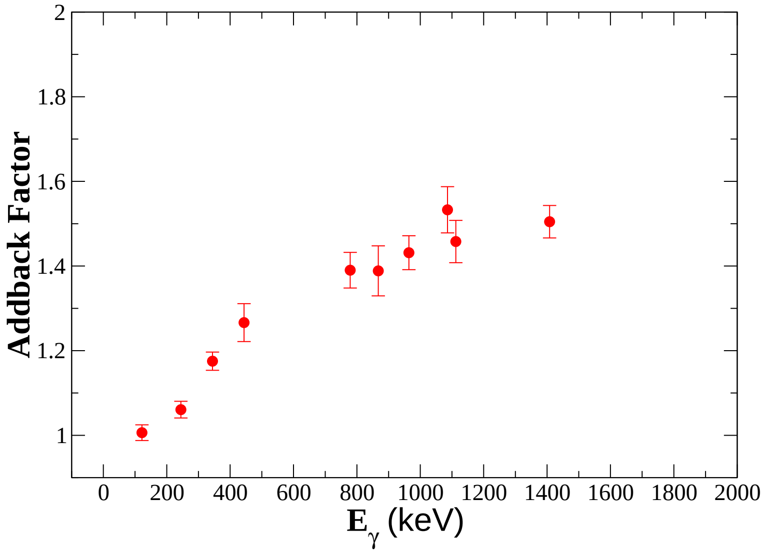

Figure 3.4: Variation of add-back factor with γ-ray energy.

• **Large photopeak efficiency in add-back mode:** Due to photoelectric effect γ-ray is fully absorbed by any one of the individual crystal of a clover HPGe detector. Due to Compton scattering some energy of the γ-ray is absorbed by any one crystal, and the rest scattered energy can be absorbed by other neighboring crystal. When we add the counts of each crystal of a clover detector due to photo electric absorption it is known as add mode.

But if we add the correlated events in the two adjacent crystals then the events which are Compton scattered from one crystal and gets absorbed in the adjacent crystal also contribute to the full energy peak. So, the full energy peak now contains the photo electric events of all four crystals and also part of the Compton events. This is known as add-back. This is done offline where the information about the firing of each crystal is stored on event by event basis. The above method of getting the photopeak events back in addback mode is possible due to high isolated hit probability of the clover detector. In Fig.3.4, the 'addback factor' is plotted as a function of γ-ray energy. It is defined as the ratio of the add-back counts to the sum counts of the photoelectric events obtained from the four crystals. The add-back factors for various γ-ray energies have been obtained from the ^{152}Eu source in this present thesis work. From the figure, it is observed that the ratio is close to one at lower energies which is due to the fact that the cross section of Compton scattering at these energies is very less. The factor then starts increasing with increasing γ-ray energies, because at these moderate energies, the probability of Compton scattering becomes comparable with the photo electric effect and the add-back mode starts contributing. At very high γ-ray energies, the factor almost gets saturated. This is because of the fact that at high energy, the scattered energy also becomes large and the scattering probability, compared to photoelectric absorption, in the second crystal also increases.

• **Good energy resolution (typically 2.3 keV at 1.33 MeV in add-back mode) and good timing response.**

• **Due to smaller effective opening angle of clover detector, there will be lesser Doppler broadening of γ rays.**

• **Linear polarization of γ transitions can be measured using clover detectors.**

In the present thesis work, Indian National Gamma Array (INGA) was mostly used which consisted of clover detectors.

3.5 Indian National Gamma Array (INGA)

Indian National Gamma Array (INGA) is an array of Clover HPGe detectors. INGA is a collaborative research facility. First INGA campaign was held at TIFR, Mumbai with eight clover detectors. This array is being used phase wise manner among the three accelerator centres (VECC (Kolkata), TIFR (Mumbai), and IUAC (New Delhi)). In this thesis work, experiments were carried out using different configurations of INGA array at all these accelerator centres. Some of the salient features of the respective configurations of INGA have been described in the following subsection. The table 1.1 summarises the nuclei studied and measurements performed in this thesis work.

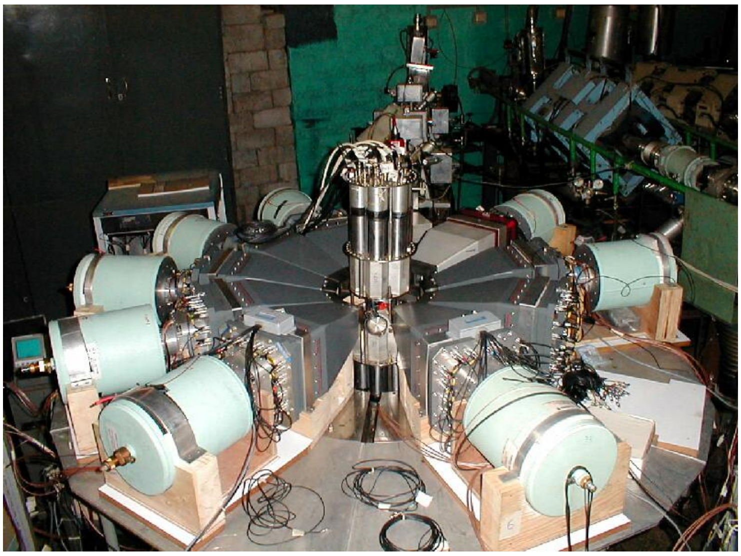

Figure 3.5: The INGA Phase-I setup at TIFR.

3.5.1 INGA Phase-I at TIFR

First INGA campaign was performed at TIFR, Mumbai in the year 2001 with 8 Compton-suppressed clover Ge detectors. Setup of this array has been shown in Fig. 3.5. The detectors were arranged in a median plane configuration at 25 cm away from the target and placed at $120°$, $90°$, $60°$, $\pm30°$,$-70°$, $-105°$ and $-145°$ angles with respect to the beam direction. In this setup, a 14-element NaI(Tl) multiplicity filter, in the form of two clusters, was placed above and below the target chamber. NIM and CAMAC standard electronics modules have been used for signal processing of the Clover detectors. The master gate was (Ge.$\overline{ACS}$) generated using the anti-coincidence between BGO anti-Compton shield (ACS) and the Clover Ge detectors. To extract the γ multiplicity the 16 channel CAMAC discriminator module was used. Fold events were selected using HEX discriminator by adjusting its threshold. LINUX based advanced multi-parameter data acquisition system LAMPS [5], is developed at BARC, was used to acquire on-line list mode coincidence data.

Figure 3.6: The INGA Phase-III setup at VECC.

3.5.2 INGA Phase-III at VECC

Third INGA campaign was performed at VECC, Kolkata, with 8 Compton-suppressed clover Ge detectors. Fig. 3.6. shows the setup of this array. The structure could hold upto ten detectors. The detector to target distance was 22 cm. The clover detectors were arranged in three angles with 2 clovers each at 40° and 125° angles while four clovers at 90° angle. NIM and CAMAC standard electronics modules have been used for signal processing in INGA at VECC [6]. The clover modules [6, 7], specially designed for processing signals for clover detectors, were used in INGA at VECC. These modules were designed and fabricated at IUAC, New Delhi and have been used to process energy and timing signals from Compton suppressed Clover Ge detectors. One module contains five TFAs and five CFDs for four crystals of a Clover and ACS. It can supports all the crystals of Clover detector with the corresponding ACS. Pileup rejection can be done by this module. CAMAC based multi-parameter data acquisition system LAMPS [5] has been used.

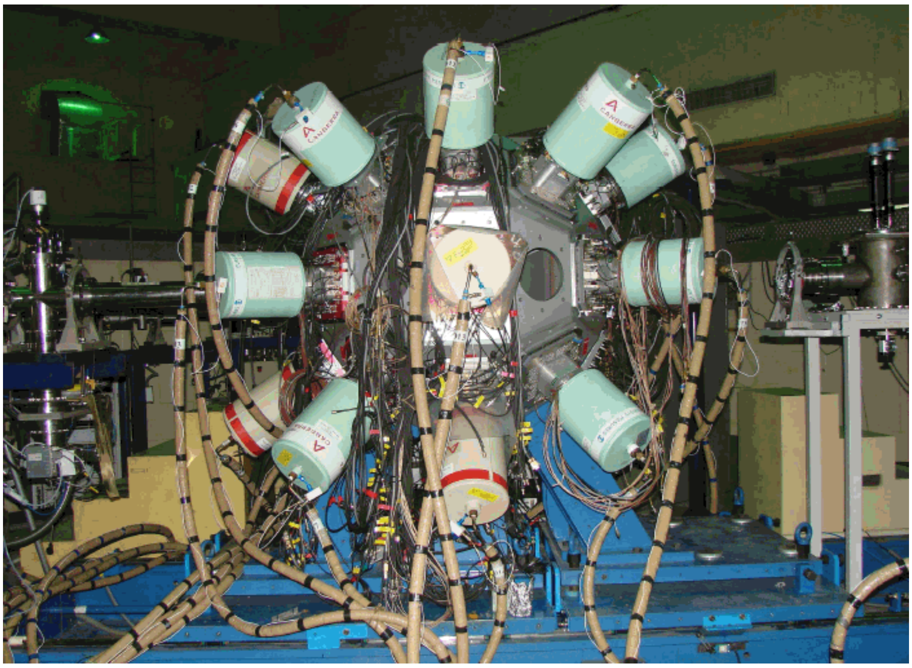

Figure 3.7: The INGA Phase-IV setup at IUAC.

3.5.3 INGA Phase-IV at IUAC

Phase-IV INGA [8] campaign was carried out at IUAC, New Delhi. This array has the provision of placing 24 Clover detectors in 4π geometry along with anti-Compton shield (ACS) at five different angles. Distance between target and detector was 24 cm. The total photopeak efficiency of the array is $\sim$ 5%. A side view of INGA at IUAC is shown in Fig. 3.7. The array consists of two parts, the forward hemisphere and the backward hemisphere. The forward hemisphere consists of two rings around the target position having angles of 32° and 57° with respect to the beam axis. On the other hand, backward hemisphere consists of three rings around the target position having angles of 90°, 123° and 148° with respect to the beam axis. Backward array can hold 16 Clover detectors and forward array holds 8 Clover detectors. The orientation of the detectors of the phase-IV INGA in five rings have been listed in Table 3.2. The ACSs can be mounted with an accuracy of $\pm$ 0.5° with respect to the beam axis and their positions are reproducible with an accuracy of $\pm$ 0.5 mm with respect to the target position.

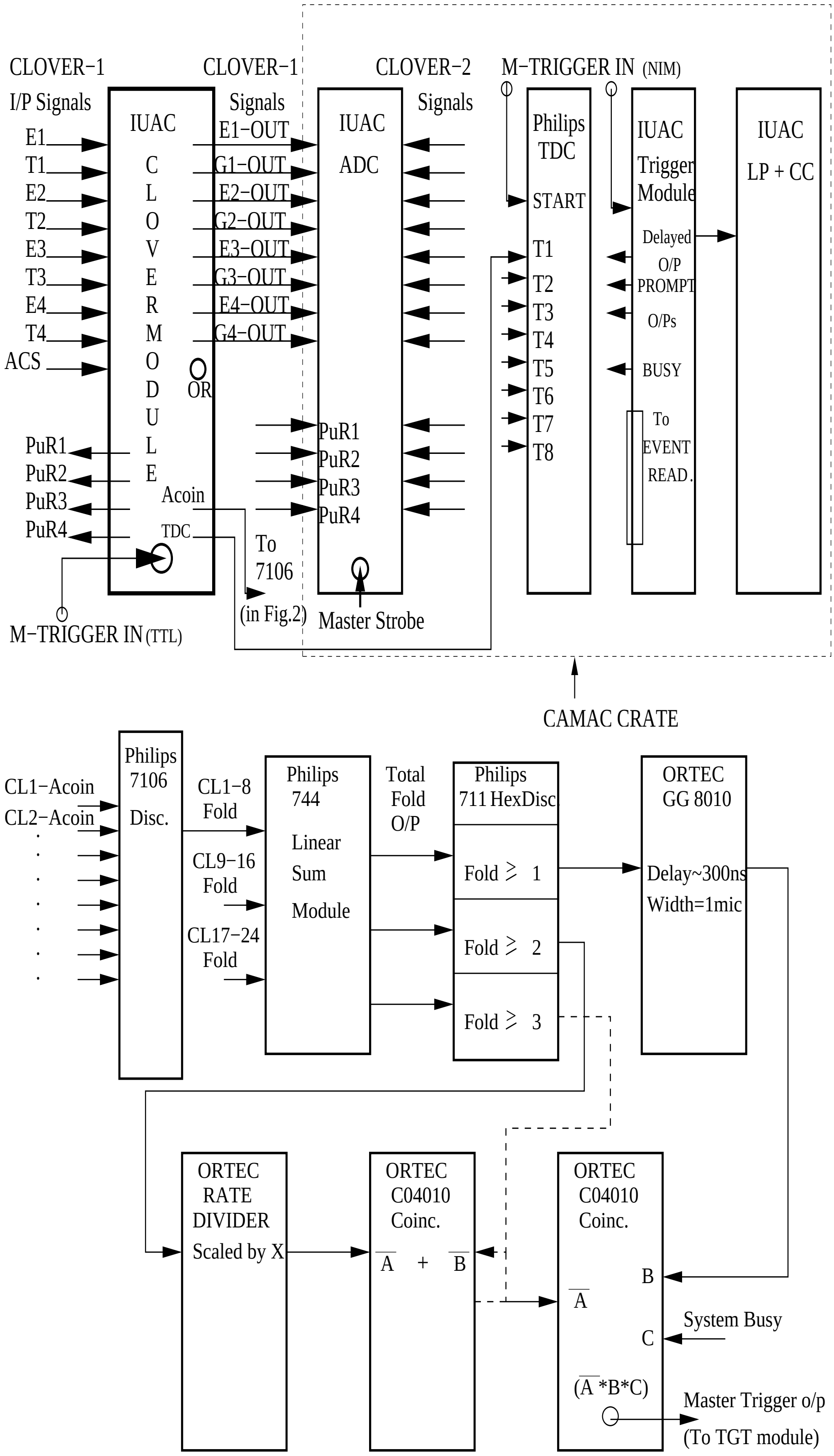

Figure 3.8: The Electronics setup in INGA Phase-IV.

Table 3.1: Orientation of the detectors in INGA Phase-IV.

Ring No.	Detector No.	Distance from target (in cm)	Polar angle (θ) (in deg.)	Azimuthal angle (ϕ) (in deg.)
I	1	24	148	0
I	2	24	148	90
I	3	24	148	180
I	4	24	148	270
II	5	24	123	45
II	6	24	123	135
II	7	24	123	225
II	8	24	123	315
III	9	24	90	0
III	10	24	90	45
III	11	24	90	90
III	12	24	90	135
III	13	24	90	180
III	14	24	90	225
III	15	24	90	270
III	16	24	90	315
IV	17	24	57	45
IV	18	24	57	135
IV	19	24	57	225
IV	20	24	57	315
V	21	24	32	0
V	22	24	32	90
V	23	24	32	180
V	24	24	32	270

The target chamber is made of glass tube (5.08 cm diameter) to minimize the attenuation of the γ rays.

The block diagram of the electronics setup for INGA Phase-IV at IUAC has been shown in figure 3.8. Clover electronics modules [7] have been used to process energy and timing signals from Clover detectors. The energy and timing outputs from preamplifier are fed into the clover module. The energy signals are amplified by spectroscopy amplifiers, and they are fed into ADCs for digitization. The shaping time for spectroscopy amplifiers has been set ~ 3 μs. Logic signals have been generated from timing signals of all the four crystals and ACS. To get Compton suppressed signal (ACOIN) from each Clover detector, timing signals from individual crystals of each Clover are 'OR'ed, followed by VETO from the ACS signal. Fold $(\gamma, \gamma\gamma, \gamma\gamma\gamma)$ is selected from the analog sum of all the Compton suppressed logic (timing) signals (ACOIN) by setting proper threshold in the Hex discriminator (Phillips 711). The output of Hex discriminator is 'AND'ed with the BUSY signal in anti-coincidence mode (Ge.$\overline{ACS}$.$\overline{BUSY}$) and Master Trigger is generated. The Master Trigger is fed to the ADCs and the common start of the TDCs.

CAMAC based data acquisition system with the digital hardware distributed over three 24-slot CAMAC crates was used. 14-bit, 8 channel ADCs (AD814) [9] and 12-bit TDCs (Phillips 7186) have been used to digitize the energy and timing signals, respectively. Each CAMAC crate contains 8 ADCs and one TDC module. The data readout and buffering are accomplished by a List Processing Crate Controller (LPCC) CAMAC module [10] made at IUAC. Synchronization of individual crates are done with Trigger generator (TG) [11]. LINUX based multi-crate data acquisition program CANDLE [12] was used to acquire on-line list mode coincidence data.

3.5.4 INGA Phase-V at TIFR

Phase-V INGA [13, 14, 15] has been hosted at TIFR, Mumbai. The array was designed for 24 Compton suppressed Clover detectors. Geometry of the array was spherical. The Clover detectors were arranged in seven angles, with 3 clovers each at 23°, 40°, 65°, 115°, 140° and

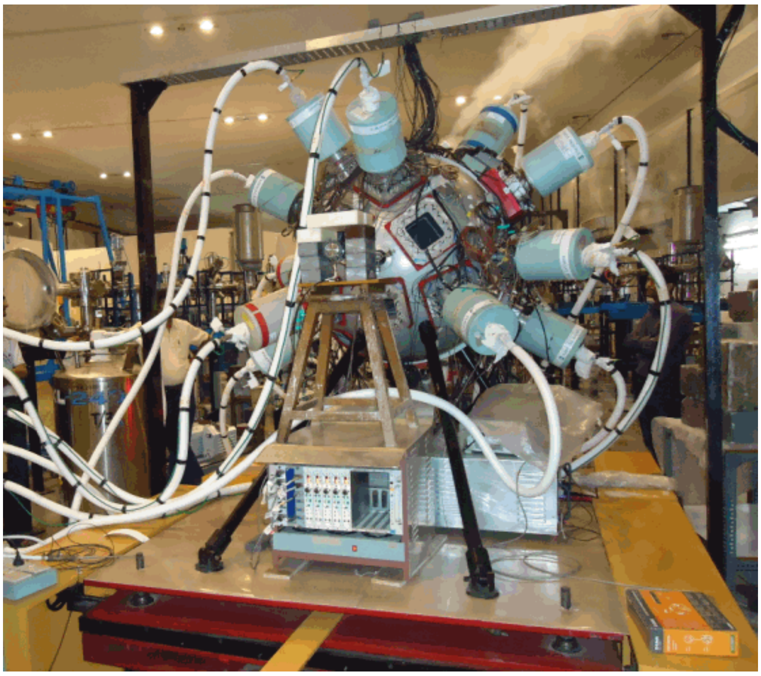

Figure 3.9: The INGA Phase-V setup at TIFR.

157° while 6 clovers were at 90°. Setup of this array has been shown in Fig. 3.9. The distance between the target and the crystal of the Clover detector is 25 cm. The total photopeak efficiency of the array is $\sim 5\%$ at $E_\gamma \sim 1$ MeV. The orientation of the detectors of the phase-V INGA have been listed in Table 3.3.

A digital data acquisition (DDAQ) system, with 112 channels based on Pixie-16 modules developed by XIA LLC [16] has been adopted first time for the INGA, in this phase. This system has provision for the digitization of 96 channels of 24 Clover detectors with 100 MHz sampling rate. It can operate both in trigger-less as well as multi-fold coincidence mode. Time stamped data were collected when at least two clovers were fired in coincidence. A time window of 150 ns was set for this coincidence between the fast triggers of individual channels and the coincidence trigger was kept open for 1.5 μs. The BGO signals from the anti-Compton shields of the respective clovers were used for vetoing the individual channels. The detailed description of the DDAQ has been given in the Refs. [13, 14, 15]. The data sorting routine "Multi pARameter timestamped based COincidence Search program (MARCOS)", developed at TIFR, sorts the

Table 3.2: Orientation of the detectors in INGA Phase-V.

Pocket No.	Distance from target (in cm)	Polar angle (θ) (in deg.)	Azimuthal angle (ϕ) (in deg.)
1	25	157	0
2	25	157	120
3	25	157	240
4	25	140	60
5	25	140	180
6	25	140	300
7	25	115	30
8	25	115	150
9	25	115	270
10	25	90	0
11	25	90	60
12	25	90	120
13	25	90	180
14	25	90	240
15	25	90	300
16	25	65	90
17	25	65	210
18	25	65	330
19	25	40	180
20	25	40	60
21	25	40	300
22	25	23	120
23	25	23	240
24	25	23	0

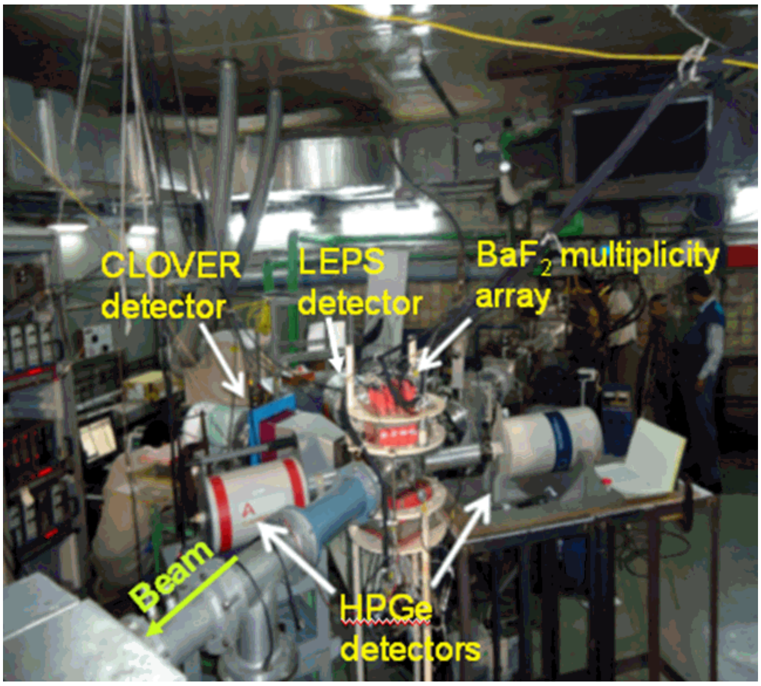

Figure 3.10: Experimental setup at VECC.

time stamped data to generate $\gamma - \gamma$ matrix and $\gamma - \gamma - \gamma$ cube in a Radware compatible format for further analysis.

3.5.5 In-House Experimental setup at VECC

Excited states in ^{197}Tl were populated by the fusion-evaporation reaction using modest in-house facility with α beam of energy 48 MeV from the K = 130 Cyclotron at VECC, Kolkata. The experimental set up consisted of two single-crystal HPGe, one clover HPGe and one LEPS (HPGe) detector placed, respectively, at 30°, 135°, 90° and 135° angles with respect to the beam direction and in a median plane configuration. The diameter and length of the LEPS crystal, used in the present work are 68 mm and 11.5 mm, respectively. A 50 element multiplicity filter [17], consisted of two arrays of 25 BaF_2 crystals each, was also used. Experimental setup has been shown in Fig. 3.10. The energy and timing from each detector and an RF-γ TAC were recorded in list mode using $\gamma - \gamma$ trigger. NIM and CAMAC standard electronics modules

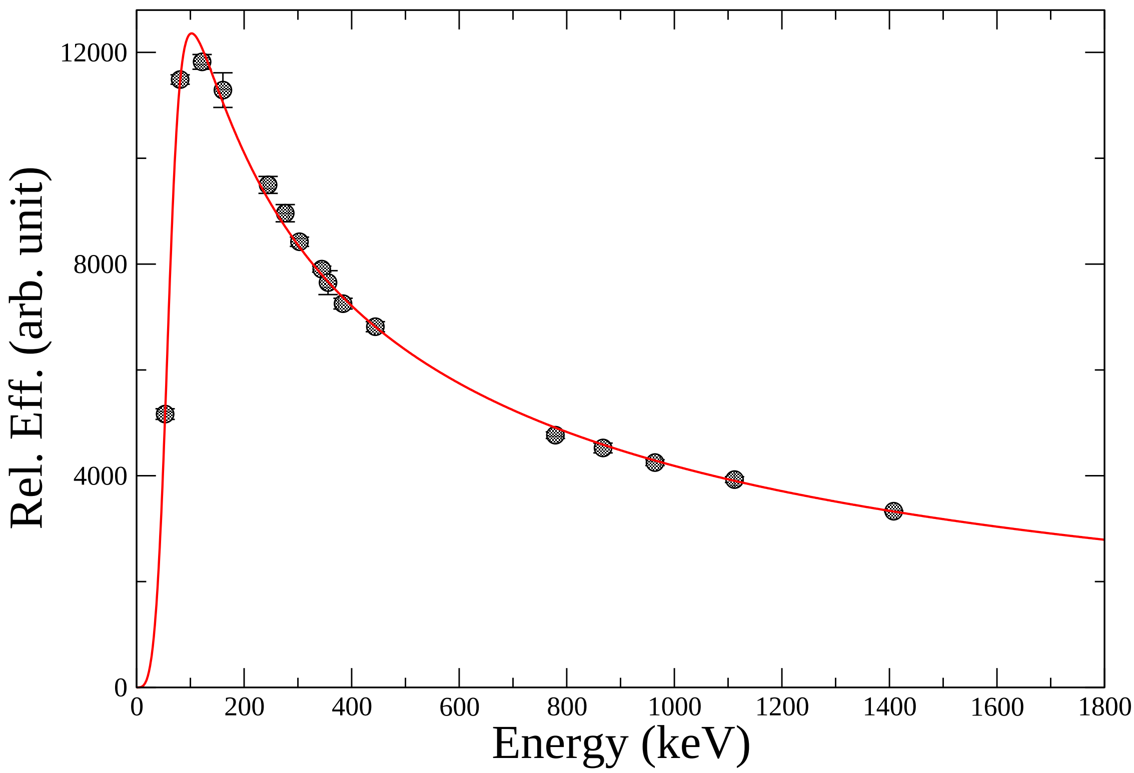

Figure 3.11: Average efficiency curve for the fifteen clover detectors of INGA Phase-V at TIFR.

have been used for signal processing in this setup. The clover module was used for the clover detector. LINUX based advanced multi-parameter data acquisition system LAMPS [5], was used to acquire on-line list mode coincidence data.

3.6 Offline Data Analysis

Offline data analysis has been carried out using the programas INGASORT [18], LAMPS [5] and RADWARE [19] throughout the present work. Nuclear level scheme is like a fingerprint of different kinds of excitations (single particle, collective) in nuclei. To develop the level schemes

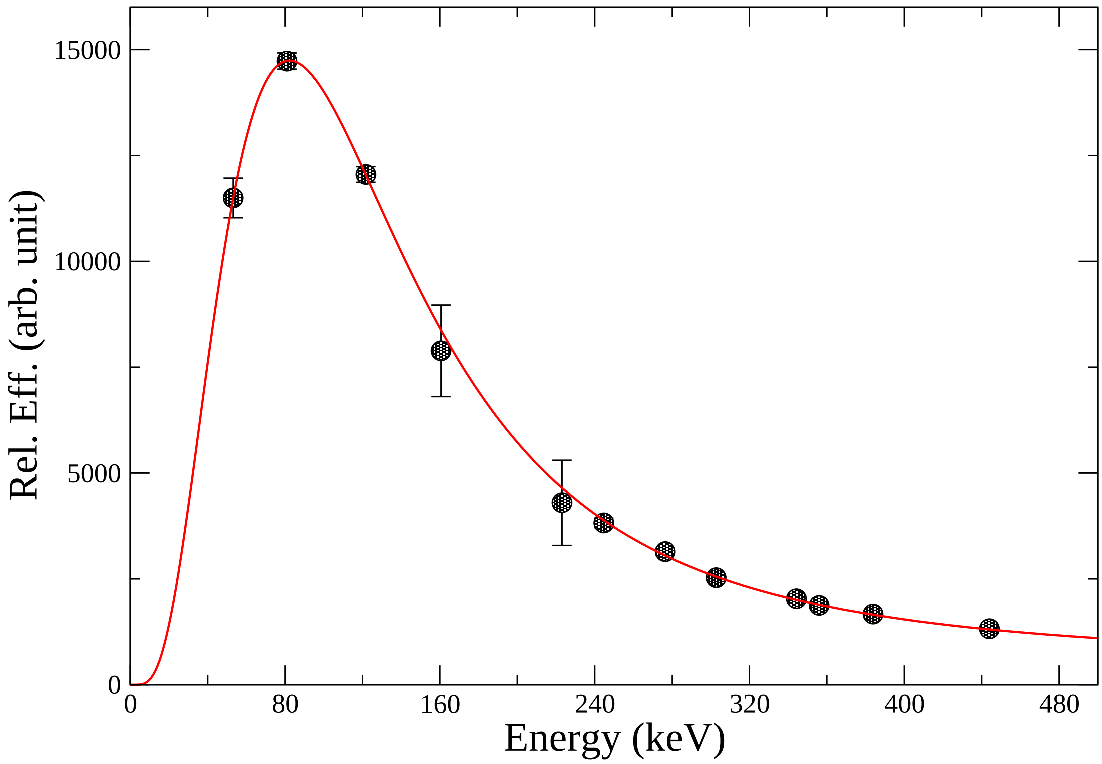

Figure 3.12: Relative efficiency curve for one segment of the LEPS (Low-Energy Photon Spectrometer) detector.

of ^{134}Cs, ^{194,197}Tl and ^{195,198}Bi, the LIST mode data have been sorted into two-dimensional symmetric $\gamma-\gamma$ (4K $\times$ 4K) matrices and $\gamma-\gamma-\gamma$ cubes, after energy and efficiency calibration of all the detectors. The coincidence and intensity relations have been used to built up the level scheme.

In γ-ray spectroscopy the experimental observables are energy, intensity and relative time of γ-rays, whereas spin, parity etc. are deduced quantities from the experimental data. The energy of the different gamma rays are determined by carring out the energy calibration using known gamma sources (^{152}Eu and ^{133}Ba). From the multipolarity of γ transition one can determine the spin of excited states. The DCO (Directional Correlation from Oriented states) ratio and Polarization measurements have been done for J^{π} assignments of the levels.

3.6.1 Energy and Efficiency Calibration

The energy of the incident γ-rays are digitised in the Analog to Digital Converter (ADC) for each HPGe crystal of clover detectors, where the channel number of ADC is proportional (if there is no offset) to the energy of the incident γ-ray. Generally, the gain of each crystal of clover detector is different. For that reason, the correlation between the channel and the energy has to be established using known radioactive sources. We have used ^{152}Eu and ^{133}Ba standard sources for energy calibration. The γ-ray energies were plotted against the channel numbers and fitted using a polynomial fit,

$$E = \sum_{\mu=1}^{n} (a + b_{\mu} x^{\mu}), \tag{3.6}$$

where E is the energy in keV, x is the channel number, a and b_{μ} are the calibration constants. In present thesis work, we have done a quadratic energy calibration.

In γ-ray spectroscopy, the relative efficiencies of γ-ray are used for determining the relative intensities of the γ transitions. To get the relative efficiency, we have used ^{152}Eu and ^{133}Ba standard sources throughout the present work. Relative efficiency of the Clover detectors have been extracted in the add-back mode. The area of each peak was obtained from a spectrum in which counts (add-back) from all the clover detector have been added. The experimental data were fitted with the following equation, using the “effit” subroutine of the RADWARE [19] package.

$$\ln(\epsilon) = \{(A + Bx + Cx^2)^{-G} + (D + Ey + Fy^2)^{-G}\}^{1/-G}, \tag{3.7}$$

where, ϵ is the efficiency, x = $\ln(\frac{E_\gamma}{100})$, y = $\ln(\frac{E_\gamma}{1000})$ and the γ-ray energy E_γ, is in keV. A representative relative average efficiency curve (add-back mode) obtained for the INGA Phase-V (TIFR) with clover detectors has been shown in Fig. 3.11. On the other hand, relative efficiency curve for one segment of the LEPS detector has been shown in Fig. 3.12. Relative efficiency of the LEPS detector (peaking around 80-keV) is higher than that for the clover detector (peaking around 100-keV) for low energy photons. For the LEPS detector the relative efficiency for 53.2-keV γ ray becomes 78 % of the peak value, while at the same energy the relative efficiency for the clover detector is 42 % of its peak value. It is also observed from Fig. 3.11 and from Fig. 3.12 that relative efficiency of the LEPS detector falls off more rapidly with increasing energy than the clover detector. The relative efficiency at 383.9-keV becomes 11 % of the peak value for the LEPS detector, while at the same energy the relative efficiency for the clover detector is 59 % of its peak value.

3.6.2 Determination of multipolarity of γ transitions

The angular distribution of γ rays depends on the multipolarity λ of emitted γ photon, which inturn depends on the change in the angular momentum (spin) between the initial (J_i) and final (J_f) states. From the multipolarity of γ transition one can determine the spin of excited states. The theoretical angular distribution from a state J_i to a state J_f by mixed multipole radiation of order λ, λ' can be written as [20]

$$W(\theta) = \sum_{\mu} A_\mu P_\mu(cos\theta) \tag{3.8}$$

where the co-efficient A_μ depend on the multipolarity of the γ photon, mixing ratio δ and the m-population width. $P(\theta)$ are Legendre polynomials. Previously, multipolarity of the γ transition has been determined from the angular distribution data. Due to the complexity of the singles spectra observed in fusion-evaporation reactions and limited number of angle combinations of modern γ arrays, a full angular distribution is very difficult. In these situations, multipolarities of the γ-ray transitions have been determined from the angular correlation analysis using the method of directional correlation from the oriented states (DCO) ratio, following the prescriptions of Krämer-Flecken et al. [21]. For the DCO ratio analysis, the coincidence events were sorted into an asymmetry matrix keeping the energy of the γ rays detected by the detectors at (θ_1) in one axis, and the γ ray energies detected by the detectors at (θ_2) on the other axis. The DCO ratios (for the gamma ray γ_1 gated by the gamma ray of known multipolarity γ_2) are obtained, from the γ-ray intensities (I_γ) at two angles θ_1 and θ_2, as

$$R_{DCO} = \frac{I_{\gamma_1} \ at \ \theta_1, \ gated \ by \ \gamma_2 \ at \ \theta_2}{I_{\gamma_1} \ at \ \theta_2 \ gated \ by \ \gamma_2 \ at \ \theta_1} \tag{3.9}$$

By putting gates on the transitions with known multipolarity along the two axes of the above matrix, the DCO ratios are obtained for each γ ray. For stretched transitions, the value of R_{DCO} would be close to unity for the same multipolarity of γ_1 and γ_2. while, if one transition is pure dipole and the other pure quadrupole, the ratio would be $\sim$ 2 or 0.5. For different multipolarities, the value of R_{DCO} depends on the detector angles (θ_1 and θ_2) and the mixing ratio (δ). By DCO method one can determine the multipolarities of the weak transitions.

Apart from the DCO analysis, one can determine the multipolarity of the γ photon from the R_{asym} analysis following the refs. [22, 23]. This procedure is based on the observed angular distribution for dipole and quadrupole transitions, near 0° and 90° with respect to the beam axis. An asymmetry ratio R_{asym}, which is independent of the multipolarity of the gating transition, is defined by,

$$R_{asym} = \frac{I_{\gamma_1} \text{ at } \theta_1, \text{ gated by } \gamma_2 \text{ at } \theta_3}{I_{\gamma_1} \text{ at } \theta_2, \text{ gated by } \gamma_2 \text{ at } \theta_3} \tag{3.10}$$

In this ratio, all angular correlation effects are almost averaged out and the measured γ ray intensities follow the ordinary angular distribution features as a function of the detector angle with respect to the beam direction. In order to extract the R_{asym}, two matrices were constructed with data from the θ_3 detector on x-axis and data from the θ_1 and θ_2 detectors on the y axis, respectively.

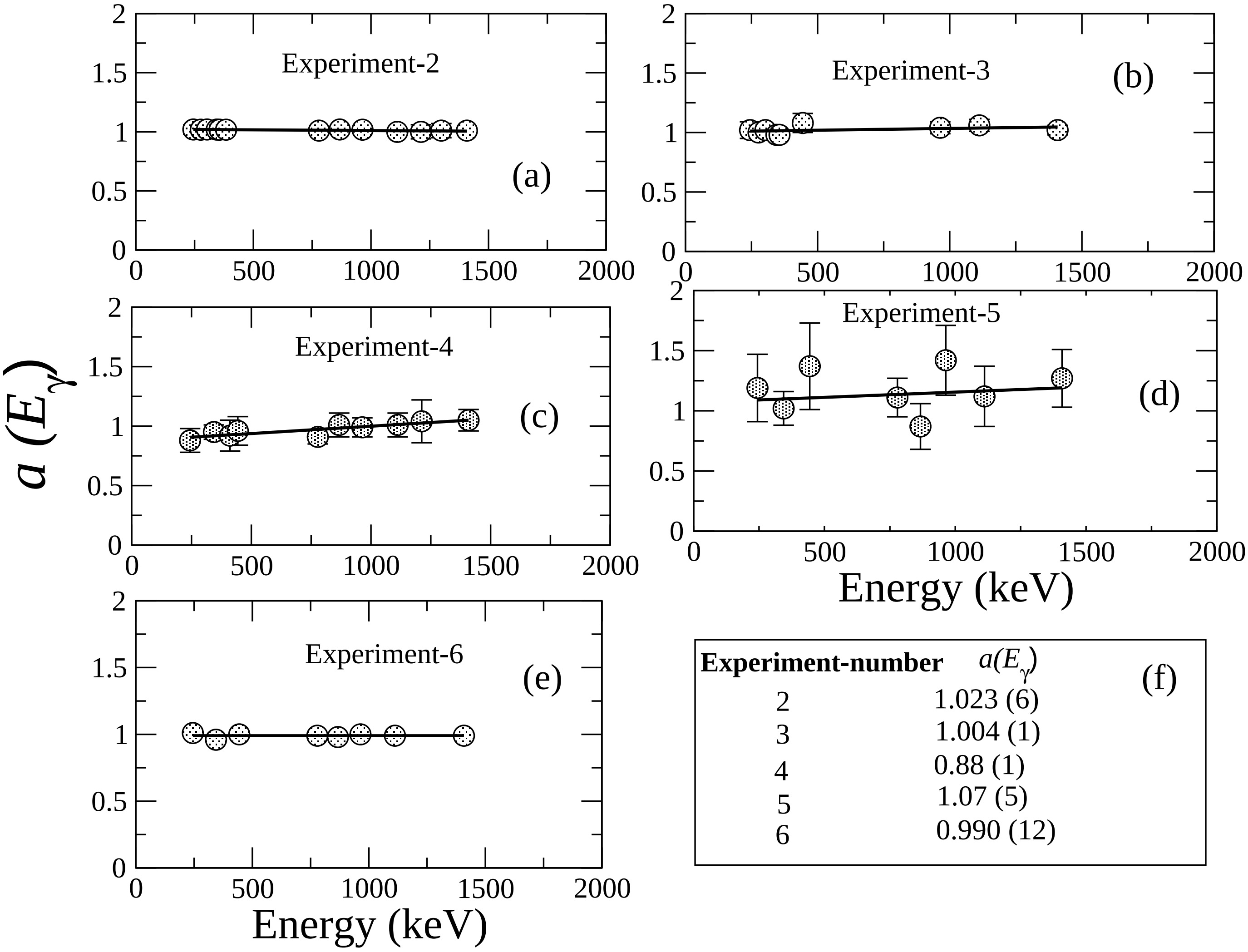

Figure 3.13: The asymmetry correction factor $a(E_\gamma) = \frac{N_\parallel}{N_\perp}$ obtained in different experiments, as mentioned in table 1.1, for different γ-ray energies (E_γs) using ^{152}Eu and ^{133}Ba sources. The solid lines correspond to linear fits of the data. The error bars on the data, for experiment-2, -3 and -6, are smaller than the size of the symbol.

3.6.3 Polarization measurement

The use of Clover HPGe detectors allowed us to assign definite parities to the excited states from the measurement of the integrated polarization asymmetry (IPDCO) ratio, as described

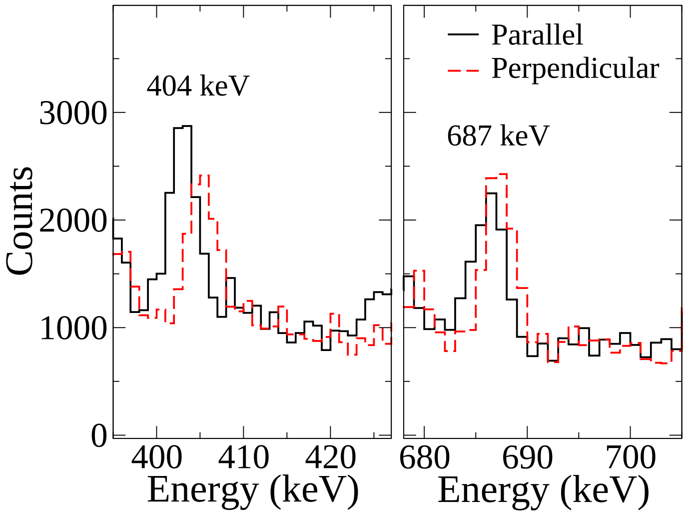

Figure 3.14: The perpendicular (dashed) and parallel (solid) components of the two γ rays in ^{194}Tl, obtained from the IPDCO analysis in the present work. The perpendicular component has been shifted in energy for clarity. 404-keV is a magnetic type transition where as 687-keV is a electric type transition.

in [24, 25], from the parallel and perpendicular scattering of a γ-ray photon inside the detector medium. The IPDCO ratio measurement gives qualitative idea about the type of the transitions (E/M). The IPDCO asymmetry parameters have been deduced using the relation,

$$\Delta_{IPDCO} = \frac{a(E_\gamma)N_\perp - N_\parallel}{a(E_\gamma)N_\perp + N_\parallel}, \tag{3.11}$$

where $N_\parallel$ and $N_\perp$ are the counts for the actual Compton scattered γ rays in the planes parallel and perpendicular to the reaction plane. The corrections due to the asymmetry in the array and response of the Clover segments, defined by $a(E_\gamma) = \frac{N_\parallel}{N_\perp}$ were obtained from the ^{152}Eu and ^{133}Ba sources. The data of $a(E_\gamma)$ for different experiments as mentioned in chapter one (table 1.1) and their fitting are shown in Fig. 3.13(a)-Fig. 3.13(e), respectively. The values of $a(E_\gamma)$ for different experiments have been tabulated in Fig. 3.13(f). We have performed integrated polarization asymmetry measurement (IPDCO) for γ rays in ^{134}Cs, from the data obtained in the second experiment. A positive value of IPDCO ratio indicates an electric transition where as a negative value favors a magnetic transition. The low energy cut off for the polarization measurement was about 200 keV throughout the present work. For the (IPDCO) analysis the data from the 90° detectors were used, since the polarization sensitivity is maximum at $\theta = 90°$. The parallel ($N_{\parallel}$) and perpendicular (a(E_γ)*$N_\perp$) counts for the two γ rays in ^{194}Tl are shown in Fig. 3.14. It shows that the magnetic (404-keV) and the electric (687-keV) transitions can easily be identified.

3.6.4 Deduced quantities for rotational bands

To characterize a rotational band one needs to deduce the quantities, like rotational frequency, moments of inertia, aligned angular momentum and routhian energies etc. from the level scheme. The **rotational frequency**, for an axially symmetric deformed nucleus which rotates about an axis (x) perpendicular to the symmetry axis, can be written as [26],

$$\hbar\omega(I) = \frac{dE(I)}{dI_x} \approx \frac{E(I+1) - E(I-1)}{I_x(I+1) - I_x(I-1)}, \tag{3.12}$$

$$\approx \frac{E_\gamma}{2}(I \gg K), \tag{3.13}$$

in analogy with a classical rotor. Where I_x is the projection of the total angular momentum onto the rotation axis and is given by:

$$I_x(I) = \sqrt{I(I+1) - K^2} \approx \sqrt{\left(I + \frac{1}{2}\right)^2 - K^2}. \tag{3.14}$$

K is the projection of the total angular momentum onto the symmetry axis. The value of K is, normally, set equal to the bandhead spin for strongly coupled band.

Two moments of inertia are defined for deformed nucleus: kinematic moment of inertia and dynamic moment of inertia. The **Kinematic moment of inertia** is defined as,

$$J^{(1)} = \frac{\hbar I_x(I)}{\omega(I)}. \tag{3.15}$$

and the **Dynamic moment of inertia** is defined as,

$$J^{(2)} = \frac{\hbar dI_x(I)}{d\omega(I)}, \tag{3.16}$$

$$\approx \frac{4}{\Delta E_\gamma}\hbar^2 MeV^{-1}, \tag{3.17}$$

for even-even nuclei. The dynamic moment of inertia, $J^{(2)}$, is independent of spin, I. This property is very useful in cases where spin and parity of a given rotational band are not known (e.g for superdeformed bands).

The **experimental aligned angular momentum**, i_x, the single particle contribution to the nuclear angular momentum, is given by,

$$i_x = I_x(I) - I_x^{ref}(I). \tag{3.18}$$

where,

$$I_x^{ref}(I) = \Im_0\omega + \omega^3\Im_1 \tag{3.19}$$

is the reference angular momentum of the core and is calculated in terms of the Harris parameters [27]. $\Im_0$ and $\Im_1$ are the Harris parameters. These Harris parameters, can be determined by fitting the experimental points in the I_x versus ω plot.

The **experimental Routhian** (sigle-particle) is defined by,

$$e^{\omega}_{expt}(I) = E^{\omega}_{expt}(I) - E^{\omega}_{ref}(I) \tag{3.20}$$

where,

$$E^{\omega}_{expt}(I) = \frac{1}{2}\left[E(I+1) + E(I-1)\right] - \omega(I)I_x(I) \tag{3.21}$$

and the reference is given by

$$E^{\omega}_{ref}(I) = -\frac{1}{2}\omega^2\Im_0 - \frac{1}{4}\omega^4\Im_1 + \frac{1}{8\Im_0}. \tag{3.22}$$

The experimentally obtained values of the above alignments and Routhians can be directly compared with the values obtained in theoretical calculations.

Bibliography

[1] Gamma Sphere Online Booklet (nucalf.physics.fsu.edu/∼riley/gamma/).

[2] Ali Al-Khatib's Thesis (High-Spin γ-Ray Spectroscopy of ^{124}Ba, ^{124}Xe and ^{125}Xe).

[3] G.F. Knoll, Radiation Detection and Measurement.

[4] S.L. Shepherd et al., Nucl. Instrum. Methods Phys. Res. **A 434**, 373 (1999).

[5] A. Chatterjee, Priv. comm. (2001); http://www.tifr.res.in/∼pell/lamps.html.

[6] R. Raut et al., Proc. DAE-BRNS Symp. Nucl. Phys. **47B**, 578 (2004).

[7] S. Venkataramanan et al., Proc. DAE-BRNS Symp. Nucl. Phys. **52**, 149 (2007).

[8] S. Muralithar et al., Nucl. Instrum. Methods Phys. Res. **A 622**, 281 (2010).

[9] E.T. Subramanium et. al., Rev. Sci. Instr. **79**, 103503 (2008).

[10] E.T. Subramanium et. al., Rev. Sci. Instr. **77**, 096102 (2006).

[11] Kusum Rani, IUAC Annual Report 2003-2003, 43.

[12] Ajit Kumar et. al., Proc. on DAE-BARNS Symposium on Nucl. Phys. **44B**, 390 (2001).

[13] R. Palit, Proc. DAE Symposium on Nuclear Physics, BITS Pillany, Rajasthan, India, Vol. **55**, I11 (2010).

[14] R. Palit, AIP Conf. Proc. **1336**, 573 (2011).

[15] R. Palit et al., Nucl. Instrum. Methods Phys. Res. **A 680**, 90 (2012).

[16] H. Tan et al., Nuclear Science Symposium Conference Record, NSS 08, IEEE, p 3196 (2008).

[17] Deepak Pandit et al., Nucl. Instrum. Methods Phys. Res. **A 624**, 148 (2010).

[18] R.K. Bhowmik et al., Proc. DAE Symp. Nucl. Phys. **44B**, 422 (2001).

[19] D. C. Radford Nucl. Instrum. Methods Phys. Res. **A 361**, 297 (1995).

[20] H. Morinaga and T. Yamazaki, In-beam gamma-ray spectroscopy (North-Holland Pub. Co., Amsterdam, 1976).

[21] A. Krämer-Flecken et al., Nucl. Instrum. Methods Phys. Res. **A 275**, 333 (1989).

[22] M. Piiparinen et al., Nucl. Phys. **A 605**, 191 (1996).

[23] N. S. Pattabiraman et al., Phys. Rev. **C 65**, 044324 (2002).

[24] K. Starosta et al., Nucl. Instrum. Meth. Phys. Res. **A 423**, 16 (1999).

[25] Ch. Droste et al., Nucl. Instrum. Meth. Phys. Res. **A 378**, 518 (1996).

[26] R. Bengtsson and S. Fraunendorf, Nucl. Phys. **A 327**, 139 (1979).

[27] S.M. Harris, Phys. Rev. **138** B509 (1965).

Chapter 4

High spin band structures in doubly-odd ^{194}Tl

4.1 Introduction

The nuclei near A $\sim$ 190 in the Pb (Z = 82) region are known for rich variety of structural phenomena and very interesting shape properties. The shape of a nucleus in this region depends largely on the position of the Fermi levels and on the proximity of the shell closures and the shape driving effects of the levels. The thallium nuclei with proton number $Z = 81$ are situated in a transition region between the deformed prolate rare earth nuclei and the spherical lead nuclei at $Z = 82$. The heavy mass thallium nuclei, with proton and neutron Fermi levels close to the spherical shell gaps $Z = 82$ and $N = 126$, respectively, are spherical in the ground state with the ground state spin-parity as $1/2^+$ [1, 2, 3] corresponding to the proton hole in $3s_{1/2}$ orbital. However, low lying $9/2^-$ isomeric states are observed in odd-A thallium isotopes in A = 190 region; the excitation energy of which increases with the increase in the neutron number from N = 110 to N = 118 [4]. The strongly coupled rotational bands based on this isomer were interpreted as arises due to the intruder π $9/2^-$[505] Nilsson state originating from the $h_{9/2}$ proton orbital with oblate deformation [5, 6, 7, 8]. On the other hand, decoupled $i_{13/2}$

neutron bands have been identified in odd-A Hg (Z = 80) isotopes in this A = 190 mass region [9, 10]. Therefore, in even-mass Tl isotopes in this region, collective rotational bands based on the $\pi h_{9/2} \otimes \nu i_{13/2}$ configuration are expected. Indication of such bands have been found in a few odd-odd Tl isotopes in this mass region [11, 12, 13, 14, 15, 16]. But, in most cases there are ambiguities on level energies, spins, and parities. Recently, the experimental studies on the structures of ^{190}Tl [11] and ^{198}Tl [17] have been reported with unambiguous assignment of spin and parities of the above band. These studies indicate interesting properties of the $\pi h_{9/2} \otimes \nu i_{13/2}$ bands, like chiral symmetry breaking in ^{198}Tl and low spin signature inversion in ^{190}Tl. The high spin data on the other odd-odd Tl nuclei are scarce. The high spin states in ^{194,196}Tl were studied more than 30 years ego [13, 14]. Although, the indication of rotational bands based on the $\pi h_{9/2} \otimes \nu i_{13/2}$ configuration was reported in these studies, no definite spin-parity assignments could be done. In all these nuclei, the $\pi h_{9/2} \otimes \nu i_{13/2}$ band is known only upto about 16^- except for ^{196}Tl in which it was extended tentatively up to $(20+I_o{}^-)$ spin. A structural change, most likely a pair alignment, seems to take place above 16^- in these nuclei but it could not be characterized well because of the lack of information.

Moreover, in the Tl isotopes, in this mass region, both the protons and the neutrons occupy the high-j orbitals. So, different kinds of collective and single particle excitations, like magnetic rotation [18, 19] and chirality, are expected to develop for non-axial deformation. The total routhian surface (TRS) calculations for ^{190}Tl and ^{198}Tl show nearly oblate shapes, with triaxiality parameter $\gamma \sim -60^o$, for the $\pi h_{9/2} \otimes \nu i_{13/2}$ configuration in these nuclei [11, 17]. However, the side band in ^{198}Tl, with the features of chiral bands, was interpreted in the two-quasiparticle plus rotor model with a non-axiality of $\gamma = 44^o$ [17]. Therefore, detailed experimental as well as theoretical investigations are required for the understanding of the structure of the bands based on the $\pi h_{9/2} \otimes \nu i_{13/2}$ configuration in the odd-odd Tl nuclei.

In this work, we have studied the spectroscopy of ^{194}Tl with an aim, in particular, to study the nature of the band built on the $\pi h_{9/2} \otimes \nu i_{13/2}$ configuration and to search for a possible magnetic rotational band. The high spin level structures in ^{194}Tl were studied by Kreiner et al. [13] using ^{18}O beam on ^{181}Ta target. The level scheme of ^{194}Tl was obtained, in that work, using two Ge(Li) detectors. The observed band structure was interpreted to be based on the $\pi h_{9/2} \otimes \nu i_{13/2}$ configuration but the information was limited to a few energy levels up to $\sim$ 2 MeV with uncertain spin-parity and level energy assignments. Possible observation of chiral partner bands in ^{194}Tl has been claimed recently [20] but no such level scheme has been reported yet.

4.2 Experimental Method and Data Analysis

The γ-ray spectroscopy of ^{194}Tl has been studied at the 14-UD BARC-TIFR Pelletron at Mumbai, India using the Indian National Gamma Array (INGA) with 15 Clover detectors at the time of the experiment. The excited states of ^{194}Tl were populated by fusion-evaporation reactions ^{185,187}Re(^{13}C, xn)^{194}Tl at 75 MeV of beam energy. The target was a thick (18.5 mg/cm^2) natural rhenium target. The recoils were stopped inside the target. The isotopic ratio of ^{185}Re and ^{187}Re in the natural rhenium is 37:63. According to the PACE-IV calculations, the 4n and 5n channels are the dominant ones at the beam energies encompassed inside the target in this experiment. The energy loss of the beam inside the target was calculated as 17 MeV. Therefore, the beam energy at the exit of the target would be below the Coulomb barrier. Hence, all the recoils, produced in this experiment, were stopped inside the target. The clover detectors were arranged in six angles with 2 clovers each at $\pm 40^\circ$ and $\pm 65^\circ$ while four clovers were at 90° and three were at -23° angles. A digital data acquisition (DDAQ) system (described in Section 3.5.4), with 112 channels based on Pixie-16 modules developed by XIA LLC [21] has been used. About 2.4×10^9 such coincidence events were recorded in this experiment.

E_γ-E_γ matrix and E_γ-E_γ-E_γ cube have been constructed from the collected γ-γ coincidence data. To construct these, a coincidence window of $\pm$400 ns was selected. The clover detectors were calibrated for γ-ray energies and efficiencies by using the ^{133}Ba and ^{152}Eu radioactive sources. Single and double gated γ-ray spectra from the E_γ-E_γ matrix and E_γ-E_γ-E_γ cube are shown in Figs. 4.1 and 4.2, respectively. The relevance of these spectra in the level scheme has been discussed in the next section. The intensities of the gamma rays were obtained from the E_γ-E_γ matrix using a single gated spectrum.

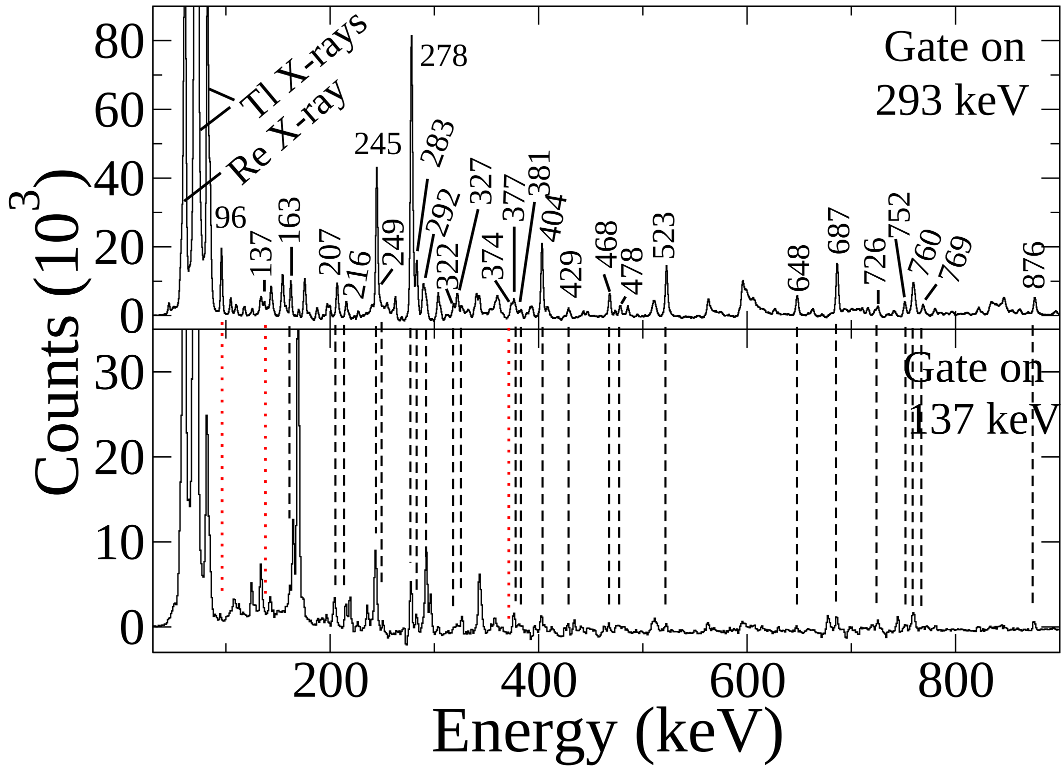

Figure 4.1: Coincidence spectra by gating on 293-keV (top) and 137-keV (bottom) γ transitions. The unmarked peaks are the contaminants.

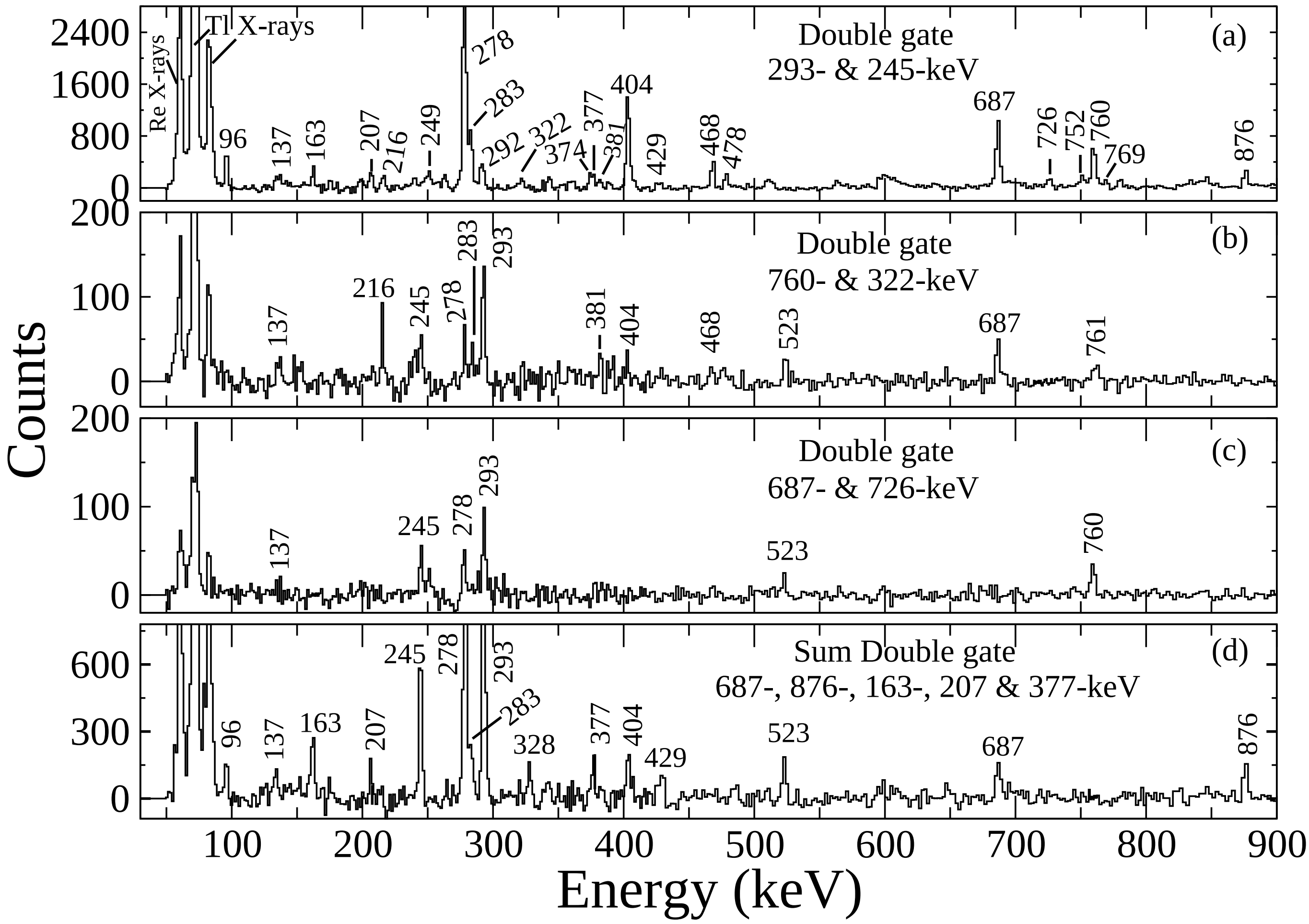

Figure 4.2: Coincidence spectra corresponding to a double gate of (a) 293-& 245-keV, (b) 760- & 322-keV, (c) 687- & 726 keV and (d) a sum double gated spectra corresponding to the transitions in ^{194}Tl.

The multipolarities of the γ-ray transitions have been determined from an angular correlation analysis using the method of directional correlation from the oriented states (DCO) ratio. For the DCO ratio analysis, the coincidence events were sorted into an asymmetry matrix with data from -23° detectors on one axis and 90° detectors on the other axis. The validity of the DCO ratio measurements was checked with the known transitions in ^{194}Tl and with the calculated values. In the present geometry, the value of DCO ratio calculated [22] for a pure dipole transition gated by a stretched quadrupole transition is 1.65 and for a quadrupole transition gated by a pure dipole, the calculated value is 0.61. These compare well with the experimental values of 1.69(3) and 0.58(2), respectively, for the known pure dipole (293-keV, E1) and stretched quadrupole (687-keV and 648-keV, E2) transitions.

Definite parities to the excited states have been measured from the integrated polarization asymmetry (IPDCO) ratio, as described in section 3.6.3, from the parallel and perpendicular scattering of a γ-ray photon inside the detector medium. The correction due to the asymmetry in the array and response of the Clover segments, defined by $a(E_\gamma) = \frac{N_\parallel}{N_\perp}$, was checked using ^{152}Eu and ^{133}Ba sources and was found to be 1.004(1), which is close to unity, as expected. By using the fitted parameter a(E_γ), the Δ_{IPDCO} of the γ rays in ^{194}Tl have been determined. The Δ_{IPDCO} could not be measured for the low energy and weaker transitions. The low energy cut off for the polarization measurement was about 200 keV. The validity of the method of the IPDCO measurement was confirmed from the known transitions in ^{194}Tl.

4.2.1 Experimental Results

The level scheme of ^{194}Tl, as obtained in the present work, is shown in Fig. 4.3. A total of 19 new γ rays have been found and placed in the level scheme. They are marked with asterisks (*) in the level scheme of Fig. 4.3. The deduced excitation energy, spin, and parity of the excited levels and the multipolarity of the γ rays, together with other relevant information concerning their placement in the proposed level scheme, are summarized in Table 4.1.

Table 4.1: Energies (E_γ), intensities (I_γ), DCO ratios (R_{DCO}), IPDCO ratios (Δ_{IPDCO}) and deduced multipolarities of the γ rays in ^{194}Tl. The energies of initial states (E_i) and spins and parities of initial (J_i^π) and final (J_f^π) states are also given.

E_γ (in keV)	E_i (in keV)	$J_i^\pi \rightarrow J_f^\pi$	I_γ[1]	R_{DCO} (Err)	Δ_{IPDCO} (Err)	Deduced Multipolarity
96.1(1)	430.0	$10^- \rightarrow 9^-$	5.95(9)	1.59(17)[2]	-	M1+E2
136.9(2)	430.0	$10^- \rightarrow 8^-$	2.73(6)	0.96(14)[2]	-	E2
162.5(1)	2679.0	$17^- \rightarrow 16^-$	2.24(4)	1.67(20)[2]	-	M1
207.1(1)	2886.1	$18^- \rightarrow 17^-$	2.16(4)	1.72(18)[2]	-	M1
215.5(2)	3698.6	$20^{(-)} \rightarrow 19^{(-)}$	1.40(2)	1.51(14)[2]	-	M1+ E2
244.9(1)	953.2	$12^- \rightarrow 11^-$	14.92(41)	1.61(5)[2]	-0.10(2)	M1(+E2)
248.6(3)	3125.5	$18^- \rightarrow 17^-$	0.94(2)	1.64(19)[2]	-0.13(10)	M1+E2
278.4(1)	708.4	$11^- \rightarrow 10^-$	41.86(62)	1.62(3)[2]	-0.14(1)	M1(+E2)
283.2(1)	1640.0	$14^- \rightarrow 13^-$	10.00(15)	1.85(14)[3]	-0.24(4)	M1(+E2)
291.9(2)	2399.6	$16^- \rightarrow 15^-$	3.06(7)	1.46(10)[4]	-	M1+E2
293.1(1)	293.1	$8^- \rightarrow 7^+$	100.0(4)	1.69(3)[2]	0.07(2)	E1
322.2(1)	3483.0	$19^{(-)} \rightarrow 18^{(-)}$	2.04(6)	1.13(9)[4]	-	M1+E2
327.7(2)	3213.8	$19^- \rightarrow 18^-$	3.37(5)	1.71(23)[2]	-0.25(6)	M1
373.8(2)	708.4	$11^- \rightarrow 9^-$	1.17(4)	0.95(14)[2]	-	E2
376.9(1)	3590.7	$20^- \rightarrow 19^-$	1.91(5)	1.67(21)[2]	-0.22(8)	M1
381.3(2)	4079.8	$(21^-) \rightarrow 20^{(-)}$	0.40(4)	-	-	-
403.5(1)	1356.7	$13^- \rightarrow 12^-$	12.67(19)	1.85(5)[4]	-0.05(2)	M1+E2
428.6(2)	4019.3	$21^- \rightarrow 20^-$	1.03(2)	1.69(37)[2]	-	M1
468.4(1)	2108.5	$15^- \rightarrow 14^-$	4.13(7)	1.50(7)[2]	-0.20(8)	M1+E2
478.3(2)	2877.6	$17^- \rightarrow 16^-$	1.70(3)	1.73(24)[2]	-0.13(10)	M1+E2
523.1(1)	953.2	$12^- \rightarrow 10^-$	11.87(18)	0.68(2)[4]	0.08(3)	E2

Table 4.1: Continued...

E_γ (in keV)	E_i (in keV)	$J_i^\pi \to J_f^\pi$	I_γ [1]	R_{DCO} (Err)	Δ_{IPDCO} (Err)	Deduced Multipolarity
648.3(1)	1356.7	$13^- \to 11^-$	5.42(8)	0.65(4) [4]	0.39(5)	E2
686.7(1)	1640.0	$14^- \to 12^-$	13.62(20)	0.58(2) [4]	0.08(4)	E2
725.8(3)	3125.5	$18^- \to 16^-$	2.27(6)	0.57(6) [4]	-	E2
751.8(2)	2108.5	$15^- \to 13^-$	3.80(6)	0.54(4) [4]	0.27(8)	E2
759.5(2)	2399.6	$16^- \to 14^-$	10.84(24)	1.03(14) [5]	0.30(10)	E2
761.1(2)	3160.8	$18^{(-)} \to 16^-$	10.23(43)	0.58(9) [6]	-	E2
769.1(2)	2877.6	$17^- \to 15^-$	3.87(6)	0.68(3) [4]	0.07(4)	E2
876.4(1)	2516.4	$16^- \to 14^-$	6.90(11)	0.67(4) [4]	0.11(3)	E2

The level scheme of ^{194}Tl has been extended upto an excitation energy of $\sim$ 4.1 MeV and $(21^-)\hbar$ spin in the present work and is a much improved one compared to its previously known level scheme reported in Ref. [13]. The 2^- ground state (not shown in Fig. 4.3) and the 7^+ isomeric state, ($T_{1/2}$ = 32.8 min) in this nucleus, were known from the beta decay studies [11]. No γ-ray transition was known to decay from the isomeric state. The excitation energy of this state was also not known. Both the ground and the isomeric states decay by electron capture decay. The excitation energies of the states in the level scheme presented in Fig. 4.3 have been given with respect to the isomeric state as was presented in Ref. [11, 17] for ^{190,198}Tl. The proposed level scheme is based on the following arguments.

A 293-keV γ ray from the 8^- to the 7^+ isomeric state in ^{194}Tl was known, from the systematic of the Tl isotopes, to be a hindered $E1$ transition. The DCO ratio and the positive value of the IPDCO ratio, obtained in the present work, confirm this assignment. A 137-keV γ ray has

[1] Relative γ ray intensities normalized to 100 for the 293.1-keV γ-ray.
[2] From the 686.7 keV (E2) DCO gate;
[3] From the 648.3 keV (E2) DCO gate;
[4] From the 293.1 keV (E1) DCO gate;
[5] From the 725.8 keV (E2) DCO gate;
[6] From the 468.4 keV (M1) DCO gate;

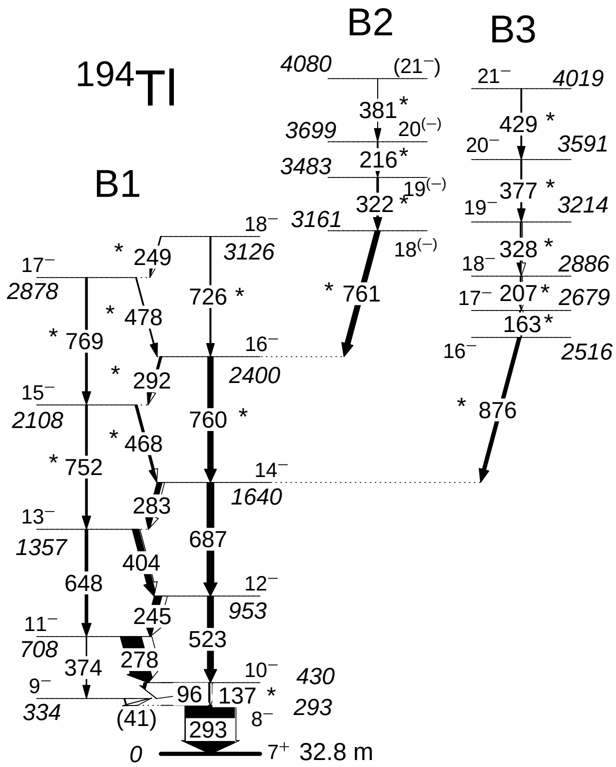

Figure 4.3: Level scheme of ^{194}Tl obtained from this work. The new γ-rays are indicated by asterisks.

been observed in the present work which is in coincidence with the known 293-keV transition from the 8^- to the 7^+ state, as can be seen from Fig. 4.1 (top panel). A spectrum gated by this 137-keV γ lines, shown in the bottom panel of Fig. 4.1, shows all the γ rays in ^{194}Tl present in the 293-keV gated spectrum, except for the lines at 96 keV and 374 keV. This γ ray is also observed in the double gated spectra shown in Fig. 4.2. This clearly indicates that there is a 137 keV γ-ray transition above the 293-keV transition and in parallel to the 96-keV transition. It establishes the 334-keV level as the previously unknown energy upon which the rest of the band is built. The DCO ratio for the 137-keV γ ray has been measured in this work gated by the 687-keV γ ray, which was known to be a quadrupole ($E2$) transition [13]. The value of this ratio comes out to be close to unity (see Table 4.1), indicating the stretched quadrupole nature of the 137-keV transition. Although, the energy of this γ ray is too low for the IPDCO measurement, the $M2$ assignment for this low-energy transition may be completely ruled out from the lifetime consideration. Therefore, by considering the 137-keV γ ray as an

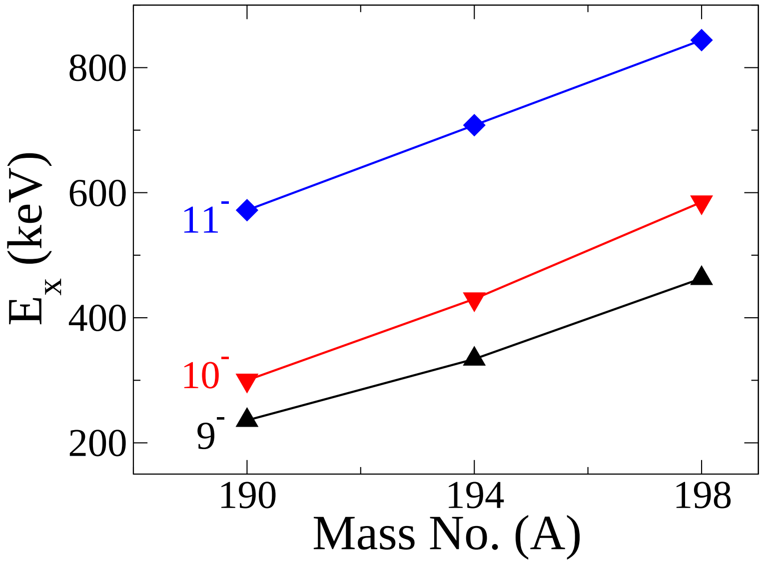

Figure 4.4: Excitation energies of the 9^-, 10^- and 11^- states in odd-odd isotopes of Tl as a function of mass No. A. Only the data for those isotopes are plotted for which the definite excitation energies are known with respect to the 7^+ isomeric state.

$E2$ transition, the spin and parity of the 430-keV level has been assigned, in this work, as 10^-. The 374-keV γ ray was reported as a tentative one in Ref.[13]. The double gated spectrum of 293- and 245-keV shown in Fig. 4.2(a) has a peak at 374 keV which confirms its placement. The $E2$ nature of this transition is also evident from the measured R_{DCO} value (close to unity) gated by a known $E2$ transition. The placement of the above γ rays indicates that there should be a 41-keV transition from the 9^- to the 8^- state. This low energy highly converted ($\alpha \sim 200$) transition has not been observed in this work as our experimental set up was not suited to detect such transitions.

With these placements, the excitation energy of the states above 8^- has been established (with respect to 7^+ isomeric state) and a comparison with the level scheme of ^{190,198}Tl can be made. The excitation energies of the 9^-, 10^- and 11^- states in ^{194}Tl compare well with those in ^{190,198}Tl as shown in Fig. 4.4. The smooth variation of increasing energies of these states with the mass no. A indicates that the placement of the new low lying transitions in ^{194}Tl, in the present work, satisfies the systematic behaviour of the excitation energies of the Tl isotopes.

All the γ rays reported in ref.[13] have been observed in the present work up to the 1640-keV state. The 741.9-, 458.6-, and 289.4- keV γ rays, reported in ref.[13] and placed above 1640-keV state, were not observed in our data. Instead, we have observed the cascade of 468-, 292-, 478- and 249-keV M1+E2 γ-rays above the 1640-keV state along with the cross-over E2 transitions. It may be pointed out that a more efficient experimental set up was used in the present work than in the earlier work. With these transitions, the ground state band B1 has been extended upto an excitation energy of 3.13 MeV and spin of $18\hbar$.

We have also observed two other band like structures B2 and B3, for the first time in ^{194}Tl. They are placed above the 16^- and 14^- states of the ground band B1, respectively. The γ lines belonging to these bands have been seen in the single and double gated spectra shown in Fig. 4.1 and Fig. 4.2(a). The double gate on 760- and 322-keV of band B2 (Fig. 4.2(b)) shows clearly the 761-keV γ ray, indicating its double placement. The 687-keV line is observed in this spectrum but not the 726-keV line. The 216- and the 381-keV γ rays, belonging to this band, are also observed in this spectrum. The double gated spectrum of 687- and 726-keV (Fig. 4.2(c)) shows the 760-keV line, slightly lower in energy than the one in Fig. 4.2(b). Therefore, the higher energy transition (i.e 761-keV) of the 760-keV doublet corresponds to the linking transition between the bands B2 and B1 and hence, the lower energy transition (i.e 760-keV) of the doublet corresponds to the member of the band B1. The 216-, 322- and 381-keV γ rays are not observed in the spectrum of Fig. 4.2(c) and therefore, they form the members of the band B2.

To get an unambiguous value of the DCO ratios for the 760-and 761-keV transitions, the gating transitions were selected carefully. The DCO ratio values of the doublet can not be distinguished for any choice of a pure E2 transitions, below the 14^- level, as a gating transition. However, in the 468-keV and 292-keV gate, the 760-keV transition (in band B1) would be absent and an unambiguous value of the DCO ratio can be obtained for the 761-keV linking transition. But the 292-keV would be contaminated by the strong 293-keV ground state transition. On the other hand, there is no contamination in 468-keV γ ray and, moreover, the negative value of the IPDCO ratio indicates that the 468-keV transition is an M1 transition with very little E2 admixture, if any. So, the 468-keV gate was chosen to obtain the DCO ratio of the 761-

keV linking transition and similarly, the 726-keV E2 transition has been chosen to obtain the DCO ratio value of the 760-keV in-band transition. The DCO ratios of the 760- and 761-keV transitions, obtained in this way, suggest that both of them are quadrupole transitions. The IPDCO ratio measurement of the in-band 760-keV transition, clearly suggests that it is an E2 transition. The IPDCO ratio could not be obtained for the 761-keV transition and an E2 character for this linking transition has been assumed to assign the parity of band B2, tentatively, as negative. The M2 character, for the 761-keV transition could not, however, be ruled out and, hence, the parity of band B2 could be positive as well. Lifetime measurement of the $18^{(-)}$ state is necessary to overcome this ambiguity. The weisskopf estimate of the halflives corresponding to E2 and M2 character of this transition would be $\sim$ 50 pico-sec and $\sim$ 5 ns, respectively. In the present work, we could not distinguish these two.

The 876-keV γ ray is observed in the double gated spectrum in Fig. 4.2(a) but not in the double gated spectra in Fig. 4.2(b) or 4.2(c). This shows that the 876-keV γ ray must decay to the 14^- state of band B1. This γ ray could be observed with any combination of double gates below the 1640-keV level but was not observed with any γ ray above this level. This indicates that the 876-keV γ ray must decay to the 14^- state of the band B1. The cascade of γ rays in band B3 has been observed in Fig. 4.2(a). A sum double gated spectrum constructed from the combination of the 687-, 876-, 163-, 207 & 377-keV γ rays is shown in Fig. 4.2(d). This spectrum clearly shows the 163-, 207-, 328-, 377- & 429-keV γ rays belonging to this band. The E2 nature of the 876-keV γ ray is evident from its DCO and IPDCO ratios. Therefore, the bandhead of band B3 has been assigned as 16^-. The ordering of the γ rays in this band are based on their intensities. The spins and parities of the states in this band are assigned from the measured DCO and IPDCO ratios of the transitions wherever possible. The IPDCO ratios could be measured only for the 328- and the 377-keV transitions in this band. The negative values of the IPDCO ratios for these two transitions together with their R_{DCO} values give clear evidence that they are predominantly M1 in nature. The IPDCO ratios could not be obtained for the other transitions in this band because of their low energies (163- and 207-keV) or low intensities (429-keV). However, the R_{DCO} values of these transitions are very close to the calculated values for pure dipole transitions. Moreover, since these γ rays are in-band with the 328- and the 377-keV M1 transitions, so, we have assigned M1 nature for all the γ rays in this band.

4.3 Discussion

The ground state of the odd-A Tl isotopes are $1/2^+$, corresponding to the $3s_{1/2}$ orbital near the proton Fermi level. In the isotone ^{193}Hg, the experimentally observed $5/2^-$ and $13/2^+$ states lie very close (within 40- and 141-keV, respectively) to the $3/2^-$ ground state [24]. These states correspond to the $f_{5/2}$, $i_{13/2}$, and $p_{3/2}$ orbitals, respectively, near the neutron Fermi level. Correspondingly, the configurations of the ground state (2^-) and the 7^+ isomeric state in odd-odd ^{194}Tl have been attributed to $\pi s_{1/2} \otimes \nu p_{3/2}$ and $\pi s_{1/2} \otimes \nu i_{13/2}$, respectively. The 8^- state, at an excitation energy of 293-keV, in this nucleus, has been interpreted as the band head of the $\pi h_{9/2} \otimes \nu i_{13/2}$ configuration [13]. These orbitals lie near the proton and the neutron Fermi levels of ^{194}Tl for an oblate deformation. Since this is associated with the excitation of the odd-proton from the $s_{1/2}$ orbital to $h_{9/2}$ orbital, therefore, the systematic behavior of the energy difference between the $1/2^+$ and the $9/2^-$ states ($\Delta E_{9/2^- \rightarrow 1/2^+}$) in odd-A Tl nuclei should be similar to the energy difference between the 8^- and the 7^+ states ($\Delta E_{8^- \rightarrow 7^+}$) in odd-odd Tl nuclei, as a function of neutron number or mass number. The similarity between these differences is evident from the plot shown in Fig. 4.5. Rotational bands based on the same configuration have also been observed in the neighboring odd-odd Tl nuclei.

The alignments (i_x) for band B1 in ^{194}Tl has been shown in Fig. 4.6 as a function of rotational frequency $\hbar\omega$. The alignments for the neighboring odd-A nuclei ^{193}Tl and ^{193}Hg are also shown in Fig. 4.6 which have been deduced from the corresponding level schemes reported by Reviol et al. [27] and Hubel et al. [10], respectively. It can be seen that the band in ^{194}Tl has an initial alignment of about $5\hbar$. This value is in good agreement with the value obtained from the initial alignments of the neighboring odd-A nuclei using the additivity rule [25, 26]. This supports the assigned conguration of the band B1 as $\pi h_{9/2} \otimes \nu i_{13/2}$.

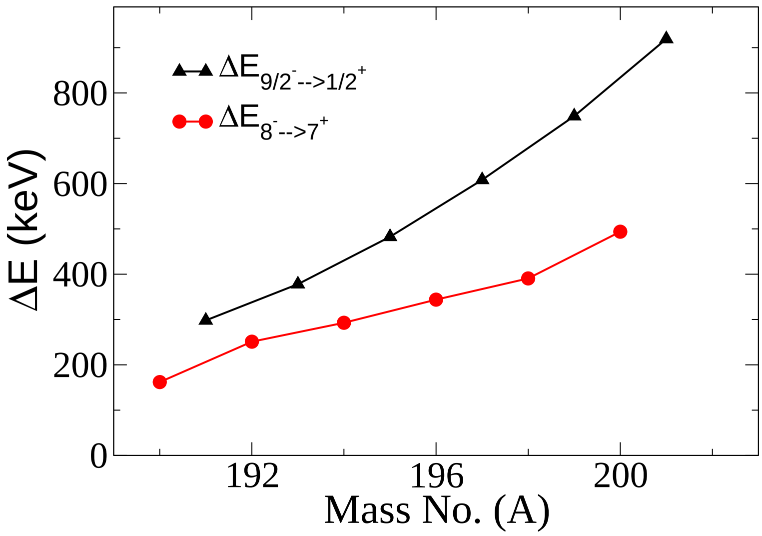

Figure 4.5: Systematic of the energy difference between the $1/2^+$ & the $9/2^-$ states ($\Delta E_{9/2^- \to 1/2^+}$) in odd-A Tl and between the 8^- & the 7^+ states ($\Delta E_{8^- \to 7^+}$) states in odd-odd Tl nuclei as a function of mass no. A.

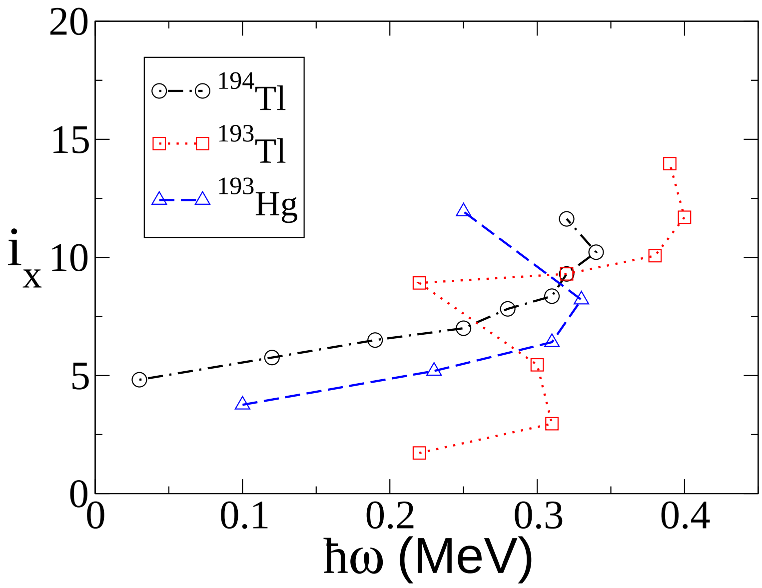

Figure 4.6: Experimental alignments (i_x) as a function of the rotational frequency ($\hbar\omega$) for the $\pi h_{9/2}$ band in ^{193}Tl [27], $\nu i_{13/2}$ band in ^{193}Hg [10] and band B1 in ^{194}Tl. The Harris reference parameters are chosen to be $J_0 = 8.0\hbar^2\ MeV^{-1}$ and $J_1 = 40\hbar^4\ MeV^{-3}$.

The moment of inertia, $J^{(1)}$ for band B1 in ^{194}Tl and the similar bands in ^{192,196,198}Tl are shown in Fig. 4.7, as a function of the rotational frequency $\hbar\omega$. It can be seen that the moment of inertia are quite similar in these odd-odd Tl isotopes for the above band. This indicates similar deformation for these nuclei. It can also be seen that the particle alignments in these isotopes are also taking place at about similar frequency. The band B1 in ^{194}Tl, in the present work, could be extended just beyond the band crossing at $\hbar\omega_c \sim 0.34$ MeV.

The band crossing in the odd-odd Tl isotopes can be understood from the band crossings in the even-even core of Hg isotopes and the band crossings in the odd-A Tl isotopes. In ^{192}Hg [10], the first two observed band crossings, at $\hbar\omega_{c1} \sim 0.210$ MeV and at $\hbar\omega_{c2} \sim 0.362$ MeV, were interpreted as due to the alignments of the $i_{13/2}$ neutrons (G $\rightarrow$ AB & AB $\rightarrow$ ABCD crossing, following the nomenclature of Hubel et al [10]). The alignment of protons take place at even higher frequency. The band crossings in odd-Z ^{193}Tl, in which the first proton crossing is blocked, were also interpreted as due to the alignments of the same $i_{13/2}$ neutrons. The crossing frequency of $\hbar\omega_c \sim 0.34$ MeV in ^{194}Tl agrees well with the $\hbar\omega_{c2}$ value in ^{192}Hg. Therefore, the observed band crossing in doubly-odd ^{194}Tl may be attributed to the alignment of neutrons in the $i_{13/2}$ orbital. The similarity and the systematic trend of the observed AB $\rightarrow$ ABCD crossing frequencies for the ^{190}Hg ($\hbar\omega_{c2} \sim 0.352$ MeV), ^{192}Hg ($\hbar\omega_{c2} \sim 0.362$ MeV) and ^{194}Hg ($\hbar\omega_{c2} \sim 0.348$ MeV) [10] are also in good agreement with the crossing frequencies of the ^{192}Tl ($\hbar\omega_c \sim 0.32$ MeV), ^{194}Tl ($\hbar\omega_c \sim 0.34$ MeV) and ^{196}Tl ($\hbar\omega_c \sim 0.31$ MeV).

A low spin signature inversion has been observed in the rotational bands in odd-odd nuclei involving high-j configurations. In particular, the signature inversion has been reported for the prolate deformed odd-odd nuclei in the rare earth region with a $\pi h_{9/2} \otimes i_{13/2}$ configuration [28]. In the A $\sim$ 190 region, the low-spin signature inversion for a band associated with the oblate $\pi h_{9/2} \otimes i_{13/2}$ configuration has been observed for the first time in ^{190}Tl [11]. In the present work, similar inversion has been observed for the above band in ^{194}Tl as well. The signature inversion in a band can be identified experimentally in the plot of energy staggering, defined by $S(I) = [E(I) - E(I-1)]/2I$, where E(I) is the energy of the state with spin I, has been plotted in Fig. 4.8 for the negative parity yrast band of ^{194}Tl along with the same for ^{190,198}Tl. The staggering plots of these three nuclei show remarkably similar behaviour with low-spin

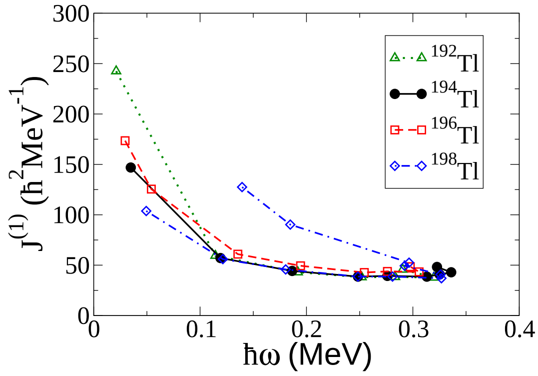

Figure 4.7: Experimental values of the moment of inertia J$^{(1)}$ as a function of the rotational frequency ($\hbar\omega$) for the band B1 in ^{194}Tl are compared with the similar bands in ^{192,196,198}Tl.

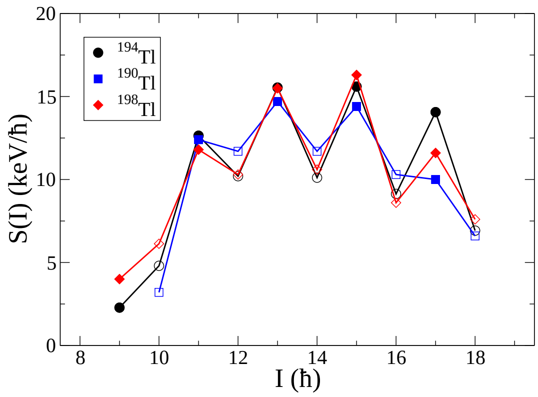

Figure 4.8: The staggering, S(I) = [E(I) - E(I-1)]/2I, plots as a function of spin (I) for the negative parity yrast bands in ^{194}Tl along with those in ^{190,198}Tl.

signature inversion at the same spin value of $11\hbar$. The J-dependent residual $p-n$ interaction was used to interpret the signature inversion in ^{190}Tl. The similarity in the staggering plots suggests that residual $p-n$ interaction remains similar for the heavier odd-odd isotopes of ^{194,198}Tl.

Band B3 in ^{194}Tl is a negative parity band with a band head spin-parity of $16\hbar$ at an excitation energy of 2.5 MeV. This band could be extended up to $21\hbar$ with predominantly M1 transitions. No E2 cross over transitions could be observed in this band. Band B3 starts at an energy which is somewhat higher than the crossing of the 2- and 4-quasiparticle configurations of band B1. Therefore, band B3 seems to be a 6-quasiparticle band with two more protons in the $\pi h_{9/2}$ and $\pi s_{1/2}$ orbitals near the Fermi level. The configuration of the band B3 could, therefore, be assigned as $\pi h^2_{9/2} s^{-1}_{1/2} \otimes \nu i^{-2}_{13/2} p_{3/2}$. The respective proton and neutron orbitals constitute the 2-quasiparticle states in this nucleus at the lower excitation energies (2^- state, 7^+ state and the 8^- band head of band B1). The initial aligned angular momentum of $7\hbar$, deduced for this band, agrees well with the calculated one, assuming the above configuration. The particle-hole configuration of this band with proton particles in high-j, high-Ω and neutron holes in high-j, low-Ω orbitals is favorable for magnetic rotation (MR) and, therefore, the excited states, in this band, may be generated by shears mechanism. This band, with 5 particle-hole pairs, seems to follow the same general features of MR bands [19, 29]. For the MR bands, the level energies (E) and the spin (I) in the band follow the pattern $E(I) - E(I_o) \sim A * (I - I_o)^2$ where, E_o and I_o are the energy and the spin of the band head, respectively. The plot of $E(I) - E(I_o)$ vs $(I - I_o)^2$, for this band is shown in Fig. 4.9. The solid line is the fitting of the data using the above relation. The good fitting of the data clearly indicates that the band B3 closely follows the above relation. By considering a higher limit of the intensity of the unobserved crossover E2 transitions as the level of the background in our data, the lower limit of the B(M1)/B(E2) ratios have been estimated to be $>28\ \mu^2/(eb)^2$. This compares well with the typical value of $\geq 20\ \mu^2/(eb)^2$ for an MR band. The dynamic moment of inertia $J^{(2)} \sim 24\ \hbar^2\ \mathrm{MeV}^{-1}$ obtained for this band is also within the typical value of $J^{(2)} \sim 10 - 25\ \hbar^2\ \mathrm{MeV}^{-1}$ for an MR band. All these indicate that the band B3 is, most likely, an MR band.

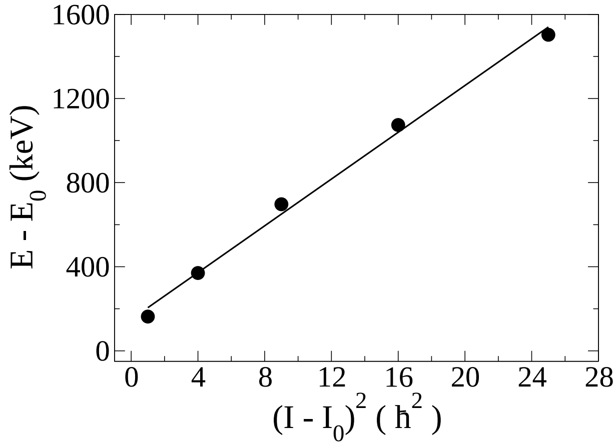

Figure 4.9: Relative energy (E) vs. spin (I) curve for the band B3 built on the 16^- band-head. E_o and I_o are the band head energy and spin, respectively. The fitted curve is shown by the solid lines.

The band like structure B2 lies at an excitation energy of 3.16 MeV with a band head spin of $18\hbar$. The parity of this band remains tentative and this band is also not well developed. Therefore, characterization of this band would be rather premature. However, from the systematic of the odd-A Tl nuclei, it appears that this band may be generated with an additional proton pair in the $i_{13/2}$ orbital with the 4-quasiparticle configuration of the band B1 above its band crossing.

4.3.1 TRS calculations

The Total Routhian Surface (TRS) calculations have been performed for the bands B1 and B3 in ^{194}Tl. The contour plots of the TRS, calculated for ^{194}Tl have been shown in Fig. 4.10. The top panel in this Figure is for the 2-quasiparticle $\pi h_{9/2} \otimes \nu i_{13/2}$ configuration corresponding to band B1 and the bottom panel is for the 6-quasiparticle $\pi h^2_{9/2} s^{-1}_{1/2} \otimes \nu i^{-2}_{13/2} p_{3/2}$ configuration calculated at rotational frequencies of $\hbar\omega = 0.11$ MeV and 0.16 MeV, respectively. This plot clearly shows the minimum of the TRS at a deformation of $\beta_2 \sim 0.15$ and $\gamma \sim -57^o$ for the band B1, indicating an oblate shape for ^{194}Tl in this configuration. The surfaces calculated for the same 2-quasiparticle configurations in ^{196}Tl and in ^{198}Tl are shown in Fig. 4.11. The minima in the routhian surfaces are also found to be at oblate deformation in these two nuclei as well.

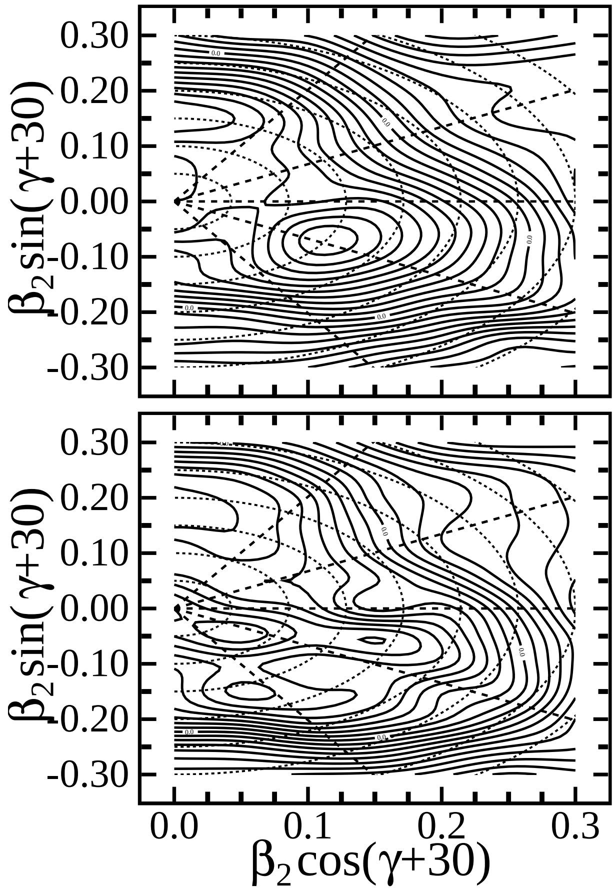

Figure 4.10: Contour plots of the Total Routhian Surfaces (TRS) in the β_2 - γ deformation mesh for the configurations of the bands B1 (top) and B3 (bottom) in ^{194}Tl at rotational frequencies $\hbar\omega = 0.11$ MeV and 0.16 MeV, respectively. The contours are 400 keV apart

The oblate shapes in these nuclei are predicted to persist over a rotational frequency range up to the band crossing. It can be seen from Fig. 4.10 and Fig. 4.11 that the deformations for these neighboring odd-odd Tl isotopes are quite similar. This corroborates well with the similar values of the experimental moment of inertia of these isotopes shown in Fig. 4.7.

The minimum of the TRS for the band B3 in ^{194}Tl (bottom panel in Fig. 4.10) appears at the deformation of $\beta_2 \sim 0.06$ and $\gamma \sim -80^o$. This indicates that this band corresponds to a very small quadrupole deformation β_2 with a triaxial shape. The lack of quadrupole deformation is consistent with the non-observation of E2 transitions and the conjecture of MR nature of this band.

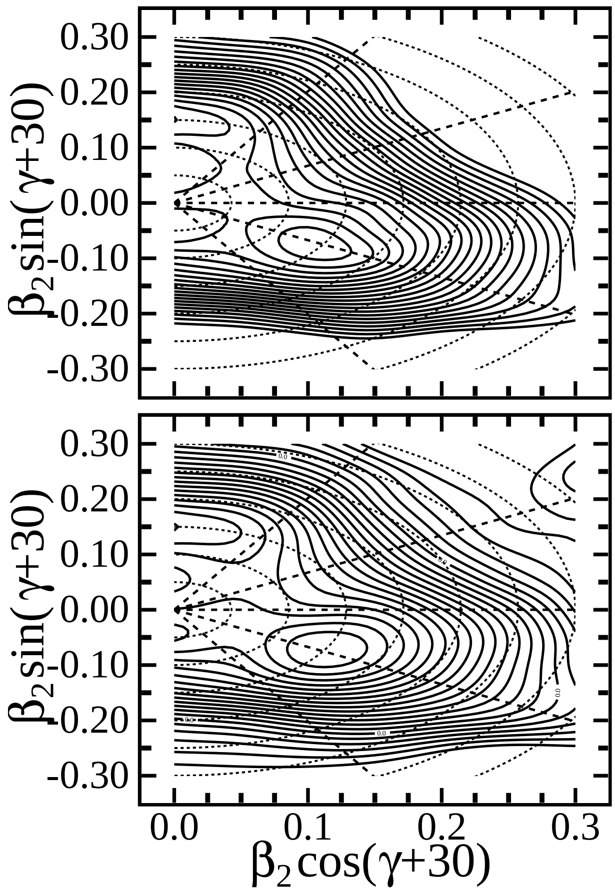

Figure 4.11: Same as Fig. 4.11 but for ^{196}Tl (bottom) and ^{198}Tl (top) in the same configuration as band B1 of ^{194}Tl.

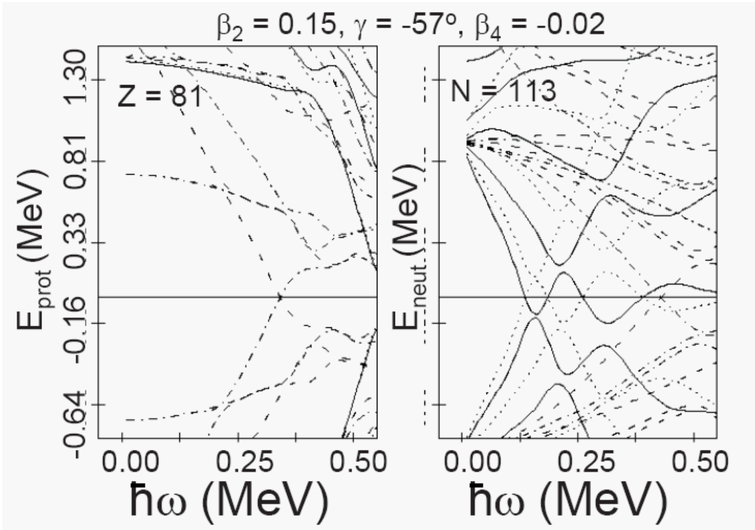

Figure 4.12: Calculated quasiparticle routhians as a function of rotational frequency $\hbar\omega$ for Z = 81 (left) and N = 113 (right) for the deformation $\beta_2 = 0.15$ $\gamma = -57^o$ and $\beta_4 = -0.02$. The quantum numbers (π, α) of the levels are drawn as: solid line (+,+1/2), dotted line (+,-1/2), dash-dotted line(-,+1/2) and dashed line (-,-1/2).

The calculated quasiparticle routhians for protons (Z = 81) and neutrons (N = 113) in ^{194}Tl are shown in the left and right panels, respectively, in Fig. 4.12 for deformation parameters $\beta_2 = 0.15, \gamma = -57^o$, and $\beta_4 = -0.02$ corresponding to the minimum in the TRS in Fig. 4.10. These calculations predict the first neutron pair alignment (AB crossing) at around $\hbar\omega \sim 0.14$ MeV and a second one (CD crossing) around $\hbar\omega \sim 0.23$ MeV. These values are in good agreement with the values obtained using similar calculations for ^{193}Tl in Ref. [27] by Reviol et al. The same nomenclature as that of Ref.[27] has been used in our calculations to label the quasiparticle levels. The observed band crossings at $\hbar\omega \sim 0.28$ MeV and at $\hbar\omega \sim 0.37$ MeV in ^{193}Tl were identified as due to the first and second neutron pair alignments by Reviol et al. The calculated crossing frequencies, however, found to underpredict both the experimental crossing frequencies by the same amount, and this discrepancy was attributed to the fact that the core deformation is not stiff, as assumed in these calculations. In addition to the first proton pair alignment, as in ^{193}Tl, the first neutron pair alignment is also blocked in the odd-odd nucleus ^{194}Tl. Therefore, the experimental band crossing in ^{194}Tl, observed at a rotational frequency

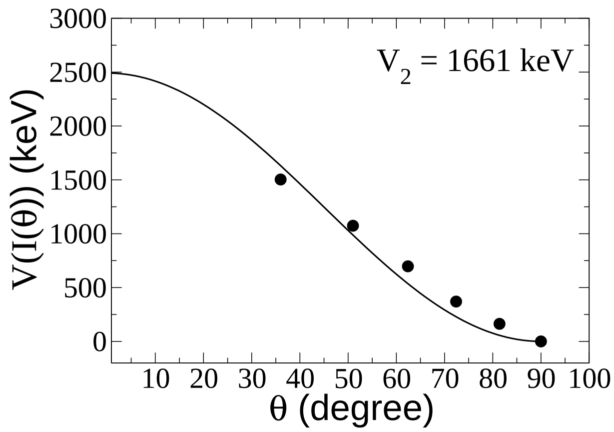

Figure 4.13: The effective interaction between the angular momentum vectors, j_π and j_ν, as a function of shears angle θ for the band B3 in ^{194}Tl as obtained in the semiclassical formalism.

of $\hbar\omega \sim 0.34$ MeV is due to the second neutron pair alignment. This value of the crossing frequency is in fairly good agreement with the second crossing in ^{193}Tl but at a slightly lower frequency. The experimental crossing frequency in ^{194}Tl is lowered by 0.03 MeV compared to the second crossing in ^{193}Tl. This difference of the experimental crossing frequencies could be reproduced well in the calculated second neutron pair alignment frequencies for ^{194}Tl ($\hbar\omega \sim 0.23$ MeV), as obtained in our calculation, and that for the ^{193}Tl ($\hbar\omega \sim 0.26$ MeV) as obtained by Reviol et al. [27].

4.3.2 Semiclassical calculations for the band B3

To investigate the shears mechanism of the band B3, it has been studied by the semiclassical approach of Machiavelli *et al.* [19, 30, 31]. With the $\boldsymbol{j}_\pi$ and $\boldsymbol{j}_\nu$ values of 8.5$\hbar$ and 13.5$\hbar$, respectively, for the proposed $\pi h^2_{9/2} s^{-1}_{1/2} \otimes \nu i^{-2}_{13/2} p_{3/2}$ configuration of the band B3, the band head spin is calculated to be 16 $\hbar$ assuming perpendicular coupling. This is in excellent agreement with the observed spin of the band head of this band. The maximum spin for this configuration has been calculated as $22^-\hbar$, corresponding to $\theta = 0^o$, which is again consistent with the highest spin observed in the present work. Therefore, the angular momentum along the entire range of the band is, most likely, generated through the shears mechanism. The good agreement of the initial and final spin values of this band with the calculations implies that the spins are generated solely by the shears mechanism with very little or no contribution from the rotation of the core. This fact is, again, corroborated well by the small quadrupole deformation obtained for this band in the TRS calculations. The V_2 is the strength of the interaction between the blades of the shears, can be calculated by using the experimentally observed energy levels of the shears band. In Fig. 4.13, the $V(I(\theta))$ is plotted as a function of θ. V_2 has been extracted from this plot by a fit of Eqn. 2.29. The fitted curve is shown as the solid line in Fig. 4.13. The extracted value of V_2 comes out to be 1661 keV. It was suggested by Clark et al. [32] that this is due to the fact that more than two blades are recoupling via the shears mechanism. It may be pointed out that the MR bands in the Pb nuclei are mostly based on the configurations involving high-j proton particles and high-j neutron holes. In the present case, however, the suggested configuration of band B3 contains, along with the high-j proton particles and neutron holes, a pair of proton hole ($s_{1/2}$) and neutron particle ($p_{3/2}$) both in the low-j orbitals which may lead to form another blade of the shears. In that case, considering 5 particle-hole pair, the effective interaction per particle-hole pair would be 332-keV, in good agreement with the typical value of ($\sim$ 300 keV) this region.

4.4 Conclusion

The γ-ray spectroscopy of the high spin states in the odd-odd nucleus ^{194}Tl has been studied in the fusion evaporation reaction using the ^{185,187}Re target with ^{13}C beam at 75 MeV. A new and improved level scheme of ^{194}Tl is presented in this work which includes 19 new γ-ray transitions. The DCO ratio and the Polarization assymmetry ratio measurements have been performed to assign the spin and parities of the levels. The $\pi h_{9/2} \otimes \nu i_{13/2}$ band (B1) in this nucleus has been extended just beyond the band crossing and up to 18^-. The uncertainties in the excitation energies and spins in this band have been removed. The observed band crossing in the 2-quasparticle band in ^{194}Tl has been compared with the neighboring even-even Hg core and the neighboring Tl isotopes. The energy staggering and the low-spin signature inversion observed for this negative parity yrast band has been found to be similar to ^{190,198}Tl. We have not found any indication of doubly degenerate band structure, in ^{194}Tl, arises due to chiral symmetry breaking. Two new side bands (B2 and B3) have been observed for the first time, in this odd-odd nucleus. 6-quasiparticle configurations for these bands have been suggested. Total Routhian Surface calculations suggest oblate shape for the band B1 similar to those in the neighboring odd-odd isotopes. Rather small deformation and a triaxial shape is suggested for the band B3 from these calculations. The Band B3 has been suggested to be an MR band and has been discussed in the frame work of the semiclassical approach. The observed band head spin and the range of spin values of this band are in agreement with such calculations.

Bibliography

[1] R.M. Diamond and F.S. Stephens, Nucl. Phys. **A 45**, 632 (1963).

[2] V.T. Gritsyna and H.H. Foster, Nucl. Phys. **A 61**, 129 (1965).

[3] J.O. Newton, S.D. Cirilov, F.S. Stephens and R.M. Diamond Nucl. Phys. **A 148**, 593 (1970).

[4] J.O. Newton, F.S. Stephens and R.M. Diamond Nucl. Phys. **A 236**, 225 (1974).

[5] R.M. Lieder et al., Nucl. Phys. **A 299**, 255 (1978).

[6] A.J. Kreiner et al., Phys. Rev. **C 38**, 2674 (1988).

[7] M.G. Porquet et al., Phys. Rev. **C 44**, 2445 (1991).

[8] W.Reviol et al., Phys. Scr. **T 56**, 167 (1995).

[9] I.G. Bearden et al., Nucl. Phys. **A 576**, 441 (1994).

[10] H. Hübel et al., Nucl. Phys. **A 453**, 316 (1986).

[11] C.Y. Xie et al., Phys. Rev. **C 72**, 044302 (2005).

[12] A.J. Kreiner et al., Phys. Rev. **C 21**, 933 (1980).

[13] A.J. Kreiner et al., Phys. Rev. **C 20**, 2205 (1979).

[14] A.J. Kreiner et al., Nucl. Phys. **A 308**, 147 (1978).

[15] A.J. Kreiner et al., Nucl. Phys. **A 282**, 243 (1977).

[16] A.J. Kreiner et al., Phys. Rev. **C 23**, 748 (1981).

[17] E.A. Lawrie et al., Phys. Rev. **C 78**, 021305(R) (2008).

[18] H. Hübel, Prog. Part. Nucl. Phys. **54**, 1 (2005).

[19] R.M. Clark and A.O. Macchiavelli, Annu. Rev. Nucl. Part. Sci. **50**, 1 (2000).

[20] P.L. Masiteng et al., Acta Phys. Pol. **B 40**, 657 (2009).

[21] H. Tan et al., Nuclear Science Symposium Conference Record, NSS 08, IEEE, p 3196 (2008).

[22] E.S. Macias et al, Computer Phys. Comm **11**, 75 (1976).

[23] Balraj Singh, Nucl. Data Sheets **107**, 1531 (2006).

[24] E. Achterberg et al., Nucl. Data Sheets **107**, 1 (2006)

[25] R. Bengtsson and S. Frauendorf, Nucl. Phys. **A 327**, 139 (1979).

[26] R. Bengtsson and S. Frauendorf, Nucl. Phys. **A 314**, 27 (1979).

[27] W. Reviol et al., Nucl. Phys. **A 548**, 331 (1992).

[28] I. Hamamoto, Phys. Lett. **B 235**, 221 (1990).

[29] A.K. Jain et al., Pramana **75**, 51 (2010).

[30] A.O. Macchiavelli *et al.*, Phys. Rev. C **57**, R1073 (1998).

[31] A.O. Macchiavelli *et al.*, Phys. Rev. C **58**, R621 (1998).

[32] R.M. Clark and A.O. Maccchiavelli, Nucl. Phys. **A682**, 415c (2001).

Chapter 5

Onset of deformation at $N = 112$ in Bi nuclei: γ-ray spectroscopy of ^{195}Bi

5.1 Introduction

Variety of interesting structural phenomena have been observed in the nuclei near A $\sim$ 190 region. Experimental evidence of the coexistence of spherical, oblate and prolate shapes, observed in the lead nuclei [1, 2] has opened up a renewed research interest in this region, both theoretically and experimentally. There were several spectroscopic investigations to study the shapes and single particle level structures in the nuclei below Z = 82 shell closure. However, there were only a few above it.

The Nilsson diagram corresponding to this region shows that both the [505]$9/2^-$ and the [606]$13/2^+$ proton orbitals have strong shape driving effect towards oblate shape. The [541]$1/2^-$ and [660]$1/2^+$ proton orbitals, on the other hand, have strong shape driving effect towards prolate shape. The competing nature of different Nilsson orbitals are reflected in the calculated shapes of different nuclei in this region which show the occurrence of various shapes including shape coexistence [3]. Two proton excitations across the shell gap are generally responsible for oblate deformed structure in this region where as, multiparticle excitations having four or more protons induces prolate deformations [4].

As mentioned in chapter 1, in the Bismuth nuclei (Z = 83), a variety of structure is obtained from spherical to superdeformed shapes as one goes down in neutron number from the spherical shell closure at $N = 126$. The observation of rotational bands in ^{191,193}Bi [5] indicates a deformed shape in bismuth nuclei for neutron number $N = 109$ and 110. On the other hand, the absence of any regular band like structure of the low lying states in the heavier odd-A Bismuth isotopes suggests spherical shapes for these nuclei at lower excitation energies. These low lying states in $^{197-201}$Bi could be interpreted in terms of shell model and weak coupling of the odd proton to the neutron-hole states in the neighboring Pb core [6, 7]. Recently, a shears band has been reported at high excitation (> 4 MeV) in ^{197}Bi [8]. The total Routhian surface (TRS) calculations indicate oblate deformation for this configuration. This suggests that deformation sets in for the multi-quasiparticle state at high excitation in ^{197}Bi.

On the other hand, in even-even Po (Z = 84) [9] isotopes, a clear evidence of structural change has been observed for neutron number $N \leq 114$.

The odd proton nucleus ^{195}Bi, with neutron number $N = 112$, is an interesting transitional nucleus whose two immediate odd-A neighbors on either side have different shapes at low excitation energies. As mentioned above, the spherical shape dominates in heavier ^{197}Bi and the deformed shape dominates in ^{193}Bi. The excitation energy of the $13/2^+$ state (corresponding to the $\pi i_{13/2}$ orbital), with respect to the $9/2^-$ state (corresponding to the $\pi h_{9/2}$ orbital), in Bismuth isotopes decreases quite rapidly with the decrease in neutron number. This was believed to be due to the difference between the interactions of $\pi i_{13/2} - \nu i_{13/2}$ and $\pi h_{9/2} - \nu i_{13/2}$ pairs. At $N = 112$ the $13/2^+$ state, originated from $\pi i_{13/2} \otimes \nu_{0^+}$ configuration, is expected to be below the $11/2^-$ and $13/2^-$ states, originated from the $\pi h_{9/2} \otimes \nu_{2^+}$ configuration. This is experimentally confirmed from the observation of $13/2^+$ as the first excited state in ^{195}Bi [10]. The oblate driving nature of the proton $i_{13/2}$ orbital is expected to induce oblate deformation in ^{195}Bi.

Lönnroth et al. [10] have studied the high spin states in ^{195}Bi using a ^{19}F beam on a ^{182}W target and a ^{30}Si beam on a ^{169}Tm target. Six γ rays were identified in their work. The highest state known was a $(29/2^{-})$, 750 ns isomer, the excitation energy of which was not known. Superdeformed bands have also been identified in this region in Bi isotopes in a Gammasphere experiment [11] showing the rich variety of shapes one can expect in this region. However, no rotational like band structure has been observed at lower excitation energy in ^{195}Bi.

5.2 Experimental procedures and data analysis

The γ-ray spectroscopy of ^{195}Bi has been performed at Variable Energy Cyclotron Centre, Kolkata using the Indian National Gamma Array (INGA) with 8 clover HPGe detectors at the time of the experiment. The excited states in this nucleus were populated by fusion evaporation reaction ^{181}Ta(^{20}Ne,6n)^{195}Bi. The 145 MeV $^{20}Ne^{+}$ ion beam from the K130 cyclotron was degraded by about 15 MeV using a 3.6 mg/cm^2 Al foil placed at 30 cm upstream to the centre of the INGA detector array. A thick (14.5 mg/cm^2) ^{181}Ta target was used and the recoils were stopped inside the target. The clover detectors were arranged in three angles with 2 clovers each at 40° and 125° angles and four clovers at 90° angle. The master trigger was set as $\gamma - \gamma$ (and a small run with $\gamma - \gamma - \gamma$) coincidence to collect list mode data. Time and pulse height information of each γ ray was stored using a CAMAC based data acquisition system. Time to Digital Converters (TDCs), used for individual γ-ray timing, were started by the master trigger pulse and stopped by the individual clover time pulse. The $\gamma - \gamma$ time difference between the γ rays in an event ($\gamma - \gamma$ TAC) was obtained, in the software, by subtracting each pair of TDCs recorded in that event. A hardware Time to Amplitude Converter (TAC) module was also used to record the time between the master trigger and the RF signal of the cyclotron (RF-γ TAC) to separately identify the "beam-on" and "beam-off" events. The clover detectors were calibrated for γ-ray energies and relative efficiencies by using ^{133}Ba and ^{152}Eu radioactive sources.

A prompt E_γ - E_γ matrix (matrix-1) was constructed gated by the prompt peak in the RF-γ TAC and a delayed E_γ - E_γ matrix (matrix-2) was constructed gated by the delayed part (100 - 230 ns away from the prompt peak) in the same TAC. Both of these matrices were also gated by the prompt peak of the $\gamma - \gamma$ TAC constructed by the software.

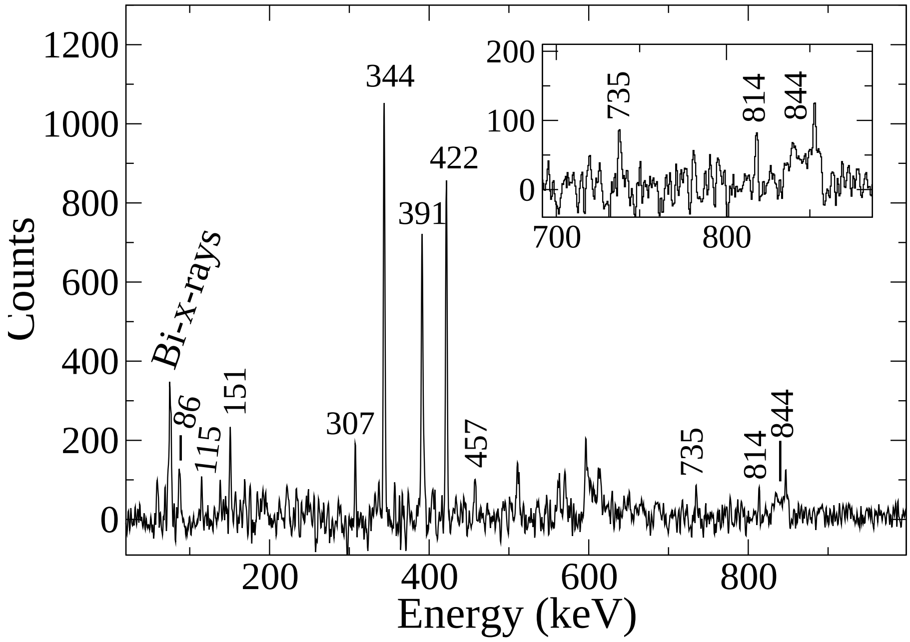

Figure 5.1: Coincidence spectrum gated by 887-keV γ ray.

The first excited state in ^{195}Bi is an isomer with a 32 ns halflife which decays by 887-keV γ ray. There are other high spin isomers in ^{195}Bi which were identified with halflives of 80 ns and 750 ns by Lönnroth et al. [10]. However, the time delay curves for the transitions decaying from these isomers were shown to contain significant amount of prompt components. The $\gamma - \gamma$ coincidence time window in our experiment was 400 ns wide. During the analysis, we set a tighter coincidence gate of 100 ns, for constructing both the E_γ - E_γ matrices, which is sufficiently wide to allow coincidences with the 887 keV transition. Data were analyzed using both the matrices. Gates were put on the known γ-ray transitions in a prompt matrix for obtaining the coincidence relation.

Figure 5.1 shows the γ−ray spectrum gated by the known 887-keV transition in ^{195}Bi projected from matrix-1. A few new γ lines at 86, 307, 457, 735, 814 and 844 keV have been observed

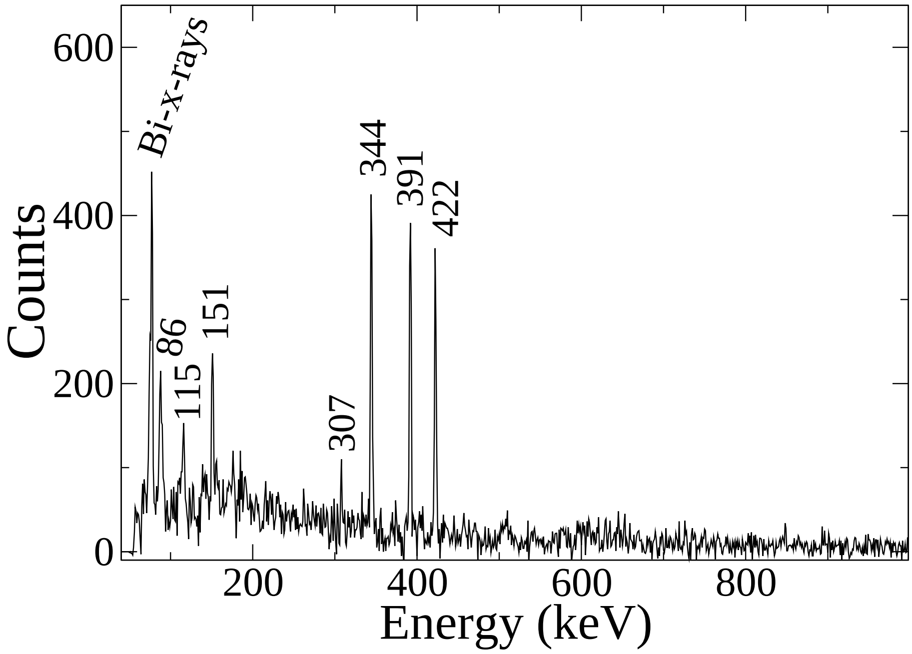

Figure 5.2: Delayed coincidence spectrum gated by 887-keV γ ray.

in this spectrum. On the basis of their coincidence relations, they are placed in the level scheme. The gated spectrum shown in Fig. 5.2 is projected from matrix-2 using the same gating transition of 887-keV. Since the 151-keV γ ray is a direct decay from the 80 ns isomer, the relative intensity of this γ ray has been found to be more in Fig. 5.2 than in Fig. 5.1, as expected. While the ratio of the intensities of 151- and 391-keV γ rays is 0.17(4) in Fig. 5.1, the same ratio has been found to be 0.25(2) in Fig. 5.2. Interestingly, the ratio of intensities of the 391- and 422-keV γ rays has also been found to be different in the two spectra. This has been discussed in the next section.

The multipolarities of the γ-ray transitions have been determined from the angular correlation analysis using the method of directional correlation from oriented states (DCO) ratios. For the DCO ratio analysis, the coincidence events were sorted into an asymmetry matrix with data from 90° detectors on one axis and 40° detectors on the other axis. The value of the DCO ratio of a pure dipole transition, gated by a pure quadrupole transition has been calculated as 1.84 in the above geometry. The procedure has been validated by the γ rays of known multipolarity which were produced in the present experiment. The values R_{DCO} = 1.03(7) and 0.98(4) were obtained for the known quadrupole (E2) transitions in ^{194}Pb and ^{196}Pb [12], respectively, and R$_{DCO}$ = 1.54(23) was obtained for a known mixed (M1+E2) transition [6] when gated by known quadrupole transitions. To obtain the DCO ratios for the γ rays in ^{195}Bi, the 887-keV γ ray was taken as the gating transition which was known to be of the $M2(+E3)$ type. The measured K-conversion coefficient (α_K) of this transition and the half-life of 32 ns measured for the $13/2^+$ state [10] indicate that the 887-keV γ ray is predominantly M2. So, the DCO values obtained for the γ rays in ^{195}Bi, in the present work, may be compared with the values calculated using a quadrupole gate.

We have performed integrated polarization asymmetry measurement (IPDCO), as described in section 3.6.3, from the parallel and perpendicular scattering of a γ-ray photon inside the detector medium. A correction factor due to the asymmetry in the array and response of the clover segments was incorporated which is defined by $a(E_\gamma) = \frac{N_\parallel}{N_\perp}$. The value of this asymmetry parameter, for an ideal array, should be close to unity. In the present experiment this was obtained for different gamma ray energies using ^{152}Eu source and an average value was found to be 1.07(5). The IPDCO ratios could not be obtained for the γ rays having low energy (E$_\gamma \leq 300$ keV) and low intensity.

Table 5.1: Energies (E_γ), intensities (I_γ), DCO ratios (R$_{DCO}$), IPDCO ratios (Δ_{IPDCO}) and deduced multipolarities of the γ rays in ^{195}Bi. The energies of initial states (E_i) and spins and parities of initial (J_i^π) and final (J_f^π) states are also given.

E_γ (in keV)	E_i (in keV)	$J_i^\pi \rightarrow J_f^\pi$	I_γ [1]	R_{DCO} (Err)	Δ_{IPDCO} (Err)	Deduced Multipolarity
86.3(2)	2395.8	$29/2^{(-)} \rightarrow 25/2^{(-)}$	9.3(15)	1.04(20) [2]	-	E2
114.9(3)	2309.5	$25/2^{(-)} \rightarrow 23/2^+$	9.7(11)	1.41(29) [2]	-	E1
150.7(2)	2194.6	$23/2^+ \rightarrow 19/2^+$	10.8(9)	1.08(20) [2]	-	E2
307.4(3)	1537.8	$17/2^{(+)} \rightarrow 15/2^+$	9.6(11)	1.59(33) [2]	-	(M1+E2)
343.7(1)	1230.6	$15/2^+ \rightarrow 13/2^+$	48.4(37)	1.24(7) [2]	-0.09(3)	M1+E2

Table 5.1: Continued...

E_γ (in keV)	E_i (in keV)	$J_i^\pi \rightarrow J_f^\pi$	I_γ [1]	R_{DCO} (Err)	Δ_{IPDCO} (Err)	Deduced Multipolarity
391.3(2)	1621.6	$17/2^+ \rightarrow 15/2^+$	38.0(30)	1.46(12) [2]	-0.08(3)	M1+E2
421.6(1)	2465.6	$(21/2^+) \rightarrow 19/2^+$	6.1(80)	1.33(18) [2]	-	(M1+E2)
421.7(1)	2043.9	$19/2^+ \rightarrow 17/2^+$	37.0(80)	1.35(19) [4]	-0.13(4)	M1+E2
457.4(6)	2923.0	$(23/2^+) \rightarrow (21/2^+)$	8.5(15)	1.56(40) [2]	-	M1+E2
734.7(6)	1621.6	$17/2^+ \rightarrow 13/2^+$	6.7(13)	-	-	(E2)
813.6(3)	2043.9	$19/2^+ \rightarrow 15/2^+$	5.7(10)	-	-	(E2)
843.6(4)	2465.6	$(21/2^+) \rightarrow 17/2^+$	4.4(13)	-	-	(E2)
886.7(1)	886.7	$13/2^+ \rightarrow 9/2^-$	100(6)	0.61(7) [3]	-0.08(3)	M2

The spin and parity of the excited states in ^{195}Bi has been assigned from the above two measurements. In Fig. 5.3, the DCO and the IPDCO ratios are plotted for the γ rays in ^{195}Bi along with those for some of the transitions in other nuclei, produced in the same experiment and with known multipolarities. The DCO ratios, for all the transitions shown in Fig. 5.3, were obtained by gating on a known quadrupole transition except for the 887-keV γ ray in ^{195}Bi. The DCO ratio for this γ ray was obtained from a dipole gate of 391-keV. The 689- and 965-keV γ rays, belonging to ^{196}Pb and ^{194}Pb, respectively, were known to be E2 and are consistent with our measurement. Similarly, the 1009-keV γ ray was known to be a $M1+E2$ transition in ^{197}Bi which also agrees with our measurements.

[1] Relative γ ray intensities are estimated from prompt spectra and normalized to 100 for the total intensity of 886.7 keV γ rays.

[2] From 886.7 keV (M2) DCO gate;

[3] From 391.3 keV (M1+E2) DCO gate;

[4] From 150.7 keV (E2) DCO gate;

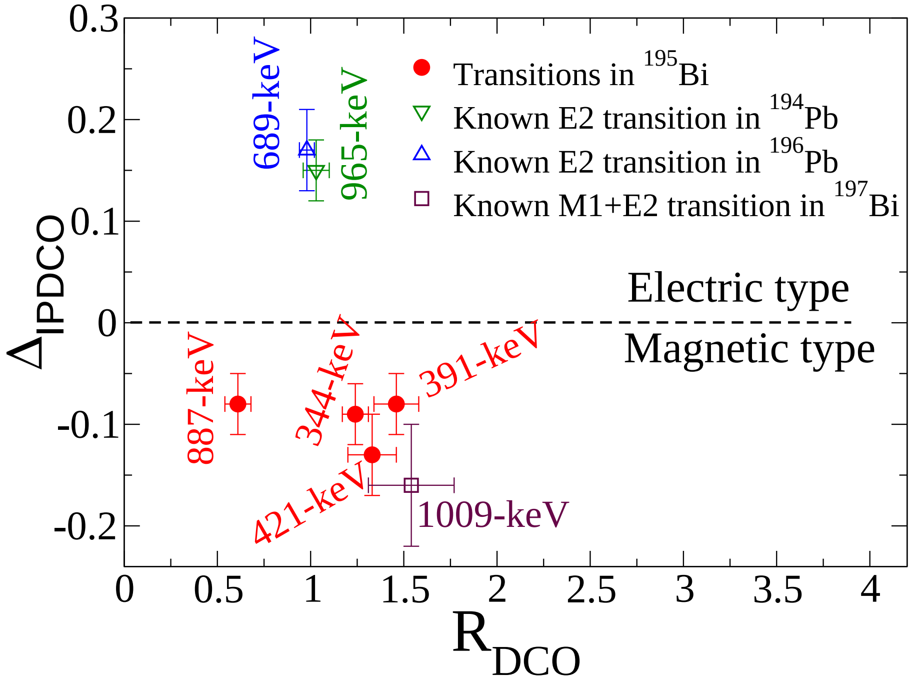

Figure 5.3: The DCO and the IPDCO ratios for the γ rays in ^{195}Bi and for a few known transitions in ^{194,196}Pb obtained from the present work. The DCO values are obtained by gating on a quadrupole transition except for the 887-keV γ ray which was gated by a dipole transition.

5.3 Results

The results obtained in the present work for the excited states in ^{195}Bi are summarized in Table 5.1. The level scheme of ^{195}Bi, as obtained in the present work, is shown in Fig. 5.4. This level scheme includes 7 new γ-ray transitions over and above the ones reported earlier [10]. These new lines have been placed in the level scheme and are marked by "*" in Fig. 5.4. The 344- and 391- keV γ-rays were assigned as dipoles in character from the angular distribution measurements by Lönnroth et al. [10]. The conversion co-efficient measurements, performed in the same study, were not clean enough to determine their electric or magnetic character. In the present work, these transitions were found to be of mixed $M1(+E2)$ character from their R_{DCO} and Δ_{IPDCO} values (see Fig. 5.3). It may be noted that the possibility of a mixed transition was not ruled out in Ref. [10] for the 344 keV γ ray. Similarly, $E2$ multipolarity was tentatively assigned by Lönnroth et al. for the 422 keV transition decaying from the 2044 keV state. In the present work, however, this γ ray has been found to be a $M1(+E2)$ transition based on the DCO and the IPDCO values. Moreover, the weak cross-over transitions (735- and 814-keV) were also observed in the present work and are shown in Fig. 5.1.

It can be seen that the intensity of 422-keV is greater than that of 391-keV transition in Fig. 5.1, whereas it is less than that of 391-keV transition in the delayed gate in Fig. 5.2. This clearly indicates the presence of another 422-keV prompt transition. This γ ray has been placed above the 2044-keV state in the level scheme. The presence of the cross-over 844-keV γ ray supports this placement. A 457-keV γ ray is also observed in this work and was found to be in coincidence with 887-, 344-, 391-, and 422-keV γ rays. This γ ray was not found to be in coincidence with the 151- or 115-keV γ rays and was not well observed in the delayed gate. Therefore, this γ ray is placed above the 2466 keV state. A 307-keV γ ray, observed in this work, has been found to be in coincidence with the 887- and 344-keV γ rays only and has been placed accordingly. This γ line is also observed in the delayed spectrum in Fig. 5.2. This indicates that the 1538-keV state is partially fed by an isomer, which could not be identified in our work.

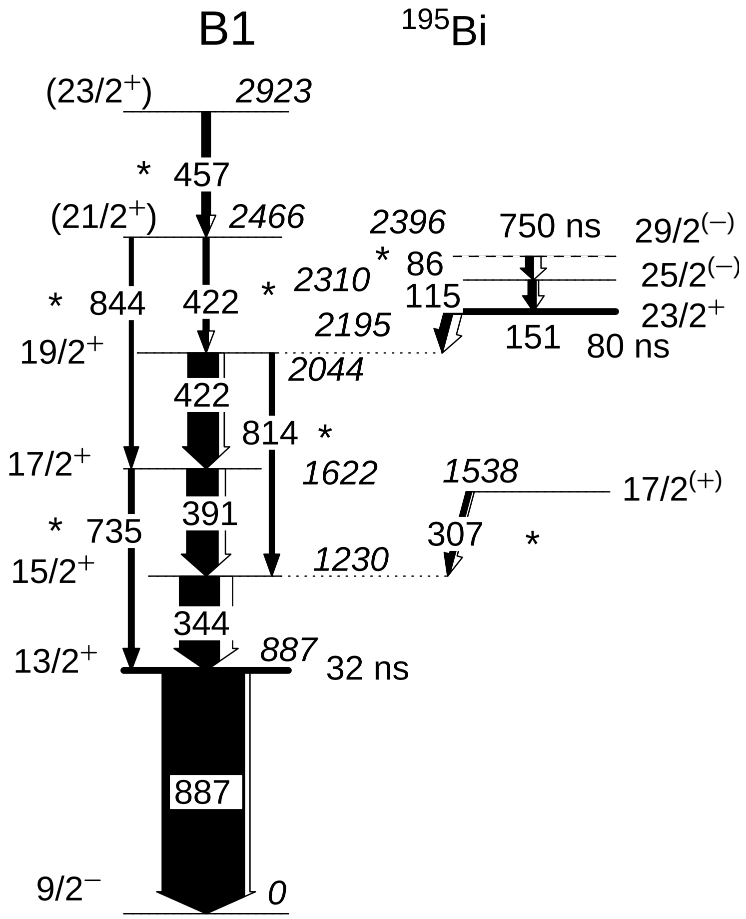

Figure 5.4: Level scheme of ^{195}Bi obtained from this work. The new γ-rays are indicated by asterisks.

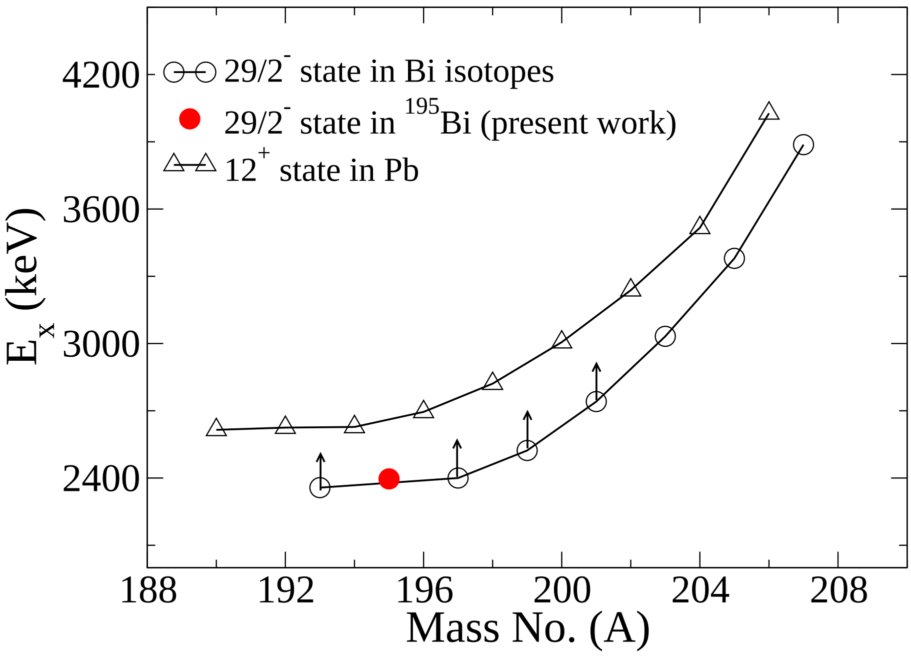

Figure 5.5: Systematic of the excitation energy of the $29/2^-$ isomeric state in odd-odd Bi nuclei (open circle) and that of the 12^+ state in even-even Pb nuclei (open triangle). The arrows indicate that the values are the lower limit. The excitation energy of the $29/2^-$ isomer in ^{195}Bi from the present work is shown as a solid circle.

In Ref. [10], no decay γ ray was reported from the 750 ns, $29/2^{(-)}$ isomer and hence, the excitation energy of this isomer was uncertain. In the present work, there are indications of a 86-keV transition decaying from this isomer. It may be noted that this γ ray could as well be observed in the spectra shown in Ref. [10] but it is difficult to assign this γ ray as the $K_{\beta 1}$ X-ray of Bi has a similar energy (87.3 keV) [13]. From the delayed spectrum gated by 887-keV, we have obtained the ratio of intensities of the 77-keV line ($K_{\alpha 1}$ of Bi) and the 86-keV line as 2.66(36) whereas, the ratio of $K_{\alpha 1}$ and $K_{\beta 1}$ X-rays (from the table in Ref. [13]) is 4.32. This suggests that there are additional contribution in the intensity around 86 keV. The same ratio obtained from a spectrum gated by 86-keV, in which the contribution of the 86-keV γ may be absent but the contribution from the $K_{\beta 1}$ X-ray will be present, yields a value of 4.04(80). This is in fairly good agreement with the tebulated value in Ref. [13]. The ratio of intensities of $K_{\alpha 1}$ and $K_{\alpha 2}$ was also obtained, from our data, as 1.77(12), which again agrees well with the value of 1.67 obtained from the table and shows that our data give a good estimate of the relative intensities for the pure X-rays.

It is worth mentioning here that in the spectrum gated on the 86-keV line, there may still be a contribution from the 86-keV γ line. This may be due to coincidence of the 87-keV X-rays from the conversion of the 115-keV line, which can be in coincidence with the 86-keV γ ray. Therefore, there would be some contribution of 86-keV γ ray effectively from 115-keV gate. Hence, measured ratio of $K_{\alpha 1}$ and $K_{\beta 1}$, obtained from the spectrum gated by 86-keV, would decrease from the true value by this effect which is indeed observed (4.04 in place of 4.32). The contribution may be calculated by using the K conversion coefficient ($\sim$0.26) multiplied by the fraction of intensity of $K_{\beta 1}$ ($\sim$11%) out of K_{total}. This comes out to be $\sim$3%. Similar contribution may also come from 151-keV transition for which the K conversion coefficient is similar to that of 115 keV. Therefore, the total contribution would be not exceeding $\sim$6%. The observed difference of the ratios is also found to be indeed in that order. Therefore, the effect of this is within the uncertainties of the observed ratio.

In the present work, the spin and parity of the 2310-keV state have been found to be $25/2^{(-)}$. A $25/2^{-}$ state has also been observed at similar excitation energy in the neighboring isotope of ^{193}Bi [5]. It is suggested that the $29/2^{(-)}$ isomer in ^{195}Bi decays to the $25/2^{(-)}$ state by a 86 keV $E2$ transition. The measured halflife of the isomer is also consistent with the Weisskopf estimate for a 86 keV $E2$ transition. Therefore, the excitation energy of the $29/2^{(-)}$ isomer is proposed to be 2396 keV. The systematic of the excitation energies of the $29/2^{-}$ isomer in Bismuth isotopes, which arises due to the $\pi h_{9/2} \otimes \nu_{12^+}$ coupling, is shown in Fig. 5.5. The same for the 12^+ state in the Pb nuclei are also shown in the same figure. It can be seen that the excitation energy of the $29/2^{(-)}$ isomer in ^{195}Bi is consistent with the systematic.

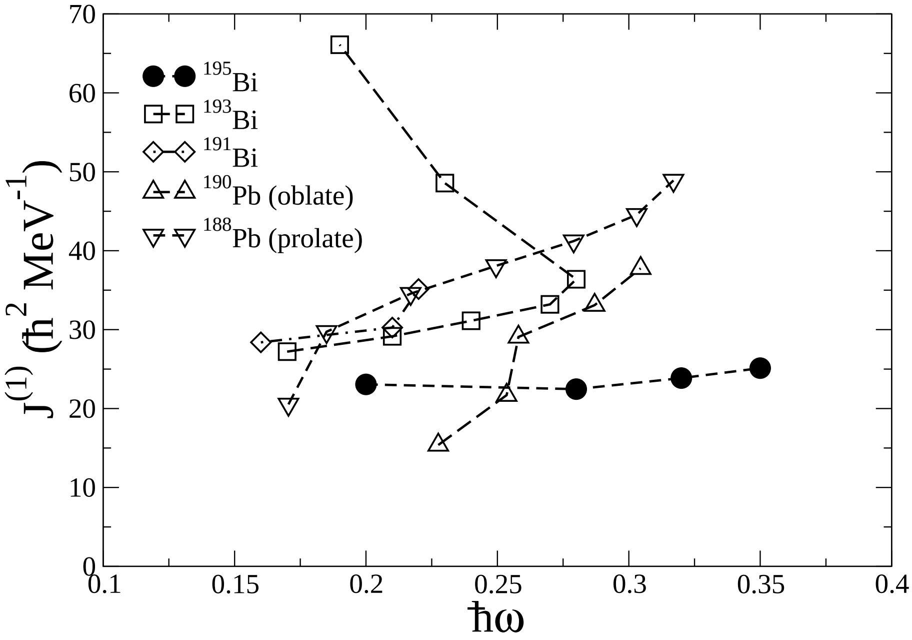

Figure 5.6: Kinematic moments of inertia ($J^{(1)}$) as a function of rotational frequency $\hbar\omega$ for the proposed rotational band based on the $13/2^+$ state in ^{195}Bi along with those for neighboring odd-A bismuth and even-even Pb isotopes.

5.4 Discussion

The band B1 in ^{195}Bi closely resembles the rotational bands based on the $13/2^+$ band head in ^{193}Bi and ^{191}Bi [5]. This band has the configuration of $\pi i_{13/2}$ coupled to the 2p-2h 0^+ intruder state of the Pb core with oblate deformation. Although, the $\pi i_{13/2}$ state has been observed through out the isotopic chain of Bi nuclei, the rotational bands based on the above

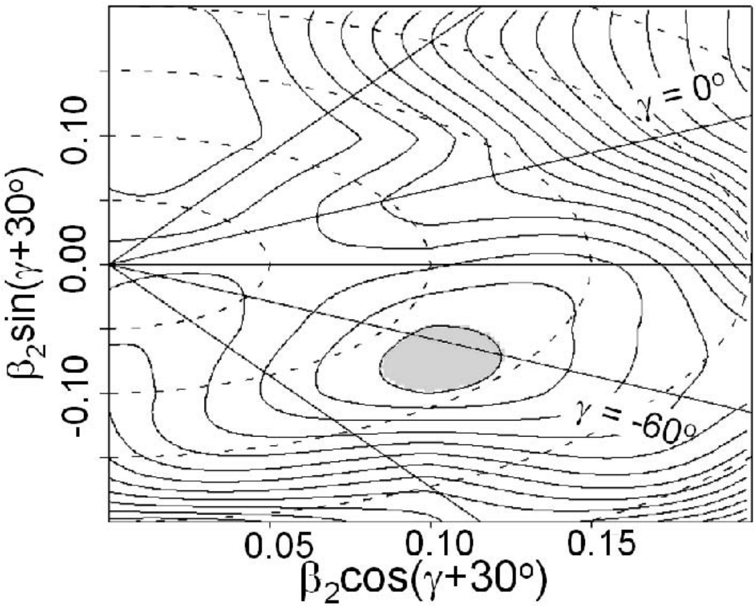

Figure 5.7: Total Routhian surfaces calculated for the $13/2^+$ configurations in ^{195}Bi.

configuration was observed only in the isotopes lighter than $A = 195$, prior to the present work. Therefore, the neutron number $N = 110$ was considered to be the border for the observation of deformed shape in odd-A Bi isotopes. With the observation of rotational band structure based on the $13/2^+$ band in ^{195}Bi, the border has been extended to $N = 112$ in the present work. The kinematic moments of inertia, $J^{(1)}$, have been plotted in Fig. 5.6 for the above band in Bi isotopes along with those for the prolate and oblate structures in the Pb nuclei [14, 15] as in Ref. [5]. This figure clearly shows that while the moment of inertia values in ^{191}Bi are closer to the prolate band in ^{188}Pb, the initial values in ^{195}Bi are closer to the oblate band in ^{190}Pb. For ^{193}Bi, the values are in between these two. This suggests a gradual change in the structure of the $i_{13/2}$ band in odd-A Bi isotopes. As the neutron number increases, the oblate structure seems to dominate over the prolate one.

It may also be noticed in Fig. 5.6 that there is a band crossing in ^{191}Bi around the rotational frequency of $\hbar\omega \sim 0.21$ MeV. This band crossing frequency increases to $\hbar\omega \sim 0.28$ MeV in ^{193}Bi. If one extrapolates the difference in the crossing frequencies in the above two isotopes, the crossing in ^{195}Bi is expected at or beyond $\hbar\omega \sim 0.35$ MeV which agrees well with the non-observation of any band crossing in ^{195}Bi in the present work.

The high spin single particle states in ^{193}Bi were interpreted as being due to the coupling of the $h_{9/2}$ proton with the states in the neighboring even-even ^{192}Pb core. As mentioned earlier, the $29/2^-$ isomer is the result of the coupling of $\pi h_{9/2}$ with the 12^+ in the Pb core. The $25/2^{(-)}$ state in ^{195}Bi could be interpreted as due to the coupling of the proton in the same orbital with the 8^+ in the Pb core in accordance with the interpretation for the same state in ^{193}Bi [5]. The isomer at 2195 keV was assigned to be a $25/2^+$ state in ^{195}Bi by Lönnroth et al. [10]. But this state was not observed in ^{193}Bi. The same state has been assigned to be a $23/2^+$ state in the present work which may be interpreted as the coupling of the $h_{9/2}$ proton with the 7^- state in the Pb core. In ^{193}Bi, the excitation energy of an isomer ($t_{1/2} > 10\mu s$), observed above the 2127-keV state, suggests that this state may have the same configuration. The $17/2^{(+)}$ state, observed at an excitation energy of 1538 keV in this work may be interpreted as the $\pi h_{9/2} \otimes \nu_{5^-}$ state, which agrees well with the calculations shown in Ref. [10].

5.5 TRS calculations

The onset of deformation in ^{195}Bi has been discussed in the cranking formalism. In this formalism, the total Routhian surface (TRS) calculations are performed using the Strutinsky shell correction method. The TRSs are calculated for the different values of the rotational frequencies $\hbar\omega$ and for different configurations labeled by parity (π) and signature (α) quantum numbers. At each frequency, the spin can be projected. The TRSs, calculated for the positive parity and $\alpha = +1/2$ configuration, are shown in Fig. 5.7 for the spin value of $13/2^+$. A minimum in the TRS is obtained at an oblate deformation with $\beta_2 = 0.13$. This shows that the deformation driving [606]$13/2^+$ orbital, originated from the $\pi i_{13/2}$ level, induces oblate deformation in ^{195}Bi. This is in qualitative agreement with the fact that the moment of inertia of ^{195}Bi is closer to the oblate deformed band in ^{190}Pb as shown in Fig. 5.6. Therefore, the observed onset of deformation in ^{195}Bi agrees with the cranking model predictions.

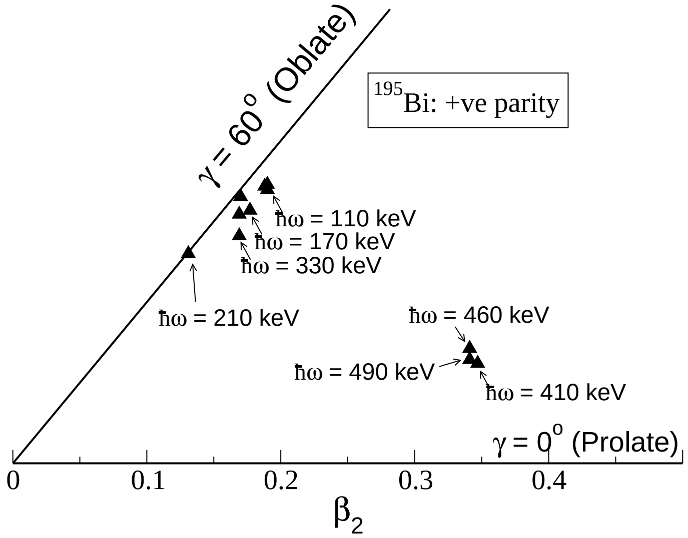

Figure 5.8: Minima in the TRSs calculated for the $\pi i_{13/2}$ configuration in ^{195}Bi for different values of rotational frequencies $\hbar\omega$.

The TRSs have been calculated at different rotational frequencies for the same configuration ($\pi i_{13/2}$) in ^{195}Bi and the values of the deformation parameters (β_2 and γ) corresponding to the minimum at each frequency are plotted in Fig. 5.8. It can be seen that the calculated shape remains oblate below $\hbar\omega = 400$ keV, after which it starts to deviate from oblate toward triaxial deformation.

5.6 Conclusion

The γ-ray spectroscopy of the high spin states in ^{195}Bi has been studied using the fusion evaporation reaction with ^{20}Ne beam on a ^{181}Ta target and using the INGA array with 8 clover HPGe detectors. A new level scheme with 7 new γ rays has been proposed for ^{195}Bi. A rotational band based on a $13/2^+$ band head has been proposed in ^{195}Bi, similar to those observed in the lighter isotopes ^{191,193}Bi. This indicates that the onset of deformation takes place in the isotopic chain of Bi nuclei at $N = 112$. The excitation energy of 2396 keV proposed for the $29/2^{(-)}$ isomer has been found to be consistent with the systematic of the energy of this isomer in the neighboring odd-A Bi isotopes. The TRS calculations using the Woods-Saxon potential show oblate deformation for the $13/2^+$ configurations in ^{195}Bi. The same calculations at higher angular frequencies predict a change in shape from oblate to triaxial deformation around the rotational frequency of $\hbar\omega = 0.4$ MeV. More experimental work is needed to test this prediction.

Bibliography

[1] A.N. Andreyev et al., Nature **405**, 430 (2000).

[2] G.D.Dracoulis et al., Phys. Rev. **C 67**, 051301(R) (2003).

[3] K. Heyde et al., Phys. Rep. **102**, 291 (1983).

[4] J. L. Wood et al., Phys. Rep. **215**, 101 (1992).

[5] P. Nieminen et al., Phys. Rev. **C 69**, 064326 (2004).

[6] T. Chapuran et al., Phys. Rev. **C 33**, 130 (1986).

[7] W.F. Piel et al., Phys. Rev. **C 31**, 2087 (1985).

[8] G.K. Mabala et al., Euro. Phys. J. **A 25**, 49 (2005).

[9] L.A. Bernstein et al. Phys. Rev. **C 52**, 621 (1995).

[10] T. Lönnroth et al. , Phys. Rev. **C 33**, 1641 (1986).

[11] R.M Clark et al., Phys. Rev. **C 53**, 117 (1996).

[12] B. Singh, Nucl. Data Sheets **107**, 1531 (2006); H. Xiaolong, ibid **108** 1093 (2007).

[13] Table of Isotopes V 1.0, March 1996, Eds. R.B. Firestone, V.S. Shirley, Wiley-Interscience.

[14] G. D. Dracoulis, A. P. Byrne, and A. M. Baxter, Phys. Lett. B **432**, 37 (1998).

[15] J. Heese et al., Phys. Lett. B **302**, 390 (1993).

Chapter 6

Study of intruder $\pi i_{13/2}$ state in ^{197}Tl using α-induced γ-ray spectroscopy

6.1 Introduction

The proton Fermi level of thallium nuclei lies below the Z = 82 spherical shell closure. The ground state of the odd-A Tl nuclei are $1/2^+$ [1, 2, 3] corresponding to the proton hole in $3s_{1/2}$ (below the Z = 82 spherical shell closure) orbital. The low-lying excited levels in the odd-A thallium nuclei in A = 190 region have been interpreted by the occupation of the odd proton in $\pi d_{3/2}$ and $\pi d_{5/2}$ orbitals. However, the "intruder" $\pi h_{9/2}$ and $\pi i_{13/2}$ orbitals are required to describe the higher spin levels in thallium (Z = 81) nuclei. These orbitals, intrudes from the major shell above Z = 82 in to the shell below it for both prolate and oblate deformation. These orbitals, play significant role in breaking the spherical symmetry in nuclei by inducing non-spherical shapes in them. The $\pi i_{13/2}$ level lies above the Z = 92 spherical sub-shell closure. Therefore, the "intruder" $\pi i_{13/2}$ level in the lighter Tl nuclei provides a playground to study the properties of the levels for the heavy nuclei above Z = 92 which are otherwise difficult to study.

Rotational bands based on the intruder $\pi[505]9/2^-$ Nilsson state with oblate deformation and decoupled band based on $\pi h_{9/2}$ intruder level with prolate deformation have been reported in the odd-A $^{189-197}$Tl nuclei [4, 5, 6, 7]. Similarly, the strongly couple oblate band based on $\pi[606]13/2^+$ Nilsson state and weakly coupled prolate band from the $\pi i_{13/2}$ orbital have also been observed in neutron deficient (N < 114) isotopes ^{191,193}Tl [7, 8]. However, excited state corresponding to the intruder $\pi i_{13/2}$ orbital has not yet been observed in ^{195,197}Tl. It has been seen that the excitation energy of the $13/2^+$ state corresponding to the $\pi i_{13/2}$ orbital in the odd-A thallium nuclei increases gradually with the neutron number [9] and hence, it may become non-yrast for the heavy thallium isotopes. The non-yrast states can be better studied using light ion beams like α-induced fusion-evaporation reactions. As a part of this thesis work, the γ-ray spectroscopy of ^{197}Tl has been studied using α beam in order to investigate the proton intruder states along with the multi-quasiparticle states which may be originated from the coupling of the odd proton with the aligned neutron pairs in this nucleus. To identify the intruder levels, it is necessary to deduce the spin and parities of the excited states unambiguously. So, a clover HPGe detector was used as a γ-ray polarimeter to deduce the multipolarity of the γ rays which helps in unambiguous determination of the parity of the excited states.

The high spin level structures in ^{197}Tl were earlier investigated by R. M. Lieder et al. [4] way back in 1978. They had used two Ge(Li) detectors to detect the γ rays in coincidence and for angular distribution study. They have proposed a level scheme from these studies which included a band based on $\pi h_{9/2}$ orbital and a three-quasiparticle band.

6.2 Experimental Method and Data Analysis

In the present work, the excited states of ^{197}Tl were populated by fusion evaporation reaction ^{197}Au(^{4}He, 4n)^{197}Tl using α beam of energy 48 MeV from the K-130 Cyclotron at Variable Energy Cyclotron Centre, Kolkata. A 5 mg/cm^2 self supporting ^{197}Au target was used in this experiment. The experimental set up consisted of a single-crystal large HPGe detector, a clover HPGe detector and a LEPS detector which were placed at 30°, 90° and 135° angles, respectively, with respect to the beam direction. LEPS detector was used for the detection of low-energy photons. The detectors were arranged in a median plane configuration. A 50-element (25 each on the top and on the bottom) BaF_2 multiplicity array was also used. The energy and timing from each Ge detector and the multiplicity fold information were recorded in the list mode using γ-γ trigger. A hardware Time to Amplitude Converter (TAC) module was used to record the time between the master trigger and the RF signal of the cyclotron (RF-γ TAC) to identify the "beam-on" and "beam-off" events. About 4.3×10^7 coincidence events were recorded in this experiment. The detectors were calibrated for γ-ray energies and efficiencies by using the ^{133}Ba and ^{152}Eu radioactive sources. The collected γ-γ coincidence data were sorted into a γ-γ matrix using the data from the single-crystal HPGe and clover HPGe detectors for offline analysis. This two dimensional matrix was created with a gate on the prompt peak in the RF-γ TAC. A prompt time window of $\pm$50 ns was chosen. The analysis has been done by using the program RADWARE [10].

Definite spin and parity of the excited states were assigned from the DCO and the PDCO ratios as described in section 3.6.2 and 3.6.3, respectively. For the DCO ratio analysis, the coincidence events were sorted into an asymmetry matrix with data from 30° detector (θ_2) on one axis and 90° detector (θ_1) on the other axis.

For better sensitivity of the polarization (PDCO ratio) measurement, the clover detector was placed at 90° in the median plane. The correction factor for the response of the Clover segments, was checked using ^{152}Eu and ^{133}Ba sources and was found to be 0.990(12) [see Fig.3.13(e)]. The low energy cut off for the polarization was about 200 keV in this experiment. The validity of the methods of DCO and the PDCO measurements were checked from the transitions with known multipolarities in ^{197}Tl.

6.2.1 Experimental Results

Single gated γ-ray spectra obtained in this work and gated by 387-keV and 561-keV γ rays are shown in Fig. 6.1(a) and Fig. 6.1(b), respectively. These spectra show all known γ lines

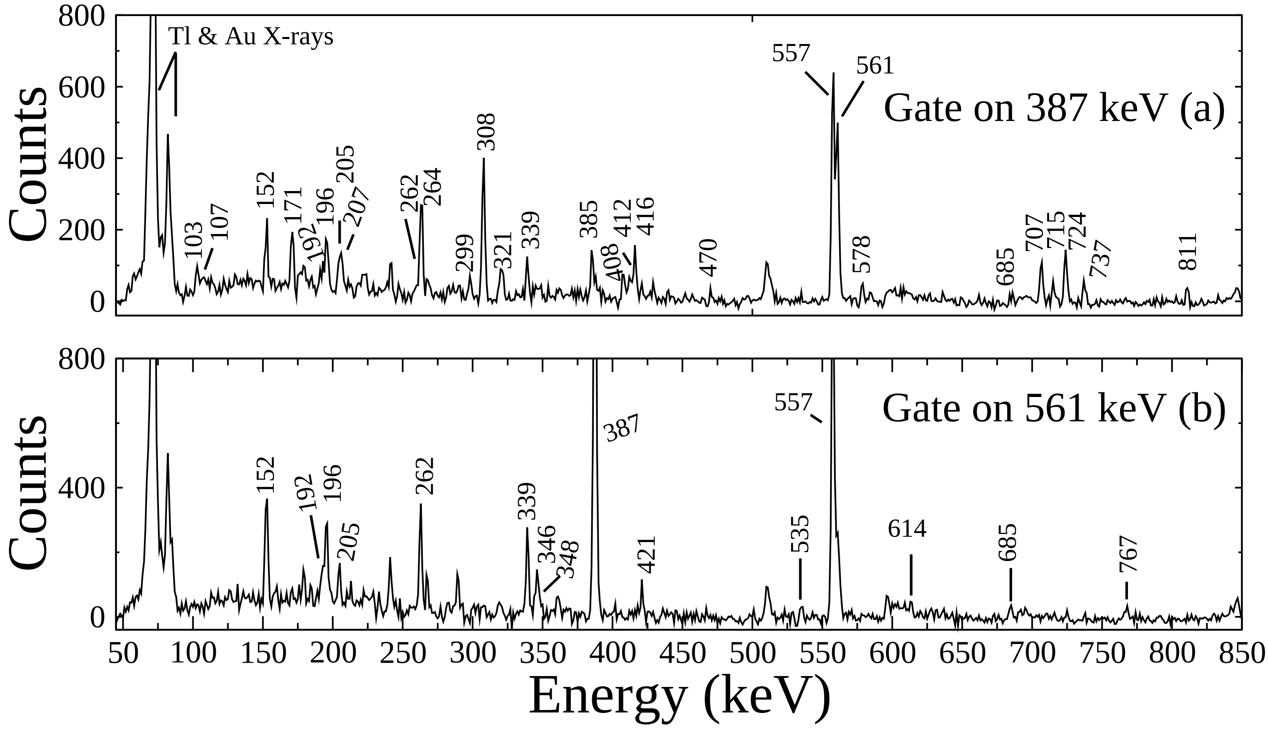

Figure 6.1: Coincidence spectra by gating on 387-keV (a) and 561-keV (b) γ transition.

reported by R. M. Lieder et al. [4]. Tentatively assigned 470-keV transition from 3066.9-keV level and 534.9-keV transition from 2800.8-keV level, reported in [4], have been observed clearly in Figs. 6.1(a) and (b), respectively. Therefore, these γ-ray transitions have been firmly placed in the level scheme.

In-beam γ-ray spectra, taken in singles mode, for one segment of the LEPS detector are shown in Fig. 6.2(a) and 6.2(b) for lower energy part and higher energy part, respectively. It is evident from the spectrum of Fig. 6.2(a) that one can clearly resolve different X-rays ($K_{\alpha 1}$, $K_{\alpha 2}$, $K_{\beta 1}$ and $K_{\beta 2}$) of Tl and Au in a LEPS detector. This shows the importance of LEPS detector for X-rays and low energy γ rays. However, the drastic reduction in efficiency of a LEPS detector, compared to a clover detector, for the detection of higher energy γ rays (as shown in Fig. 3.12) is also evident from the relative height of the 339-keV peak with respect to the 152-keV peak in Fig. 6.2(b) (for LEPS) and in Fig. 6.1(b) (for Clover).

An improved level scheme of ^{197}Tl, obtained in this work, is given in Fig. 6.3. The ground state in ^{197}Tl is known to be a long-lived ($T_{1/2}$ = 2.84 hour) $1/2^+$ state [11]. An isomeric state ($J^\pi = 9/2^-$) with a halflife of 0.53 s is also known in this nucleus at 608-keV of excitation energy [11]. In the present work, the γ rays above this isomer have been observed in the coincidence spectra. The 223- and 385-keV γ rays, below the isomer, were also observed in the present work but in the singles spectrum. The deduced excitation energy, spin and parity of the excited levels and the multipolarity of the γ rays, together with other relevant information concerning their placement in the proposed level scheme, are summarized in Table 6.1.

Table 6.1: Energies (E_γ), intensities (I_γ), DCO ratios (R_{DCO}), PDCO ratios (Δ_{PDCO}) and deduced multipolarities of the γ rays in ^{197}Tl. The energies of initial states (E_i) and spins and parities of initial (J_i^π) states are also given.

E_γ (in keV)	E_i (in keV)	J_i^π	I_γ [1]	R_{DCO} (Err)	Δ_{PDCO} (Err)	Deduced Multipolarity
102.6(1)	3169.5	$27/2^-$	2.4(3)	1.90(34) [2]	-	M1+E2
107.2(3)	3276.7	$29/2^-$	1.1(2)	1.41(34) [2]	-	M1+E2
152.4(1)	2266.1	$17/2^-$	10.1(8)	1.06(8) [3]	-	M1(+E2)
171.1(1)	2596.6	$21/2^-$	6.9(6)	1.51(17) [4]	-	M1+E2
192.2(2)	3760.1	$27/2^-$	2.0(2)	1.16(18) [3]	-	M1+E2
195.9(1)	2461.7	$19/2^-$	5.1(3)	1.08(12) [3]	-	M1(+E2)
204.6(3)	3964.7	$29/2^-$	1.8(2)	1.12(16) [3]	-	M1+E2

Table 6.1: Continued...

E_γ (in keV)	E_i (in keV)	$J_i^\pi \rightarrow J_f^\pi$	I_γ [1]	R_{DCO} (Err)	Δ_{PDCO} (Err)	Deduced Multipolarity
206.6(2)	3066.9	$25/2^-$	6.2(7)	1.33(18) [4]	-	M1+E2
222.6(1)	608.1	$9/2^-$	29.0(20)	-	-	E3 [8]
262.5(3)	2528.6	$19/2^-$	2.0(3)	0.86(9) [3]	-0.19(9)	M1+E2
263.8(1)	2860.3	$23/2^-$	8.4(8)	1.51(19) [5]	-0.05(2)	M1+E2
298.7(3)	2018.1	$17/2^-$	2.3(2)	1.52(25) [4]	-0.19(9)	M1+E2
307.8(2)	1303.2	$13/2^-$	18.2(15)	1.50(15) [5]	-0.07(2)	M1+E2
320.6(3)	2040.0	$17/2^-$	4.0(3)	1.34(18) [4]	-0.13(5)	M1+E2
339.1(2)	2800.8	$21/2^-$	4.6(4)	1.09(11) [3]	-0.25(7)	M1(+E2)
345.8(2)	3146.7	$23/2^-$	1.8(2)	1.15(11) [3]	-0.27(10)	M1+E2
347.6(3)	2461.7	$19/2^-$	0.4(1)	-	-	E2
385.2(1)	2425.5	$19/2^-$	3.7(5)	1.78(17) [6]	-0.27(9)	M1+E2
385.5(1)	385.5	$3/2^+$	100(5)	-	-	M1+E2 [8]
387.3(1)	995.4	$11/2^-$	64.0(60)	1.39(12) [5]	-0.09(2)	M1+E2
407.7(2)	2425.5	$19/2^-$	5.0(4)	1.56(15) [5]	-0.08(3)	M1+E2
411.8(1)	3688.4	$31/2^-$	1.8(3)	1.69(35) [2]	-0.07(3)	M1+E2
416.5(2)	1719.3	$15/2^-$	31.0(40)	1.86(16) [2]	-0.08(3)	M1+E2
421.2(1)	3567.9	$25/2^-$	2.1(2)	1.08(15) [3]	-0.19(7)	M1(+E2)
470.2(3)	3066.9	$25/2^-$	0.5(1)	-	-	E2
534.9(2)	2800.8	$21/2^-$	0.5(1)	-	-	E2
557.1(1)	2596.9	$21/2^-$	3.6(5)	1.06(18) [4]	0.28(9)	E2
557.5(2)	1552.9	$13/2^+$	39.0(30)	1.03(10) [3]	0.13(2)	E1
560.9(2)	2113.8	$15/2^-$	30.0(31)	1.07(11) [7]	0.09(1)	E1
578.2(1)	2596.6	$21/2^-$	6.5(6)	1.02(14) [5]	0.14(3)	E2
613.6(3)	3760.1	$27/2^-$	0.7(1)	-	-	E2
685.1(1)	3146.7	$23/2^-$	0.5(1)	0.61(10) [3]	0.21(8)	E2
695.4(1)	1303.2	$13/2^-$	22.0(21)	1.03(8) [5]	0.10(1)	E2

Table 6.1: Continued...

E_γ (in keV)	E_i (in keV)	$J_i^\pi \rightarrow J_f^\pi$	I_γ [1]	R_{DCO} (Err)	Δ_{PDCO} (Err)	Deduced Multipolarity
706.6(2)	2425.5	$19/2^-$	7.4(8)	1.09(11) [6]	0.08(2)	E2
714.8(2)	2018.1	$17/2^-$	7.5(8)	1.00(9) [6]	0.09(2)	E2
723.9(2)	1719.3	$15/2^-$	7.7(8)	0.99(8) [2]	0.17(3)	E2
737.2(2)	2040.0	$17/2^-$	4.7(5)	1.01(10) [6]	0.22(5)	E2
767.1(1)	3567.9	$25/2^-$	1.6(2)	0.56(9) [3]	0.05(2)	E2
810.6(2)	2113.8	$15/2^-$	4.0(4)	1.95(28) [6]	-0.12(4)	M1+E2

The relative intensity of the γ rays were obtained from the singles spectrum of Clover detector with proper efficiency correction. However, the relative intensities for the doublets at 557.1-, 557.5- and 262.5-, 263.8-keV were separately obtained from gated spectra with proper normalization with the singles measurement. Gated spectra were used to obtain the relative intensities of 385.2- and 411.8-keV transitions as well.

The spin and the parity of the states were deduced in the previous work from the multipolarities of the γ rays of ^{197}Tl, determind from the angular distribution measurements [4]. These measurements, however, would not provide unambiguous assignment of parity of the states. The polarization measurement, carried out in the present work, helped to assign the parity of the states. The parallel ($N_{\parallel}$) and perpendicular (a(E_γ)*$N_{\perp}$) counts for the 695- and 387-keV γ rays, belonging to the lowest two transitions in the $9/2^-$ band in ^{197}Tl, are shown in Fig. 6.4,

[1] Relative γ ray intensities are estimated from singles measurement and normalized to 100 for the total intensity of 385.5 keV γ rays.

[2] From 706.6 keV (E2) DCO gate;

[3] From 560.9 keV (E1) DCO gate;

[4] From 723.9 keV (E2) DCO gate;

[5] From 714.8 keV (E2) DCO gate;

[6] From 695.4 keV (E2) DCO gate;

[7] From 152.4 keV (M1) DCO gate;

[8] From ref. [4];

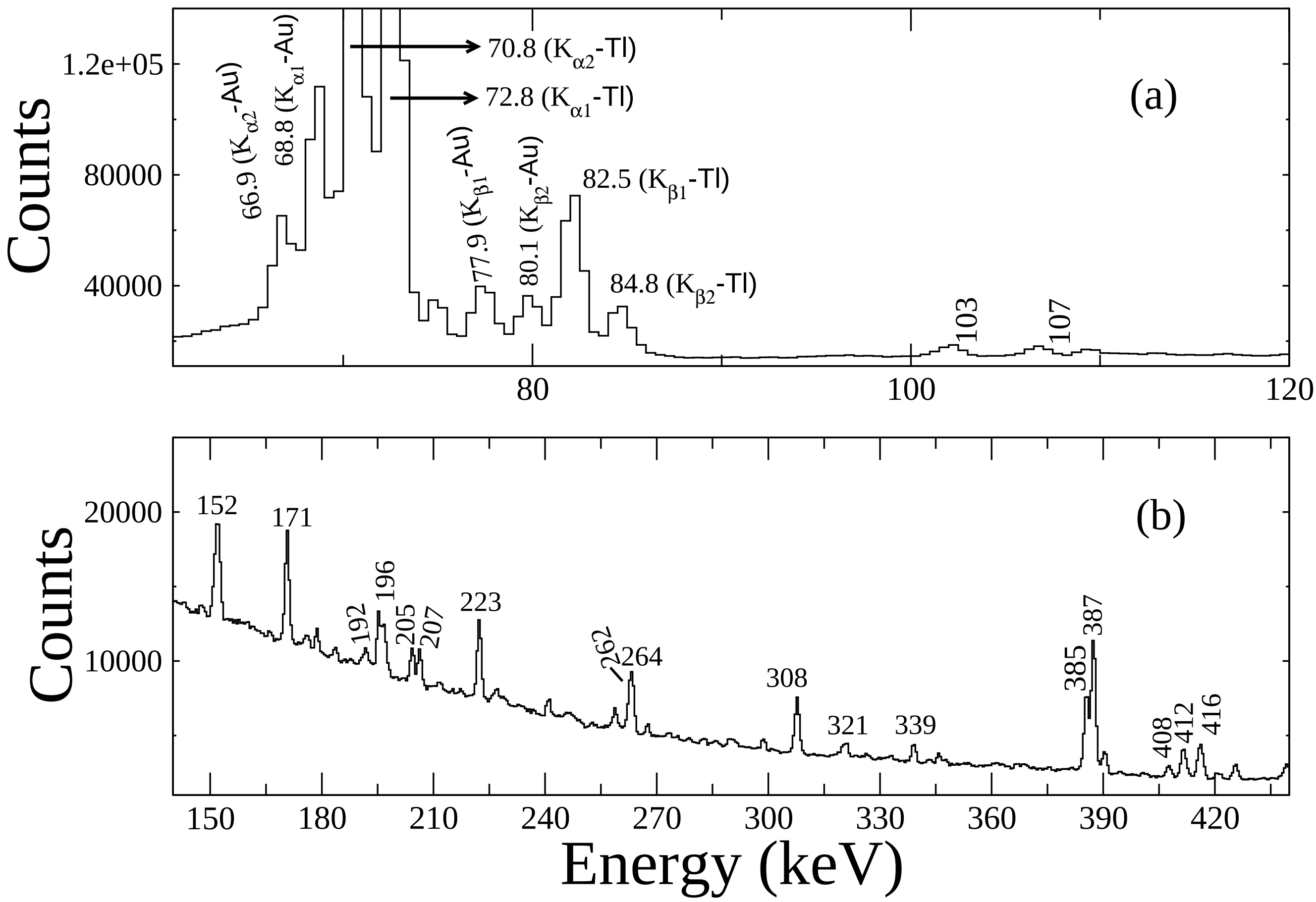

Figure 6.2: Singles in-beam gamma ray spectra ((a) lower energy and (b) higher energy part) for one segment of the LEPS detector.

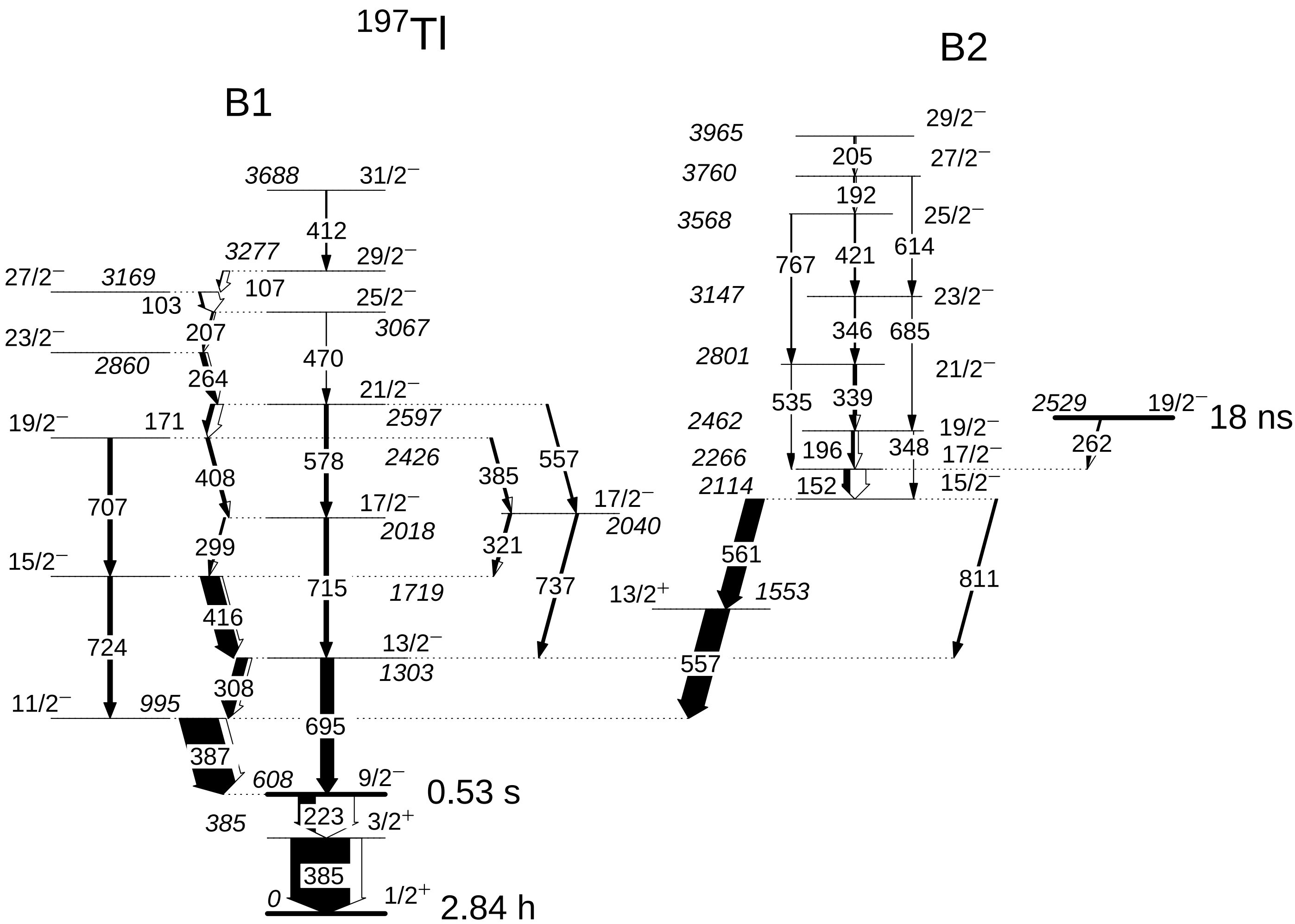

Figure 6.3: Level scheme of ^{197}Tl obtained from this work.

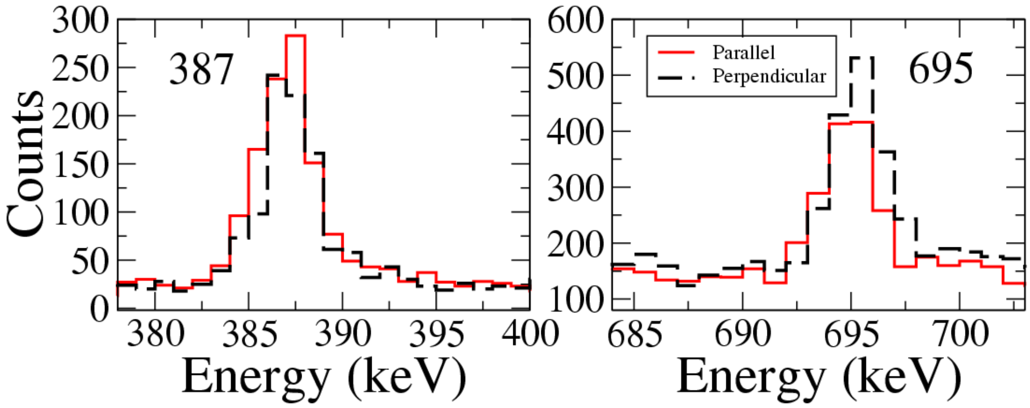

Figure 6.4: The perpendicular (dashed-black colour) and parallel (solid-red colour) components of the two γ rays in ^{197}Tl, obtained from PDCO analysis in the present work. 387-keV is a magnetic type transition where as 695-keV is a electric type transition.

as obtained from the polarization measurement. The results of this measurements clearly seen to corroborate with those in Ref.[4].

The perpendicular and parallel counts, obtained from the polarization measurements, corresponding to the 557.5- and 560.9-keV γs from 1552.9- and 2113.8-keV states, respectively are shown in Fig. 6.5. These measurements along with the DCO ratios (see Table 6.1) of these γ rays indicate that both of these are E1 transitions and hence the spin-parity of the 1552.9- and 2113.8-keV states are $13/2^+$ and $15/2^-$, respectively. The multipolarity of the 810.6-keV γ transition, from the 2113.8-keV state to the 1303.2-keV state, has been correctly found to be of mixed dipole (M1+E2) character, in the present work, from the DCO and the polarization measurements (see Fig. 6.5 and Table 6.1). This lends additional support to the new J^π assignments of the 2113.8-keV and the 1552.9-keV states in this work. It may be pointed out that the level schemes of ^{195}Tl and ^{197}Tl are very similar [4] and hence, the spin-parity of the 1484- and 2037-keV states in ^{195}Tl may be assigned as $13/2^+$ and $15/2^-$, respectively. Moreover, a better statistics for the higher lying γ rays, collected in the present work, helped to establish definite J^π assignments of the 3169.5- and 3276.7-keV states which were only tentatively assigned in the previous work [4].

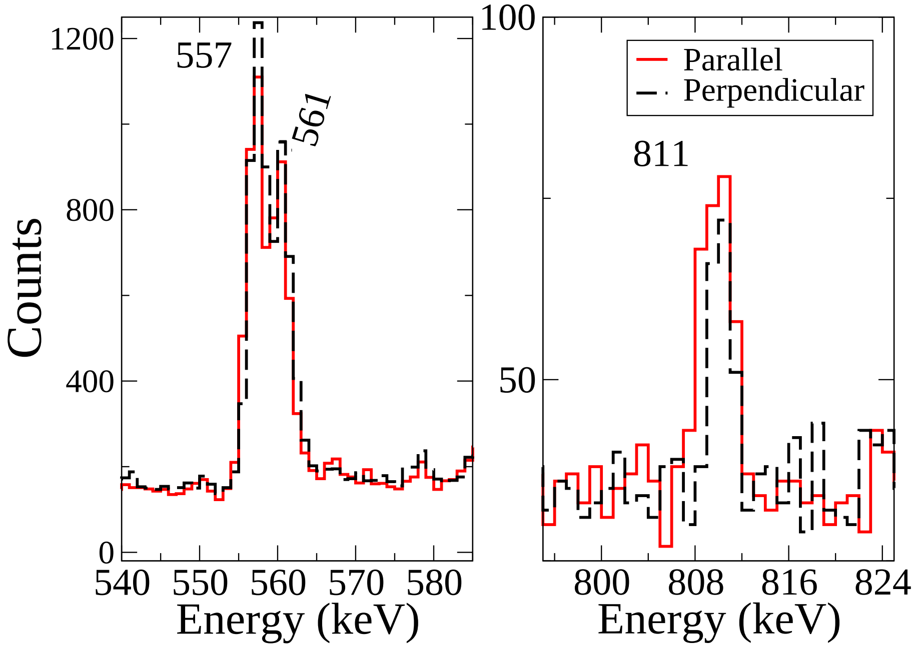

Figure 6.5: The perpendicular (dashed-black colour) and parallel (solid-red colour) components of the three γ rays in ^{197}Tl, obtained from PDCO analysis in the present work.

6.3 Discussion

The $h_{9/2}$, $i_{13/2}$ and $s_{1/2}$ orbitals are available for the odd proton near the Fermi surface in Thallium nuclei. On the other hand, the $i_{13/2}$, $f_{5/2}$ and $p_{3/2}$ orbitals are available for the neutrons near the Fermi surface in these nuclei. A $13/2^+$ state may originate in odd-mass Thallium isotopes from the occupation of the $\pi[606]13/2^+$ "intruder" orbital by the odd proton and this high-Ω orbital may drive the nucleus to a collective oblate shape. In ^{197}Tl a $13/2^+$ state has been identified, in this work, at an excitation energy of 1552.9 keV. This $13/2^+$ state is proposed to have the above "intruder" configuration.

The variations of the excitation energies of the $\pi[606]13/2^+$ "intruder" configuration in the odd-A Tl isotopes are shown in Fig. 6.6 as a function of the neutron number. The same for the Bi isotopes are also shown in this Figure for comparison. The excitation energy of the $13/2^+$ state in ^{197}Tl, shown as an open circle, has been seen to follow the systematic behaviour of the odd-A Tl isotopes. For the lighter isotopes, the excitation energy of the $13/2^+$ state in Tl

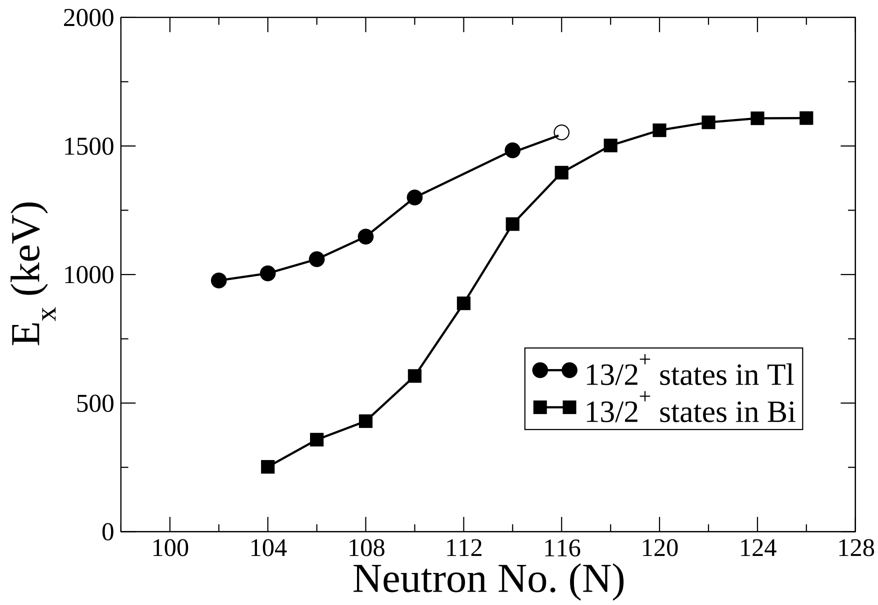

Figure 6.6: Excitation energy (E_x) of $13/2^+$ state in Tl and Bi isotopes as a function of neutron number. The excitation energy of the $13/2^+$ state in ^{197}Tl from the present work is shown as an open circle.

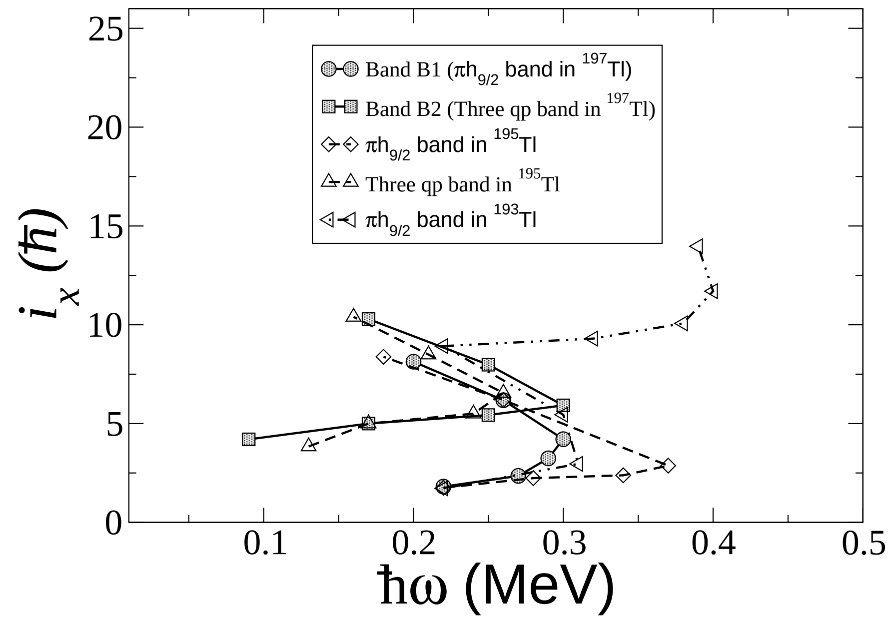

Figure 6.7: Experimental alignments (i_x) as a function of the rotational frequency ($\hbar\omega$) for the $\pi h_{9/2}$ band in ^{193}Tl [8], ^{195}Tl [4] and ^{197}Tl along with three quasiparticle (qp) band in ^{195}Tl [4] and ^{197}Tl. The Harris reference parameters are chosen to be $J_0 = 8.0\hbar^2\ MeV^{-1}$ and $J_1 = 40\hbar^4$ MeV^{-3}.

isotopes are at much higher energies compared to those in Bi isotopes. This is understood from the fact that the proton Fermi level of Bi isotpes lies above the $Z = 82$ shell closure and hence, the $\pi i_{13/2}$ orbital can be accessible at lower energies for oblate deformation. As the neutron number increases, the excitation energy of the $13/2^+$ state is observed to increase for both Bi and Tl, and tends to saturate, suggesting spherical shapes for heavier isotopes.

Band B1, based on $9/2^-$ band head, has been proposed to built on $\pi h_{9/2}$ configuration in comparison with the similar bands observed in other odd-A Tl nuclei [4, 8]. The alignments (i_x) for this band in ^{193}Tl [8], ^{195}Tl [4] and ^{197}Tl are shown in Fig. 6.7 as a function of rotational frequency $\hbar\omega$. It can be seen from this Figure that the initial alignments of all the three isotopes are very similar. The experimental band crossing of the $\pi h_{9/2}$ band in ^{197}Tl, ^{195}Tl and ^{193}Tl [8] take place at the rotational frequencies of $\hbar\omega \sim 0.30$ MeV, 0.36 MeV and 0.28 MeV, respectively. Although there are differences in the crossing frequencies, the gain in alignments after the band crossing are also seen to be very similar for three isotopes. The first band crossing observed in ^{193}Tl [8] was interpreted as due to the neutron pair alignments in the $i_{13/2}$ orbital. In comparison to that, the observed band crossing of band B1 in ^{197}Tl may also be attributed to the neutron pair alignment in $\nu i_{13/2}$ orbital. Therefore, the configuration of the higher lying states in this band (above 2425.5-keV) would be $\pi h_{9/2} \otimes \nu i^2_{13/2}$.

The excitation energy of the band B2 in ^{197}Tl indicates that this negative parity band is based on a three quasiparticle (qp) configuration. This band is also very similar to the one in ^{195}Tl. The plots of the i_x values for this three qp band (B2) are also shown in Fig. 6.7 along with those for ^{195}Tl [4]. A similar increase in the alignment for this band compared to the band B1 (at lower $\hbar\omega$) is observed for both the nuclei, indicating similar configuration for this band in these two nuclei. Considering that the band B2 is above the $\pi i_{13/2}$ state and the availability of Nilsson levels for the neutrons, near the Fermi surface, in these two Tl isotopes, a $\pi i_{13/2} \otimes \nu i_{13/2} p_{3/2}$ configuration is proposed for this three qp band. A strong transition from the bandhead at 2113.9 keV of this band to the $\pi i_{13/2}$ configuration at 1552.9-keV supports this assignment. The experimental band crossings of this band in ^{197}Tl and ^{195}Tl have been observed to take place at $\hbar\omega \sim 0.30$ MeV and 0.26 MeV, respectively.

6.3.1 TRS calculations

The total Routhian surface (TRS) calculations have been performed for the $\pi h_{9/2}$ (band B1) and the $\pi i_{13/2}$ configuration in ^{197}Tl. The contour plots of the TRSs, calculated for the band B1 have been shown in Fig. 6.8. This Figure clearly shows a minimum in the TRS at a deformation of $\beta_2 \sim 0.15$ and $\gamma \sim -58^o$, indicating an oblate shape for ^{197}Tl for the $\pi h_{9/2}$ configuration. The surfaces calculated for the $\pi i_{13/2}$ configuration in ^{197}Tl has been shown in Fig. 6.9. The minimum in the Routhian surfaces, in this case, has been found to be at $\beta_2 \sim 0.08$ and $\gamma \sim -50^o$, indicating an oblate shape with very small deformation. The observation of rotational band based on $\pi h_{9/2}$ configuration and the non-observation of any rotational band on $\pi i_{13/2}$ configuration are corroborated by the deformation parameters obtained from the TRS calculations.

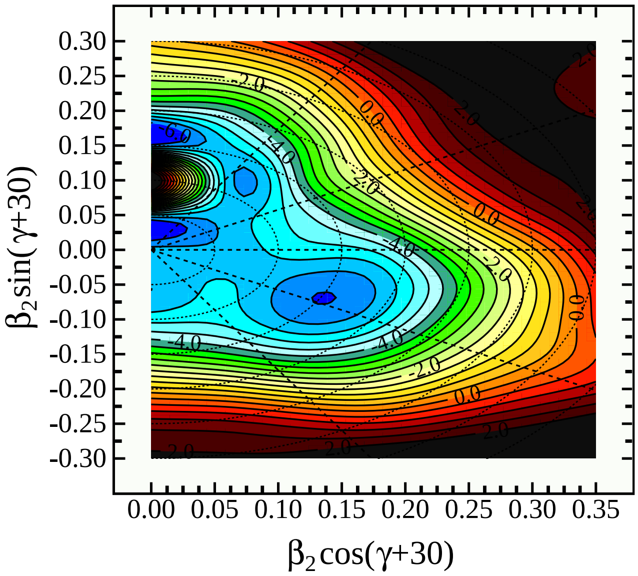

Figure 6.8: Contour plots of the total Routhian surfaces (TRSs) in the β_2 - γ deformation mesh for the $\pi h_{9/2}$ configuration of the band B1 in ^{197}Tl. The contours are 400 keV apart.

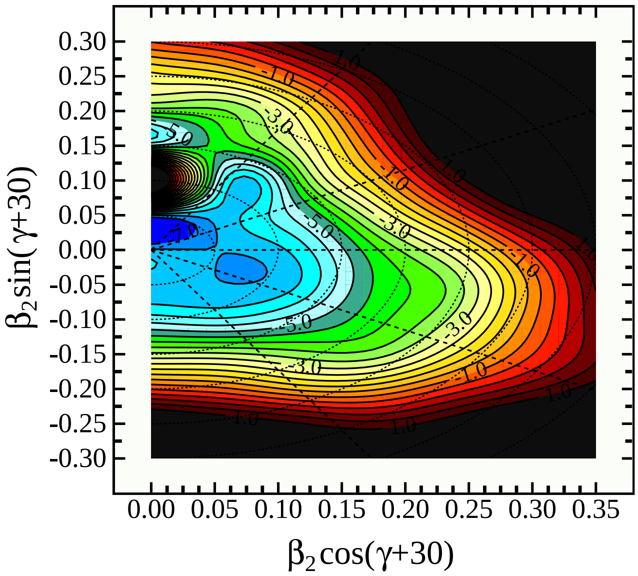

Figure 6.9: Contour plots of the total Routhian surfaces (TRSs) in the β_2 - γ deformation mesh for the $\pi i_{13/2}$ configuration of the $13/2^+$ state in ^{197}Tl. The contours are 400 keV apart.

6.4 Summary

The γ-ray spectroscopy of the odd-A ^{197}Tl has been studied in the fusion-evaporation reaction of ^{197}Au target with ^{4}He beam at 48 MeV. An improved level scheme of ^{197}Tl is presented in this work. The DCO ratio and the polarization asymmetry ratio measurements have been carried out to assign the spins and parities of the levels. A proton $i_{13/2}$ intruder state has been identified for the first time in this nucleus, in the present work. A negative parity for band B2 has been assigned from polarization measurements and new a configuration has been assigned for this three quasiparticle band. TRS calculations show oblate deformation for the $\pi h_{9/2}$ configuration and a near spherical shape for the $\pi i_{13/2}$ configuration in ^{197}Tl.

Bibliography

[1] R.M. Diamond and F.S. Stephens, Nucl. Phys. **A 45**, 632 (1963).

[2] V.T. Gritsyna and H.H. Foster, Nucl. Phys. **A 61**, 129 (1965).

[3] J.O. Newton, S.D. Cirilov, F.S. Stephens and R.M. Diamond Nucl. Phys. **A 148**, 593 (1970).

[4] R.M. Lieder et al., Nucl. Phys. **A 299**, 255 (1978).

[5] A.J. Kreiner et al., Phys. Rev. **C 38**, 2674 (1988).

[6] M.G. Porquet et al., Phys. Rev. **C 44**, 2445 (1991).

[7] W.Reviol et al., Phys. Scr. **T 56**, 167 (1995).

[8] W.Reviol et al., Nucl. Phys. **A 548**, 331 (1992).

[9] R. B. Firestone et al., Table of Isotopes (John Wiley and Sons, Inc., New York (1999)).

[10] D. C. Radford, Nucl. Instrum. Methods Phys. Res. **A 361**, 297 (1995).

[11] Huang Xiaolong and Zhou Chunmei, Nucl. Data Sheets **104**, 283 (2005).

Chapter 7

Study of magnetic rotation in ^{198}Bi

7.1 Introduction

"Magnetic rotation (MR)", as mentioned in section 2.7, is one of the most interesting phenomena in nuclear structure physics which are observed in near-spherical nuclei by the coupling of particles and holes in high-j orbitals. These bands are expected for the nuclei in mass region $A \sim 190$ with proton Fermi level near the spherical shell closure at $Z = 82$. Because of the proximity of the spherical magic number, the shapes of many of the Pb and Bi nuclei are near-spherical. Since the proton Fermi level in these nuclei lies above the $Z = 82$ magic gap, the high-j $h_{9/2}$ and $i_{13/2}$ orbitals are available for the proton particles. On the other hand, the neutron holes can occupy the $i_{13/2}$ orbital. For small oblate deformation, the protons occupy the high-Ω Nilsson orbitals and neutron holes are in low-Ω Nilsson orbitals. Therefore, these nuclei posses ideal conditions for the occurrence of MR bands. The first MR band was, indeed, observed in Pb isotopes and subsequently MR bands were observed in several other Pb and Bi isotopes in this region and in the nuclei in other regions also [1, 2, 3, 4, 5]. However, in many cases the excitation energies and definite spin-parities could not be assigned for the MR bands, in particular for the Bi isotopes [6, 7]. Therefore, proper characterization could not be made for these bands as the configurations assignments were uncertain.

The information about the high spin states in ^{198}Bi is very limited. Apart from the ground state ($T_{1/2}$ = 10.3 min), two other low-lying isomeric states were only known until recently. Among these, the (7^+) state ($T_{1/2}$ = 11.6 min) decays by β-decay and no γ-transition is known from this state. Therefore, the excitation energy of this state remains unknown. A 10^- isomeric state was reported by U. Hagemann et al. [8], in the year 1972, at an excitation energy of 248 keV with respect to the 11.6-min isomeric state. This state was interpreted as a member of the $|\ \nu i^{-1}_{13/2} \otimes \pi h_{9/2}; J\rangle$ multiplet. More recently, excited states in ^{198}Bi were studied by X.H. Zhou et al. [9] through γ-ray spectroscopy following ^{187}Re(^{16}O,5n) reaction using six Compton suppressed HPGe detectors. The γ rays above the 10^- isomer in this nucleus were assigned from the γ-ray excitation functions and a level scheme was proposed by them from the γ-γ coincidence measurements. In this measurement, definite spin parity were assigned for a few states only and the level scheme was known upto $\sim$ 4 MeV. The higher lying states in ^{198}Bi have been interpreted by considering the coupling of the $h_{9/2}$ proton with the high-spin states observed in ^{197}Pb above the $13/2^+$ isomeric state. Later on, G. Zwartz et al. [6] proposed three unconnected MR type bands in ^{198}Bi, namely Band 1, Band 2 and Band 3 from the measurement of B(M1)/B(E2) ratios. In this experiment γ-ray transitions were assigned in ^{198}Bi by examining associated BGO calorimeter energy spectrum. However, neither the spin-parity (J^π) nor the excitation energies of the states are known and hence, the configuration of these bands also remained uncertain.

As a part of this thesis work, detailed γ-ray spectroscopy of ^{198}Bi, including the MR bands, has been studied in order to establish the connection between the MR bands and the lower lying states in this nucleus. Definite J^π assignments have been made for most of the states in the present study.

7.2 Experiment and Results

Excited states of ^{198}Bi were populated via the fusion-evaporation reactions ^{185,187}Re(^{16}O, xn)^{198}Bi at 112.5 MeV of beam energy from the 15-UD Pelletron at IUAC, New Delhi, India using the INGA array (INGA phase-IV). The target was a thick (18.5 mg/cm^2) natural rhenium target. The recoils were stopped inside the target itself. The isotopic ratio of ^{185}Re and ^{187}Re in the natural rhenium is 37:63. The clover detectors in the phase-IV of INGA array were arranged in five angles with respect to the beam direction having four clovers each at 90° and 148°, two clovers each at 123° and 57° and three clovers at 32° angles. List mode data were recorded using γ-γ-γ trigger. About 2.4 × 10^8 coincidence events were recorded in this experiment. E_γ-E_γ matrix and E_γ-E_γ-E_γ cube were constructed from the collected coincidence data. To construct these, a coincidence window of ±400 ns was selected. The clover detectors were calibrated for γ-ray energies and efficiencies by using ^{133}Ba and ^{152}Eu radioactive sources. The multipolarities of the γ-ray transitions have been determined from the angular correlation analysis using the method of directional correlation from the oriented states (DCO) ratio. For the DCO ratio analysis, the coincidence events were sorted into an asymmetry matrix with data from 148° detectors on one axis and 90° detectors on the other axis. Definite parities of the excited states have been assigned from the integrated polarization asymmetry (IPDCO) ratio, as described in section 3.6.3, from the parallel and perpendicular scattering of a γ-ray photon inside the detector medium. The correction due to the asymmetry in the array and response of the Clover segments, was checked using ^{152}Eu and ^{133}Ba sources and was found to be 0.88(1).

The polarization method was verified from the γ rays of known electric or magnetic character. The parallel ($N_{\parallel}$) and perpendicular (a(E_γ)*$N_{\perp}$) counts for the three γ rays in ^{198}Bi are shown in Fig. 7.1. It can be clearly seen that the counts in the parallel scattered component is more than the perpendicular one for the 626-keV and 673-keV γ rays which are known to be of magnetic type from ref. [9]. The 630-keV transition, the nature of which was not known earlier, has also been shown in Fig. 7.1, It is evident that the perpendicular scattered component is more than the parallel one for this γ ray and, hence, this transition is assigned as electric-type in the present work. Similarly, the type of several other transitions were obtained, in this work, from the IPDCO measurements.

An improved level scheme, of ^{198}Bi obtained in this work, is given in Fig. 7.2. The deduced excitation energy, spin and parity of the excited levels and the multipolarity of the γ rays, to-

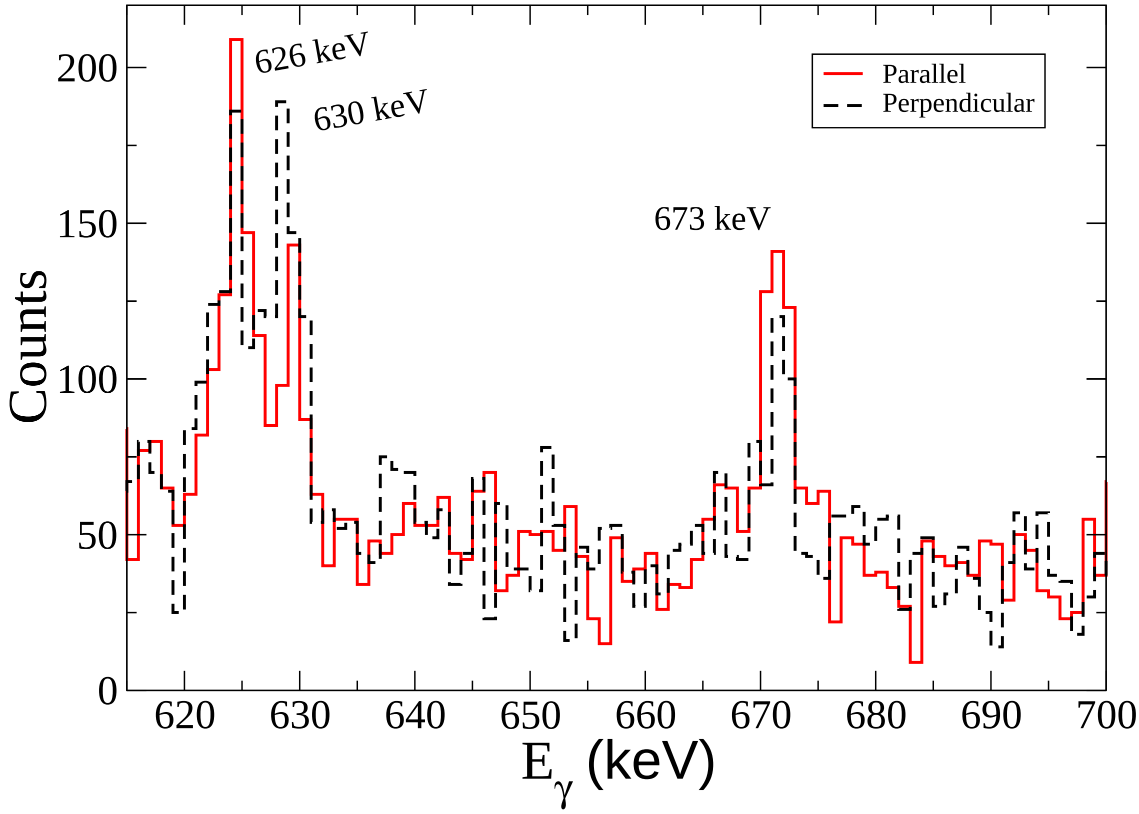

Figure 7.1: The perpendicular (dashed black coloured) and parallel (solid red coloured) components of the three γ rays in ^{198}Bi, obtained from IPDCO analysis in the present work. 626-keV and 673-keV transitions are known as magnetic type transition where as 630-keV transition is an electric type transition.

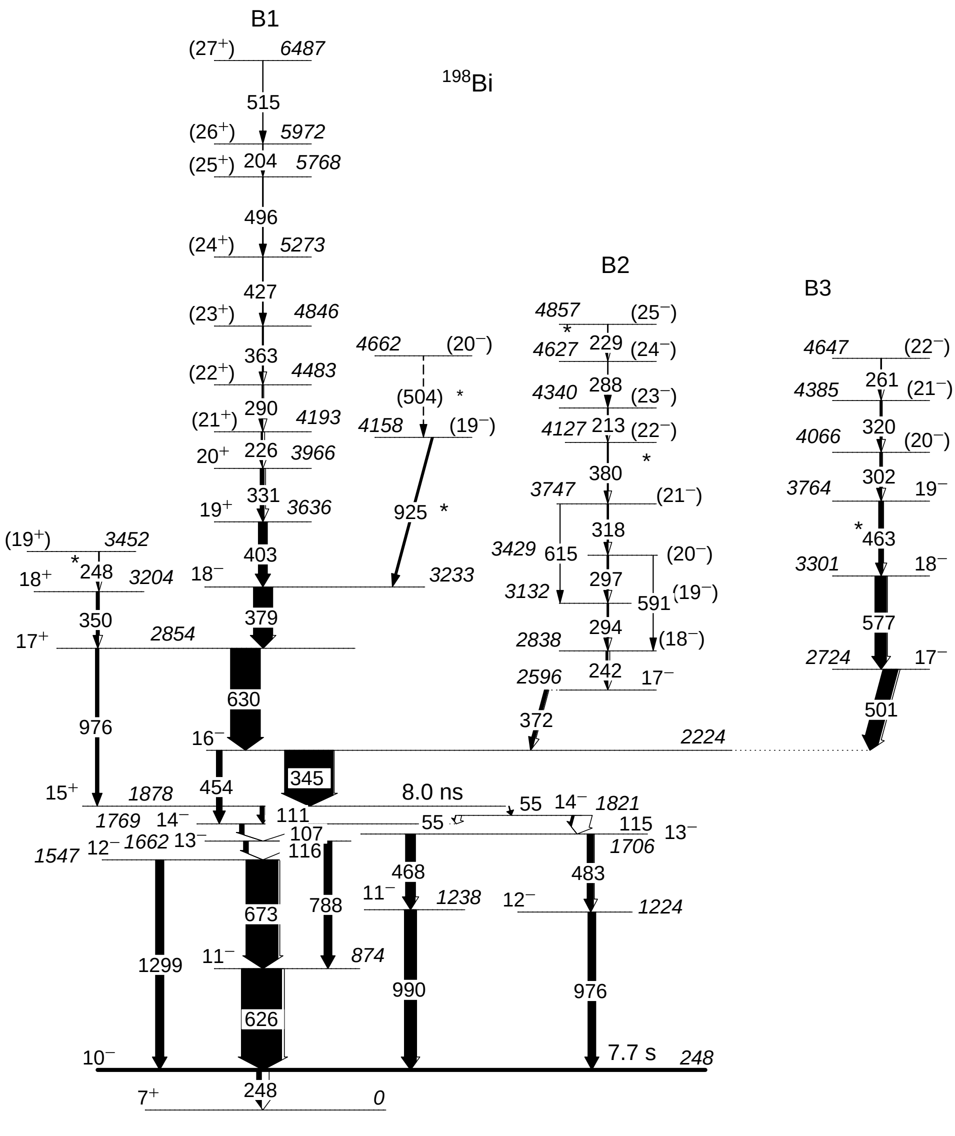

Figure 7.2: Level scheme of ^{198}Bi obtained from this work. The new γ rays are indicated by asterisks.

gether with other relevant information concerning their placement in the proposed level scheme, are summarized in Table 7.1.

Representative single gated γ-ray spectra are shown in Figs. 7.3(a) and 7.3(b). These spectra show the known γ lines corresponding to the low-lying transitions and a few γ-lines (242-, 297-, 318-, 226-, 501- and 577-keV) belonging to the proposed MR bands. The other weaker γ lines could be observed in the sum-gated spectra which have been discussed later on. The 55-keV γ-ray doublet, reported in Ref. [9], could not be observed as the energy threshold was little more than 55-keV in the present experiment. The 223-keV γ ray, reported by X.H. Zhou et al. [9], is also not observed in the present data. So, it was not placed in the level scheme shown in Fig. 7.2.

Table 7.1: Energies (E_γ), intensities (I_γ), DCO ratios (R_{DCO}), IPDCO ratios (Δ_{IPDCO}) and deduced multipolarities of the γ rays in ^{198}Bi. The energies of initial states (E_i) and spins and parities of initial (J_i^π) and final (J_f^π) states are also given.

E_γ (in keV)	E_i (in keV)	$J_i^\pi \rightarrow J_f^\pi$	I_γ [1]	R_{DCO} (Err)	Δ_{IPDCO} (Err)	Deduced Multipolarity
106.6(2)	1769.0	$14^- \rightarrow 13^-$	9.6(12)	0.95(24) [2]	-	M1+E2
110.8(4)	1878.2	$15^+ \rightarrow 14^-$	8.6(11)	0.98(26) [3]	-	E1
115.2(3)	1821.5	$14^- \rightarrow 13^-$	5.1(7)	0.65(14) [4]	-	M1+E2
115.8(2)	1662.4	$13^- \rightarrow 12^-$	10.0(12)	1.05(25) [5]	-	M1+E2
203.5(3)	5971.3	$(26^+) \rightarrow (25^+)$	1.0(2)	-	-	(M1) [6]
212.9(2)	4339.7	$(23^-) \rightarrow (22^-)$	1.1(2)	-	-	(M1) [6]
226.2(6)	4192.5	$(21^+) \rightarrow 20^+$	3.0(4)	-	-	(M1) [6]
229.2(1)	4856.7	$(25^-) \rightarrow (24^-)$	0.6(1)	-	-	(M1)
242.2(2)	2838.2	$(18^-) \rightarrow 17^-$	4.3(5)	-	-	(M1) [6]
248.3(3)	3452.2	$(19^+) \rightarrow 18^+$	0.8(1)	-	-	(M1+E2)
261.2(4)	4646.6	$(22^-) \rightarrow (21^-)$	1.1(2)	-	-	(M1) [6]

Table 7.1: Continued...

E_γ (in keV)	E_i (in keV)	$J_i^\pi \rightarrow J_f^\pi$	I_γ [1]	R_{DCO} (Err)	Δ_{IPDCO} (Err)	Deduced Multipolarity
287.8(3)	4627.5	$(24^-)\rightarrow(23^-)$	0.8(1)	-	-	(M1)[6]
290.3(2)	4482.8	$(22^+)\rightarrow(21^+)$	1.6(2)	-	-	(M1)[6]
294.1(3)	3132.3	$(19^-)\rightarrow(18^-)$	2.8(3)	-	-	(M1)[6]
296.6(3)	3429.3	$(20^-)\rightarrow(19^-)$	2.4(3)	-	-	(M1)[6]
301.8(3)	4065.5	$(20^-)\rightarrow 19^-$	4.2(6)	-	-	(M1)[6]
317.5(3)	3747.0	$(21^-)\rightarrow(20^-)$	2.1(3)	-	-	(M1)[6]
319.8(4)	4385.3	$(21^-)\rightarrow(20^-)$	3.2(5)	-	-	(M1)[6]
330.6(2)	3966.3	$20^+\rightarrow 19^+$	8.2(10)	1.01(20)[7]	-0.27(10)	M1
345.5(1)	2223.6	$16^-\rightarrow 15^+$	100.0(30)	0.97(10)[7]	0.14(5)	E1
349.9(4)	3204	$18^+\rightarrow 17^+$	5.0(4)	0.94(26)[3]	-	M1+E2
362.9(3)	4845.7	$(23^+)\rightarrow(22^+)$	1.6(2)	-	-	(M1)[6]
372.4(2)	2596.0	$17^-\rightarrow 16^-$	7.2(6)	0.96(17)[7]	-	M1
379.1(1)	3233.2	$18^-\rightarrow 17^+$	39.0(20)	1.01(14)[3]	0.45(17)	E1
379.8(1)	4126.8	$(22^-)\rightarrow(21^-)$	1.8(2)	-	-	(M1)
402.6(4)	3635.8	$19^+\rightarrow 18^-$	18.3(12)	0.91(10)[7]	0.41(17)	E1
426.5(3)	5272.2	$(24^+)\rightarrow(23^+)$	1.3(2)	-	-	(M1)[6]
453.7(3)	2223.6	$16^-\rightarrow 14^-$	11.4(7)	0.61(12)[5]	0.20(5)	E2
462.5(2)	3763.7	$19^-\rightarrow 18^-$	8.90(7)	0.98(19)[3]	-	M1
468.2(1)	1706.3	$13^-\rightarrow 11^-$	19.8(10)	0.53(10)[3]	0.18(4)	E2
483.4(1)	1706.3	$13^-\rightarrow 12^-$	13.0(12)	1.01(25)[3]	-0.29(10)	M1(+E2)
495.5(4)	5767.8	$(25^+)\rightarrow(24^+)$	1.2(2)	-	-	(M1)[6]
500.8(1)	2724.4	$17^-\rightarrow 16^-$	30.4(15)	0.97(11)[3]	-0.21(9)	M1
504	4662	$(20^-)\rightarrow(19^-)$	1.0(1)	-	-	-
515.1(5)	6486.4	$(27^+)\rightarrow(26^+)$	0.8(2)	-	-	(M1)[6]
576.7(1)	3301.2	$18^-\rightarrow 17^-$	23.7(15)	1.04(26)[3]	-0.29(10)	M1
591.3(3)	3429.3	$(20^-)\rightarrow(18^-)$	0.5(1)	-	-	(E2)[6]

Table 7.1: Continued...

E_γ (in keV)	E_i (in keV)	$J_i^\pi \rightarrow J_f^\pi$	I_γ [1]	R_{DCO} (Err)	Δ_{IPDCO} (Err)	Deduced Multipolarity
615.2(5)	3747.0	$(21^-)\rightarrow(19^-)$	0.6(1)	-	-	(E2) [6]
625.8(1)	873.8	$11^-\rightarrow10^-$	82.9(29)	1.07(16) [3]	-0.18(6)	M1(+E2)
630.5(1)	2854.1	$17^+\rightarrow16^-$	61.1(25)	0.99(10) [3]	0.27(7)	E1
672.8(1)	1546.6	$12^-\rightarrow11^-$	66.0(24)	0.84(12) [3]	-0.31(6)	M1(+E2)
787.5(1)	1662.4	$13^-\rightarrow11^-$	16.2(11)	0.63(12) [3]	0.43(9)	E2
924.8(2)	4158.0	$(19^-)\rightarrow18^-$	4.3(6)	-	-	(M1+E2)
975.9(2)	1223.8	$12^-\rightarrow10^-$	16.0(12)	0.54(11) [3]	0.09(2)	E2
976.4(3)	2854.1	$17^+\rightarrow15^+$	7.1(6)	0.65(18) [5]	-	E2
990.1(2)	1238.1	$11^-\rightarrow10^-$	24.6(10)	1.61(29) [3]	-0.21(6)	M1+E2
1298.7(2)	1546.6	$12^-\rightarrow10^-$	17.0(8)	0.62(14) [3]	0.19(7)	E2

Zhou et al. could establish the definite spin and parity of the levels up to the 1662-keV from the angular distribution measurements. The 107-keV transition, feeding to this level from the 1769-keV level, has been assigned as mixed (M1+E2) transition in this work and, hence, the spin-parity of 14^- has been assigned for the 1769-keV level. The DCO and the polarization measurement for the 454-keV transition, feeding from the 2224-keV level to this 14^- level, indicate that this is an E2 transition. Therefore, spin-parity of the 2224-keV state has been assigned as 16^-. On the other hand, the multipolarity of a strong 345-keV transition, decaying from this level to the 1878-keV level, has been found to be an E1 transition. This allows us

[1] Relative γ ray intensities are estimated from prompt spectra and normalized to 100 for the total intensity of 345.5 keV γ rays.

[2] From 115.8 keV (M1+E2) DCO gate;

[3] From 345.5 keV (E1) DCO gate;

[4] From 975.9 keV (E2) DCO gate;

[5] From 625.8 keV (M1(+E2)) DCO gate;

[6] Adopted from ref. [6];

[7] From 379.1 keV (E1) DCO gate;

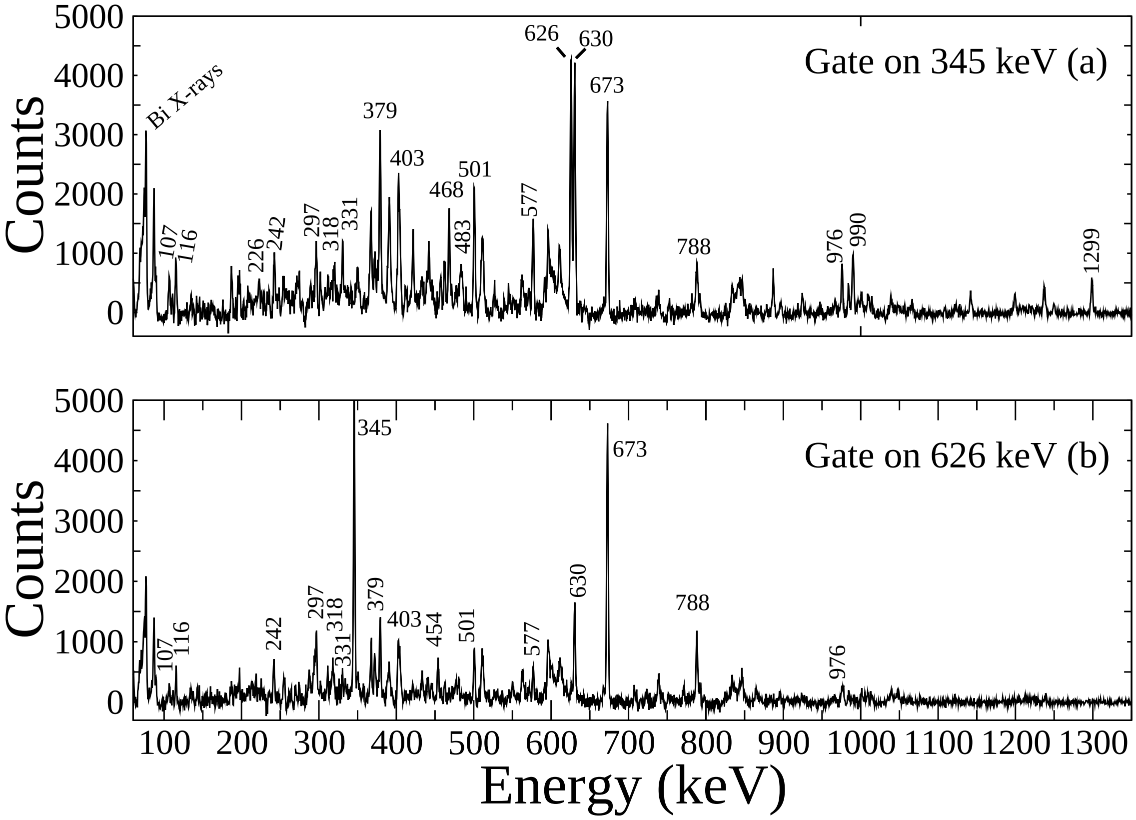

Figure 7.3: Single gated spectra of ^{198}Bi gated by 345-keV (a) and 626-keV (b) transitions. The unmarked peaks are the contaminants.

to determine, firmly, the spin-parity of the isomeric 1878-keV state as 15^+. The DCO ratio of the 630-keV transition indicate its dipole nature and, as mentioned earlier, polarization measurements show that this is an electric transition. Therefore, another change of parity occurs between the 2224- and the 2854-keV levels and a $J^\pi = 17^+$ is assigned for the 2854-keV level. The 976-keV γ-ray from the 2854-keV level to the 1878-keV isomer, has been found to be an E2 transition. This lends further support to the J^π assignment of the 2854-keV level. The J^π assignments of the levels at 2224 and 2854 keV are important for the assignment of spin and parity and, hence, the configuration of the proposed MR bands in ^{198}Bi. The spin and parity assignments of the other levels in ^{198}Bi have been done from the results of the DCO and polarization measurements. However, the DCO ratios of the transitions belonging to the MR bands, except for the 372, 463, 501 and 577-keV transitions, could not be measured due to their low intensities. For this reason, the multiplicity of these transitions as reported by G. Zwartz et al. [6] has been adopted.

Fig. 7.4 shows three different coincidence spectra which were generated with suitable sum gate on several in-band transitions of previously known three MR bands [6]. The peaks marked by * and + belong to the MR bands and the previously known lower-lying transitions [9] in ^{198}Bi, respectively. The sum gated spectrum of 204-, 226- and 427-keV from band B1 [6] (Fig. 7.4(a)) clearly shows all the transitions of previously known MR band (B1) along with the known lower-lying transitions in ^{198}Bi. In this spectrum γ lines belong to other two MR bands B2 and B3 (previously known) were not observed but the lower-lying transitions 331-, 403-, 379-, 345-, 673-, 626-keV and other transitions of ^{198}Bi have been observed. Therefore, we have placed MR band B1 above the 3966-keV state.

On the other hand, the sum gated spectrum of 242-, 297- and 372-keV of band B2 [6] (Fig. 7.4(b)) shows all transitions of the MR band B2 along with the known lower-lying γ lines in ^{198}Bi. In this spectrum transitions of other two MR bands B1 and B3 were not observed. The 345-, 673-, 626- keV lines and other γ lines of ^{198}Bi have been observed in this spectrum. However, the transitions at 331, 403, 350 and 630 keV are absent in this spectrum. Therefore, the band B2 has been placed on top of the 2596-keV level.

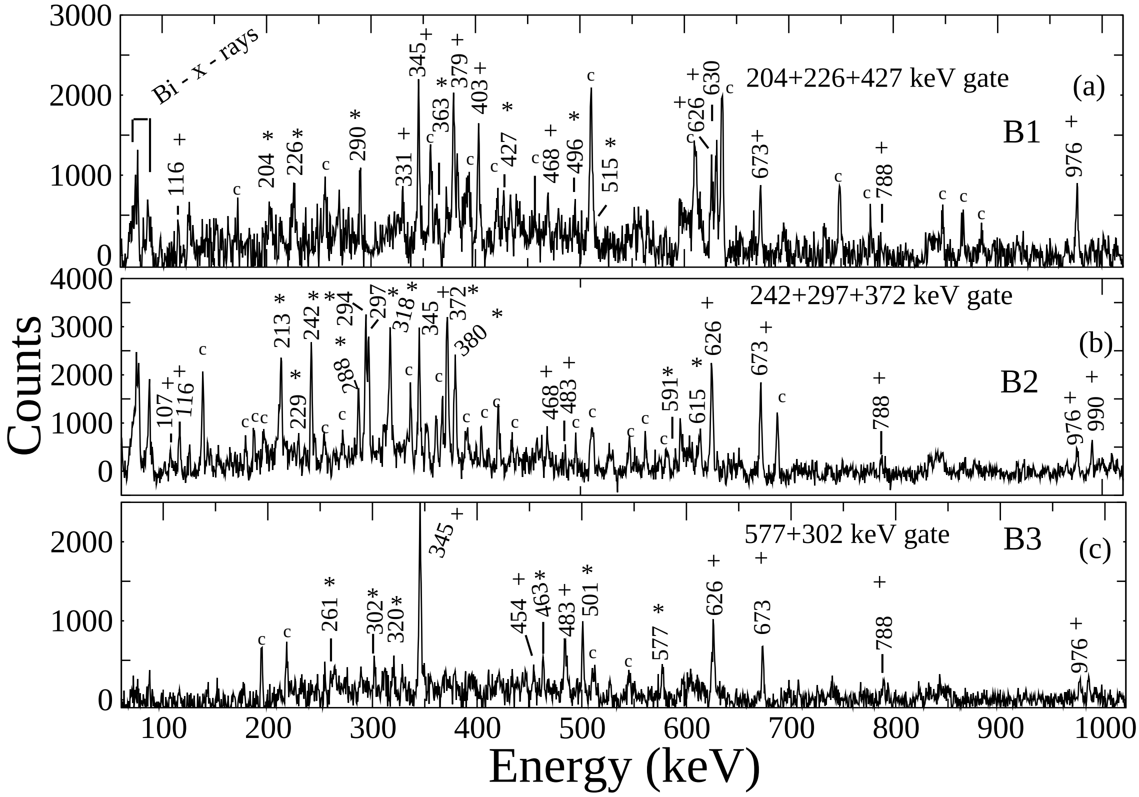

Figure 7.4: The spectra with gates on several in-band transitions (magnetic dipole bands from ref. [6]) have been summed. The peaks marked by * and + belong to the MR bands and the previously known lower-lying transitions [9] in ^{198}Bi, respectively. Contaminated γ rays are indicated by c.

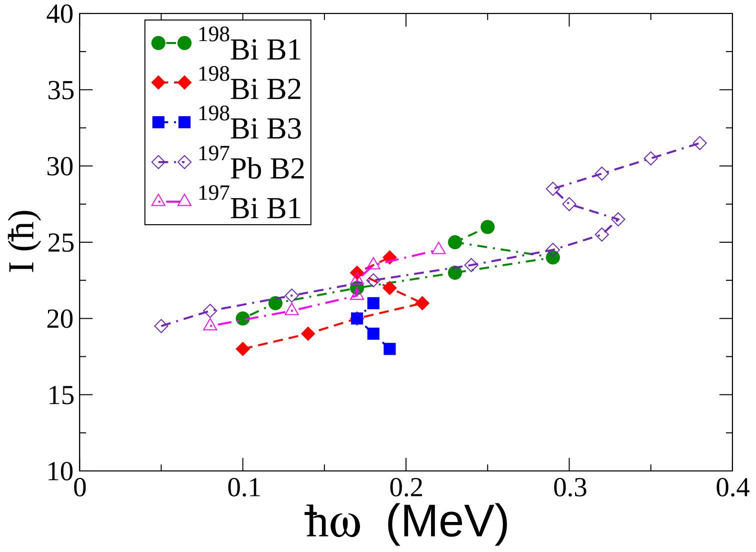

Figure 7.5: I (spin) vs. $\hbar\omega$ (rotational frequency) plot for the MR bands in ^{197}Bi [5],^{198}Bi and ^{197}Pb (B2) [10].

Two cross-over E2 transitions have been observed in band B2: the 615-keV (from the 4757-keV level) γ ray between the 318- and 297-keV M1 transitions; and the 591 keV (from 4439 keV state) γ ray between the 297- and 294-keV M1 transitions. B(M1)/B(E2) ratios for these two levels found to be 6.6 (14) and 9.2 (21) $\mu^2/(eb)^2$, respectively, which agrees well with the values reported by G. Zwartz et al. [6].

The sum gated spectrum of 577-keV and 302-keV (Fig. 7.4(c)) shows all the γ lines in the band (B3) along with the known lower-lying γ lines in ^{198}Bi. In this spectrum, transitions of other two MR bands B1 and B2 have not been observed. Known γ lines at 331, 403, 379, 350 and 630 keV were not observed in this spectrum. However, 345-, 673-, 626-keV and other known lower-lying transitions in ^{198}Bi have been identified. Therefore, we have placed MR band B3 above the 2224-keV state. We have placed 463-keV new transition in band B3. The bandhead spins for the bands B1, B2 and B3 are proposed to be 19^+, 17^- and 17^-, respectively.

7.3 Discussion

The $h_{9/2}$, $i_{13/2}$ and $s_{1/2}$ orbitals are available for the protons and $i_{13/2}$, $f_{5/2}$ and $p_{3/2}$ orbitals are available for the neutrons near the respective Fermi surfaces in ^{198}Bi. These orbitals, play important roles for the generation of magnetic rotation in the Pb-Bi region. In this region, the MR bands are built on proton particles in high-j orbitals ($\pi h_{9/2}$ and $\pi i_{13/2}$) coupled to the neutron hole states ($\nu i^{-n}_{13/2}$). The spin (I) vs. $\hbar\omega$ plots for the MR bands in ^{198}Bi are shown in Fig. 7.5 along with those for the MR bands in the neighboring nuclei ^{197}Bi [5] and ^{197}Pb (band B2) [10]. This plot shows that the bands B1 and B2 in ^{198}Bi are quite similar to the MR bands in ^{197}Bi [5] and ^{197}Pb [10]. Band B3 in ^{198}Bi looks different in nature compared to other MR bands of ^{198}Bi.

Band B2 of ^{197}Pb [10] is built on the 4794-keV level with $J^{\pi} = 37/2^{+}$ and configuration of this band was assigned as $\pi h_{9/2} i_{13/2} s^{-2}_{1/2} \otimes \nu i^{-2}_{13/2} p^{-1}_{3/2}$. On the other hand, the configurations of the MR band in ^{197}Bi [5] was assigned as $\pi i_{13/2} h^{2}_{9/2} \otimes \nu i_{13/2} \nu j$, where j = $(p_{3/2}, f_{5/2})$. These assignments suggest that the $\pi h_{9/2}$, $\pi i_{13/2}$, $\pi s_{1/2}$, $\nu i_{13/2}$, $\nu p_{3/2}$ and $\nu f_{5/2}$ orbitals should be involved in the configurations of the MR bands in the neighboring odd-odd nucleus ^{198}Bi. The configurations of the MR bands in ^{198}Bi are proposed to be $\pi h^{2}_{9/2} s_{1/2} \otimes \nu i^{-3}_{13/2}$ for band B1, $\pi i_{13/2} h^{2}_{9/2} \otimes \nu i^{-2}_{13/2} p^{-1}_{3/2}$ for band B2 and $\pi h^{2}_{9/2} s_{1/2} \otimes \nu i^{-2}_{13/2} f^{-1}_{5/2}$ for band B3.

Bands B1 and B2 have been investigated in the frame work of a semiclassical model [1, 2, 11, 12], in the present work. For the proposed configuration of band B1, the $\boldsymbol{j}_{\pi}$ and $\boldsymbol{j}_{\nu}$ values are $8.5\hbar$ and $16.5\hbar$, respectively, and, hence, the bandhead spin is calculated to be 19 $\hbar$ assuming perpendicular coupling between $\boldsymbol{j}_{\pi}$ and $\boldsymbol{j}_{\nu}$; which is in agreement with the observed bandhead of band B1. Maximum spin for this band can be calculated as $25\hbar$ in this model. Whereas in this study, band B1 is observed up to $27\hbar$. However, it can be seen from the level scheme in Fig. 7.2 and from Fig. 7.5 that a band crossing seems to take place beyond the spin value of $25\hbar$ ($\hbar\omega \sim 0.29$) and, therefore, the configuration of band B1 above $25\hbar$ is different than the proposed configuration below it. So, both the minimum and the maximum observed spin values are in good agreement with the calculated ones for the proposed configuration.

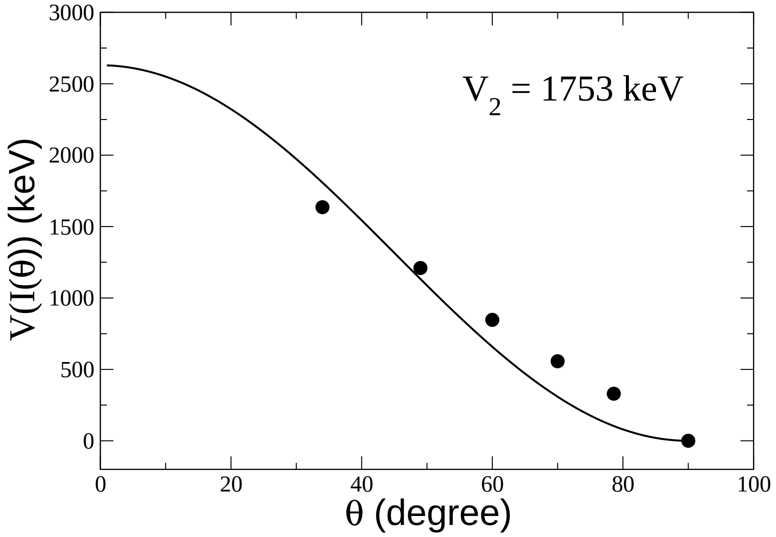

Figure 7.6: The effective interaction between the angular momentum vectors, j_π and j_ν, as a function of shears angle θ for band B1 in ^{198}Bi.

In this model, the interaction strength between the blades of the shears, V_2, can be obtained using equation 2.29 (see Chapter 2) using the experimentally observed energy levels of this shears band. $V(I(\theta))$, obtained in this way for band B1, has been plotted as a function of θ in Fig. 7.6. V_2 has been extracted from this plot by a fit of equation 2.29. The fitted curve is shown as the solid line in Fig. 7.6. The extracted value of V_2 comes out to be 1753 keV leading to the interaction strength per particle-hole pair as 195 keV considering that all the nine possible particle-hole pairs, in this configuration, are contributing to the shears mechanism. This is some what less compared to a typical value of $\sim$ 300 keV [2] observed in the Pb nuclei in this region. One of the possible reasons could be that the $\pi s_{1/2}$ orbital is not contributing to the shears mechanism. If the contribution of $\pi s_{1/2}$ orbital is excluded, then the V_2 per particle-hole pair comes out to be $\sim$ 300 keV, in good agreement with the typical values in this region.

Similarly, for band B2, the $\boldsymbol{j}_\pi$ and $\boldsymbol{j}_\nu$ are 13.5$\hbar$ and 10.5$\hbar$, respectively, corresponding to its proposed configuration of $\pi i_{13/2} h^2_{9/2} \otimes \nu i^{-2}_{13/2} p^{-1}_{3/2}$. The calculated minimum (bandhead) and maximum spin values, for this band, are 17$\hbar$ and 24$\hbar$. This band is, however, observed up to 25$\hbar$, a much higher value compared to the maximum possible for the above configuration. It can, however, be seen from the level scheme in Fig. 7.2 and from Fig. 7.5 that a band crossing seem

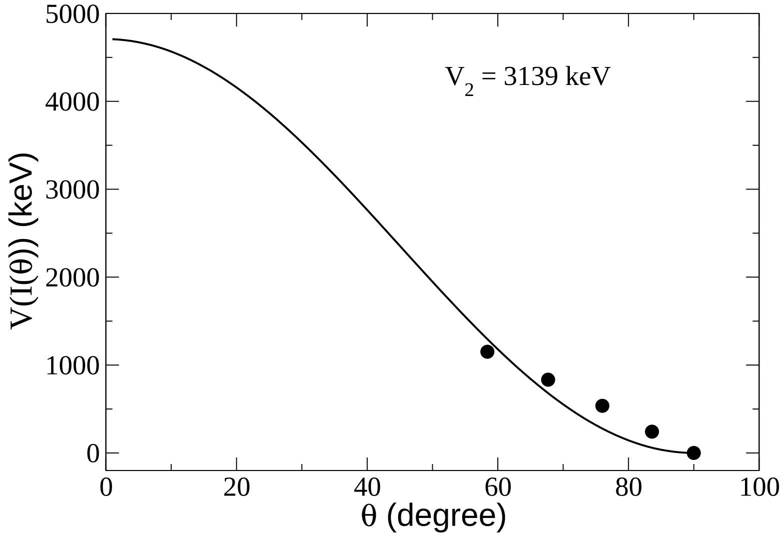

Figure 7.7: The effective interaction between the angular momentum vectors, j_π and j_ν, as a function of shears angle θ for band B2 in ^{198}Bi.

to occur in this band also beyond $21\hbar$ of spin ($\hbar\omega \sim 0.21$). Therefore, the above mentioned six quasiparticle configuration for this band changes to an eight quasiparticle configuration above $21\hbar$. So, in the subsequent calculations of $V(I(\theta))$ the values of θ were restricted up to about 60° corresponding to the spin value of $21\hbar$ as shown in Fig. 7.7. The extracted value of V_2, from this plot, comes out to be 3139 keV leading to the interaction strength per particle-hole pair (considering nine particle-hole pairs) to be 349 keV. This is in good agreement with the typical values in this region. It may be noted that the configuration of band B2 does not contain the $\pi s_{1/2}$ orbital. This corroborates the conjecture obtained from band B1 that the $\pi s_{1/2}$ orbital may not be contributing to the shears mechanism.

The minimum and maximum spin values calculated for band B3 are $17\hbar$ and $23\hbar$, respectively, assuming its proposed configuration. Although these values are in good agreement with the observation, this band seems to be very different in nature compared to the other MR bands in ^{198}Bi. The energy of the γ rays, in this band, decreases gradually with the increase in spin (see the level scheme in Fig. 7.2) in sharp contrast to those in band B1 and B2. Moreover, the spin (I) vs $\hbar\omega$ plot for band B3, shown in Fig. 7.5, is much different than for band B1 and B2. Therefore, the band B3 in ^{198}Bi may not be an MR band and more experimental work is required (for example, lifetime measurements of the levels in this band) to understand the exact nature of this band, which is beyond the scope of the present thesis work.

7.4 Summary

The high-spin states in the odd-odd nucleus ^{198}Bi have been studied by fusion-evaporation reaction with ^{nat}Re target and ^{16}O beam at 112.5 MeV. A new and improved level scheme of this nucleus is presented in this work. The DCO ratio and the Polarization assymmetry ratio measurements have been performed to assign spin and parities of the levels. Three unconnected MR bands, proposed for ^{198}Bi in a previous experiment, have been firmly placed in the level scheme and have been connected with the known lower-lying states in this nucleus. The excitation energies and J$^{\pi}$ assignments have also been established for the proposed MR bands. With these assignments, the configurations for these three bands could be proposed. The Band B1 and B2 have been discussed in the frame work of a semiclassical approach and the interaction strengths per particle-hole pair have been extracted for these two bands from this semiclassical approach. It has been seen that the $\pi s_{1/2}$ may not be contributing to the shears mechanism in ^{198}Bi. It is, however, not known yet whether this conjecture is true for all the MR bands observed throughout the nuclear chart. The band B3 does not seem to be an MR band in the present work and further experimental and theoretical investigations are needed to understand the explicit nature of this band.

Bibliography

[1] H. Hübel, Prog. Part. Nucl. Phys. **54**, 1 (2005).

[2] R.M. Clark and A.O. Macchiavelli, Annu. Rev. Nucl. Part. Sci. **50**, 1 (2000).

[3] G. Baldsiefen et al., Nucl. Phys. **A 574**, 521 (1994).

[4] A.K. Singh et al., Nucl. Phys. **A 707**, 3 (2002).

[5] G.K. Mabala et al., Eur. Phys. J. **A 25**, 49 (2005).

[6] G. Zwartz et al., J. Phys. G: Nucl. Part. Phys. **26** 849 (2000).

[7] P.J. Dagnall et al., J. Phys. G: Nucl. Part. Phys. **20** 1591 (1994).

[8] U. Hagemann et al., Nucl. Phys. **A 197** 111 (1972).

[9] X.H. Zhou et al., Phys. Rev. **C 54** 2948 (1996).

[10] A. Görgen et al., Nucl. Phys. **A 683** 108 (2001).

[11] A.O. Macchiavelli et al., Phys. Rev. C **57**, R1073 (1998).

[12] A.O. Macchiavelli et al., Phys. Rev. C **58**, R621 (1998).

Chapter 8

Structure of odd-odd nucleus ^{134}Cs at high spin

8.1 Introduction

To extend our investigation to the nuclei near N = 82, we have studied the high spin states in odd-odd nucleus ^{134}Cs (Z = 55, N = 79). Many of the nuclei in the A $\sim$ 130 mass region are known to be γ-soft and triaxial in nature. Interesting phenomena, such as observation of doublet bands and magnetic rotational (MR) bands which arise due to chiral symmetry breaking and shears mechanism, respectively, have been observed in many nuclei in this region [1, 2, 3, 4, 5]. These occur due to the coupling between the single particle and the collective degrees of freedom in nuclei, with moderate to small deformation. Therefore, both the shape of a nucleus and the position of the Fermi level play important role in determining the structure of a band. As mentioned earlier in chapter 1, a stable triaxial shape is necessary for the occurrence of the chiral bands and the MR bands are, generally, realized for small deformation [6, 7, 8]. A change in the structure of a band, built on a particular configuration, is possible, if shape changes from a well deformed triaxial to a γ-soft one as a function of particle number or angular momentum. However, no such change over has been reported so far, in the $A \sim 130$ region.

For the Cs ($Z = 55$) isotopes, the proton and the neutron Fermi surfaces lie near the bottom and the top parts, respectively, of the unique parity $h_{11/2}$ subshell. The respective orbitals have prolate and oblate shape driving effects. These opposing shape driving effects on a triaxial γ-soft core, induce relatively stable triaxial deformation for the odd-odd isotopes of Cs. This manifests into the observation of the so called "chiral bands" in the odd-odd Cs isotopes with neutron numbers ranging from N = 71 to N = 77, for the $\pi h_{11/2} \otimes \nu h_{11/2}$ configuration [5, 9, 10, 11, 12]. However, as the neutron number increases towards the N = 82 shell closure, it is not clear if the shape driving effects of the neutrons are strong enough to stabilize the triaxial shape and, hence, whether the similar band structure would still persist. Moreover, when approaching the N = 82 shell closure, the potential energy surfaces tend to be γ-soft with small deformation. These conditions are ideal for destroying the chiral arrangement and emergence of the MR bands. ^{132}Cs is the heaviest isotope of Cs for which the $\pi h_{11/2} \otimes \nu h_{11/2}$ configuration was identified with a rotational band structure along with a possible chiral partner [5]. In addition to the chiral doublet bands, different multi-quasiparticle bands including a magnetic rotational band have been reported in ^{132}Cs [13]. The above configuration has not yet been identified in ^{134}Cs. Apart from the low-lying states, studied by (n,γ) and (d,p) reactions [14, 15], very little information is known about the high spin states in ^{134}Cs. A few of the high energy states up to $\sim$ 2 MeV were identified in ref. [9] but with no spin-parity assignments. We have investigated, the high spin states in ^{134}Cs with an aim, to study the nature of the band built on the $\pi h_{11/2} \otimes \nu h_{11/2}$ configuration and also to identify other multiquasiparticle band structure.

8.2 Experiment and results

The high spin states in ^{134}Cs were populated by two experiments carried out at the 14-UD BARC-TIFR Pelletron at Mumbai, India. In the first experiment, the reaction ^{130}Te(^{11}B, α3n) at 52 MeV was used and the emitted γ rays were detected using an array of 8 Compton-suppressed clover Ge detectors. The detectors were arranged in a median plane configuration at 25 cm away from the target and were placed at 120°, 90°, 60°, ±30°,−70°, −105° and −145° angles with respect to the beam direction. The target used was a 2.2 mg/cm^2 enriched (99.9%)

^{130}Te, evaporated on to a 2.0 mg/cm^2 Au backing. In this experiment, the data were taken in the list mode with the condition that at least two clover detectors are fired in coincidence. This experiment was optimized for the production of La isotopes [16, 17]. However, there was indication that the excited states in ^{134}Cs were also produced. They are apparently produced by incomplete fusion reaction. Therefore, the yield of ^{134}Cs was low in this experiment.

In the second experiment, the ^{130}Te(^{7}Li, 3n) reaction was used at 30 MeV of beam energy. The target was a 750 μg/cm^2, enriched (99.9%) ^{130}Te, evaporated on a 6.0 mg/cm^2 Au backing and placed at an angle of $\sim 60^o$ with respect to the beam direction such that, there is no shadowing effect to the detectors due to the target holder. In this experiment, the setup consisted of seven Compton-suppressed clover HPGe detectors placed at 25 cm from the target in a median plane at 30°, ±90°, 105°, ±145° and −45° with respect to the beam direction. In this experiment, a 14-element NaI(Tl) multiplicity filter, in the form of two equal clusters, was placed above and below the horizontal plane. The master trigger in this experiment, for collecting γ-γ coincidence data in the list mode, was generated with the condition that at least two clover detectors and two NaI(Tl) detectors have fired in coincidence.

Table 8.1: Energies (E_γ), intensities (I_γ), DCO ratios (R$_{DCO}$), R_{asym}, IPDCO ratios (Δ_{IPDCO}) and deduced multipolarities of the γ rays in ^{134}Cs. The energies of initial states (E_i) and spins and parities of initial (J_i^π) and final (J_f^π) states are also given.

E_γ (in keV)	E_i (in keV)	$J_i^\pi \rightarrow J_f^\pi$	I_γ [1]	R_{DCO} (Err)	R_{asym} [7] (Err)	Δ_{IPDCO} (Err)	Deduced Multipolarity
88.1(8)	345.1	$7^- \rightarrow 6^-$	9.5(8)	0.77(6) [2]	-	-	M1+E2
127.4(3)	2096.8	$12^+ \rightarrow 11^+$	10.0(9)	0.72(8) [3]	1.48(76)	-	M1+E2
134.3(3)	2096.8	$12^+ \rightarrow 12^-$	3.7(4)	1.02(17) [5]	-	-	E1
154.6(3)	2251.7	$13^+ \rightarrow 12^+$	42.2(35)	0.98(13) [2]	1.18(17)	-	M1
157.3(2)	1551.1	$10^+ \rightarrow 9^+$	37.2(31)	0.89(7) [2]	1.27(19)	-	M1
205.7(3)	345.1	$7^- \rightarrow 8^-$	10.1(9)	-	-	-	M1 [8]

Table 8.1: Continued...

E_γ (in keV)	E_i (in keV)	$J_i^\pi \rightarrow J_f^\pi$	I_γ [1]	R_{DCO} (Err)	R_{asym} [7] (Err)	Δ_{IPDCO} (Err)	Deduced Multipolarity
205.6(1)	641.1	$8^- \rightarrow 7^-$	42.7(35)	0.73(4)[3]	1.12(19)	-0.05(6)	M1+E2
211.6(6)	2463.0	$14^+ \rightarrow 13^+$	9.9(9)	0.86(12)[3]	1.48(43)	-	M1(+E2)
231.2(2)	2106.5	$(12^-) \rightarrow (11^-)$	1.5(2)	-	-	-	-
231.5(3)	2328.3	$13^+ \rightarrow 12^+$	9.5(10)	1.58(14)[5]	-	-	M1+E2
245.8(4)	257.0	$6^- \rightarrow 5^+$	7.4(6)	-	-	-	E1[8]
272.5(4)	2369.3	$13^+ \rightarrow 12^+$	2.1(2)	1.70(39)[5]	-	-	M1+E2
295.9(1)	434.6	$7^- \rightarrow 8^-$	53.2(44)	0.75(6)[3]	1.41(27)	-0.09(4)	M1(+E2)
296.1(4)	641.1	$8^- \rightarrow 7^-$	9.4(8)	0.99(5)[2]	-	-0.18(9)	M1
362.3(6)	1391.0	$(10^-) \rightarrow 9^-$	2.3(3)	-	-	-	(M1+E2)
370.7(3)	3850.6	$15^+ \rightarrow 14^+$	4.9(6)	0.90(11)[4]	1.19(58)	-	M1+E2
374.6(7)	2345.0	$12^+ \rightarrow 11^+$	9.7(9)	0.95(12)[3]	1.62(49)	-	M1
379.3(5)	3821.0	$(16^+) \rightarrow (15^+)$	3.9(5)	-	-	-	-
387.6(3)	1027.7	$9^- \rightarrow 8^-$	8.1(7)	-	1.13(64)	-	M1+E2
390.2(5)	2096.8	$12^+ \rightarrow 11^-$	3.0(4)	1.77(38)[5]	-	-	E1
404.6(4)	2112.0	$(12^-) \rightarrow 11^-$	4.5(5)	-	-	-	-
418.5(2)	1969.7	$11^+ \rightarrow 10^+$	36.4(31)	1.06(11)[3]	1.40(30)	-0.24(7)	M1
443.8(4)	2788.8	$13^+ \rightarrow 12^+$	9.1(8)	0.87(11)[3]	-	-	M1
485.5(4)	1876.3	$(11^-) \rightarrow (10^-)$	1.9(3)	-	-	-	-
513	3302	$(14^+) \rightarrow 13^+$	-	-	-	-	-
539.6(2)	2096.8	$12^+ \rightarrow 11^-$	45.1(44)	1.81(19)[5]	1.40(20)	0.24(11)	E1
544.8(2)	2797.2	$14^+ \rightarrow 13^+$	12.8(16)	0.84(9)[4]	-	-	M1+E2
571.3(3)	3256.0	$(14^+) \rightarrow 13^+$	1.5(2)	-	-	-	-
587.2(5)	2684.0	$13^+ \rightarrow 12^+$	4.5(5)	2.12(31)[5]	-	-	M1+E2
609.7(3)	748.3	$9^- \rightarrow 8^-$	28.3(23)	0.78(11)[4]	-	-0.27(8)	M1
644.7(3)	1393.8	$9^+ \rightarrow 9^-$	27.5(23)	0.99(11)[4]	-	0.32(9)	E1
679.2(7)	1707.0	$(11^-) \rightarrow 9^-$	3.3(4)	-	-	-	-

Table 8.1: Continued...

E_γ (in keV)	E_i (in keV)	$J_i^\pi \rightarrow J_f^\pi$	I_γ [1]	R_{DCO} (Err)	R_{asym} [7] (Err)	Δ_{IPDCO} (Err)	Deduced Multipolarity
681.2(2)	819.8	$10^- \rightarrow 8^-$	100(6)	0.63(3) [4]	0.51(7)	0.10(4)	E2
683.5(5)	1027.7	$9^- \rightarrow 7^-$	9.7(10)	0.57(6) [6]	-	-	E2
693.7(9)	1513.5	$11^- \rightarrow 10^-$	8.6(12)	1.43(18) [5]	-	-	M1+E2
716.4(3)	2106.5	$(12^-) \rightarrow (10^-)$	2.1(3)	-	-	-	-
724.9(1)	2976.6	$14^+ \rightarrow 13^+$	5.9(6)	1.04(14) [4]	-	-	M1+E2
737.2(2)	1557.1	$11^- \rightarrow 10^-$	54.6(55)	2.10(23) [5]	1.56(21)	-0.20(3)	M1(+E2)
750.3(1)	1391.0	$(10^-) \rightarrow 8^-$	3.3(5)	-	-	-	-
752.7(3)	1393.8	$9^+ \rightarrow 8^-$	31.6(27)	1.05(13) [2]	1.61(40)	0.26(5)	E1
816.2(5)	1250.8	$(8^-) \rightarrow 7^-$	2.1(3)	-	-	-	-
847.5(5)	1876.3	$(11^-) \rightarrow 9^-$	2.2(3)	-	-	-	-
886.8(5)	1706.6	$11^- \rightarrow 10^-$	10.5(11)	2.09(15) [5]	-	-0.19(12)	M1+E2
897.0(1)	2860.0	$(14^-) \rightarrow 12^-$	3.1(4)	-	-	-	-
979.6(6)	3442.1	$(15^+) \rightarrow 14^+$	8.0(8)	-	-	-	-
1142.8(4)	1962.5	$12^- \rightarrow 10^-$	20.0(21)	0.97(6) [5]	-	0.12(9)	E2
1152.1(1)	3403.6	$14^+ \rightarrow 13^+$	3.9(5)	0.93(21) [4]	-	-	M1+E2
1228.2(6)	3479.6	$14^+ \rightarrow 13^+$	13.7(14)	1.56(21) [5]	-	-0.31(12)	M1+E2
1317	3424	$(14^-) \rightarrow (12^-)$	-	-	-	-	-

[1]Relative γ ray intensities are estimated from prompt spectra and normalized to 100 for the total intensity of 681.2 keV γ rays.

[2]From 245.8 keV (E1) DCO gate;

[3]From 752.7 keV (E1) DCO gate;

[4]From 154.6 keV (M1) DCO gate;

[5]From 681.2 keV (E2) DCO gate;

[6]From 205.7 keV + 205.6 keV DCO gate;

[7]$\frac{W(90^\circ)}{W(30^\circ)}$ gate on 60°;

[8]From ref. [14, 15]

The collected γ-γ coincidence data, from the above two experiments, were sorted into separate $E_\gamma - E_\gamma$ matrices. An $E_\gamma - E_\gamma - E_\gamma$ cube was also constructed from the data obtained in the first experiment. The multipolarities of the γ-ray transitions have been determined from the angular correlation analysis using the methods of directional correlation from oriented states (DCO) and R_{asym} ratio analysis as described in section 3.6.2. For the DCO ratio analysis, the coincidence events were sorted into an asymmetry matrix with data from 145° detector (θ_2) on one axis and 90° detector (θ_1) on the other axis. In order to obtain the R_{asym} ratio, two angle dependent matrices were constructed between 90^o vs. 60^o and between 30^o vs. 60^o, respectively. R_{asym} ratio was found to be > 1 for dipole transitions and < 1 for quadrupole transitions.

We have performed integrated polarization asymmetry measurement (IPDCO), as described in section 3.6.3 from the data obtained in the second experiment, to get a qualitative idea about the type of the transitions (E/M). The correction due to asymmetry in the array and response of the Clover segments, defined by $a(E_\gamma) = \frac{N_\parallel}{N_\perp}$, was checked using ^{152}Eu and ^{133}Ba sources and was found to be 1.023(6); which is close to unity, as expected. For the IPDCO analysis, the data from the 90^o detectors were used.

Fig. 8.1 shows the level scheme of ^{134}Cs, obtained in the present work. A total of thirty-two new γ rays have been found and placed in the level scheme in this work. They are marked as "*" in the level scheme. The levels above the 8^- isomeric state at 139 keV are observed in the present work. Some of the low lying levels below this isomer, which were not observed in the present work, are also shown in Fig. 8.1 for completeness. The level scheme is extended, in the present work, up to 3.85 MeV along with the J^π assignments for most of the high spin states. The measured parameters along with the deduced excitation energy, spin and parity of the excited levels and the multipolarities of the γ rays are shown in Table 8.1.

Representative single gated γ ray spectra are shown in Fig. 8.2-8.8. Sum of double gated γ ray spectra is also shown in Fig. 8.4(b). These spectra show all the known γ lines (127-keV, 155-keV, 157-keV, 206-keV, 246-keV, 296-keV, 388-keV, 419-keV, 540-keV, 610-keV, 645-keV, 681-keV, 737-keV, 753-keV and 816-keV) reported by Koike et al. [9] along with the new γ lines. In 206-keV gate (shown in Fig. 8.2), known γ lines are observed along with 231-keV, 362-keV,

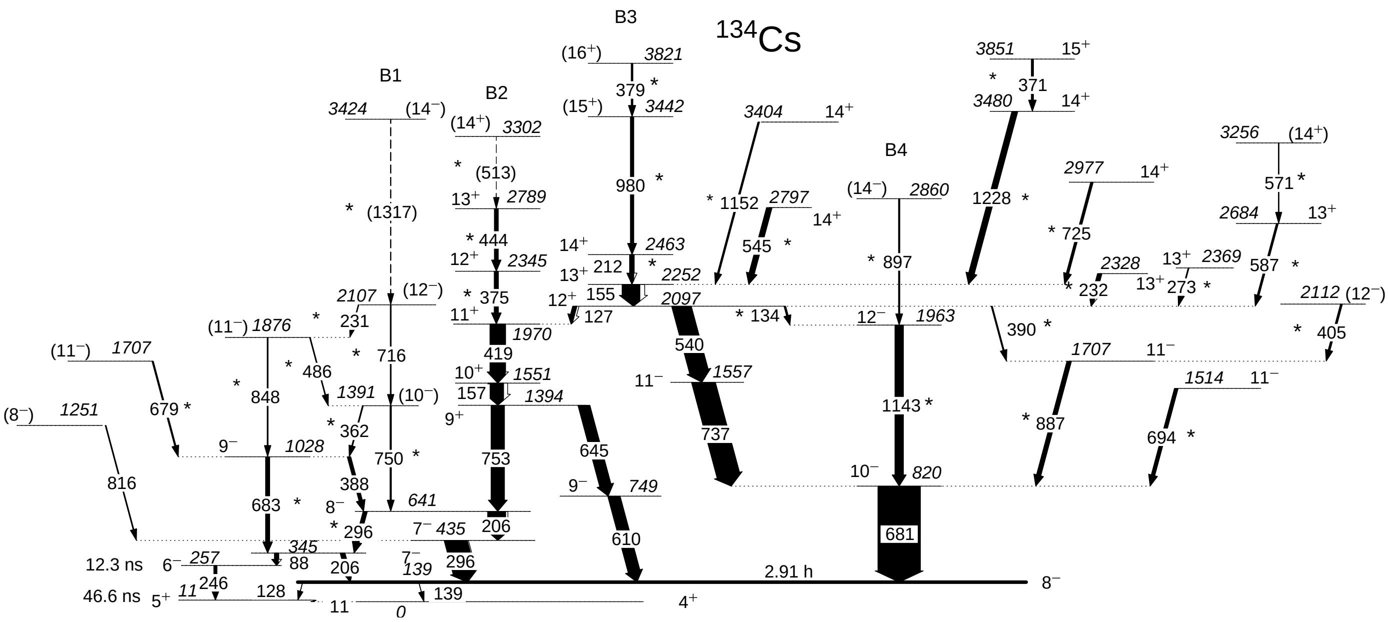

Figure 8.1: Level scheme of ^{134}Cs, as obtained from the present work. The low-lying states up to 435-keV are mostly adopted from the earlier works [14, 15]. The new γ rays are indicated by asterisks.

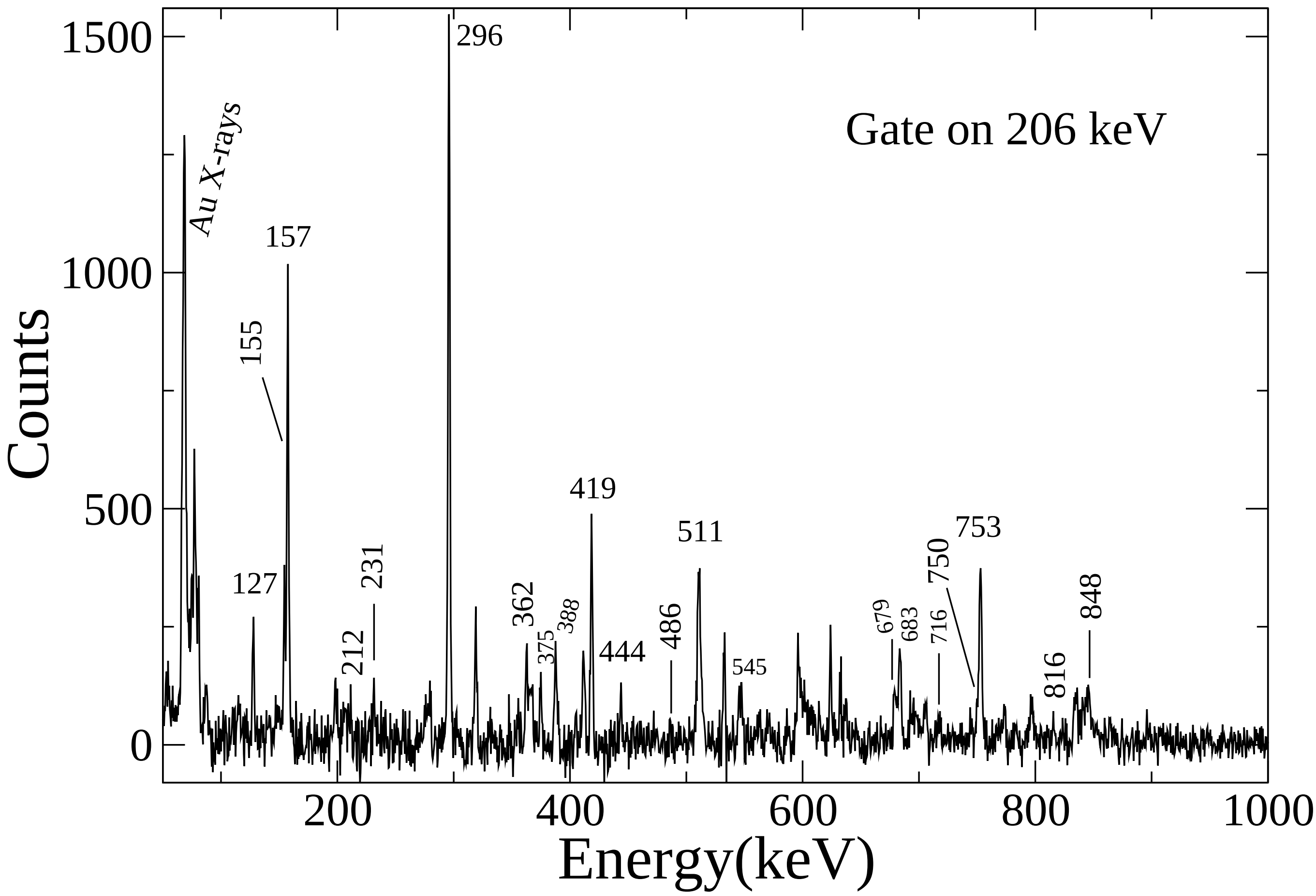

Figure 8.2: Single gated spectra of ^{134}Cs gated by 206-keV transition. The unmarked peaks are the contaminants.

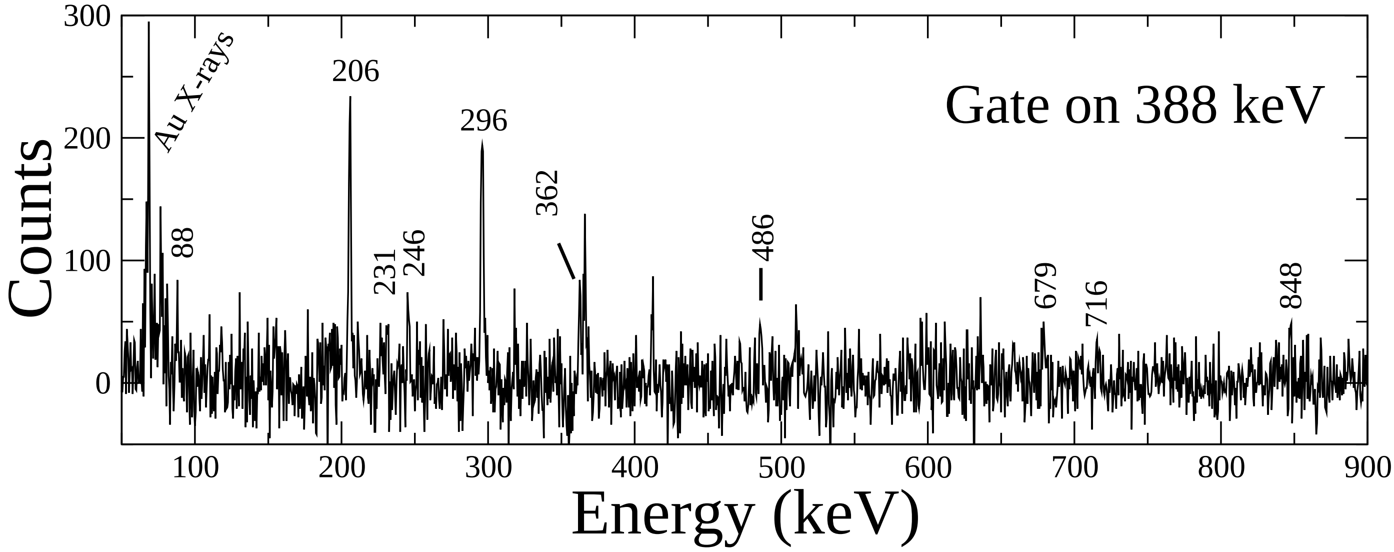

Figure 8.3: γ-ray Spectra of ^{134}Cs gated by 388-keV transition. The unmarked peaks are the contaminants.

486-keV, 679-keV, 683-keV, 716-keV, 750-keV and 848-keV new γ lines. The 683-keV and 750-keV γ lines are not observed in 388-keV gate (shown in Fig. 8.3), instead we have identified 231-keV, 362-keV, 486-keV, 679-keV, 716-keV and 848-keV γ lines along with previously known γ lines. Therefore, we have placed band B1 above the 345-keV state. Single gated spectrum of 157-keV and sum double gated spectrum of 296-keV, 206-keV, 753-keV, 157-keV and 419-keV are shown in Fig. 8.4(a) and Fig. 8.4(b), respectively. These spectra show all the γ lines of band B2.

The 246 keV transition was known previously to decay from the 12.3 ns 6^- isomeric level at 257 keV [14]. The γ-γ coincidence window of $\pm$40 ns was chosen in the analysis of our data. Therefore, a gate on 246 keV transition should be able to show the γ rays which are in coincidence with that transition. The 246 keV-gated spectrum is shown in Fig. 8.5(b). The γ lines corresponding to ^{134}Cs are marked, in this spectrum, by their energies. This spectrum shows the 155-, 157-, 419- and 753-keV γ lines which were observed in the heavy ion reactions of T. Koike et al. [9]. The 206 keV γ ray, observed in coincidence with 753 keV γ ray (shown in Fig. 8.5(a)) by Koike et al., is not observed in this spectrum. On the other hand, a 296 keV γ ray is clearly observed in coincidence with 246 keV. However, as shown in Fig. 8.2,

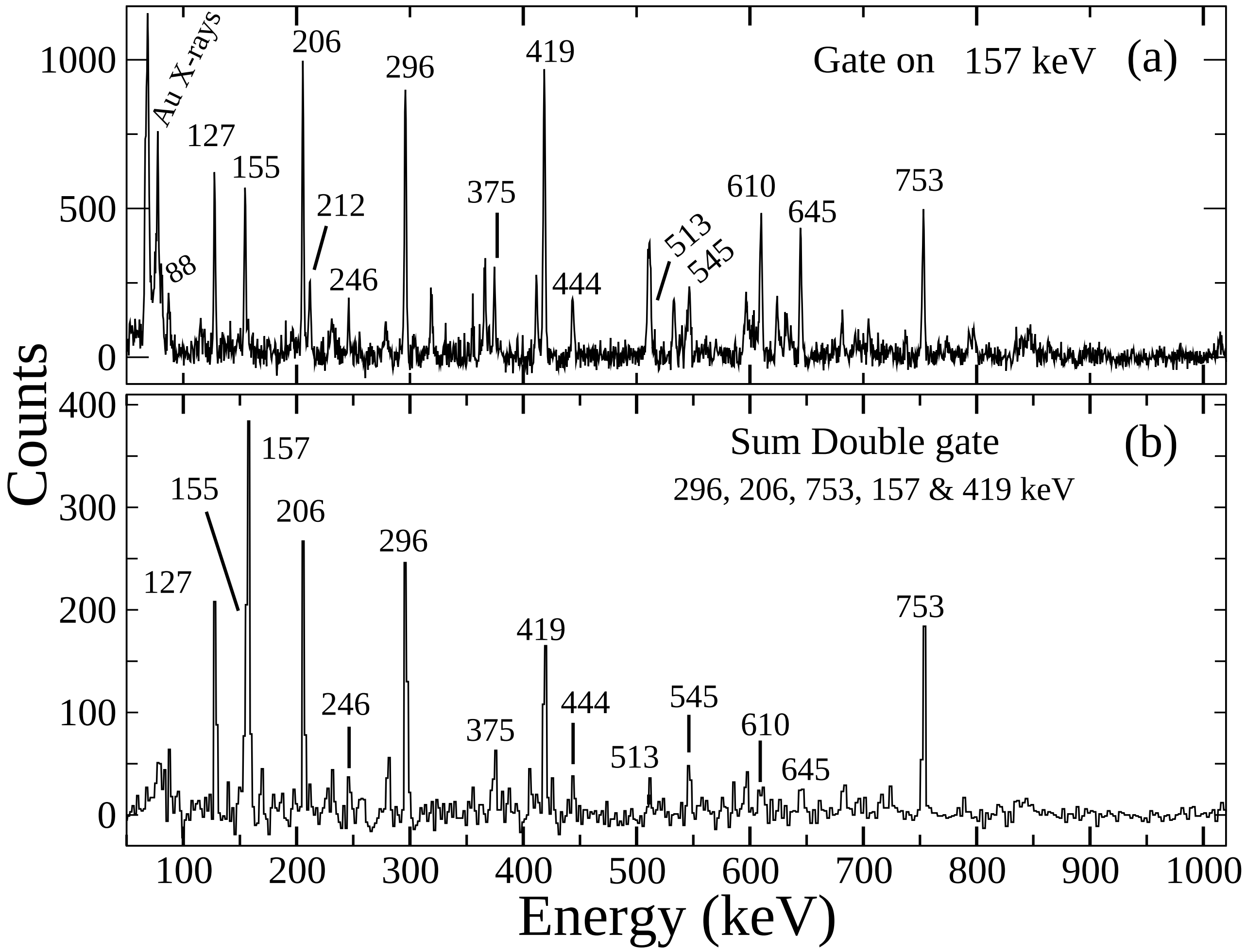

Figure 8.4: (a) Single-gated and sum of double (b) gated spectra of ^{134}Cs showing the γ-rays transitions in the level scheme presented in Fig. 8.1. The unmarked peaks are the contaminants.

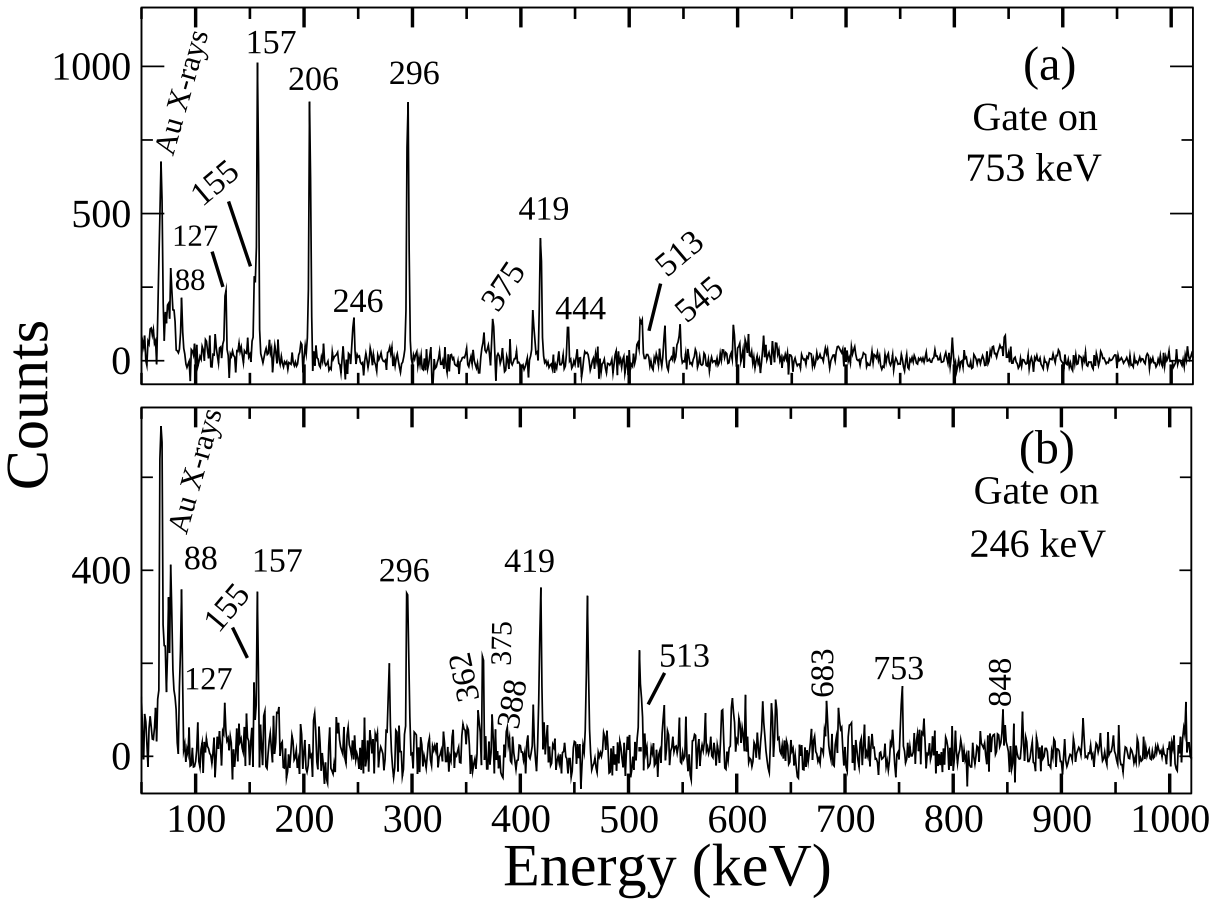

Figure 8.5: γ-ray Spectra of ^{134}Cs gated by (a) 753-keV transition and (b) 246-keV transition. The unmarked peaks are the contaminants.

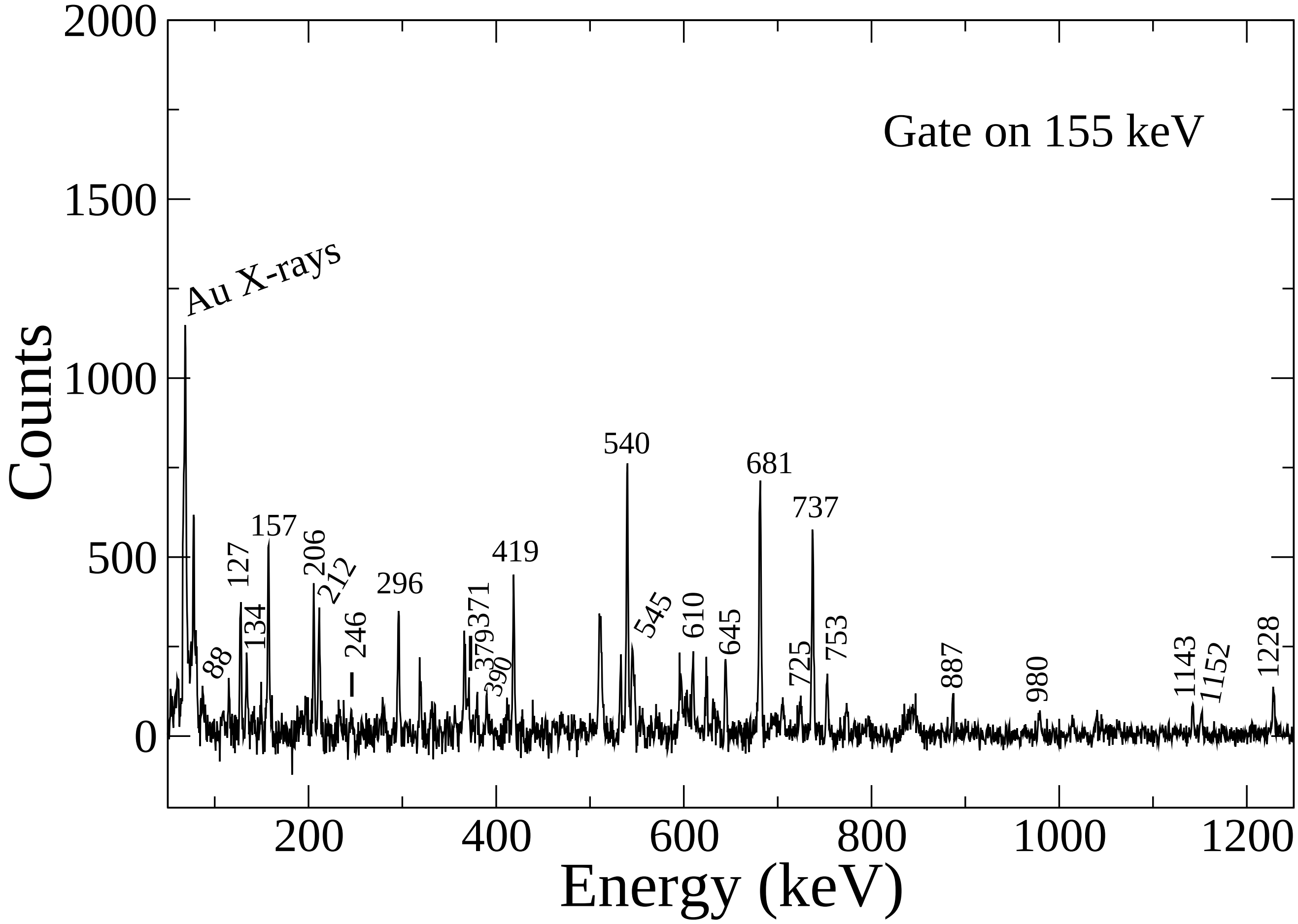

Figure 8.6: Single gated spectra of ^{134}Cs gated by 155-keV transition. The unmarked peaks are the contaminants.

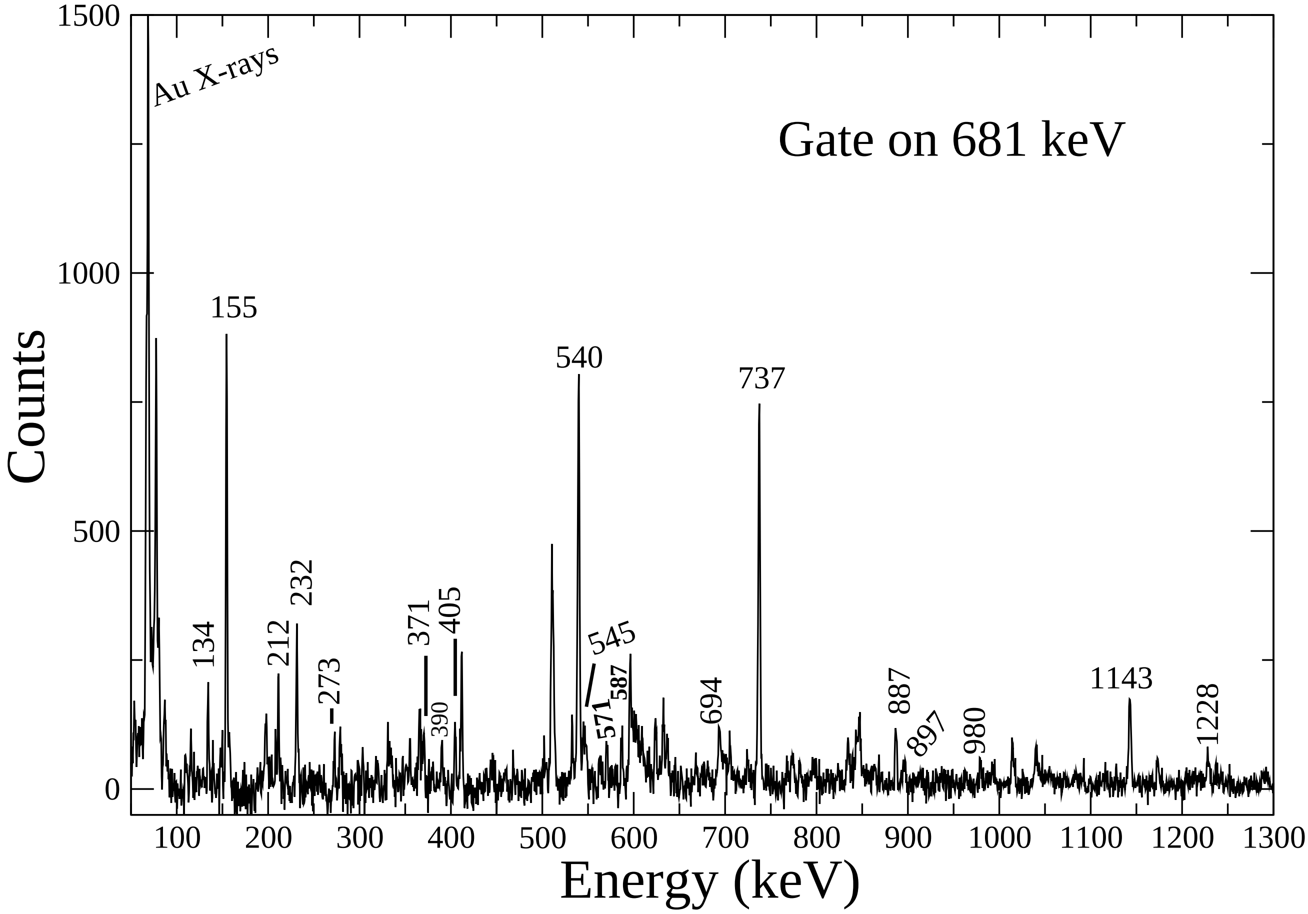

Figure 8.7: Single gated spectra of ^{134}Cs gated by 681-keV transition. The unmarked peaks are the contaminants.

(spectrum gated by the 206 keV transition) a strong 296 keV γ line in coincidence with the 206 keV transition has been observed. This indicates double placement of 296 keV γ transition. Therefore, we have placed a 296 keV γ ray transition to de-excite from the 641 keV state to the 7^- state at 345 keV. This placement also explains the observation of other γ rays in Fig. 8.5(b). A careful fitting of the γ ray peaks at 296 keV in the above two spectra (Fig. 8.5(a) and Fig. 8.5(b)) gives two slightly different energies of the lines (295.9 and 296.1 keV, respectively for the strong and the weak transitions). The known coincidence γ ray of 88 keV is also observed in the spectrum of Fig. 8.5(b). The fact that both 88 keV and 753 keV γs are in coincidence with the 246 keV, confirms the earlier placement of the 246 keV transition [14] as opposed to the one shown in ref. [9].

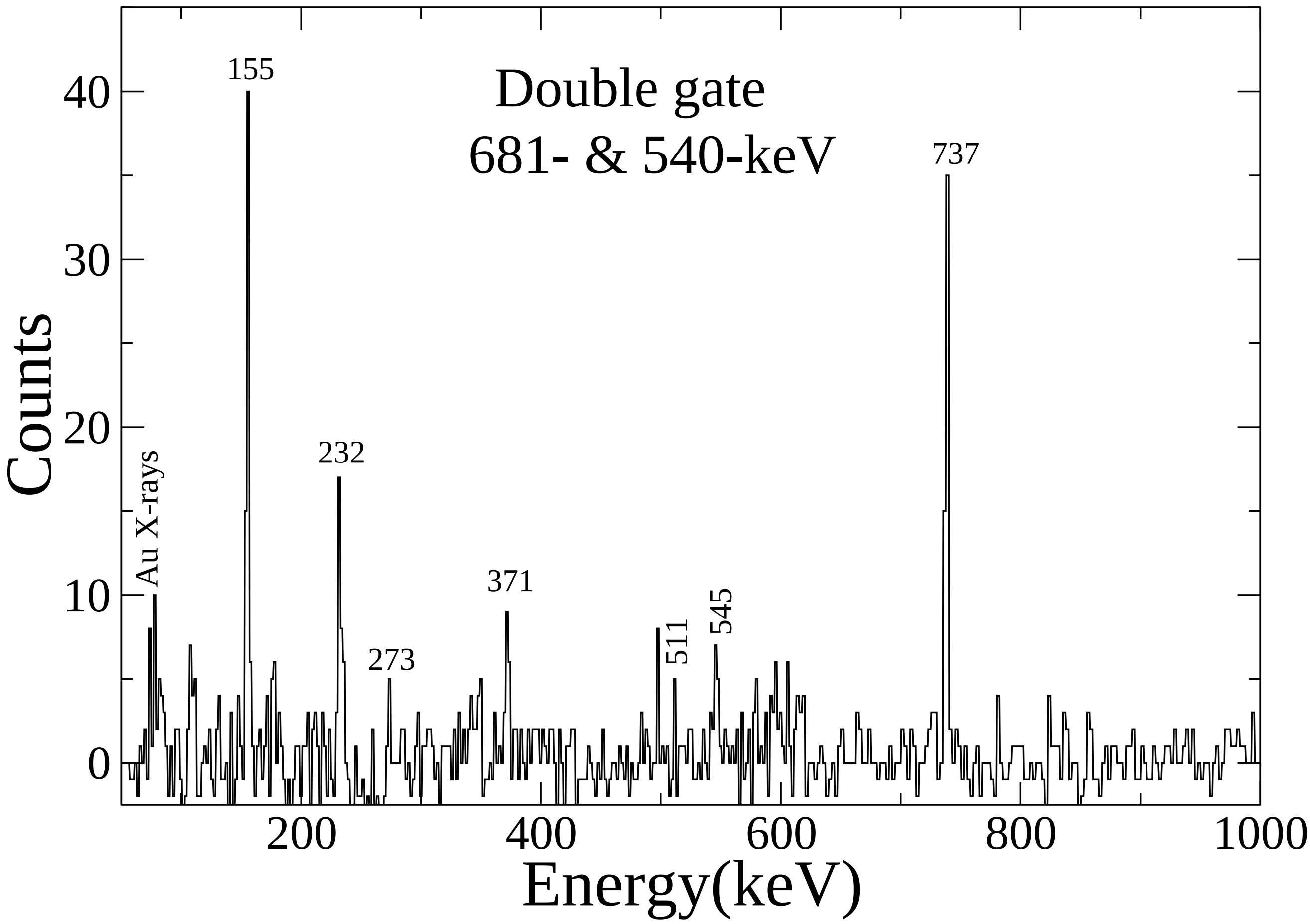

Figure 8.8: Coincidence spectra corresponding to a double gate of 681 keV and 540-keV γ transitions.

In 155-keV (shown in Fig. 8.6) gate we have identified 540-, 737- and 681-keV lines along with transitions of band B2 (except 375-, 444- and 513-keV) and band B3. Moreover, in 681-keV (shown in Fig. 8.7) gate transitions of band B2 and 127-keV γ line are not observed. In this spectrum 155-, 540- and 737-keV γ lines and transitions of band B4 along with other new lines are observed. Therefore, we have confirmed the previous [9] placement of 155-, 540-, 737- and 681-keV transtions. One double gated spectrum is shown in Fig. 8.8 with gates on 681 keV and 540 keV transitions. Although the statistics in this double gated spectrum is not much, but it clearly shows the 155 keV γ ray along with the 737 keV and some of the transitions above 155 keV. This clearly establishes the decay path via the sequence of 540-737-681 keV γ rays.

375-keV and 444-keV γ rays lines are observed with 157-keV (Fig. 8.4(a)), 206-keV (Fig. 8.2) and 753-keV (Fig. 8.5(a)) gated spectra, while they are not observed in 155-keV (Fig. 8.6) and 681-keV (Fig. 8.7) gated spectra. Therefore, we have placed 375-keV and 444-keV γ transitions above the 1970-keV state.

As mentioned earlier, the spins and parities of the levels were assigned from the R_{DCO}, R_{asym} and Δ_{IPDCO} measurements. The R_{asym} values provide additional support to determine the multipolarity of the transitions. The parallel ($N_{\parallel}$) and perpendicular ($a(E_\gamma)$*N$\perp$) counts for the two γ rays in ^{134}Cs are shown in Fig. 8.9. It can be clearly seen that the 753-keV transition is electric type, while 419-keV transition is the magnetic type transition. A 9^+ state is known in all the lighter odd-odd Cs isotopes (A = 126 - 132) corresponding to the $\pi h_{11/2} \otimes \nu h_{11/2}$ configuration [9]. This state, in ^{134}Cs, has been identified and characterized for the first time in this work. By gating on the previously known pure dipole (E1) transition of 246 keV [14], the 296-keV (from the 641-keV level) and the 753-keV γ rays were found to be M1 and E1, respectively, from their measured DCO ratio (~ 1) and the negative & positive values of the IPDCO ratios (see Table 1). The spin-parity of the 345 keV level was known to be 7^- [14]. Therefore, the spin-parity of the 641- and 1394-keV levels are identified as 8^- and 9^+, respectively.

The DCO values of the γ rays, in the band built on this 9^+ band-head, indicate that these are predominantly dipole in nature. The M1 nature of the 419-keV γ ray is evident from the negative value of its IPDCO ratio. The IPDCO ratios could not be obtained for the other

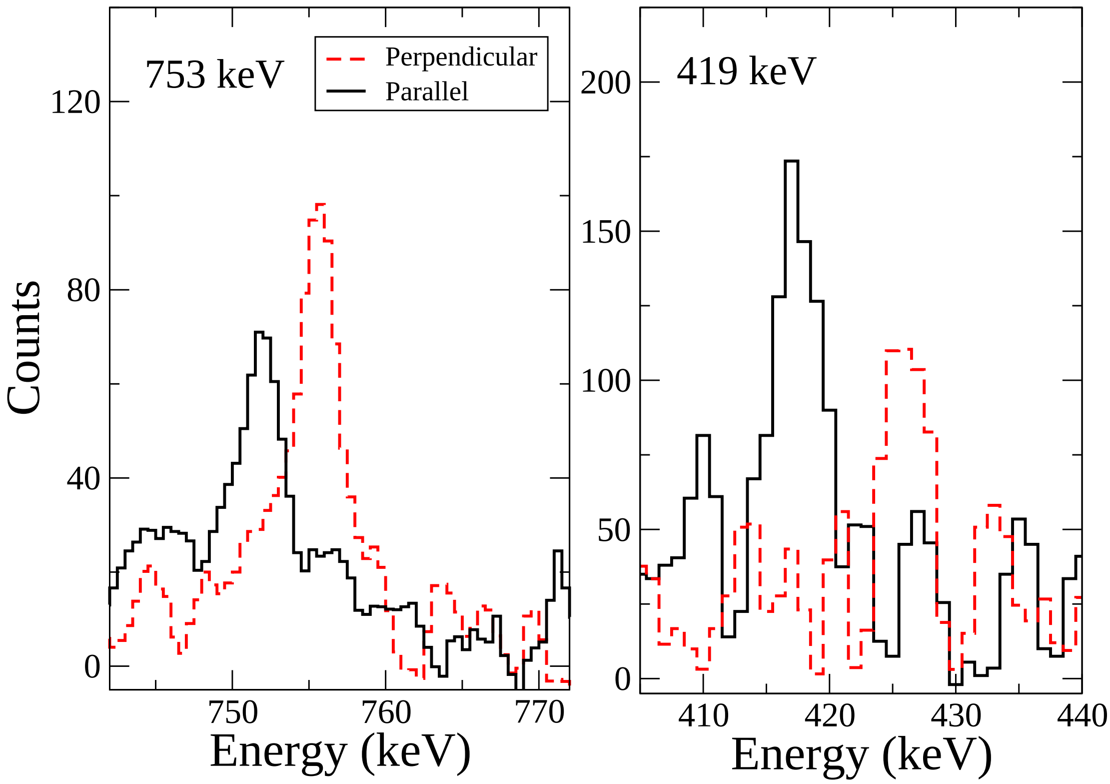

Figure 8.9: The perpendicular (dashed) and parallel (solid) components of the two γ rays in ^{134}Cs, obtained from the IPDCO analysis in the present work. The perpendicular component has been shifted in energy for clarity. The 753-keV (419-keV) γ ray can clearly be identified as electric (magnetic) type.

γ rays in this band, because of the fact that either their energies or intensities are too low. However, as these transitions are in-band with the 419-keV; the 157-, 375-, 444- and (513)-keV γ rays are considered to be M1.

The R_{DCO} value of 0.63(3) for the 681 keV γ ray transition from the 820 keV state gated by the 155 keV M1 γ ray indicates quadrupole nature of this transition. The R_{asym} value of < 1 supports this assignment. Moreover, a positive value of Δ_{IPDCO} indicates that this transition is E2 in character. Therefore, $J^{\pi} = 10^{-}$ is assigned for the level at 820 keV. The positive value of Δ_{IPDCO} for the 540 keV transition along with its dipole character, obtained from the R_{DCO} and R_{asym} values (see table 8.1), confirms the parity changing character (E1) of this transition required for its decay from a 12^{+} state to a 11^{-} state.

8.3 Discussion

8.3.1 Band B1

The band B1 is built on $J^{\pi} = 7^{-}$ level at 345 keV excitation energy. Similar bands are found in ^{130}Cs [19] and ^{132}Cs [13]. These bands are also built on $J^{\pi} = 7^{-}$ level at 375-keV and 312-keV excitation energy, respectively. Configuration of the band built on $J^{\pi} = 7^{-}$ level in ^{130}Cs [19] has been assigned as $\pi g_{7/2} \otimes \nu h_{11/2}$. The alignments plot of band B1 of ^{134}Cs along with the similar bands in ^{130}Cs [19] and ^{132}Cs [13] are shown in Fig. 8.10.

The strong coupling in these bands indicates that the higher-Ω orbitals are involved for the odd particles. The low values of single particle alignments at the band head support this (see Fig. 8.10). The low excitation energy ($\sim$ 345 keV), strong coupling and negative parity of these bands indicate that the odd-proton and odd-neutron occupy the $g_{7/2}$ and $h_{11/2}$ orbitals, respectively, which lie near the Fermi levels. Initial alignments found to be very similar for all these bands (see Fig. 8.10). Therefore, configuration of band B1 in ^{134}Cs is suggested to be $\pi g_{7/2} \otimes \nu h_{11/2}$.

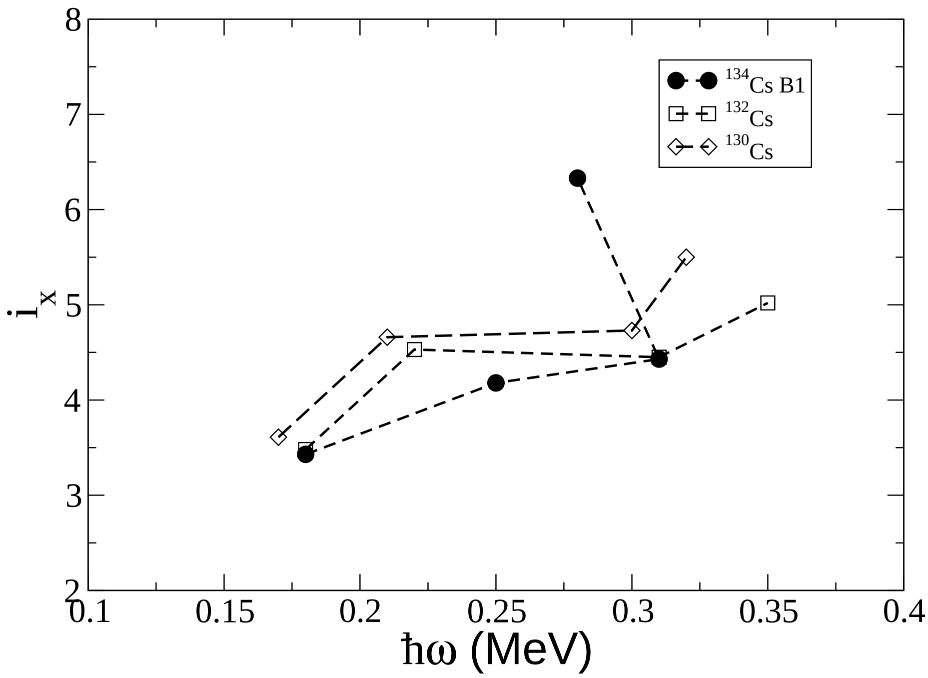

Figure 8.10: Alignment plots of band B1 as a function of the rotational frequency ($\hbar\omega$) of ^{134}Cs along with the similar bands in ^{130}Cs [19] and ^{132}Cs [13]. The Harris reference parameters are chosen to be $J_0 = 5.8\hbar^2\ MeV^{-1}$ and $J_1 = 50.8\hbar^4\ MeV^{-3}$.

8.3.2 Band B2

The band B2 of ^{134}Cs is built on $J^\pi = 9^+$ level at 1394 keV excitation energy. The low-lying negative parity states in ^{134}Cs were interpreted as the $\nu h_{11/2}$ coupled to $\pi d_{5/2}$ or $\pi g_{7/2}$ [14]. An E1 transition (753 keV), between one of these states and the 9^+ band-head, indicates that there is a change in configuration which must involve a change in parity. The spin, parity and the excitation energy of the state at 1394-keV favor a change in proton configuration from $d_{5/2}$ (or $g_{7/2}$) to $h_{11/2}$. The band head spins of the $\pi h_{11/2} \otimes \nu h_{11/2}$ configuration in the lighter odd-odd Cs isotopes are 9^+. The energy of this 9^+ state in ^{134}Cs smoothly extends the systematic of the variation of the band-head energies of the $\pi h_{11/2} \otimes \nu h_{11/2}$ configuration in an isotopic chain as described below.

Liu et al. [18] have been assigned band head spin of $\pi h_{11/2} \otimes \nu h_{11/2}$ yrast bands in odd-odd Cs isotopes by studying the smooth variation of excitation energy systematics for the $\pi h_{11/2} \otimes \nu h_{11/2}$ bands in odd-odd $^{118-132}$Cs. The variation of the excitation energy of the 9^+, 10^+, 11^+, 12^+, 13^+ and 14^+ states for the $\pi h_{11/2} \otimes \nu h_{11/2}$ bands in odd-odd Cs isotopes are shown in Fig. 8.11. The excitation energy of above states of ^{134}Cs are shown by filled circle. The level energies are rescaled with respect to the 10^+ state and 11^+ state for even spin and odd spin level, respectively. Our assignment of the 1394-keV, 9^+ state of band B2 in ^{134}Cs as the band head of the above configuration is corroborated by this smooth variation, as prescribed by Liu et al. [18] (see Fig. 8.11).

The alignments plot of band B2 of ^{134}Cs along with the $\pi h_{11/2} \otimes \nu h_{11/2}$ bands in ^{128,130,132}Cs [9, 5] are shown in Fig. 8.12. Initial alignment is found to be very similar (about $5\hbar$) for band B2 of ^{134}Cs (see Fig. 8.12) with the $\pi h_{11/2} \otimes \nu h_{11/2}$ bands in ^{128,130,132}Cs [9, 5]. Therefore, band-head configuration of band B2 in ^{134}Cs has been assigned to be $\pi h_{11/2} \otimes \nu h_{11/2}$.

The structure of the bands built on the $\pi h_{11/2} \otimes \nu h_{11/2}$ configuration in ^{128,130,132}Cs [9, 5] along with the band B2 of ^{134}Cs are shown in Fig. 8.13. Well developed $\pi h_{11/2} \otimes \nu h_{11/2}$ rotational bands have been observed for the ^{128,130,132}Cs [9, 5] isotopes. For the lighter Cs isotopes (^{128,130,132}Cs [9, 5]) these bands along with a side bands with same J^π value were

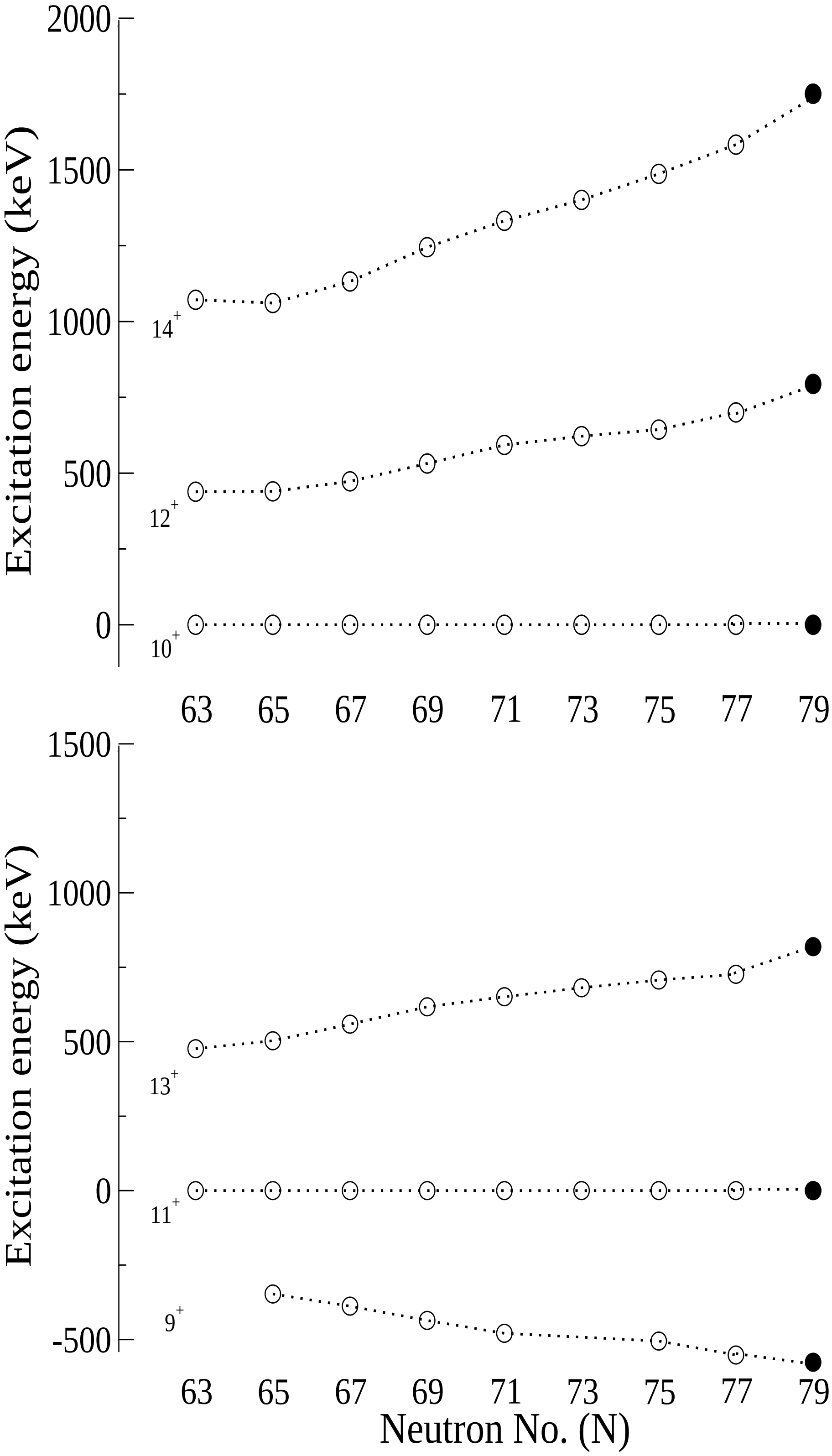

Figure 8.11: Excitation energy systematics of $\pi h_{11/2} \otimes \nu h_{11/2}$ bands in doubly odd isotopes $^{118-134}$Cs. Solid circles correspond to the present result.

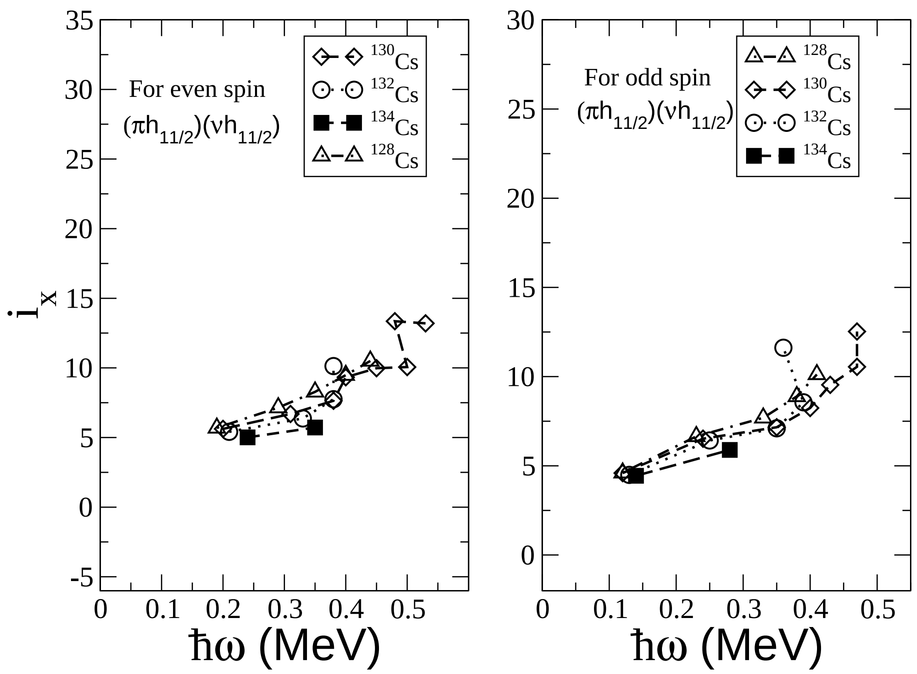

Figure 8.12: Alignment plots of band B2 as a function of the rotational frequency ($\hbar\omega$) of ^{134}Cs along with the $\pi h_{11/2} \otimes \nu h_{11/2}$ bands in ^{128,130,132}Cs [9, 5]. The Harris reference parameters are chosen to be $J_0 = 5.8\hbar^2\ MeV^{-1}$ and $J_1 = 50.8\hbar^4\ MeV^{-3}$.

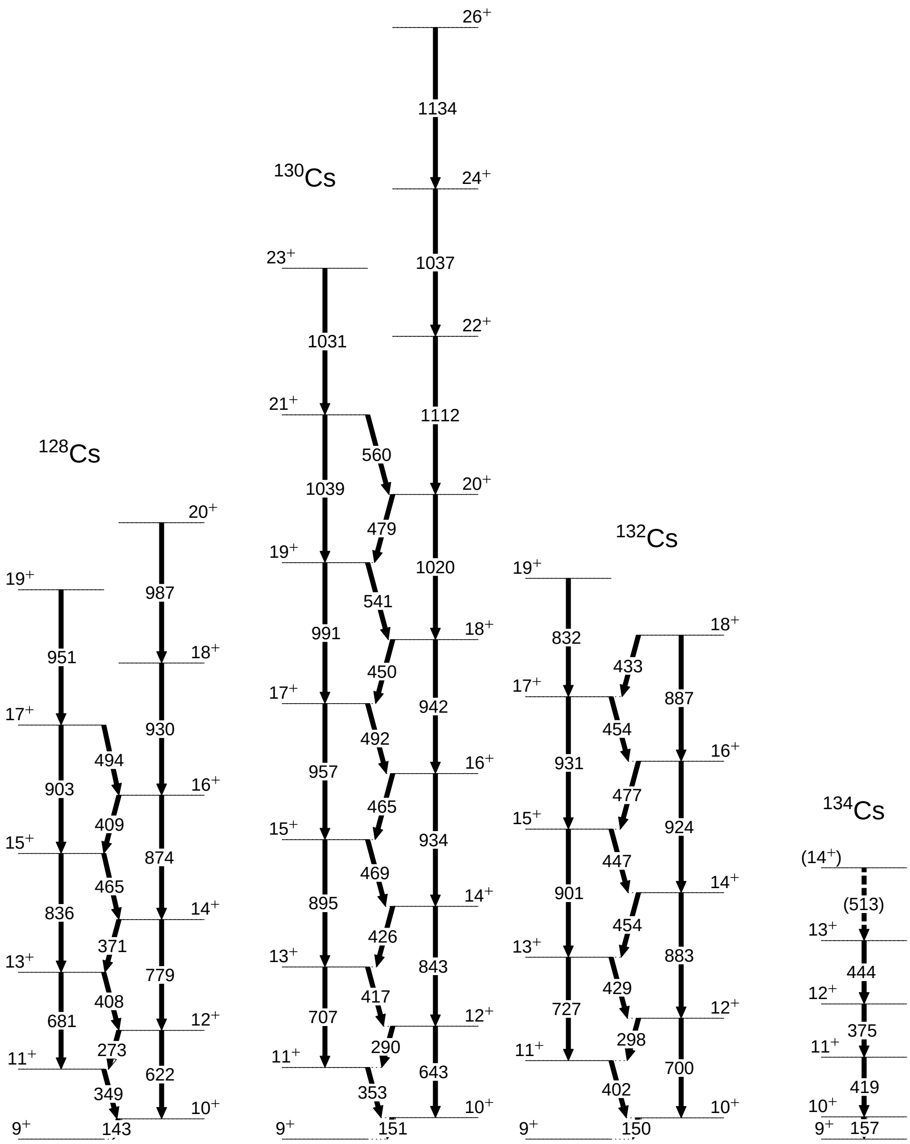

Figure 8.13: Structure of the bands built on the $\pi h_{11/2} \otimes \nu h_{11/2}$ configuration in odd-odd Cs isotopes. Data are taken from the references [11, 12, 5] for the ^{128,130,132}Cs, respectively.

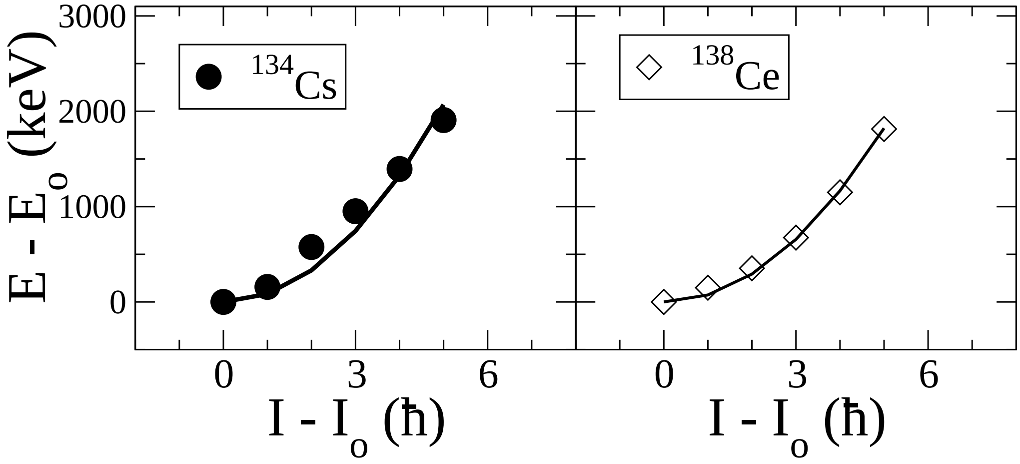

Figure 8.14: Relative energy vs. spin curves for the band built on the 9^+ band-head for ^{134}Cs (left) and for a known MR band in ^{138}Ce (right). The fitted curves are shown by the solid lines (see text for details).

interpreted as chiral partner band. The above band-like structure in ^{134}Cs looks distinctly different in nature (see Fig. 8.13), compared to the bands built on the same configuration in other lighter isotopes of Cs [9, 5]. This band in ^{134}Cs does not have the features of a well developed rotational band with E2 cross-over transitions, as observed in the lighter isotopes. A side band observed in the lighter isotopes, which was interpreted as the so called "chiral partner band", has not been observed in ^{134}Cs. Clearly, structural change of the unique-parity $\pi h_{11/2} \otimes \nu h_{11/2}$ configuration takes place in ^{134}Cs.

The features of the levels in this dipole band have been compared with the general criteria of an MR band [8, 20]. For the MR bands, the level energies (E) and the spins (I) in the band follow the pattern $E - E_o \sim A_o * (I - I_o)^2$ where, E_o and I_o are the energy and spin of the band-head, respectively and A_o is a constant. The plot of $E - E_o$ vs. $I - I_o$ is shown in Fig. 8.14, for the above band in ^{134}Cs and a known MR band, of ^{138}Ce [4], in this region. The two plots look very similar. The solid lines, in this figure, are the fitting of the data using the above relation. The good fitting for the transitions in ^{134}Cs indicates a band-like structure. Considering the upper limit of the intensities of the unobserved, crossover transitions as the level of the background in our data, the lower limit of the B(M1)/B(E2) ratio has been estimated to be $>18\ \mu^2/(eb)^2$. This compares well with the typical value of $\geq 20\ \mu^2/(eb)^2$ for an MR band. The dynamic moment of inertia $J^{(2)} \sim 16\ \hbar^2\ MeV^{-1}$ obtained for this band in ^{134}Cs, is also within the typical value of $J^{(2)} \sim 10 - 25\ \hbar^2\ MeV^{-1}$ for an MR band. All these indicate that the above band is, most likely, an MR band. This band is crossed by band B3 above 11^+ which, subsequently, becomes yrast. The small irregularity in the band around this spin value seems to be because of the interaction between the two bands. Such irregularities are, however, not uncommon for the suggested MR bands in this region [21].

The experimental observations clearly indicate that the structure of the band built on the $\pi h_{11/2} \otimes \nu h_{11/2}$ configuration, in odd-odd Cs isotopes, has been changed quite drastically from a more regular collective rotational band which resembles chiral doublet bands for N < 79 to a band like structure which resembles an MR band for $N = 79$. The quadrupole deformation (β_2) and the $\gamma-$softness plays important roles in determining the methods of generation of angular momentum in a nucleus. In order to understand the difference in the observed band structures, the shapes of the odd-odd Cs isotopes in $\pi h_{11/2} \otimes \nu h_{11/2}$ configuration have been studied by calculating the total Routhian surfaces (TRSs). The TRS were calculated in $\beta_2 - \gamma$ deformation mesh points and minimized in hexadcapole deformation β_4. The representative contour plots of the TRSs are shown in Fig. 8.15 for ^{126}Cs and ^{134}Cs in the $\pi h_{11/2} \otimes \nu h_{11/2}$ configuration. Fig. 8.15 shows that the $\gamma-$ softness is much larger for heavier isotope ^{134}Cs than in ^{126}Cs, for which a stable triaxial minimum is realized.

The variation in the TRS energies, E_{TRS} (relative to the minimum), for the above configuration, is shown in Fig. 8.16 as a function of the triaxiality parameter γ for the odd-odd Cs isotopes. The β_2 values (shown in the inset as a function of mass number A), for these, were kept close to the minimum of the TRS. It can be seen from Fig. 8.16 that ^{126}Cs has a minimum close to $\gamma \sim -30^o$. As the neutron number increases, another minimum near $\gamma \sim -90^o$ appears. The two minima, however, are separated by a well defined barrier which vanishes for the neutron rich isotopes of ^{134}Cs and ^{136}Cs. In other words, while there are stable triaxial shapes for lighter isotopes, the energy surfaces become more and more $\gamma-$soft as the neutron number increases. It is also observed from the inset that β_2 decreases gradually for the heavier isotopes; which is expected as the neutron number approaches the N = 82 shell closure.

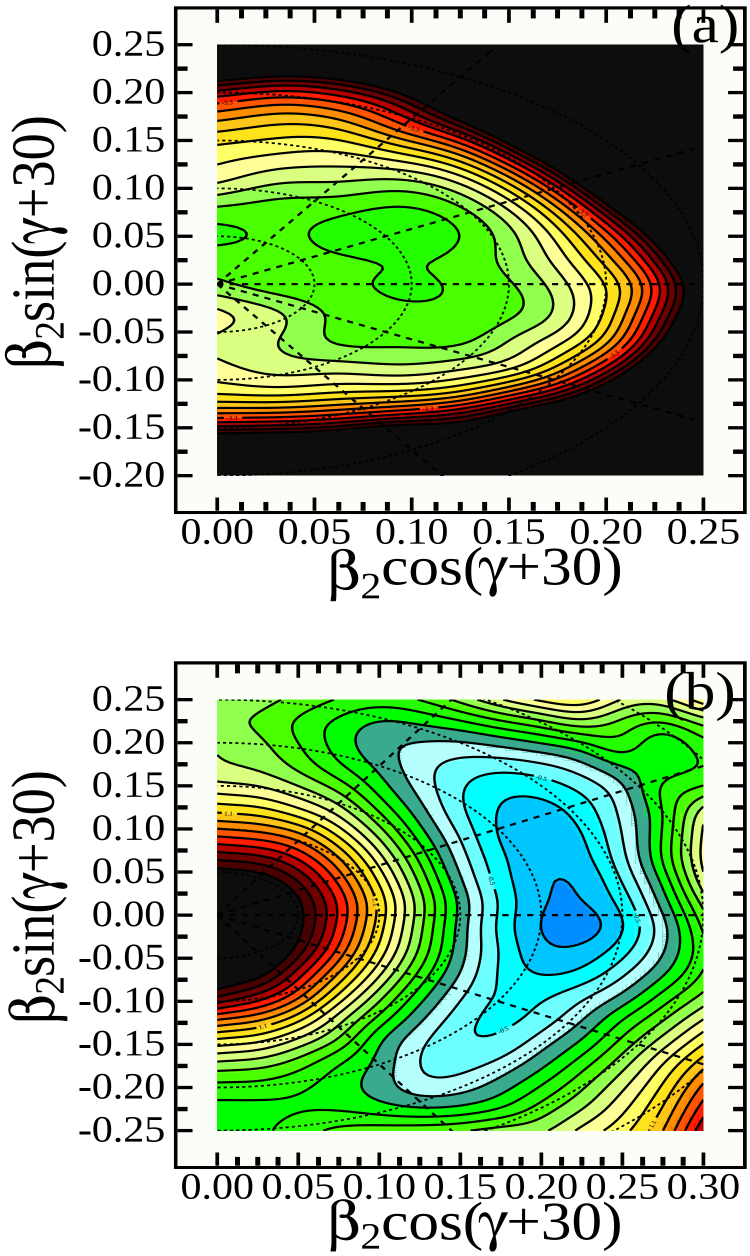

Figure 8.15: Contour plots of the Total Routhian Surfaces (TRSs) in the β_2 - γ deformation mesh for the $\pi h_{11/2} \otimes \nu h_{11/2}$ configuration calculated at rotational frequency $\hbar\omega = 0.2$ MeV in ^{134}Cs (a) and in ^{126}Cs (b). The contours are 150 keV apart.

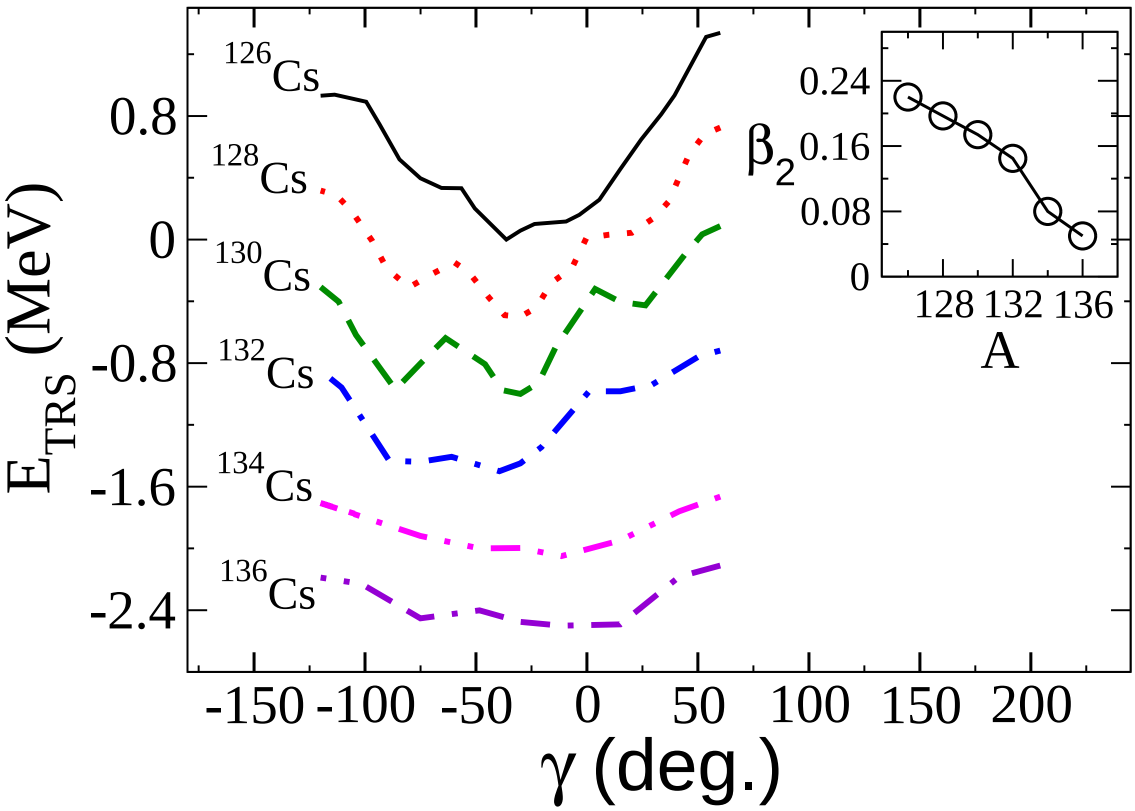

Figure 8.16: The calculated TRS energies, E_{TRS} (relative to the minimum) as a function of the triaxiality parameter γ for the odd-odd Cs isotopes in $\pi h_{11/2} \otimes \nu h_{11/2}$ configuration. An offset is given to each plot for clarity. The calculated values of the deformation β_2, obtained from the minimum of the TRS, are shown in the inset for those isotopes.

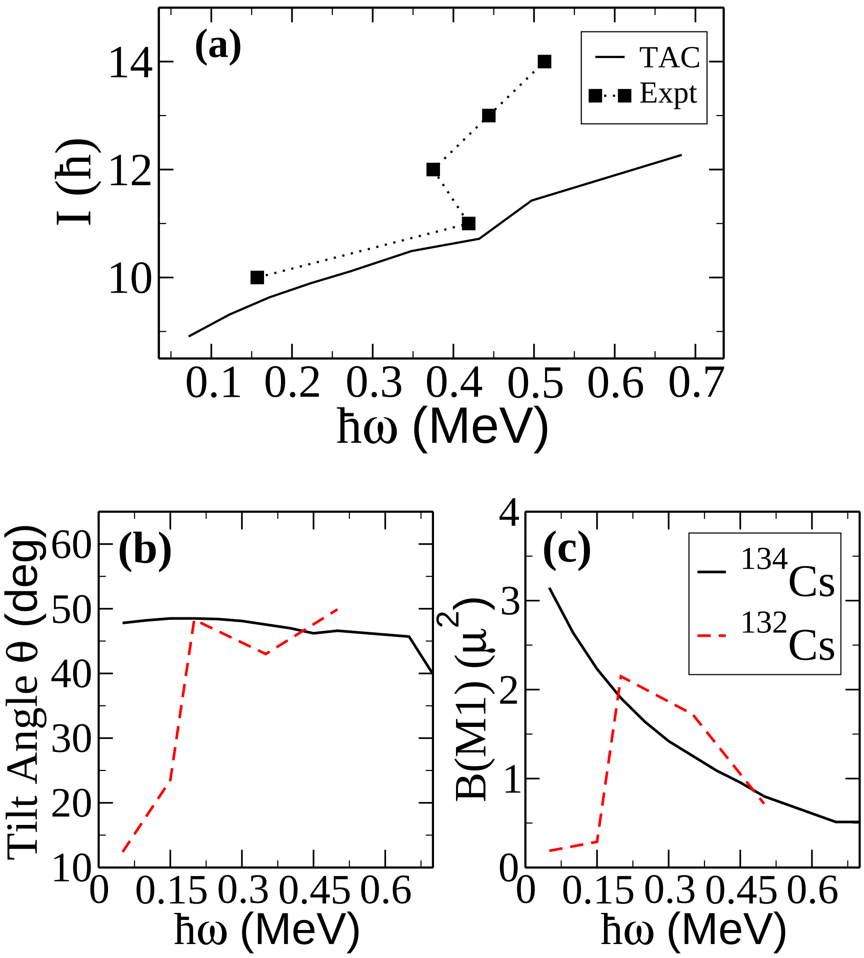

Figure 8.17: Results of the TAC calculations for the $\pi h_{11/2} \otimes \nu h_{11/2}$ bands in ^{132,134}Cs. (a) Experimental and calculated plots of frequency ($\hbar\omega$) vs. spin (I) for ^{134}Cs. (b) & (c) Tilt angle & B(M1) values as a function of $\hbar\omega$ for ^{134}Cs (solid line) and ^{132}Cs (dashed line).

The stable triaxial deformation, together with the relatively large β_2 value (between 0.22 and 0.15), favors the regular collective rotational like structure to dominate for $^{126-132}$Cs as has been reported [9]. On the other hand, ^{134,136}Cs are very $\gamma-$soft and $\beta_2 < 0.1$. The lack of substantial quadrupole deformation is reflected in the absence of E2 transitions in ^{134}Cs. Moreover, as the neutron number increases, neutron Fermi level moves towards the upper part of the $h_{11/2}$ subshell and neutron holes are created in the high$-\Omega$ orbital. These are favorable conditions for the onset of shears mechanism in ^{134,136}Cs. A band structure, similar to ^{134}Cs, is expected in ^{136}Cs as well.

The Tilted Axis Cranking (TAC) calculations [6, 22, 23, 24, 25] have been carried out for the $\pi h_{11/2} \otimes \nu h_{11/2}$ configuration in ^{134}Cs and ^{132}Cs. The planar hybrid version of the TAC was used for the calculations. The procedure has been outlined in ref. [21, 26]. The Woods-Saxon potential, with universal parameters, was used in these calculations also. The pairing parameters for protons and neutrons were chosen as 80% of the odd-even mass difference. These calculations produce minimum at a deformation of $\epsilon_2 = 0.072$ for ^{134}Cs, in good agreement with the TRS calculations. Fig. 8.17 shows the results of the TAC calculations. The experimental and calculated plots of cranking frequency $\hbar\omega$ vs. spin (I), for the above band in ^{134}Cs (Fig. 8.17(a)), have reasonably good agreement for the lower spin states before the band crossing. An average tilt angle of $\theta = 48.3^o$ is obtained for ^{134}Cs in the TAC calculations which remains remarkably constant throughout the band as shown in Fig. 8.17(b). The calculated B(M1) values for ^{134}Cs decrease with frequency, as shown in Fig. 8.17(c), which is a typical characteristic of a shears (MR) band. However, the calculations for ^{132}Cs, shown also in Fig. 8.17(b) and 8.17(c) (dotted lines), show contrasting behaviors, at least at the lower frequencies. Therefore, the TAC calculations clearly suggest that the $\pi h_{11/2} \otimes \nu h_{11/2}$ band in ^{134}Cs behaves differently than its immediate odd-odd neighbour ^{132}Cs. Hence, it may be concluded that there is a change of character of the $\pi h_{11/2} \otimes \nu h_{11/2}$ configuration at N = 79 for the odd-odd Cs isotopes, which can be understood as a change in shape from both the TRS and the TAC calculations.

8.3.3 Band B3

The band B3 is built on $J^\pi = 12^+$ level at 2097-keV excitation energy. Similar bands are identified in ^{132}Cs [5] and ^{134}La [27] with $\pi g_{7/2} \otimes \nu g_{7/2} h^2_{11/2}$ configuration. The plot of excitation energy vs. spin for B2 and B3 of ^{134}Cs are shown in Fig. 8.18. The solid line are the fits of the data using the rigid rotor formula A0 + A1*I(I+1). The band B3 crosses the 2-quasipartcle band B2 around 11^+ and becomes yrast. It indicates, 4-quasipartcle configuration involved in band B3. Therefore, configuration of band B3 in ^{134}Cs is suggested to be $\pi g_{7/2} \otimes \nu g_{7/2} h^2_{11/2}$.

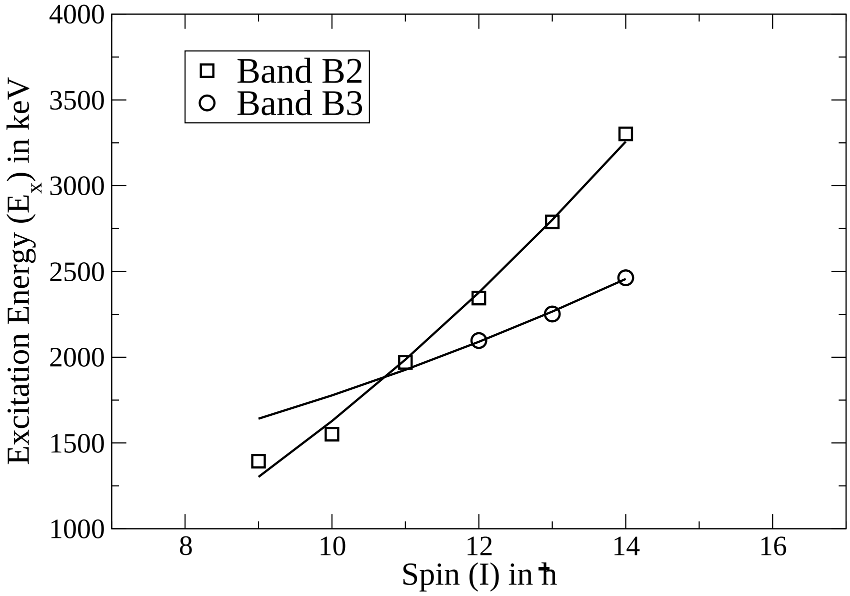

Figure 8.18: E_x vs. I plot of bands B2 and B3 in ^{134}Cs.

8.3.4 Band B4

The band B4 is similar to the observed doubly decoupled bands in the isotones ^{136}La [16] and ^{138}Pr [28]. For an odd-odd nucleus double decoupling can occur only if Fermi levels for both proton and neutron lie near the $\Omega = 1/2$ states [29]. Thus, as in ^{138}Pr [28], the neutron in the $h_{11/2}$ orbit in ^{134}Cs is decoupled and this is only possible for an oblate deformation. Decoupling for the proton would be obtained in the $\pi[431]1/2^+$ orbital of $d_{5/2}$ parentage for an oblate deformation. Therefore, we have assigned the $\pi[431]1/2^+ \otimes \nu h_{11/2}$ configuration, for band B4, with the band head given by $I^\pi = j^p + j^n = 5/2 + 11/2 = 8^-$.

8.4 Summary

A new and improved level scheme of ^{134}Cs, compared to the previously known ones [9], has been proposed up to an excitation energy of 3.85 MeV with 32 new γ rays identified and placed in the level scheme. Definite spin and parities of the levels are assigned from the DCO, R_{asym} and IPDCO measurements. Four band structures have clearly been observed in this odd-odd nucleus with neutron and proton numbers close to the spherical magic numbers and configuration have also been proposed for these bands. The $\pi h_{11/2} \otimes \nu h_{11/2}$ band (B2) has been identified and characterized for the first time in ^{134}Cs. The present experimental observations indicate that the structure of the band built on this configuration for ^{134}Cs is distinctly different from its lighter odd-odd isotopes. The nearly degenerate rotational doublet band structure (chiral band), observed for the lighter odd-odd isotopes of Cs, does not persist in the $N = 79$ isotope ^{134}Cs. The TRS and the TAC calculations support the observed change in the band structure. The TAC calculations indicate a possible MR nature for this configuration in ^{134}Cs, in sharp contrast to ^{132}Cs. However, to establish the explicit nature of this change, in particular a possible transition from an aplanar configuration for $N < 79$ to a planar configuration for $N \geq 79$, more experimental work and detailed 3-D TAC calculations are needed. Band B1 looks like a strongly coupled band, where as band B4 has been interpreted as doubly decoupled band. For band B3, 4-quasipartcle configuration has been proposed.

Bibliography

[1] K. Starosta et al., Nucl. Phys. **A 682**, 375c (2001).

[2] C.M. Petrache et al. Z. Phys. **A 344**, 227 (1992); C.M. Petrache et al., Nucl. Phys. **A 597**, 106 (1996).

[3] C.W. Beausang et al., Nucl. Phys. **A 682**, 394c (2001).

[4] T. Bhattacharjee et al., Nucl.Phys. **A 825**, 16 (2009).

[5] G. Rainovski et al., Phys. Rev. **C 68**, 024318 (2003).

[6] S. Frauendorf, Rev. Mod. Phys. **73**, 463 (2001).

[7] H. Hubel, Prog. Part. Nucl. Phys. **54**, 1 (2005).

[8] R.M. Clark and A.O. Macchiavelli, Annu. Rev. Nucl. Part. Sci. **50**, 1 (2000).

[9] T. Koike et al., Phys. Rev. **C 67**, 044319 (2003).

[10] S. Wang et al., Phys. Rev. **C 74**, 017302 (2006)

[11] E. Grodner et al., Phys. Rev. Lett. **97**, 172501 (2006).

[12] A.J. Simons et al., J. Phys. G: Nucl. Part. Phys. **31**, 541 (2005).

[13] G. Rainovski et al., J. Phys. G: Nucl. Part. Phys. **29** 2763 (2003).

[14] M. Bogdanovic et al., Nucl. Phys. **A 470**, 13 (1987).

[15] V.L. Alexeev et al., Nucl. Phys. **A 248**, 249 (1975).

[16] T. Bhattacharjee et al., Nucl. Phys. **A 750** 199 (2005).

[17] S. Chanda et al., Nucl. Phys. **A 775** 153 (2006).

[18] Y. Liu et al., Phys. Rev. **C 58**, 1849 (1998) & ibid. **C 54**, 719 (1996).

[19] P.R. Sala et al., Nucl. Phys. **A 531**, 383 (1991).

[20] A. K. Jain et al., Pramana **75**, 51 (2010).

[21] S. Kumar et al, Phys. Rev. **C 76**, 014306 (2007).

[22] S. Frauendorf, Nucl. Phys. **A 557**, 259c (1993).

[23] S. Frauendorf, Nucl. Phys. **A 667**, 115 (2000).

[24] S. Kumar, Private communication (2011).

[25] H. Pai et al., Phys. Rev. **C84**, 041301 (R) (2011).

[26] P. Agarwal et al., Phys. Rev. **C76**, 024321 (2007).

[27] R.A. Bark et al., Nucl. Phys. **A 691**, 577 (2001).

[28] M.A. Rizzutto et al., Z. Phys. **A 344**, 221 (1992).

[29] A.J. Kreiner - "Proceedings of the IV Workshop in Nuclear Physics", Buenos Aires, Argentina, 1986, ed. A.O. Macchiavelli (World Scientific Pub.Co.Pte.Ltd., Singapore, 1987), p. 337

Chapter 9

Summary and outlook

9.1 Summary

In the present thesis work, high spin level structures of ^{194}Tl, ^{195}Bi, ^{197}Tl and ^{198}Bi nuclei belonging to the A $\sim$ 190 region (near Z = 82) and of ^{134}Cs nucleus belonging to the A $\sim$ 130 region (near N = 82), have been investigated using the technique of high resolution γ-ray spectroscopy. The high spin level schemes in these nuclei have been improved considerably in the form of extension to higher angular momentum and excitation energy, observation of new band structures, identification of band crossing, determination of definite spin and parity of levels, comparison of the newly observed bands and levels with the systematics of the neighboring nuclei and interpretation of the new level structures in the light of contemporary theoretical calculations.

The excited states of these nuclei were populated by using both heavy and light (α beam from VECC cyclotron) ion induced fusion-evaporation reactions. Most of the data in this thesis work were taken using different configurations of Indian National Gamma Array (INGA) at the different accelerator centres in India i.e VECC, Kolkata; TIFR, Mumbai and at IUAC, New Delhi using heavy ion beams. Apart from those the excited states in ^{197}Tl were studied by α induced reactions, using the modest in-house facility of γ detectors at VECC, Kolkata.

CAMAC based data acquisition system was used in most of the experiments while digital signal processing (DSP) system was used in one of the experiments in this thesis work performed during the last campaign of INGA at TIFR, Mumbai. The trigger for collecting data was set when two or more clovers were fired in an event. In the analysis, $\gamma - \gamma$ coincidence matrix and $\gamma - \gamma - \gamma$ coincidence cube were constructed for obtaining coincidence relations among the $\gamma-$rays and, thereby, to build the level schemes. Definite spins and parities of the levels were assigned from the DCO and polarization measurements. For these later analysis, angle dependent asymmetry matrices were created.

The results obtained in this thesis work, were interpreted in the frame work of cranked shell model calculations using Woods-Saxon potential including pairing correlation and Struntisky shell correction. The total Routhian surfaces (TRS) were calculated using this model in the $\beta_2-\gamma$ deformation mesh points with minimization on hexadecapole deformation β_4. The minima in these plots give the equilibrium deformation of a nucleus. Such calculations were performed for different configurations for Thallium and Bismuth nuclei in mass region $A \sim 190$ and in Cesium nuclei in mass region $A \sim 130$. Moreover, for the proposed magnetic rotational (MR) bands, calculations based on a semiclassical approach were performed. In these calculations, the effective interaction per particle-hole pair has been obtained for the configuration on which the magnetic rotational band is built upon.

A new and improved level scheme of odd-odd ^{194}Tl has been established in this work which includes 19 new γ ray transitions. The $\pi h_{9/2} \otimes \nu i_{13/2}$ band (B1) in this nucleus has been extended beyond the band crossing and it has been properly characterized and discussed in the frame work of TRS calculations. In a previous work, the above band was identified but there were uncertainties in the excitation energies and spins, which have been removed and definite excitation energies, spins and parities were determined for this band in the present work. This band has been compared with the similar bands based on the same configuration in other odd-odd isotopes ^{190}Tl [1] and ^{198}Tl [2] for which complete spectroscopic information are known. Remarkable similarities have been found in the moments of inertia, band crossing frequencies and the staggering plots in these three isotopes. This suggest similar structure for all these Thallium nuclei and there by raising a question on the possible chiral band which has been recently reported in ^{198}Tl [2]. Two new side bands (B2 and B3) have also been identified in ^{194}Tl for the first time in this thesis work. One of them, a six quasiparticle band, has been identified as an MR band and has been discussed in the frame work of the semiclassical approach. It may be noted that the MR band observed in ^{194}Tl, in this work, is the first and only MR band identified in Thallium isotopes.

A rotational band built on a $13/2^+$ band head has been identified in ^{195}Bi, similar to those observed in the lighter isotopes ^{191,193}Bi and much dissimilar to the heavier ^{197}Bi, suggesting that onset of deformation takes place in the isotopic chain of Bi nuclei at $N = 112$. In other words, the neutron number $N = 112$, at which the neutron $i_{13/2}$ orbital starts to open up for neutron holes, may be considered as the border of sphericity in Bi isotopes. TRS calculations for the $13/2^+$ configurations in ^{195}Bi support this onset of deformation. The excitation energy for the $29/2^-$ isomer in this nucleus has been proposed, in this work, for the first time as 2396 keV. This has been found to be consistent with the systematic trend of the energy of this isomer in the neighboring odd-A Bi isotopes.

In ^{197}Tl, the intruder $\pi i_{13/2}$ state could be established for the first time, through polarization and DCO measurements. We have assigned negative parity for the band B2 from polarization measurements and a new configuration has been proposed for this band.

In a previous work, three MR bands were proposed to be belong to ^{198}Bi but no connection were established with the lower lying states in this nucleus. Therefore, it raises questions on the origin of those bands. In the present work, these MR bands (B1, B2 and B3) have been connected to the lower-lying states for the first time. The excitation energy of these bands could be established as these are now connected with the known excited states in this nucleus. Moreover, the configuration of these bands could be proposed as definite J^{π} assignments were made, in this work, for the states in these three bands. The bands B1 and B2 were discussed in the frame work of a semiclassical approach and the band B3 does not seem to satisfy the criteria of a MR band.

The high spin structure of ^{134}Cs nucleus with neutron number close to the magic number N = 82 has also been studied extensively in this thesis work. A new and much improved level scheme of ^{134}Cs, has been proposed up to an excitation energy of 3.85 MeV with the identification of 32 new γ rays. Four band structures have been observed in this odd-odd nucleus and the configurations have also been proposed for these bands. The most interesting among those bands is the unique parity $\pi h_{11/2} \otimes \nu h_{11/2}$ band (B2). This has been identified and characterized for the first time in ^{134}Cs. This particular band in ^{134}Cs looks very different than the same band in lighter Cs isotopes. This band has the characteristic of a MR band in sharp contrast to the bands built on the same configuration observed in the lighter odd-odd isotopes of Cs which were interpreted as chiral bands. The Tilted Axis Cranking (TAC) calculations also support the observed change in the band structure. From the TRS calculations, this structural change in Cs isotopes has been understood as due to the increase in γ-softness of the potential energy surface for the Cs isotopes with increasing neutron number. This structure is also consistent with the near spherical shape obtained for ^{134}Cs from the TRS calculations. Therefore, it signifies the onset of sphericity in Cs (Z = 55) isotopes at neutron number N = 79. In other words, the N = 77 defines the border of the well deformed structure in A $\sim$ 130 region while approaching N = 82 shell closures.

9.2 Future outlook

The encouraging results of the present thesis work open up possibility of further studies in this direction both experimentally and theoretically, such as:

In the study of ^{134}Cs, an interesting observation has been made that there is a sharp change in the structure of the band based on $\pi h_{11/2} \otimes \nu h_{11/2}$ configuration. The TAC calculation suggest that this structural change might be associated with a transition from chiral to magnetic rotation for the above configuration for N $\geq$ 79. However, the confirmation of chirality and MR nature of bands can only be obtained from the transition strengths (B(M1) and B(E2)) measurements. The lifetime of a state is inversely proportional to the transition strength. Therefore, it is important to measure the lifetime of the states of the $\pi h_{11/2} \otimes \nu h_{11/2}$ bands in the Cs isotopes. So, one of the future plan is to do transition strength measurement systematically for the odd-odd Cs isotopes from ^{130}Cs to ^{134}Cs. On the other hand, to establish the explicit nature of this change, detailed 3-D TAC calculations need to be performed for these nuclei with above configurations. Moreover, as predicated by the TRS calculations, performed in this thesis work, the $\pi h_{11/2} \otimes \nu h_{11/2}$ band in neutron rich ^{136}Cs should behave like ^{134}Cs with even more γ-softness. Therefore, it will be interesting to study the high spin states in ^{136}Cs. This can, however, be possible by deep inelastic collision experiment with ^{133}Cs beam bombarded on e.g. ^{208}Pb target at energies about 15-20 percent above the Coulomb barrier. This can be achieved using the beams from the superconducting cyclotron at VECC in near future.

On the other hand, the present thesis work has opened up the possibilities of further experimental and theoretical investigations on the structure of the high spin states in nuclei in $A \sim 190$ region. As mentioned earlier, similar band structures have been observed for the $\pi h_{9/2} \otimes \nu i_{13/2}$ configuration in ^{190,194,198}Tl although a different mechanism (chiral symmetry breaking) and a different shape (triaxial) has been reported for ^{198}Tl [2] compared to its lighter isotopes. Therefore, more experimental investigations are warranted not only to study the similar band structure in other odd-odd Tl nuclei but also, in the form of lifetime measurements of the states in this band. Also, more theoretical calculations need to be performed for the interpretation of the band structures in these nuclei particularly if very different origin is found for the very similar band structures. Moreover, the first MR band in Tl nuclei observed for the six quasi-particle configuration in ^{194}Tl, has opened up the possibilities of observing several other MR bands in Tl and Bi nuclei in this region. The high spin states in heavier Thallium isotopes may be populated using $\alpha-$induced fusion evaporation reactions. Therefore, these nuclei may be studied with INGA detector array at VECC using the high energy and high intensity α beam from the K-130 cyclotron.

In ^{195}Bi, a rotational level built on $13/2^+$ state has been observed in this work. Besides that the excitation energy of the 750 ns isomer has been established in this work. However, the experimental data on ^{195}Bi, taken in this work, suggest that there should exist more isomeric levels at high spin with halflives more than a few hundreds of nano-sec as the intensities of the γ rays from the states above 2 MeV were found to fall sharply in the prompt data. It would be interesting to search for the high spin isomeric levels in this nucleus. Moreover, not much is known for the high spin states above the isomer in ^{195}Bi and in other odd-odd isotopes of Bi. Therefore, it will indeed be interesting to study the high spin states in these nuclei. The decay of about a micro-sec isomer may be studied using the recoil spectrometer (e.g HYRA at IUAC, New Delhi) and a γ detector array at the focal plane. To study the high spin states above such isomers, recoil decay tagging techniques may be employed using INGA coupled to HYRA.

This thesis work strongly supports the fact that, 'till date nuclear physics remains an interesting subject and by no means a finished edifice'.

Bibliography

[1] C.Y. Xie et al., Phys. Rev. **C 72**, 044302 (2005).

[2] E.A. Lawrie et al., Phys. Rev. **C 78**, 021305(R) (2008).